

Fermi Edge Polaritons Formed by Electron-Hole Pairs Interacting with Cavity-Confining Photons

Yossi Michaeli

Fermi Edge Polaritons Formed by Electron-Hole Pairs Interacting with Cavity-Confining Photons

Research Thesis

Submitted in Partial Fulfillment of the Requirements for the
Degree of Master of Science in Physics

Yossi Michaeli

Submitted to the Senate of the Technion-Israel
Institute of Technology

Adar 5766 Haifa December 2010

Contents

Contents	iii
List of Figures	vi
List of Tables	x
Abstract	1
List of Symbols	2
1 Introduction	5
2 Electronic Properties of Semiconductors	6
2.1 Crystal Schrödinger Equation	6
2.1.1 Introduction	6
2.1.2 Bloch's Theorem	8
2.1.3 The $\mathbf{k} \cdot \mathbf{p}$ Method	8
2.1.3.1 Introduction	8
2.1.3.2 Löwdin-Renormalization	9
2.2 The $\mathbf{k} \cdot \mathbf{p}$ Envelope Function Method	10
2.2.1 Introduction	10
2.2.2 $\mathbf{k} \cdot \mathbf{p}$ Envelope Function Ansatz	11
2.2.3 The Zinc-Blende Models	12
2.2.3.1 Direct Interaction	12
2.2.3.2 Remote Contributions	13
2.2.3.3 Spin-Orbit Interaction	14
2.2.4 Two Band Model	17
2.3 Schrödinger-Poisson Model	22
2.3.1 Model Formulation	23
2.3.2 Two-Dimensional Electron Gas	28
3 Free Carriers Optical Transitions	35
3.1 Second Quantization	35
3.1.1 Introduction	35
3.1.1.1 Single Particle Hamiltonian	36
3.1.1.2 Two Particle Hamiltonian: Coulomb Interaction	37
3.1.1.3 Particle – Electromagnetic Field Interaction Hamiltonian	37
3.1.2 Bloch States Formulation	38
3.1.2.1 Normalization	38
3.1.2.2 Lattice-Cell Average	39
3.1.2.3 The Kinetic Term	39
3.1.2.4 The Interaction Term	39
3.1.3 Introduction of Holes	40

3.1.4 Carrier Statistics	41
3.2 Transitions Calculation	41
3.2.1 Introduction	41
3.2.2 Quantum Microscopic Polarization	43
3.2.3 Heisenberg's Equation of Motion	43
3.2.4 Solving the Equation for Free Carriers	45
3.3 Spontaneous Emission	46
3.4 Dipole Matrix Element	47
4 Coulomb Correlated Optical Transitions	51
4.1 Second Quantization	51
4.1.1 Introduction	51
4.1.2 Diagonal Approximation	53
4.1.3 Introduction of Holes	53
4.2 Transitions Calculation	54
4.2.1 Equations of Motion	54
4.2.2 Hartree-Fock Approximation	55
4.2.3 Many-Body Effects	57
4.2.3.1 Background Screening	57
4.2.3.2 Plasma Screening	57
4.2.3.3 Coulomb Hole Self Energy	59
4.2.3.4 Screened Exchange Energy	59
4.2.4 Solving the Correlated Equation	59
4.2.5 Implementation Considerations	60
4.3 Numerical Results	65
4.3.1 Bare Quantum Well	66
4.3.2 Doped Quantum Well	71
5 Semiconductor Microcavities and Polaritonic Effect	91
5.1 Optical Resonator	91
5.2 Distributed Bragg Reflector	93
5.2.1 Transfer Matrix Method (TMM)	94
5.3 Microcavity Optical Characteristics	97
5.3.1 Microcavity Reflection Spectrum	97
5.3.2 Microcavity Confined Photon	99
5.4 Microcavity Polaritons	99
5.4.1 Strong Absorber-Photon Coupling	100
5.4.1.1 Single Two-Level System	100
5.4.1.2 Multiple Two-Level Systems	102
5.4.1.3 Coupled Harmonic Oscillator	103
5.4.2 Strong Coupling in a Semiconductor Microcavity	103
5.4.2.1 Coupled Oscillator Model	103
5.4.2.2 Linear Dispersion Model and Beyond	104
5.5 Numerical Results	106
5.5.1 Bare Microcavity	106
5.5.2 Embedded Undoped QW	108
5.5.3 Embedded Doped QW	112
Summary and Outlook	128
A Symmetry Properties of Wavefunctions	131
B Two-Band Model Numerical Implementation	134
C Self-Consistent Solution of Schrödinger -Poisson Model	139

D Lindhard Screening Model	141
E Bandgap Energy Modeling of Semiconductors	144
E.1 Temperature dependence of the bandgap	144
E.2 Semiconductor Alloys	145
F Refractive Index of $Al_xGa_{1-x}As$ Alloy	148
Bibliography	151

List of Figures

2.1	Schematic representation of electronic functions in a crystal.	8
2.2	Schematic band structure classification in the Löwdin perturbation theory.	10
2.3	Band structure of bulk $GaAs$ around the Γ point at room temperature, calculated using the 8×8 $\mathbf{k} \cdot \mathbf{p}$ for two crystal directions.	15
2.4	Contours of constant energy within any [100] plane of k -space for the heavy and light hole subbands in bulk $GaAs$	19
2.5	The "in-plane" subband structure of the quantum well in the conduction band.	20
2.6	The valence subband dispersion relations and boundary conditions at the interfaces of the well.	20
2.7	Example to a 200 Å wide $GaAs/Al_{0.1}Ga_{0.9}As$ undoped quantum well valence subbands dispersion relation calculation and the appropriate density of states.	21
2.8	Example to a 200 Å wide $GaAs/Al_{0.1}Ga_{0.9}As$ quantum well conduction subbands dispersion relation calculation and the appropriate density of states.	22
2.9	Wavefunctions of the conduction and valence subbands, calculated for an undoped 200 Å wide $GaAs/Al_{0.1}Ga_{0.9}As$ quantum well.	23
2.10	Electric field strength from an infinite plane of charge of volume density $d(z)$ and thickness δz	24
2.11	Areal charge density a for a 100 Å $GaAs$ well, n -type doped to $2 \times 10^{18} cm^{-3}$, surrounded by undoped $Al_{0.2}Ga_{0.8}As$ 4 meV barriers.	25
2.12	The electric field strength \mathbf{E} due to the charge distribution shown in Fig. 2.11.	25
2.13	The potential due to the ionized donor/electron charge distribution shown in Fig. 2.11.	26
2.14	Block diagram illustrating the process of self-consistent iteration.	27
2.15	The sum of the band-edge potential V_{CB} and Poisson's potential V_p for single quantum well for the charge distribution shown in Fig. 2.11.	27
2.16	The band-edge potential and the self-consistent potential of a modulation-doped single quantum well.	28
2.17	The structure and band diagram of a modulation-doped heterojunction between $GaAs$ and $n-AlGaAs$	29
2.18	Schematic illustration of a semiconductor substrate and an epitaxial film containing a δ -doping layer.	29
2.19	Volume charge density a for a 200 Å $GaAs$ well, surrounded by $Al_{0.1}Ga_{0.9}As$ barriers, doped with two symmetrical δ -doping layers located 1000 Å from the well.	29
2.20	The band-edge potential and the self-consistent potential of a δ -doped single quantum well described in Fig. 2.19.	30
2.21	A schematic diagram of a $GaAs/AlAs$ mixed type I - type II QWs structure.	30
2.22	The calculated dispersion relations for the conduction and valence subbands, for a 200 Å wide $GaAs/Al_{0.1}Ga_{0.9}As$ quantum well at $T = 2 K$, with various 2DEG concentrations in the well region.	32
2.23	The calculated wavefunction for the conduction, valence heavy and light hole subbands for 200 Å wide $GaAs/Al_{0.1}Ga_{0.9}As$ quantum well at $T = 2 K$ with $1 \times 10^{10} cm^{-2}$ 2DEG concentration.	33
2.24	The calculated wavefunction for the conduction, valence heavy and light hole subbands for 200 Å wide $GaAs/Al_{0.1}Ga_{0.9}As$ quantum well at $T = 2 K$ with $1 \times 10^{11} cm^{-2}$ 2DEG concentration.	34
3.1	Dependence of the transition strength $ \mu_{\mathbf{k}} $ on the angle between the electron \mathbf{k} -vector and the electric field polarization vector \mathbf{E}	49
3.2	Dipole matrix elements calculated for 200 Å wide $GaAs/Al_{0.1}Ga_{0.9}As$ quantum well at $T = 2 K$, without additional doping.	50

3.3	Dipole matrix elements calculated for 200 Å wide $GaAs/Al_{0.1}Ga_{0.9}As$ quantum well at $T = 2K$, containing 2DEG with various concentrations.	50
4.1	Infinite hierarchy of operator products for the equations of motion.	55
4.2	Schematic representation of the Hartree-Fock approximation operator product in the equation of motion.	55
4.3	Outline of an approach that takes advantage of a phenomenological derivation of plasma screening, which is incorporated directly into the many-body Hamiltonian to give the screened Hartree-Fock equations.	58
4.4	The screening dielectric function $\epsilon(q)$ calculated for the 200 Å wide $GaAs/Ga_{0.9}Al_{0.1}As$ well with $n_e = 1 \times 10^9 \div 1 \times 10^{11} cm^{-2}$ at $T = 2K$	61
4.5	Calculated Coulomb-hole self energy and screened-exchange shift energy at the Brillouin zone center, for the 200 Å wide $GaAs/Ga_{0.9}Al_{0.1}As$ well with various 2DEG concentrations for various conduction and valence subbands.	62
4.6	The bandgap renormalization dispersion for the various subband transitions calculated for the 200 Å wide $GaAs/Ga_{0.9}Al_{0.1}As$ well with $n_e = 1 \times 10^{11} cm^{-2}$	62
4.7	The total bandgap renormalization at the Brillouin zone center, for the 200 Å wide $GaAs/Ga_{0.9}Al_{0.1}As$ well with various 2DEG concentrations.	63
4.8	Calculated form factors for the electron-hole, electron-electron and hole-hole combinations.	64
4.9	Schematic structure of the undoped QW examined in the numerical calculations.	66
4.10	The complex eleclctrical susceptibility calculated using the FCT model for the undoped well at $T = 2K$	67
4.11	The complex eleclctrical susceptibility calculated using the HF model for the undoped well at $T = 2K$	68
4.12	The absorption spectra for both polarizations, calculated using the FCT and HF models for the undoped well at $T = 2K$	69
4.13	Schematic band edge absorption spectrum for a 2D semiconductor according to the Elliot formula.	70
4.14	Spontaneous emission spectra calculated using the FCT and HF models for the considered undoped structure at $T = 2K$	71
4.15	The complex eleclctrical susceptibility calculated using the FCT model for the undoped well at $T = 77K$	72
4.16	The complex eleclctrical susceptibility calculated for the undoped structure using the HF model for the undoped well at $T = 77K$	73
4.17	The absorption spectra for polarizations, calculated using the FCT and HF models for the undoped well at $T = 77K$	74
4.18	Spontaneous emission spectra calculated using the FCT and HF models for the considered undoped structure at $T = 77K$	75
4.19	Schematic structure of the doped QW examined in the numerical calculations.	75
4.20	A schematic depiction of the bandgap renormalization due to the introduction of 2DEG into the well region of the structure.	76
4.21	The energetic gap between the Fermi energy and the bottom of the conduction band and the Fermi wavevector, both as a function of the 2DEG concentration.	76
4.22	The TE polarization absorption spectra calculated for the doped structure for various gas concentrations using the FCT and HF models at $T = 2K$	78
4.23	The TM polarization absorption spectra calculated for the doped structure for various gas concentrations using the FCT and HF models at $T = 2K$	79
4.24	The TE refractive index change spectra calculated for the doped structure for various gas concentrations using the FCT and HF models at $T = 2K$	80
4.25	The TM refractive index change spectra calculated for the doped structure for various gas concentrations using the FCT and HF models at $T = 2K$	81
4.26	The TE polarization absorption and spontaneous emission spectra calculated for the doped structure for various gas concentrations using the HF model at $T = 2K$	82
4.27	The TM polarization absorption and spontaneous emission spectra calculated for the doped structure for various gas concentrations using the HF model at $T = 2K$	83
4.28	Detailed view of the transition region in the absorption and spontaneous emission spectrum for the TE polarization using the HF model at $T = 2K$	84

4.29	Detailed view of the transition region in the absorption and spontaneous emission spectrum for the TM polarization using the HF model at $T = 2K$	85
4.30	The TE polarization absorption spectra calculated for the doped structure for various gas concentrations using the FCT and HF models at $T = 77K$	86
4.31	The TM polarization absorption spectra calculated for the doped structure for various gas concentrations using the FCT and HF models at $T = 77K$	87
4.32	The TE polarization absorption and spontaneous emission spectra calculated for the doped structure for various gas concentrations using the HF model at $T = 77K$	89
4.33	The TM polarization absorption and spontaneous emission spectra calculated for the doped structure for various gas concentrations using the HF model at $T = 77K$	90
5.1	Fabri-Perot etalon multiple reflections.	92
5.2	Resonator transmittance function for various values of mirror reflectance.	92
5.3	Schematic illustration of a Distributed Bragg Reflector.	93
5.4	Schematic description of light propagation through an interface between two adjacent dielectric layers and light propagation in a homogeneous medium.	95
5.5	The amplitude and phase of the normal incidence reflection calculation of a DBR structure with 35 layers with alternating high and low refraction indices.	96
5.6	A microcavity schematic structure.	97
5.7	Amplitude and phase of the normal incidence reflection function for a microcavity with two DBR's with 35 alternating high and low refractive index layers.	98
5.8	Calculation of the electric field amplitude of a microcavity for two DBR mirror configurations.	99
5.9	Microcavity confined photon dispersion curves for various resonance modes.	100
5.10	Energy levels of the uncoupled absorber and field modes and the dressed energy levels of the coupled system.	101
5.11	Schematic description of the proposed computation model.	105
5.12	Schematic profiles of the simulated microcavity devoid of the embedded QW in the cavity region.	106
5.13	Schematic description of a typical sample wafer and the cross-sectional width profile of such a wafer.	107
5.14	The reflection spectrum of the simulated microcavity structure , calculated using the transfer matrix method for width detuning $\delta = 0.94$ at $T = 2K$	107
5.15	The reflection spectrum minima energies and values, calculated for the simulated structure for various detunings.	108
5.16	Schematic profiles of the simulated microcavity with embedded undoped QW in the cavity region.	109
5.17	The total refractive index spectrum of a bare 200 Å wide $GaAs/Al_{0.1}Ga_{0.9}As$ quantum well, with a 2DEG with concentration of $n_e = 1 \times 10^{11} cm^{-2}$ in the well region.	110
5.18	The reflection spectra for various width detuning values calculated for normal incident light both polarization polarizations, at $T = 2K$	110
5.19	Reflection minima anticrossing curves for both polarizations of incident light, calculated at $T = 2K$	111
5.20	The TM polarization reflection minima anticrossing curves fitted using the coupled oscillator model, calculated at $T = 2K$	112
5.21	The TM polarization reflection minima anticrossing curves together with respective polariton admixing coefficients.	113
5.22	Schematic profiles of the simulated microcavity with embedded doped QW in the cavity region.	114
5.23	The TE reflection spectra as a function of the cavity mode energy, calculated for each of the considered 2DEG concentrations for various width detunings, at $T = 2K$	115
5.24	The TM reflection spectra as a function of the cavity mode energy, calculated for each of the considered 2DEG concentrations for various width detunings, at $T = 2K$	116
5.25	The TE reflection minima anticrossing curves extracted for each 2DEG concentration from the reflection curves	117
5.26	The TM reflection minima anticrossing curves extracted for each 2DEG concentration from the reflection curves	118
5.27	The reflection anti-crossing resonance energies as a function of 2DEG concentrations, obtained manually and from the coupled oscillator fit results for both polarizations.	119

5.28	Calculated first conduction and first three valence subbands dispersion relations for a bare doped QW with $n_e = 7 \times 10^{10} \text{ cm}^{-2}$, for $T = 2 \text{ K}$	119
5.29	The energetic distance between the anticrossing resonance lines as a function of 2DEG concentrations for both polarizations.	120
5.30	The coupling parameters extracted from the coupled oscillator fit of the reflection anti-crossing curves, for both polarizations, as a function of the 2DEG concentration.	121
5.31	The energetic distance between adjacent anti-crossing curves near resonance lines as a function of the 2DEG concentration for both polarizations.	121
5.32	The resonance interaction linewidths extracted for various resonances using the coupled oscillator model fit of the anti-crossing curves as a function of the 2DEG concentration, for both polarizations.	122
5.33	Reflection spectra for various 2DEG concentrations calculated at width detuning of $\delta \approx 0.95$, for both polarizations of the incident light.	123
5.34	The reflection spectra linewidths function of the 2DEG concentration, extracted manually (via FWHM calculation) for each of the present resonances at width detuning of $\delta \approx 0.95$, for both polarizations.	123
5.35	The fitted amplitude and width of the transmission peaks as a function of cavity mode energy, obtained for each resonance branch for both polarizations at $n_e = 3 \times 10^9 \text{ cm}^{-2}$	124
5.36	The fitted amplitude and width of the transmission peaks as a function of cavity mode energy, obtained for each resonance branch for both polarizations at $n_e = 3 \times 10^{10} \text{ cm}^{-2}$	125
5.37	The fitted amplitude and width of the transmission peaks as a function of cavity mode energy, obtained for each resonance branch for both polarizations at $n_e = 1 \times 10^{11} \text{ cm}^{-2}$	125
5.38	The polariton admixing coefficients extracted from the coupled oscillator model fit of the anti-crossing curves for $n_e = 3 \times 10^9 \text{ cm}^{-2}$	126
5.39	The polariton admixing coefficients extracted from the coupled oscillator model fit of the anti-crossing curves for $n_e = 3 \times 10^{10} \text{ cm}^{-2}$	126
5.40	The polariton admixing coefficients extracted from the coupled oscillator model fit of the anti-crossing curves for $n_e = 1 \times 10^{11} \text{ cm}^{-2}$	127
C.1	Program flow for self-consistent solution of Schrödinger -Poisson under equilibrium condition with given donor concentration.	140
D.1	Change in the carrier distribution due to an electron at the origin.	142
E.1	Temperature dependence of the $Al_xGa_{1-x}As$ alloy bandgap energy for various values of x	147
E.2	$Al_xGa_{1-x}As$ alloy bandgap energy as a function of the Al composition for various temperatures.	147
F.1	The real and imaginary parts of the refractive index of $Ga_{1-x}Al_xAs$ as a function of energy, for various temperatures and $x = 0 - 1$	149
F.2	Refractive indices for $T = 2K$	149
F.3	Refractive indices for $T = 77K$	150
F.4	Refractive indices for $T = 300K$	150

List of Tables

5.1	The extracted parameters of the simulated structure for each of the seven resonances X_i	111
5.2	The calculated intersubband transition energies for a bare doped QW with $n_e = 7 \times 10^{10} \text{ cm}^{-2}$ and the difference between them.	114
A.1	Symmetry operations of the group T_d using the Schönflies notation.	132
A.2	Basis functions of the tetrahedral symmetry group T_d	132
A.3	Direct products of the Γ_{15} representation with all representations of T_d	133
A.4	The non-vanishing momentum matrix elements between the states corresponding to different irreducible representations of the tetrahedral symmetry group.	133
E.1	Parameter values for modeling the bandgap energies (I)	145
E.3	Bandgap energies at room temperature compared to reported data (I).	145
E.5	Parameter values for modeling the bandgap energies (II).	145
E.7	Bandgap energies at room temperature compared to reported data (II).	146
E.9	Parameter values for the bandgap of alloy materials.	146

Abstract

Semiconductor microcavities (MC) are structures consisting of a heterostructure, such as a quantum well (QW) or a heterojunction, which are embedded between two high reflectivity distributed Bragg reflectors (DBR). In these structures the photonic mode is spatially confined inside the cavity layer. When the cavity layer width is comparable to the exciton wavelength, interaction between the exciton and the confined photon takes place. The interaction strength can be described in two regimes: (a) the weak coupling regime, where this interaction can be described by perturbation theory, and (b) the strong coupling regime, where the system eigenenergies are Rabi split modes termed cavity polaritons.

Recently, reflection and photoluminescence (PL) spectroscopy studies of such structures containing a two-dimensional electron gas (2DEG) have been reported, revealing sharp polaritonic lines, composed of a cavity photon which is in strong interaction with unbound electron-hole (e-h) pair excitations, located at the Fermi edge of the 2DEG. In this study, we present a theoretical framework for the modeling of MCs with embedded QWs, and thereby investigate the interaction of such electron-hole pairs with the light field excitations within these structures near the Fermi edge. We start by considering the electronic properties of a bare QW via a two-level $\mathbf{k} \cdot \mathbf{p}$ method, where the 2DEG influence is incorporated through a self-consistent the Schrödinger-Poisson model. Once the electronic properties of the QW are found, the light-matter interaction in the QW is modeled via a semi classical approach. We assume a dipole light-matter interaction, and discuss two approximated methods to model the optical properties of the considered QW: (a) the free-carrier model, where the Coulombic interaction is absent and the dephasing is modeled phenomenologically, and (b) the screened Coulomb-correlated model, where we incorporate both the Coulombic interactions between the charge carrier and also discuss the mutual screening effect. This calculation is performed with and without the presence of the 2DEG in the well region of the QW, yielding the complex electrical susceptibility, absorption and spontaneous emission spectra of the investigated of the structure.

Next, the obtained electronic and optical properties of a bare QW are then used to calculate the reflection spectra of the full MC structure, with QW embedded in their cavity region. This is achieved by using the refractive index spectrum of the QW, obtained from its electrical susceptibility calculation, in the transfer matrix calculation of the entire MC reflection spectrum. As for the bare QW, the calculation is performed with and without the presence of 2DEG of various concentrations. Finally, the formulated approach is utilized to calculate the reflection anti-crossing curves of the investigated MC structures, which are analyzed manually and through a fitting procedure to the coupled-oscillator model. This allows us to investigate the influence of the 2DEG of variable concentrations on the coupling strength of the electron-hole resonances with the cavity photons and of the polaritonic linewidths.

We show that the strong interaction of the cavity-confined photon with the interband excitations of the two-dimensional electron gas leads to the formation of cavity polaritons. The most significant result is the demonstration that cavity polaritons are indeed formed for high 2DEG densities at the Fermi edge energies. In comparison, our model calculations show that excitons are not formed in bare QWs having a 2DEG with such densities. The coherence between all these e-h pair excitations is induced by the strong interaction with the cavity mode, in contrast with the exciton-polaritons case, where the coherence stems from the Coulomb interaction between the electron and hole.

List of Symbols

k	crystal momentum
$E_n(\mathbf{k})$	electron dispersion relation
EFM	envelope function method
E	electrical field
B	magnetic field
A	vector potential
ϕ	scalar potential
H	Hamiltonian operator
E_v	valence band-edge energy
E_c	conduction band-edge energy
Δ	spin-orbit splitting energy
k	crystal momentum
ϕ	scalar potential
e	elementary charge
$k_t(k_{\parallel})$	transverse/in-plane wavevector
k_z	wavevector parallel to the growth direction
$\psi_{n\mathbf{k}}$	particle wavefunction in a solid
$u_{n\mathbf{k}}(\mathbf{r})$	Bloch's basis function
$\mathbf{p}_{nn'}$	momentum matrix elements
h_{ij}	Hamiltonian matrix entries
$F_{n\mathbf{k},m}(z)$	slowly-varying wavefunction envelope
E_p	optical matrix parameter
P	nonzero interband momentum matrix element
E_v	valence band-edge energy
E_c	conduction band-edge energy
$\sigma(\sigma_x, \sigma_y, \sigma_z)$	Pauli operators
$\gamma_1, \gamma_2, \gamma_3$	Luttinger's parameters
Δ	spin-orbit splitting energy
F_{hh}	heavy-hole subband envelope function
F_{lh}	light-hole subband envelope function
$\rho(E)$	density of states
DOS	density of states
ϵ	permittivity of the material
$\rho(z)$	volume charge density
$\sigma(z)$	areal charge density
2DEG	two-dimensional electron gas
$N(z), n_e$	electron carrier concentration
n_h	hole carrier concentration
N_{2DEG}, n_e	2DEG concentration
$f(E)$	Fermi-Dirac distribution function

E_F	the Fermi level energy or the chemical potential
k_B	Boltzman's constant
T	ambient temperature
k_F	Fermi wavevector
\hat{a}_n^\dagger and \hat{a}_n	electron creation and annihilation operators
$ 0\rangle$	vacuum ground state
FCT	free-carrier theory
\mathcal{A}	volume of the translational invariant direction
\mathcal{L}	volume of the quantized direction
\hat{b}_n^\dagger and \hat{b}_n	hole creation and annihilation operators
\hat{n}_{ck}	electron number operator in the conduction band
\hat{n}_{vk}	hole number operator in the valence band
$\hat{p}_{vc,\mathbf{k}}$	microscopic polarization
$\mu_{cv,\mathbf{k}}$	dipole matrix element
\mathbf{P}	macroscopic polarization
χ	optical susceptibility
\mathbf{D}	electric displacement
k_0	photo wavenumber
$\hat{\mathbf{e}}_i$	unit vector
χ' and χ''	the real and imaginary parts of the optical susceptibility
G	medium intensity gain
α	medium optical absorption
\Re	real part
\Im	imaginary part
γ	phenomenological decay rate
RPA	random phase approximation
$\omega_{n,m}(\mathbf{k})$	intersubband transition energy
$N(\hbar\omega)$	photon density of states
$r_{sp}(\hbar\omega)$	spontaneous emission rate per unit volume per unit energy
$I_{sp}(\hbar\omega)$	spontaneous emission intensity
KMS	Kubo-Martin-Schwinger relation
R_{sp}	spontaneous emission rate per unit volume
HF	Hartree-Fock theory
$\vartheta_{\mathbf{q}}$	Fourier transform of the Coulomb potential
$G_{\mathbf{q},\mathbf{k},\mathbf{k}'}^{n_1,n_2,n_3,n_4}$	form factor
$\Omega_{\mathbf{k}}(z,t)$	Rabi frequency
$\epsilon(\mathbf{q},\omega)$	screening dielectric function
BGR	bandgap renormalization
$\Delta E_{CH,n}$	Coulomb-hole self energy shift
$\Delta E_{SX,mn}(\mathbf{k})$	screened exchange energy shift
$\hbar\tilde{\omega}_{mn}(\mathbf{k})$	renormalized intersubband transition energy
$\Gamma_{\mathbf{k}}^{n,m}(\nu)$	Coulomb enhancement factor
R	etalon reflectance
T	etalon transmittance
F	etalon finesse coefficient
n_L, n_H	the low and high refractive index of the DBR dielectric layers
n_l, n_r	the left- and right-hand cladding material refractive indices
λ_c	the center wavelength of the high reflectivity region
E^+, E^-	forward and backward propagating waves complex amplitudes
M_i	the transfer matrix of the interface
M_p	the transfer matrix of propagation in the same material
M_{DBR}	the transfer matrix of a DBR structure
r_{DBR}	reflection coefficient of the DBR structure
t_{DBR}	transmission coefficient of the DBR structure

R_{DBR}	reflectance of the DBR structure
T_{DBR}	transmittance of the DBR structure
MC	microcavity
M_{MC}	the transfer matrix of the microcavity structure
R_{MC}	reflectance of the MC structure
T_{MC}	transmittance of the MC structure
γ_c	cavity mode linewidth
l_{eff}	the effective length of the cavity spacer
$E_{ph}(k_t)$	MC mode dispersion relation
m_{ph}	the cavity photon in-plane effective mass
H_F	Fock Hamiltonian
$f(\mathbf{r})$	complex vector function of the polarization and relative amplitude of the cavity mode
H_A	the Hamiltonian of a two-level absorber system
H_I	the interaction Hamiltonian in the dipole approximation
Ω	the atom-field coupling constant
$\gamma_{cav}, \gamma_{abs}$	cavity and absorber damping factors
Q	the cavity quality factor
γ_X	exciton linewidth
$E_X(\mathbf{k}_t)$	exciton energy
LDM	linear dispersion model
FWHM	full width at half maximum

Chapter 1

Introduction

Semiconductor microcavities (MC) are structures consisting of a heterostructure, such as a quantum well (QW) or a heterojunction, which are embedded between two high reflectivity distributed Bragg reflectors (DBR). In these structures the photonic mode is spatially confined inside the cavity layer. When the cavity layer width is comparable to the exciton wavelength, interaction between the exciton and the confined photon takes place. The interaction strength can be described in two regimes: (a) the weak coupling regime, where this interaction can be described by perturbation theory, and (b) the strong coupling regime, where the system eigenenergies are Rabi split modes termed cavity polaritons.

Recently, reflection and photoluminescence (PL) spectroscopy studies of such structures containing a two-dimensional electron gas (2DEG) have been reported, revealing sharp polaritonic lines, composed of a cavity photon which is in strong interaction with unbound electron-hole (e-h) pair excitations, located at the Fermi edge of the 2DEG. In this study, we present a theoretical framework for the modeling of MCs with embedded QWs, and thereby investigate the interaction of such electron-hole pairs with the light field excitations within these structures near the Fermi edge. We start by considering the electronic properties of a bare QW via a two-level $\mathbf{k} \cdot \mathbf{p}$ method, where the 2DEG influence is incorporated through a self-consistent Schrödinger-Poisson model. Once the electronic properties of the QW are found, the light-matter interaction in the QW is modeled via a semi classical approach. We assume a dipole light-matter interaction, and discuss two approximated methods to model the optical properties of the considered QW: (a) the free-carrier model, where the Coulombic interaction is absent and the dephasing is modeled phenomenologically, and (b) the screened Coulomb-correlated model, where we incorporate both the Coulombic interactions between the charge carrier and also discuss the mutual screening effect. This calculation is performed with and without the presence of the 2DEG in the well region of the QW, yielding the complex electrical susceptibility, absorption and spontaneous emission spectra of the investigated of the structure.

Next, the obtained electronic and optical properties of a bare QW are then used to calculate the reflection spectra of the full MC structure, with QW embedded in their cavity region. This is achieved by using the refractive index spectrum of the QW, obtained from its electrical susceptibility calculation, in the transfer matrix calculation of the entire MC reflection spectrum. As for the bare QW, the calculation is performed with and without the presence of 2DEG of various concentrations. Finally, the formulated approach is utilized to calculate the reflection anti-crossing curves of the investigated MC structures, which are analyzed manually and through a fitting procedure to the coupled-oscillator model. This allows us to investigate the influence of the 2DEG of variable concentrations on the coupling strength of the electron-hole resonances with the cavity photons and of the polaritonic linewidths.

We show that the strong interaction of the cavity-confined photon with the interband excitations of the two-dimensional electron gas leads to the formation of cavity polaritons. The most significant result is the demonstration that cavity polaritons are indeed formed for high 2DEG densities at the Fermi edge energies. In comparison, our model calculations show that excitons are not formed in bare QWs having a 2DEG with such densities. The coherence between all these e-h pair excitations is induced by the strong interaction with the cavity mode, in contrast with the exciton-polaritons case, where the coherence stems from the Coulomb interaction between the electron and hole.

Chapter 2

Electronic Properties of Semiconductors

The optical properties of nanostructures are intimately connected to the electronic states, the response of electrons within the atomic lattice to external perturbations. As such, a precise knowledge of the electronic properties is required for a proper device analysis. In bulk semiconductors, the lattice periodicity and its symmetry leads to the formation of electronic bands, continuously (within the band) relating the crystal momentum \mathbf{k} of an electron to its energy $E_n(\mathbf{k})$. The combination of different materials within a nanostructure breaks the symmetry of the semiconductor crystal, leading to *quantization effects*, i.e. modifications of the electronic properties from their bulk properties. These modifications have a pronounced impact on the electronic and optical properties of nanostructures. The present chapter covers the theory of the calculation of the electronic states in nanostructures using the *envelope function method* (EFM).

The chapter is organized as follows. We first present an extensive introduction to the Schrödinger equation within a semiconductor crystal, which will later also serve as the basis for the analysis of optical effects covered in Chapter 3 and the many body effects in optical spectra in Chapter 4. After introducing certain approximations to the crystal Schrödinger equation, the concept of solving the resulting single-particle Schrödinger equation using the bulk $\mathbf{k} \cdot \mathbf{p}$ method is presented. The subsequent section derives the equations of the $\mathbf{k} \cdot \mathbf{p}$ envelope function method used in nanostructures and simultaneously introduces the $\mathbf{k} \cdot \mathbf{p}$ model for zinc-blende crystals, with an emphasis on the two-band model. Note that the presented discussion doesn't include the influence of strain effects on the electronic properties. Finally, we present the Schrödinger-Poisson model of the electronic bands structure where the electrostatics of the system are of relevance. This model is then used to analyze the influence of a two-dimensional electron gas (2DEG), introduced by various methods into the quantum well region, on the electronic properties of the system.

2.1 Crystal Schrödinger Equation

2.1.1 Introduction

The total Hamiltonian of all electrons, atoms and the electro-magnetic field of a solid state crystal is given by

$$H = \sum_i \frac{1}{2m_i} (\mathbf{p}_i - ez_i \mathbf{A}(\mathbf{r}_i))^2 + \frac{\epsilon_0}{2} \int (\mathbf{E}^2 + c_0^2 \mathbf{B}^2) d\mathbf{r} \quad (2.1.1)$$

In the second term \mathbf{E} denotes the electric- and \mathbf{B} the magnetic field. These fields are related to the vector potential \mathbf{A} and the scalar potential ϕ via [1]

$$\mathbf{E} = -\frac{\partial \mathbf{A}}{\partial t} - \nabla \phi \quad (2.1.2)$$

$$\mathbf{B} = \nabla \times \mathbf{A}. \quad (2.1.3)$$

In the first term of (2.1.1), e is the elementary charge, z_i is the charge of particle i in units of e (-1 for electrons) and m_i denotes the particle mass. The term $\mathbf{p}_i - ez_i \mathbf{A}(\mathbf{r}_i)$ is the mechanical momentum of particle i , which is invariant to our gauge choice (see below) for \mathbf{A} and ϕ . The electrical field term \mathbf{A}^2 holds both transverse and longitudinal

contributions. In the following discussion we assume a Coulomb gauge for the vector potential, i.e. $\nabla \cdot \mathbf{A} = 0$ [1]. In this gauge the term $\frac{\partial \mathbf{A}}{\partial t} \nabla \phi$ in \mathbf{E}^2 vanishes, and so we can split this term to the transverse and longitudinal contributions $\mathbf{E}^2 = \mathbf{E}_t^2 + \mathbf{E}_l^2$. Using Poisson's equation, the longitudinal contribution can be written in terms of the charge density

$$\int \mathbf{E}_l^2 d\mathbf{r} = \int (\nabla \phi)^2 d\mathbf{r} = \langle \phi \nabla \phi \rangle - \int \phi \nabla^2 \phi d\mathbf{r} = \int \phi \frac{\rho}{\epsilon_0} d\mathbf{r}. \quad (2.1.4)$$

Next, the contributions to ϕ are distinguished between internal ϕ_{int} and external ϕ_{ext} , where the internal contributions are created by the crystal electrons and atomic cores. The internal contributions are given by the longitudinal Coulomb interaction between the charged particles i and j

$$V_{i,j} = \frac{e^2 z_i z_j}{4\pi\epsilon_0 |\mathbf{r}_i - \mathbf{r}_j|}, \quad (2.1.5)$$

with unit charges z_i and z_j . The external contribution are

$$V_{ext} = \sum_i z_i e \phi_{ext}(\mathbf{r}_i). \quad (2.1.6)$$

The crystal Hamiltonian for electrons i, j and atoms I, J then reads

$$\begin{aligned} H = & \underbrace{\sum_i \frac{(\mathbf{p}_i + e\mathbf{A})^2}{2m_0}}_{T_e} + \underbrace{\sum_I \frac{(\mathbf{p}_I + ez_I \mathbf{A})^2}{2m_I}}_{T_a} + \underbrace{\frac{1}{2} \sum_{i,j} \frac{e^2}{4\pi\epsilon_0 |\mathbf{r}_i - \mathbf{r}_j|}}_{V_{ee}} \\ & + \underbrace{\frac{1}{2} \sum_{I,J} \frac{e^2 z_I z_J}{4\pi\epsilon_0 |\mathbf{r}_I - \mathbf{r}_J|}}_{V_{aa}} - \underbrace{\frac{1}{2} \sum_{i,J} \frac{e^2 z_J}{4\pi\epsilon_0 |\mathbf{r}_i - \mathbf{r}_J|}}_{V_{ea}} + V_{ext} \\ & + \underbrace{\frac{\epsilon_0}{2} \int (\mathbf{E}_t^2 + c_0 \mathbf{B}^2) d\mathbf{r}}_{H_{EM}}, \end{aligned} \quad (2.1.7)$$

where T is the kinetic energy part of the Hamiltonian, and V the potential energy one. As the atoms have a much higher mass than the electrons, the Born-Oppenheimer approximation [2] can be used to separate the motion of electrons and atoms. The electrons will react on movements of the atoms instantaneously. Therefore, the interaction between ion cores and between electrons and ion cores can be concentrated into a potential $U(\mathbf{x})$, leading to the final crystal electron Hamiltonian

$$\begin{aligned} H = & \sum_i \left(\frac{(\mathbf{p}_i + e\mathbf{A}(\mathbf{r}_i))^2}{2m_0} + U(\mathbf{r}_i) \right) \\ & + \frac{1}{2} \sum_{i,j} \frac{e^2}{4\pi\epsilon_0 |\mathbf{r}_i - \mathbf{r}_j|} + V_{ext} + H_{EM}. \end{aligned} \quad (2.1.8)$$

The next step is to perform the *single electron approximation* or *mean field approximation* by assuming that the electron-electron interaction V_{ee} with the core- and valence electrons can also be concentrated into the potential $U(\mathbf{r})$. This step is necessary as solving the equation for 10^{23} explicitly considered electrons is an impossible task. The equation reduces to a single electron equation, where an electron experiences the mean-field potential $U(\mathbf{r})$. Within this step, the vector potential \mathbf{A} is restricted to external excitations, where the local oscillations within the crystal lattice are averaged out. Overall, the effect of the external electro-magnetic field on the atoms has been excluded. This approximation is usually justified in the case of weak fields and heavy atomic masses. The interaction between electrons and atoms is restricted to a frozen lattice. The interaction between the movement of the atoms and the electrons can be reintroduced using *phonons* [2], but this will be omitted throughout the thesis.

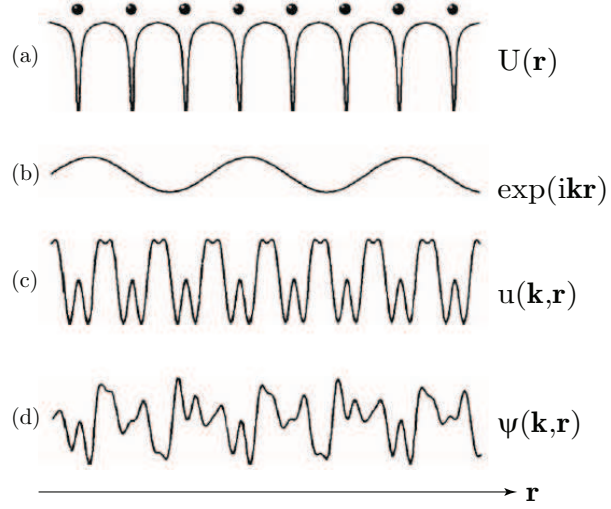


Figure 2.1: Schematic representation of electronic functions in a crystal (a) potential plotted along a row of atoms, (b) free electron wave function, (c) amplitude factor of Bloch function having the periodicity of the lattice, and (d) Bloch function ψ (after [3])

2.1.2 Bloch's Theorem

Assuming no external field, the time independent single electron Schrödinger equation to solve is given by

$$\left(-\frac{\hbar^2}{2m_0}\nabla^2 + U(\mathbf{r})\right)\psi = E\psi. \quad (2.1.9)$$

For the moment, the crystal is assumed to be homogeneous and perfect. The potential $U(\mathbf{r})$ is periodic within the lattice (see Figure 2.1). For any translation vector \mathbf{R} mapping the infinite crystal lattice to itself, the potential obeys

$$U(\mathbf{r}) = U(\mathbf{r} + \mathbf{R}) \quad (2.1.10)$$

and the wavefunction can be expressed in the form known as *Bloch function*

$$\psi_{n\mathbf{k}} = u_{n\mathbf{k}}(\mathbf{r})e^{i\mathbf{k}\cdot\mathbf{r}}, \quad (2.1.11)$$

where $u_{n\mathbf{k}}(\mathbf{r})$ denotes the lattice periodic path with

$$u_{n\mathbf{k}}(\mathbf{r}) = u_{n\mathbf{k}}(\mathbf{r} + \mathbf{R}) \quad (2.1.12)$$

and the plane wave is the slowly modulating envelope. The $n\mathbf{k}$ are the quantum numbers indexing the solutions. Applying the differential operators to the plane wave and multiplying the equation on both sides from the left with $e^{-i\mathbf{k}\cdot\mathbf{r}}$ gives the equation for the lattice periodic functions as

$$\begin{aligned} H_{\mathbf{k}\cdot\mathbf{p}}(\mathbf{k})u_{n\mathbf{k}}(\mathbf{r}) &= \left(-\frac{\hbar^2}{2m_0}\nabla^2 + \frac{\hbar}{m_0}\mathbf{k}\cdot\mathbf{p} + \frac{\hbar^2k^2}{2m_0} + U(\mathbf{r})\right)u_{n\mathbf{k}}(\mathbf{r}) \\ &= E_n(\mathbf{k})u_{n\mathbf{k}}(\mathbf{r}). \end{aligned} \quad (2.1.13)$$

An important consequence of the Bloch theorem is the fact that wavefunctions with different \mathbf{k} values are not coupled together (due to the slowly varying plane wave) and therefore (2.1.13) has a parametric dependence on the crystal momentum \mathbf{k} .

2.1.3 The $\mathbf{k}\cdot\mathbf{p}$ Method

2.1.3.1 Introduction

There is a vast number of methods to obtain solutions to (2.1.13). One of the most frequently used is the semi-empirical $\mathbf{k}\cdot\mathbf{p}$ method that serves to derive analytical expressions for the band structure, using symmetry arguments

and experimental observations. The method was initially introduced by Bardeen and Seitz (see references in [4]) and applied by many researchers. It is particularly useful to describe the band structure for direct semiconductors used in optoelectronic devices at the Γ point of the Brillouin zone with a high precision.

Hereafter a short introduction of the general concepts will be given. These concepts will later reappear within the Envelope Function Methods (EFM). This introduction is mainly based on [2].

The basic idea within the $\mathbf{k} \cdot \mathbf{p}$ theory [5] is to solve (2.1.13) for an extremal point with high symmetry of the band structure, usually the Γ point at $\mathbf{k} = 0$. There, (2.1.13) reduces to

$$\left(-\frac{\hbar^2}{2m_0} \nabla^2 + U(\mathbf{r}) \right) u_{n0}(\mathbf{r}) = E_n(0) u_{n0}(\mathbf{r}). \quad (2.1.14)$$

The solutions $u_{n0}(\mathbf{r})$ are denoted as *zone-center* functions and span the complete Hilbert space of all solutions to (2.1.13). Therefore, one may express the lattice periodic functions $u_{n\mathbf{k}}(\mathbf{r})$ away from the Γ point in terms of the zone-center functions

$$u_{m\mathbf{k}}(\mathbf{r}) = \sum_{n'} a_{m\mathbf{k}, n'} u_{n'0}(\mathbf{r}). \quad (2.1.15)$$

To obtain the coefficients $a_{m\mathbf{k}, n'}$, the expansion (2.1.15) is inserted into (2.1.13), multiplied from the left by $u_{n0}(\mathbf{r})$ and integrated over the crystal unit-cell to obtain

$$\sum_{n'} \left(\left(E_{n'}(0) + \frac{\hbar^2 k^2}{2m_0} \right) \delta_{nn'} + \frac{\hbar}{m_0} \mathbf{k} \cdot \mathbf{p}_{nn'} \right) a_{m\mathbf{k}, n'} = E_m(\mathbf{k}) a_{m\mathbf{k}, n'}, \quad (2.1.16)$$

where

$$\mathbf{p}_{nn'} = \int u_{n0}^*(\mathbf{r}) \mathbf{p} u_{n'0}(\mathbf{r}) d\mathbf{r} \quad (2.1.17)$$

is used to express the momentum matrix element between two zone-center Bloch functions. The above equation can obviously be written in matrix form, where a matrix entry is given by

$$h_{ij} = \left(E_j(0) + \frac{\hbar^2 k^2}{2m_0} \right) \delta_{ij} + \frac{\hbar}{m_0} \mathbf{k} \cdot \mathbf{p}_{ij} \quad (2.1.18)$$

and a diagonalization of the \mathbf{k} dependent, infinite matrix would lead to the exact coefficients and energies $E_m(\mathbf{k})$. As the matrix is continuous in \mathbf{k} , it is clear that the dispersion $E_m(\mathbf{k})$ will also be continuous.

As a remark, we can point out that (2.1.14) is not solved explicitly and no closed expression for $u_{n0}(\mathbf{r})$ is needed. Instead, the matrix (2.1.18) is constructed by using group theory to derive symmetry properties of the zone-center functions $u_{n0}(\mathbf{r})$. Using these symmetry properties, similarities and equivalences for the momentum matrix elements \mathbf{p}_{ij} can be deduced. A profound introduction into the group theory for semiconductors is beyond the current scope. A rough guideline illustrating the essence required by the $\mathbf{k} \cdot \mathbf{p}$ theory is presented in Appendix C. An extensive presentation can be found in [2] and [6].

2.1.3.2 Löwdin-Renormalization

While the matrix h_{ij} (2.1.18) is infinite, leading to an infinite number of bands, the assessment of light emission in optoelectronic devices usually requires only the knowledge of the lowest conduction and highest valence bands. For the relevant III-V semiconductors, the conduction and the valence bands lie at the Γ point energetically close together. Other bands can be regarded as being remote, so the interaction in-between these bands can be considered to dominate for the band structure of interest. In the model developed by Kane [7], therefore a submatrix h_{ij} of the conduction- and valence band at the Γ point is extracted out of (2.1.18) and diagonalized. Although the primary interest of Kane's model was to include spinorbit interaction, the missing interaction with remote bands resulted in a heavy-hole band structure, given by the free-electron dispersion, bending for a hole into the wrong direction. Luttinger and Kohn [8] included the interaction of remote states onto the selected set of bands, using Löwdin's perturbation theory [9]. The idea of Löwdin perturbation theory is to divide the bands in two classes S and R (see Fig. 2.2). Bands in class S are considered explicitly, i.e. the respective rows and columns of the matrix h_{ij} are kept.

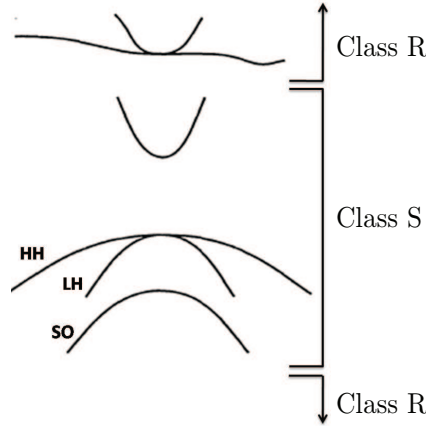


Figure 2.2: Schematic band structure classification in the Löwdin perturbation theory.

The bands R are considered being remote and their effect on the bands in class S are included in the submatrix of h_{ij} using perturbation theory. Hereby, the renormalized matrix elements are given by

$$h'_{ij} = h_{ij} + \sum_{\nu}^R \frac{h_{i\nu}h_{\nu j}}{E_i - h_{\nu\nu}}, \quad (2.1.19)$$

where i and j are in class S and ν is in R . Group theory and symmetry arguments are then used to derive similarities and vanishing terms and reduce the perturbation expressions to a few constants. By analytically diagonalizing the remaining matrix, the few remaining constants can be determined by comparing analytical dispersion expressions to experimentally determined effective masses. An important note here is that E_i denotes the energy of band i such that the renormalization of the matrix element depends on the result of the eigenvalue calculation, actually requiring self-consistency. In practice, the energies E_i are approximated by the zone-center energy $E_i(0)$, given by the matrix element h_{ii} , which is fine close the zone-center. By keeping only one single band in class S , one obtains the single band effective mass dispersion for band i as

$$E_i(0) + \left(\frac{\hbar^2 k^2}{2m_0} + \frac{\hbar}{m_0} \sum_{\nu}^R \frac{\mathbf{k} \cdot \mathbf{p}_{s\nu} \mathbf{p}_{\nu s} \cdot \mathbf{k}}{E_i - h_{\nu\nu}} \right) = E_i(0) + \frac{\hbar^2}{2} \mathbf{k}^T \frac{1}{\mathbf{m}^*} \mathbf{k}. \quad (2.1.20)$$

In the case of several bands within the class S , the resulting matrix can be written, ordered by the dependence on the wavenumber \mathbf{k} , as

$$\sum_{i,j=x,y,z} \mathbf{H}_{i,j}^{(2)} k_i k_j + \sum_{i=x,y,z} \mathbf{H}_{i,j}^{(1)} k_i + \mathbf{H}^{(0)}. \quad (2.1.21)$$

To summarize, the second order terms $\mathbf{H}_{i,j}^{(2)}$ are a result of the combination of the free carrier dispersion and the perturbation treatment of remote states in class R , while first order terms $\mathbf{H}_{i,j}^{(1)}$ stem from the direct treatment of the $\mathbf{k} \cdot \mathbf{p}$ interaction (and later from linear spin-orbit terms), while zero order terms $\mathbf{H}^{(0)}$, contain zone-center energies (and possible terms if the zone-center basis is not orthogonal).

2.2 The $\mathbf{k} \cdot \mathbf{p}$ Envelope Function Method

2.2.1 Introduction

In previous sections, the crystal was assumed to be homogeneous and infinitely extended. In nanostructures, this assumption is no longer valid and the translational symmetry is broken in certain directions. As a consequence, a carrier might be energetically confined within a lower-bandgap material, but still free to propagate within the translational invariant direction. In the case of a quantum well, the symmetry is broken by the atoms of the other species in one direction, for a quantum wire, it is broken in two directions and for a quantum dot in all three

directions. Consequently, the number of translational invariant directions is reduced from two for a quantum well to zero for a quantum dot. As a result, the Bloch function employing the plane wave ansatz has to be modified

$$\varphi_{m\mathbf{k}_t}(\mathbf{r}, z) = \sum_n u_n(\mathbf{r}, z) e^{i\mathbf{k}_t \cdot \mathbf{r}} F_{n\mathbf{k}, m}(z). \quad (2.2.1)$$

Here, \mathbf{r} denotes the coordinate of translational invariant direction(s), z is the coordinate of the direction(s) where the crystal symmetry is broken and $u_n(\mathbf{r}, z)$ is a lattice-periodic function. The crystal momentum \mathbf{k} is only defined within the translational invariant direction. The expression $F_{n\mathbf{k}, m}(z)$ is referred to as slowly-varying envelope and denotes at every position in the symmetry broken direction z , how the lattice-periodic functions are mixed together. In the bulk crystal, the plane wave term decouples the wavefunctions with different crystal momenta \mathbf{k} . In a nanostructure, this decoupling is only true for the translational invariant direction, while in the symmetry broken direction, the states are now mixed together.

As a result of the symmetry breaking, the bands are split into *subbands*, depending on the transverse crystal momentum \mathbf{k}_t . The task of the envelope function method is now to select a suitable set of lattice periodic functions $u_n(\mathbf{r}, z)$ for (2.2.1) and derive a proper equation to determine the envelopes $F_{n\mathbf{k}, m}(z)$.

2.2.2 $\mathbf{k} \cdot \mathbf{p}$ Envelope Function Ansatz

The traditional ansatz is to use the zone-center $\mathbf{k} \cdot \mathbf{p}$ lattice periodic functions $u_{n0}(\mathbf{r})$ for the expansion (2.2.1), together with a set of matching conditions. The equation for the envelopes is obtained by replacing the wave number k_i by the corresponding operator $-i\partial_i$. As in the nanostructure, different materials are involved, the wavefunction is in each material expanded into the materials zone-center functions. The result is that the effective mass like parameters from the perturbation interaction with remote states and the zone-center energies are position dependent. For the single-band effective mass approximation for e.g. the conduction band in a quantum well for $\mathbf{k}_t = 0$, the envelope equation is given by

$$\left(-\frac{\hbar^2}{2m^*(z)} \frac{\partial^2}{\partial z^2} + E_c(z) \right) F_s(z) = E(0)F_s(z). \quad (2.2.2)$$

$E_c(z)$ denotes the position dependent bulk band edge, corresponding in the direct band gap semiconductors to the conduction band energy at Γ . Once the eigenvalues $E_m(0)$ and normalized eigenfunctions $F_{s,m}(z)$ (indexed by the subband quantum number m) of (2.2.2) are obtained, the in-plane dispersion is usually approximated using the dominant effective mass of the quantum well material

$$E_m(\mathbf{k}) = E_m(0) + \frac{\hbar^2 k^2}{2m_c^*}. \quad (2.2.3)$$

The way the equation is written, it is in the presence of a material interface not Hermitian and therefore unexpected imaginary eigenvalues for the energy would result. The usual ad-hoc fix, justified by the requirement of a continuous probability flow, is to rewrite the second order differential operator [4]

$$-\frac{\hbar^2}{2m^*(z)} \nabla^2 \rightarrow -\nabla \frac{\hbar^2}{2m^*(z)} \nabla. \quad (2.2.4)$$

The particular order of the coefficient and the differential operators is commonly referred to as operator ordering. The form of (2.2.4) is denoted as Ben-Daniel and Duke ordering [10], but within the single-band effective mass theory, other orderings are suggested too (see [11] and references therein). The ordering is irrelevant within bulk materials, but plays a substantial role at a material interface: it is equivalent to the matching conditions for the bulk Bloch functions. In the case of a multi-band equation, where not only one, but several lattice periodic functions are included, one obtains in analogy to (2.2.4) for all envelopes involved $\mathbf{F}(z) = (F_1(z), F_2(z), \dots, F_M(z))^T$ a system of coupled partial differential equations

$$\mathbf{H}_{\mathbf{k} \cdot \mathbf{p}}(z) \mathbf{F}(z) = E \mathbf{F}(z), \quad (2.2.5)$$

where the $\mathbf{k} \cdot \mathbf{p}$ differential operator is given by

$$\begin{aligned}\mathbf{H}_{\mathbf{k} \cdot \mathbf{p}}(z) = & -\sum_{i,j} \partial_i \mathbf{H}_{i,j}^{(2)}(\mathbf{r}; \mathbf{k}_t) \partial_j \\ & + \sum_i \left(\mathbf{H}_{i;L}^{(1)}(\mathbf{r}; \mathbf{k}_t) \partial_i + \partial_i \mathbf{H}_{i;R}^{(1)}(\mathbf{r}; \mathbf{k}_t) \right) \\ & + \mathbf{H}^{(0)}(\mathbf{r}; \mathbf{k}_t).\end{aligned}\quad (2.2.6)$$

Here the Hermitian operator ordering has already been introduced. The problem is that within the bulk $\mathbf{k} \cdot \mathbf{p}$ Hamiltonian, terms of the type $Nk_i k_j$ with $i \neq j$ can appear, for which the operator ordering is not clear. The usual fix is to split the contribution symmetrically

$$Nk_i k_j \rightarrow \partial_i \frac{N}{2} \partial_j - \partial_j \frac{N}{2} \partial_i. \quad (2.2.7)$$

It can be shown that this particular choice, which is called *symmetrized operator ordering*, may lead to erroneous results. The traditional envelope equations for one and several bands are widely applied and used in a variety of numerical calculations of quantum wells (and superlattices) [12, 13, 14, 15, 16].

Beside its successful application to some material systems, the traditional way of deriving the envelope equations contains several ad hoc fixes, which are required within the presence of material interfaces. The operator ordering is crucial at a material interface, where the material parameters change and therefore the ad-hoc operator ordering involves unknown approximations made to the effect of the interface.

2.2.3 The Zinc-Blende Models

2.2.3.1 Direct Interaction

To apply the envelope equations (2.2.5) to direct-bandgap semiconductor nanostructures, the exact form of the $\mathbf{k} \cdot \mathbf{p}$ Hamiltonian at the Γ point is required. Ignoring spin, the top of the valence band at Γ is triply degenerate, corresponding to the Γ_{15} representation with p -type basis functions x, y and z , while the lowest-lying conduction band is of s -type symmetry, corresponding to Γ_1 . The direct interaction terms (2.1.18) of the $\mathbf{k} \cdot \mathbf{p}$ matrix for s, x, y and z are given by [5]

$$\mathbf{H}_d^{4 \times 4} = \left(\begin{array}{c|cccc} & |s\rangle & |x\rangle & |y\rangle & |z\rangle \\ \hline |s\rangle & E_c + \frac{\hbar^2}{2m_0} & iPk_x & iPk_y & iPk_z \\ |x\rangle & -ik_x P & E_v + \frac{\hbar^2}{2m_0} & 0 & 0 \\ |y\rangle & -ik_y P & 0 & E_v + \frac{\hbar^2}{2m_0} & 0 \\ |z\rangle & -ik_z P & 0 & 0 & E_v + \frac{\hbar^2}{2m_0} \end{array} \right). \quad (2.2.8)$$

Here, E_c and E_v correspond to the zone-center energies

$$E_c = \langle s | H | s \rangle \quad (2.2.9)$$

$$E_v = \langle x | H | x \rangle \quad (2.2.10)$$

$$P = -\frac{i\hbar}{m_0} \langle s | p_x | s \rangle \quad (2.2.11)$$

and P the nonzero interband momentum matrix element from the direct $\mathbf{k} \cdot \mathbf{p}$ interaction between the conduction- and the valence band. The momentum matrix element is often given as an energy parameter E_p , the *optical matrix parameter*, related to P by

$$E_p = \frac{2m_0}{\hbar^2} P^2. \quad (2.2.12)$$

For the Γ_{15} states, the nonzero momentum matrix element is of the type $\langle x | p_y | z \rangle$, where no coordinate appears twice [2] (the crystal is invariant under a rotation of 180° around one of the axes). Therefore, one would expect the direct interaction within the valence band $\mathbf{k} \cdot \langle x | \mathbf{p} | y \rangle$ resulting into a linear term in \mathbf{k} given explicitly by $k_z \langle x | p_z | y \rangle$. In fact, the first order matrix elements within Γ_{15} vanish due to time reversal symmetry of the Hamiltonian [17].

For example, a reflection in the (110) plane for $\langle x^a | p_z | y^b \rangle$ results in $\langle y^a | p_z | x^b \rangle$, while integration by parts gives $\langle x^a | p_z | y^b \rangle = -\langle y^b | p_z | x^a \rangle$. Here a and b index the degenerate level. If the states are from the same degenerate level, then $a = b$ and the matrix elements vanish. If the states are not from the same degenerate level, the interaction is nonzero.

The operator ordering in the first order terms, e.g. $H_{sx} = iPk_x$ and $H_{xs} = -ik_xP$ is an ad hoc fix. If P is allowed to vary, the here chosen ordering is required to ensure the Hamiltonians Hermiticity.

2.2.3.2 Remote Contributions

The next step is to include the interaction between the remote states and keep track of the correct operator ordering. It is clear from table A.1 that the remote contributions to the conduction band stem from remote Γ_{15} states, while the valence band states have contributions from all except the Γ_2 states. The corresponding terms are given by the matrix $\mathbf{H}_r^{4 \times 4}$ (2.2.18) and the coefficients (2.2.19). In deriving these terms, the energy for the energy-dependent renormalization has been replaced by the according band edge energies E_v and E_c . Although the approximation might be reasonable for very remote bands ν , it remains crude. The derivation of the terms these terms involves only symmetry arguments similar to the already used arguments within this chapter. The bar in \tilde{A}_c , \tilde{L} and \tilde{M} indicates the close relationship to the parameters \tilde{A}_c , \tilde{L}' and \tilde{M}' , which include the free-electron dispersion

$$\tilde{A}_c = \bar{A}_c + \frac{\hbar^2}{2m_0}, \quad \tilde{L}' = \bar{L} + \frac{\hbar^2}{2m_0}, \quad \tilde{M} = \bar{M} + \frac{\hbar^2}{2m_0}, \quad (2.2.13)$$

whereas in this case the free electron dispersion is still contained in the direct interaction matrix (2.2.8). The operator ordering in the offdiagonal terms $k_y \tilde{N}_+ k_x + k_x \tilde{N}_- k_y$ has been derived by Foreman [18]. The term \tilde{N}_+ contains the contribution from $\Gamma_1(F)$ and $\Gamma_{12}(G)$ bands, while \tilde{N}_- contains the contributions from $\Gamma_{15}(H_1)$ and $\Gamma_{25}(H_2)$ bands. In the bulk $\mathbf{k} \cdot \mathbf{p}$ theory, the ordering is irrelevant and the terms are summed together into the Kane's parameter \tilde{N}'

$$\tilde{N}' = \tilde{N}_+ + \tilde{N}_-. \quad (2.2.14)$$

Within the traditional $\mathbf{k} \cdot \mathbf{p}$ envelope function method applied to heterostructure, the symmetrized operator ordering (2.2.7) simply uses

$$\tilde{N}_+ = \tilde{N}_- = \frac{\tilde{N}'}{2}. \quad (2.2.15)$$

The parameters \tilde{L}' , \tilde{M} and \tilde{N}' are usually determined by calculating analytical expressions for the dispersion and relating them to measured effective masses. The detailed splitting of \tilde{N}' into \tilde{N}_+ and \tilde{N}_- is not directly accessible from experiment, but can be estimated [19] using the following arguments: The term \tilde{N}_- contains contributions of Γ_{15} and Γ_{25} bands. The Γ_{25} bands can only be formed by f -type and higher atomic orbitals, while Γ_{15} bands can be formed by p - d - f - and higher type orbitals [18]. Within the usual semiconductors, the influence of f orbitals is insignificant. Therefore, neglecting the influence of the Γ_{25} bands ($H_2 = 0$) and using 2.2.19, the value for \tilde{N}_- is given by

$$\tilde{N}_- = \bar{M} = \tilde{M} - \frac{\hbar^2}{2m_o}. \quad (2.2.16)$$

\tilde{N}_+ can be deduced using (2.2.14) and the experimentally determined value for \tilde{N}' . In a usual zinc-blende semiconductor such as $GaAs$, $\tilde{M} = -2.65$ and $\tilde{N}' = -17.4$ (in units of $\frac{\hbar^2}{2m_0}$). The symmetric operator ordering would therefore use $\tilde{N}_{+-} = -8.7$, while the Burt-Foreman ordering gives strongly asymmetric values $\tilde{N}_+ = -13.75$ and $\tilde{N}_- = -3.65$. In contrast to the operator ordering within the valence band, the ordering in the off-diagonal terms between the conduction and valence bands, given by the terms $k_y C k_z + k_z C k_y$, is required to be symmetric. Only remote Γ_{15} type bands mix into the s -type conduction band, and therefore, the non-vanishing elements from the perturbation are

$$k_y \langle s | p_y | y^r \rangle \langle y^r | p_z | x \rangle k_z + k_z \langle s | p_z | y^r \rangle \langle z^r | p_y | x \rangle k_y. \quad (2.2.17)$$

By crystal symmetry, these terms are equal. The term C is related to the common Kane parameter $B = 2C$. As B is usually small, it is commonly neglected, i.e. $C = 0$.

$$\mathbf{H}_r^{4 \times 4} = \left(\begin{array}{c|cccc} & |s\rangle & |x\rangle & |y\rangle & |z\rangle \\ \hline |s\rangle & kA_ck & k_yCk_z + k_zCk_y & k_xCk_z + k_zCk_x & k_yCk_x + k_xCk_y \\ |x\rangle & k_zCk_y + k_yCk_z & k_x\bar{L}k_x + k_y\bar{M}k_y + k_z\bar{M}k_z & k_x\tilde{N}_+k_y + k_y\tilde{N}_-k_x & k_x\tilde{N}_+k_z + k_z\tilde{N}_-k_x \\ |y\rangle & k_zCk_x + k_xCk_z & k_y\tilde{N}_+k_x + k_x\tilde{N}_-k_y & k_y\bar{L}k_y + k_x\bar{M}k_x + k_z\bar{M}k_z & k_y\tilde{N}_+k_z + k_z\tilde{N}_-k_y \\ |z\rangle & k_xCk_y + k_yCk_x & k_z\tilde{N}_+k_x + k_x\tilde{N}_-k_z & k_z\tilde{N}_+k_y + k_y\tilde{N}_-k_z & k_z\bar{L}k_z + k_x\bar{M}k_x + k_y\bar{M}k_y \end{array} \right), \quad (2.2.18)$$

$$\begin{aligned} \bar{L} &= F + 2G, & \bar{M} &= H_1 + H_2, \\ \tilde{N}_+ &= F - G, & \tilde{N}_- &= H_1 - H_2, \\ F &= \frac{\hbar^2}{m_0^2} \sum_{\nu}^{\Gamma_1} \frac{|\langle x | p_x | u_{\nu} \rangle|^2}{(E_v - E_{\nu})}, & G &= \frac{\hbar^2}{m_0^2} \sum_{\nu}^{\Gamma_{12}} \frac{|\langle x | p_x | u_{\nu} \rangle|^2}{(E_v - E_{\nu})}, \\ H_1 &= \frac{\hbar^2}{m_0^2} \sum_{\nu}^{\Gamma_{15}} \frac{|\langle s | p_x | u_{\nu} \rangle|^2}{(E_c - E_{\nu})}, & H_2 &= \frac{\hbar^2}{m_0^2} \sum_{\nu}^{\Gamma_{25}} \frac{|\langle x | p_x | u_{\nu} \rangle|^2}{(E_v - E_{\nu})}, \\ A_c &= \frac{\hbar^2}{m_0^2} \sum_{\nu}^{\Gamma_{15}} \frac{|\langle s | p_x | u_{\nu} \rangle|^2}{(E_c - E_{\nu})}, & C &= \frac{\hbar^2}{m_0^2} \sum_{\nu}^{\Gamma_{15}} \frac{\langle s | p_x | u_{\nu} \rangle \langle u_{\nu} | p_x | z \rangle}{(\frac{1}{2}(E_c + E_v) - E_{\nu})}. \end{aligned} \quad (2.2.19)$$

2.2.3.3 Spin-Orbit Interaction

Up to this point, the electron spin has been omitted. Within the semiconductors involving heavier atoms, the spin-orbit interaction has a large impact on the electron dispersions. The spin-orbit energy leads to additional terms in the equation (2.2.2) for the zone-center functions, namely

$$H_{SO,\mathbf{p}} = \frac{\hbar}{4m_0^2 c^2} (\nabla V \times \mathbf{p}) \cdot \boldsymbol{\sigma}, \quad (2.2.20)$$

$$H_{SO,\mathbf{k}} = \frac{\hbar}{4m_0^2 c^2} (\nabla V \times \mathbf{k}) \cdot \boldsymbol{\sigma}, \quad (2.2.21)$$

where c is the vacuum speed of light and $\boldsymbol{\sigma}$ are the *Pauli operators* acting on the electron-spin variable

$$\sigma_x = \begin{pmatrix} 0 & 1 \\ 1 & 0 \end{pmatrix}, \quad \sigma_y = \begin{pmatrix} 0 & -i \\ i & 0 \end{pmatrix}, \quad \sigma_z = \begin{pmatrix} 1 & 0 \\ 0 & -1 \end{pmatrix}.$$

The Bloch basis functions have to be extended to include the spin degree of freedom, which is done by giving the spin z -component, which can be either up $|\uparrow\rangle$ or down $|\downarrow\rangle$. The spin variable is diagonal, meaning that $\langle \uparrow|\uparrow \rangle = \langle \downarrow|\downarrow \rangle = 1$ and $\langle \uparrow|\downarrow \rangle = 0$. Using the spin, the initial basis of four states describing the lowest conduction band and the top valence bands is doubled to eight states

$$|s\uparrow\rangle, |x\uparrow\rangle, |y\uparrow\rangle, |z\uparrow\rangle, |s\downarrow\rangle, |x\downarrow\rangle, |y\downarrow\rangle, |z\downarrow\rangle. \quad (2.2.22)$$

All operators in the zone-center Hamiltonian (2.1.14) do not act on the spin variable. Therefore, the Hamiltonian is diagonal in the spin variable. Within the basis (2.2.22), the Hamiltonian is given by

$$\mathbf{H}_{rd}^{8 \times 8} = \begin{pmatrix} \mathbf{H}_d^{4 \times 4} + \mathbf{H}_r^{4 \times 4} & 0 \\ 0 & \mathbf{H}_d^{4 \times 4} + \mathbf{H}_r^{4 \times 4} \end{pmatrix}. \quad (2.2.23)$$

In contrast to this Hamiltonian, the spin-orbit interaction (2.2.20) and (2.2.21) is not diagonal in the basis (2.2.22). The reason to this lies in the symmetry of the spin. The crystal potential $V(\mathbf{r})$ without spin terms is invariant under any rotation around an angle of 2π , denoted here as \hat{E} . Under such a rotation, the wavefunction including the spin switches sign and is only invariant under the rotation of 4π . Therefore, if the point group of the crystal neglecting spin is given by \mathcal{G} , then the point group including spin will be given by the elements of \mathcal{G} and $\hat{E}\mathcal{G}$, leading to the definition of the *double-group* $\tilde{\mathcal{G}}$ of \mathcal{G} defined as

$$\tilde{\mathcal{G}} = \{g, \tilde{g} = -g\} \quad \forall g \in \mathcal{G}. \quad (2.2.24)$$

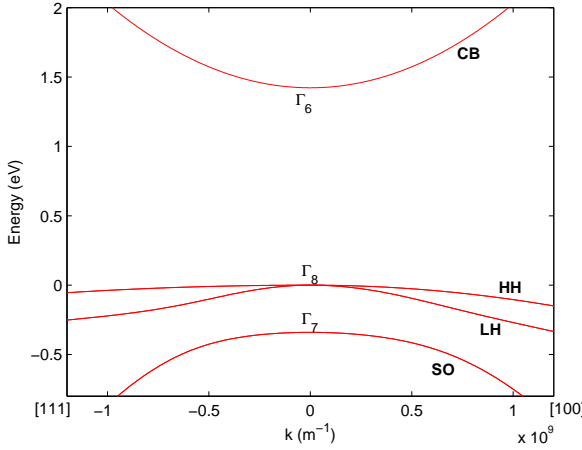


Figure 2.3: Band structure of bulk GaAs around the Γ point at room temperature, calculated using the $8 \times 8 \mathbf{k} \cdot \mathbf{p}$ for two crystal directions.

The spin-orbit interaction for $H_{SO,\mathbf{p}}$ of (2.2.20) leads, for the basis in (2.2.22), to [20]

$$\mathbf{H}_{SO,\mathbf{p}} = \frac{\Delta}{3} \begin{pmatrix} 0 & 0 & 0 & 0 & 0 & 0 & 0 & 0 \\ 0 & 0 & -i & 0 & 0 & 0 & 0 & 1 \\ 0 & i & 0 & 0 & 0 & 0 & 0 & -i \\ 0 & 0 & 0 & 0 & 0 & -1 & i & 0 \\ 0 & 0 & 0 & 0 & 0 & 0 & 0 & 0 \\ 0 & 0 & 0 & -1 & 0 & 0 & i & 0 \\ 0 & 0 & 0 & -i & 0 & -i & 0 & 0 \\ 0 & 1 & i & 0 & 0 & 0 & 0 & 0 \end{pmatrix}. \quad (2.2.25)$$

Here, the spin-orbit energy Δ is defined as

$$\Delta = -3i \frac{\hbar}{4m_0^2 c^2} \left\langle x \mid (\nabla V \times \mathbf{p})_y \mid z \right\rangle. \quad (2.2.26)$$

The k -dependent spin-orbit interaction $H_{SO,\mathbf{k}}$ of (2.2.21) is small and therefore commonly neglected [5]. The result of $H_{SO,\mathbf{k}}$ are terms linear in k , leading to an off-diagonal coupling between the conduction and the valence band. Further, the spin-orbit interaction $H_{SO,\mathbf{p}}$ is usually only included in the direct interaction, while perturbative contributions from remote bands are in general neglected. The effect of the spin-orbit interaction is to split the six-fold (threefold without spin) degeneracy of the valence band at Γ into a fourfold degeneracy with eigenvalue $\frac{\Delta}{3}$ and a two-fold degeneracy with an eigenvalue of $-\frac{2\Delta}{3}$. In other words, the states are separated by Δ . The four-fold degenerate states corresponds to the irreducible representation Γ_8 of the double group of T_d . Away from Γ , these states create the *heavy-hole* (HH) and the *light-hole* (LH) bands. The two-fold degenerate states correspond to the Γ_7 representation and lie below the Γ_8 states by $-\Delta$. The Γ_7 band is referred to as *spin-orbit split off band* (SO). The lowest conduction band (CB) states finally correspond to Γ_6 states. The situation is illustrated in Fig. 2.3, where the band structure of GaAs calculated using the here presented $\mathbf{k} \cdot \mathbf{p}$ model is plotted around $\mathbf{k} = 0$. The experimental accessible bandgap is given by the difference between the Γ_6 and the Γ_8 states. Therefore, the valence band edge E_v in (2.2.10), needs to be shifted by $-\frac{\Delta}{3}$.

The here elaborated model, including the CB, HH, LH and SO band, is commonly referred to as the $8 \times 8 \mathbf{k} \cdot \mathbf{p}$ model. For large band gap materials, the coupling between the conduction and valence bands is weak and therefore the $8 \times 8 \mathbf{k} \cdot \mathbf{p}$ model can be divided into a 6×6 model, including only the valence bands and a single band model for the spin degenerate conduction band. This division is achieved by perturbatively folding the conduction band onto the valence bands and vice versa. The $6 \times 6 \mathbf{k} \cdot \mathbf{p}$ is therefore obtained by using only the valence band part of $\mathbf{H}_{rd}^{8 \times 8} + \mathbf{H}_{SO,\mathbf{p}}$ with modified parameters L' and N' given by

$$L' = \tilde{L}' + \frac{P^2}{E_g}, \quad N_+ = \tilde{N}_+ + \frac{P^2}{E_g} \quad (2.2.27)$$

instead of \tilde{L}' and \tilde{N}_+ . The parameter \tilde{M} , and consequently \tilde{N}_- , remain unchanged. Thereby, the correct operator ordering is conserved. The conduction band parameter is obtained using

$$A_c = \tilde{A}_c + \frac{P^2}{E_g}, \quad (2.2.28)$$

which is then equal to the common conduction band effective mass. For some semiconductors, the spin-orbit splitting is large and the SO band has only little influence on the top of the valence band. Then, the $6 \times 6 \mathbf{k} \cdot \mathbf{p}$ model can be further reduced to only include the HH and LH bands. The reduction is performed by choosing a combination of basis functions (2.2.22) effectively diagonalizing the spin-orbit interaction $\mathbf{H}_{SO,\mathbf{p}}$. The new basis is labelled according to its total angular momentum J and the angular momentum around the z -axis, J_z . A possible choice, using $|J, J_z\rangle$ as notation, is given by

$$\begin{aligned} u_{hh} = \left| \frac{3}{2}, \frac{3}{2} \right\rangle &= -\frac{1}{\sqrt{2}} (|x \uparrow\rangle + i |y \uparrow\rangle), \\ u_{lh} = \left| \frac{3}{2}, \frac{1}{2} \right\rangle &= -\frac{1}{\sqrt{6}} (|x \downarrow\rangle + i |y \uparrow\rangle) + \sqrt{\frac{2}{3}} |z \uparrow\rangle, \\ \bar{u}_{lh} = \left| \frac{3}{2}, -\frac{1}{2} \right\rangle &= \frac{1}{\sqrt{6}} (|x \uparrow\rangle - i |y \uparrow\rangle) + \sqrt{\frac{2}{3}} |z \downarrow\rangle, \\ \bar{u}_{hh} = \left| \frac{3}{2}, -\frac{3}{2} \right\rangle &= \frac{1}{\sqrt{2}} (|x \downarrow\rangle - i |y \downarrow\rangle), \\ u_{SO} = \left| \frac{1}{2}, \frac{1}{2} \right\rangle &= \frac{1}{\sqrt{3}} (|x \downarrow\rangle + i |y \downarrow\rangle + |z \uparrow\rangle), \\ \bar{u}_{SO} = \left| \frac{1}{2}, -\frac{1}{2} \right\rangle &= \frac{1}{\sqrt{3}} (|x \uparrow\rangle - i |y \uparrow\rangle - |z \downarrow\rangle). \end{aligned} \quad (2.2.29)$$

The four states with total angular momentum of $\frac{3}{2}$ belong to Γ_8 and the two states with an angular momentum of $\frac{1}{2}$ form the Γ_7 (or SO) bands. Transforming the Hamiltonian into the basis (2.2.29) and neglecting the Γ_7 rows and columns finally results in the $4 \times 4 \mathbf{k} \cdot \mathbf{p}$ model. Within the $4 \times 4 \mathbf{k} \cdot \mathbf{p}$ model, it is common to use the Luttinger parameters γ_1, γ_2 and γ_3 ¹[21] instead of the Kane's parameters of the 6×6 model L' , M and N' . The Luttinger parameters are usually those given in literature. The parameters are related to each other via

$$\begin{aligned} L' &= -\frac{\hbar^2}{2m_0} (\gamma_1 + 4\gamma_2) \\ M &= -\frac{\hbar^2}{2m_0} (\gamma_1 - 2\gamma_2) \\ N' &= -\frac{\hbar^2}{2m_0} 6\gamma_3. \end{aligned} \quad (2.2.30)$$

From (2.2.30), the parameters for 8×8 model can be calculated using the renormalization (2.2.27).

In terms of the Luttinger parameters the full 8×8 Hamiltonian can be written explicitly as in (2.2.31) [4, 21, 8].

$$\mathbf{H}^{8 \times 8} = \begin{pmatrix} E_c & P_z & \sqrt{2}P_z & -\sqrt{3}P_+ & 0 & \sqrt{2}P_- & P_- & 0 \\ P_z^\dagger & P + \Delta & \sqrt{2}Q^\dagger & -S^\dagger/\sqrt{2} & -\sqrt{2}P_+^\dagger & 0 & -\sqrt{3/2}S & -\sqrt{2}R \\ \sqrt{2}P_z^\dagger & \sqrt{2}Q & P - Q & -S^\dagger & -P_+^\dagger & \sqrt{3/2}S & 0 & R \\ -\sqrt{3}P_+^\dagger & -S/\sqrt{2} & -S & P + Q & 0 & \sqrt{2}R & R & 0 \\ 0 & -\sqrt{2}P_+ & -P_+ & 0 & E_c & P_z & -\sqrt{2}P_z & -\sqrt{3}P_- \\ \sqrt{2}P_-^\dagger & 0 & \sqrt{3/2}S^\dagger & \sqrt{2}R^\dagger & P_z^\dagger & P + \Delta & \sqrt{2}Q^\dagger & -S/\sqrt{2} \\ P_-^\dagger & -\sqrt{3/2}S^\dagger & 0 & R^\dagger & -\sqrt{2}P_z^\dagger & \sqrt{2}Q & P - Q & S \\ 0 & -\sqrt{2}R^\dagger & R^\dagger & 0 & -\sqrt{3}P_-^\dagger & -S^\dagger/\sqrt{2} & S^\dagger & P + Q \end{pmatrix} \quad (2.2.31)$$

¹The full listing of these parameters is given in [4].

where

$$E_c = E_g + \frac{\hbar^2}{2m_0} (k_x^2 + k_y^2 + k_z^2), \quad (2.2.32)$$

$$P = \frac{\hbar^2}{2m_0} \gamma_1 (k_x^2 + k_y^2 + k_z^2), \quad (2.2.33)$$

$$P_{\pm} = \sqrt{\frac{1}{6}} [i\mathcal{P}(k_x \pm ik_y) + \mathcal{B}k_z(k_y \pm ik_x)], \quad (2.2.34)$$

$$P_z = \sqrt{\frac{1}{3}} (i\mathcal{P}k_z + \mathcal{B}k_x k_y), \quad (2.2.35)$$

$$Q = \frac{\hbar^2}{2m_0} \gamma_2 (k_x^2 + k_y^2 - 2k_z^2), \quad (2.2.36)$$

$$R = \frac{\hbar^2}{2m_0} \left[-\sqrt{3}\gamma_2 (k_x^2 - k_y^2) + i2\sqrt{3}\gamma_3 k_x k_y \right], \quad (2.2.37)$$

$$S = \frac{\hbar^2}{2m_0} \gamma_3 (k_x - ik_y) k_z. \quad (2.2.38)$$

The parameter Δ is, as before, the spin-orbit splitting energy. The coupling between the Γ conduction band edge state $|s\rangle$ and the Γ valence band edge state $|z\rangle$ is given by

$$\mathcal{P} = -\frac{\hbar^2}{m_0} \int_{V_c} \varphi_s \frac{\partial}{\partial z} \varphi_z. \quad (2.2.39)$$

The Kane parameter \mathcal{B} describes the inversion asymmetry. In most practical calculations, this parameter is neglected. The parameters $\gamma_1, \gamma_2, \gamma_3$ and \mathcal{P} can be determined from effective masses at the Γ point of the bulk semiconductor [4]

$$\frac{m_0}{m_{hh}(001)} = \gamma_1 - 2\gamma_2, \quad (2.2.40)$$

$$\frac{m_0}{m_{lh}(001)} = \gamma_1 + 2\gamma_2 + \lambda, \quad (2.2.41)$$

$$\frac{m_0}{m_{SO}(001)} = \gamma_1 + \frac{1}{2}\lambda r, \quad (2.2.42)$$

$$\frac{m_0}{m_{hh}(111)} = \gamma_1 - 2\gamma_3, \quad (2.2.43)$$

where the dimensionless parameters λ and r are given by

$$\lambda = \frac{4m_0 \mathcal{P}^2}{3\hbar^2 E_g}, \quad (2.2.44)$$

$$r = \frac{E_g}{E_g + \Delta}. \quad (2.2.45)$$

2.2.4 Two Band Model

The conduction band can be modeled quite easily if we assume that the interaction with the other bands is weak enough for it to be treated perturbatively, i.e. use a simple effective mass model. In the case of the valence band, however, the strong interaction between the degenerate light and heavy hole bands (near the band edge) requires that these bands are taken into account explicitly. Only when we consider energy levels deep into the valence bands (close to the SO splitting energy, about 300 meV in GaAs) do the coupling terms to the SO and conduction bands (1.5 eV splitting) can be introduced through the effective mass.

The degeneracy of the light and heavy hole bands near the band edge generates a coupling term (as in the Luttinger Hamiltonian). Including spin degeneracy, this yields a set of four coupled effective mass equations [22, 4, 23]. Fortunately, this set of coupled equations can be greatly simplified by a method described in [23]. Here

a unitary transformation of the four basis Bloch functions in (2.2.29) into a new set u_A, u_B, u_C, u_D to decouple the set of four coupled equations into two coupled ones. The Bloch functions u_i are given by

$$u_A = \frac{1}{\sqrt{2}} (u_{hh} - \bar{u}_{hh}), \quad (2.2.46)$$

$$u_B = \frac{1}{\sqrt{2}} (-u_{lh} - \bar{u}_{lh}), \quad (2.2.47)$$

$$u_C = \frac{1}{\sqrt{2}} (u_{lh} + \bar{u}_{lh}), \quad (2.2.48)$$

$$u_D = \frac{1}{\sqrt{2}} (u_{hh} + \bar{u}_{hh}). \quad (2.2.49)$$

Consequently, the $4 \times 4 \mathbf{k} \cdot \mathbf{p}$ Hamiltonian

$$\mathbf{H}^{4 \times 4} = \begin{pmatrix} P - Q & -S^\dagger & 0 & R \\ -S & P + Q & R & 0 \\ 0 & R^\dagger & P - Q & S \\ R^\dagger & 0 & S^\dagger & P + Q \end{pmatrix}. \quad (2.2.50)$$

In terms of the the new base proposed above, it can be diagonalized into two 2×2 block matrices, upper H^U and lower H^L , given by

$$H^\sigma = \begin{pmatrix} P \pm Q & W \\ W^\dagger & P \mp Q \end{pmatrix}, \quad (2.2.51)$$

where $W = |R| - i|S|$. The index $\sigma = U(L)$ refers to the upper (lower) \pm signs. The upper and lower blocks are equivalent, showing the double degeneracy of the heavy and light hole bands. It is therefore sufficient to solve the upper block and obtain its solutions. The solutions of the lower block can easily be determined from the latter.

We can identify $P - Q$ and $P + Q$ with the light hole energy (operator) \hat{H}_{lh} and the heavy hole energy \hat{H}_{hh} , respectively. Similarly to the conduction band case, the Schrödinger equation with the Hamiltonian (2.2.51) can be simplified into an effective-mass formalism with

$$\hat{H}_{lh} = -(\gamma_1 + 2\gamma_2) \frac{\partial^2}{\partial z^2} + (\gamma_1 - \gamma_2) k_t^2, \quad (2.2.52)$$

$$\hat{H}_{hh} = -(\gamma_1 - 2\gamma_2) \frac{\partial^2}{\partial z^2} + (\gamma_1 + \gamma_2) k_t^2, \quad (2.2.53)$$

$$\hat{W} = \begin{cases} \sqrt{3}k_t (\gamma_2 k_t - 2\gamma_3 \frac{\partial}{\partial z}) & \text{for [100]} \\ \sqrt{3}k_t (\gamma_3 k_t - 2\gamma_2 \frac{\partial}{\partial z}) & \text{for [110]} \end{cases} \quad (2.2.54)$$

Finally, we take into account the potential $V(z)$, which represents the (bulk) valence-band-edge offset with respect to an arbitrary reference energy. This allows us write the effective mass equation as

$$\begin{pmatrix} \hat{H}_{hh} + V & \hat{W} \\ \hat{W}^\dagger & \hat{H}_{lh} + V \end{pmatrix} \begin{pmatrix} F_{hh} \\ F_{lh} \end{pmatrix} = E(\mathbf{k}) \begin{pmatrix} F_{hh} \\ F_{lh} \end{pmatrix}, \quad (2.2.55)$$

where F_{hh} and F_{lh} are the envelope functions corresponding to u_A and u_B , respectively. Note that in this formalism, hole energies are taken to be positive.

The first step in solving the quantum well problem, is finding the solution in bulk material, where we take V to be a constant V_0 . The value of V_0 will be different in well material and barriers reflecting the different valence band edge offsets. We can now easily solve for the eigenenergies $E(\mathbf{k})$, yielding the bulk energy dispersion relations for the heavy and light hole subbands. We consider the case of a [100] plane, writing the in-plane \mathbf{k} component as k_t

$$E(\mathbf{k}) - V_0 = \gamma_1 (k_z^2 + k_t^2) \pm \sqrt{4\gamma_2^2 (k_z^2 + k_t^2) + 12 (\gamma_3^2 - \gamma_2^2) k_z^2 k_t^2}, \quad (2.2.56)$$

where the plus sign refers to the light hole solution, and the minus to the heavy hole one. This expression can be rewritten to

$$E(\mathbf{k}) = V_0 + \left[\gamma_1 \pm \gamma_2 \sqrt{1 + 3 \frac{\gamma_3^2 - \gamma_2^2}{\gamma_2^2} \frac{k_z^2 k_t^2}{(k_z^2 + k_t^2)^2}} \right] (k_z^2 + k_t^2). \quad (2.2.57)$$

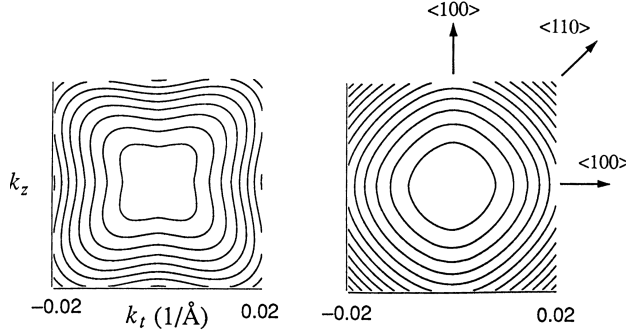


Figure 2.4: Contours of constant energy within any [100] plane of k -space for the heavy (right) and light (left) hole subbands in bulk GaAs. The energy spacing between each contour level is 0.5 meV for the HH band and 3 meV for the LH band. The effective HH mass is much larger along the [110] direction than along the [100] direction, as indicated by the larger contour spacing. The effective LH mass is seen to be much more isotropic (after [24]).

A similar derivation can be formulated for the [110] crystal planes.

Constant energy contours are shown in Fig. 2.4, illustrating that γ_3 can be related to the mass anisotropy along the [100] and [110] directions. If k_t small compared to k_z , we can expand the square root in (2.2.56)

$$E(\mathbf{k}) = V_0 + (\gamma_1 \pm \gamma_2) (k_z^2 + k_t^2) \pm 3 \frac{\gamma_3^2 - \gamma_2^2}{\gamma_2} k_t^2. \quad (2.2.58)$$

The Energy term accounting for anisotropy for a given k_t and k_z is equal for the HH and LH subbands. However, due to the lower energy of the HH bands the anisotropy term is relatively more important for HH than for LH, resulting in a clearly anisotropic HH band and a quasi isotropic LH band.

Still, we see that in bulk material, the effective masses along the z -axis [001] and x - and y - axes [100] and [010] are identical (as expected), as the dispersion relation is given by $E(\mathbf{k}) = V_0 + (\gamma_1 \pm 2\gamma_2) k^2$. We can easily find this from (2.2.56) with $k_t = 0$ for [001], and $k_z = 0$ for the x - and y - directions.

The eigenvectors of (2.2.55) are found to be, apart from a normalization constant

$$\varphi_1(\mathbf{k}, \mathbf{r}) = \begin{pmatrix} F_{hh,1} \\ F_{lh,1} \end{pmatrix} = e^{i\mathbf{k}\cdot\mathbf{r}} \begin{pmatrix} H_{lh} + V_0 - E_{hh} \\ -W^\dagger \end{pmatrix}, \quad (2.2.59)$$

$$\varphi_2(\mathbf{k}, \mathbf{r}) = \begin{pmatrix} F_{hh,2} \\ F_{lh,2} \end{pmatrix} = e^{i\mathbf{k}\cdot\mathbf{r}} \begin{pmatrix} H_{lh} + V_0 - E_{lh} \\ -W^\dagger \end{pmatrix}, \quad (2.2.60)$$

where the matrix notation implies

$$\varphi = F_{hh} u_A + F_{lh} u_B. \quad (2.2.61)$$

To solve the quantum well problem, we choose the well growth direction (direction of confinement) along the z -axis. The xy -plane is the plane of the well, as in Fig. 2.5. We can construct a confined solution from the bulk plane wave solutions by imposing boundary conditions along the confinement axis. In the plane of the well, there is no confinement and hence we retain the bulk plane wave solution. By taking a linear combination of the bulk solutions in each material, a general solution can be constructed. As illustrated in Fig. 2.6, four plane wave solutions exist at a given energy, yielding a general solution Φ of the form

$$\Phi = \sum A_\pm \varphi_1(\pm k_{z1}, k_t, \mathbf{r}) + \sum B_\pm \varphi_2(\pm k_{z2}, k_t, \mathbf{r}). \quad (2.2.62)$$

The four coefficients A_\pm and B_\pm are unknown constants. Both φ_1 and φ_2 are two-component vectors as seen in (2.2.59) and (2.2.60). We can write the components of Φ , F_{hh} and F_{lh} , as

$$F_{hh} = e^{i\mathbf{k}_t \cdot \mathbf{r}_t} \left[\sum A_\pm F_{hh,1}(\pm k_{z1}, k_t) e^{\pm i k_{hh} z} + \sum B_\pm F_{hh,2}(\pm k_{z2}, k_t) e^{\pm i k_{hh} z} \right], \quad (2.2.63)$$

$$F_{lh} = e^{i\mathbf{k}_t \cdot \mathbf{r}_t} \left[\sum A_\pm F_{lh,1}(\pm k_{z1}, k_t) e^{\pm i k_{lh} z} + \sum B_\pm F_{lh,2}(\pm k_{z2}, k_t) e^{\pm i k_{lh} z} \right]. \quad (2.2.64)$$

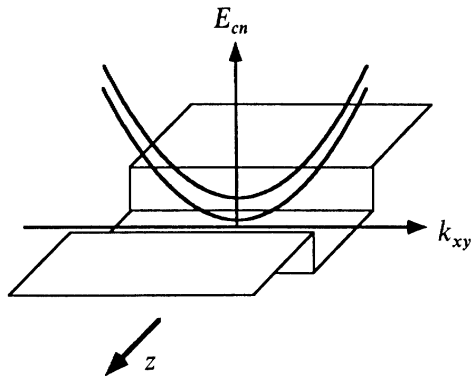


Figure 2.5: The "in-plane" subband structure of the quantum well in the conduction band. Within the plane of the well, the electron still behaves like a "free" electron. Thus, for each quantized level, a parabolic energy subband exist (after [24]).

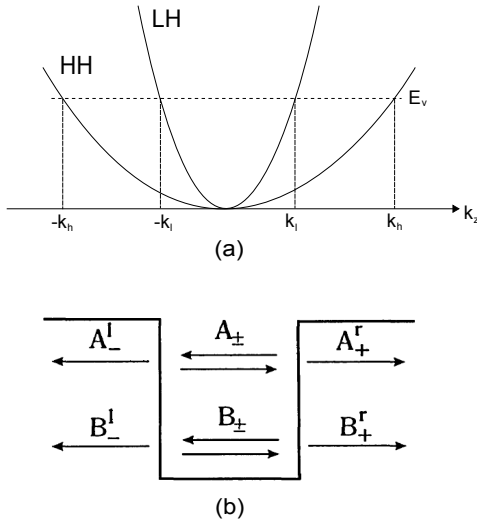


Figure 2.6: At any one energy on a bulk material, we can find four wavevectors corresponding to the heavy and light hole bands. An eigenstate of the Hamiltonian in a quantum well is then made of a linear combination of the bulk plane waves corresponding to those wave vectors. The amplitudes A_{\pm} and B_{\pm} in (a) correspond, respectively, to $\pm k_{z1}$ (light hole) and $\pm k_{z2}$ in (b) for the well layer of the quantum well (GaAs throughout this thesis). In the barriers (AlGaAs) a similar mechanism is employed. The boundary conditions at the interfaces then determine the energy eigenvalues and the coefficients.

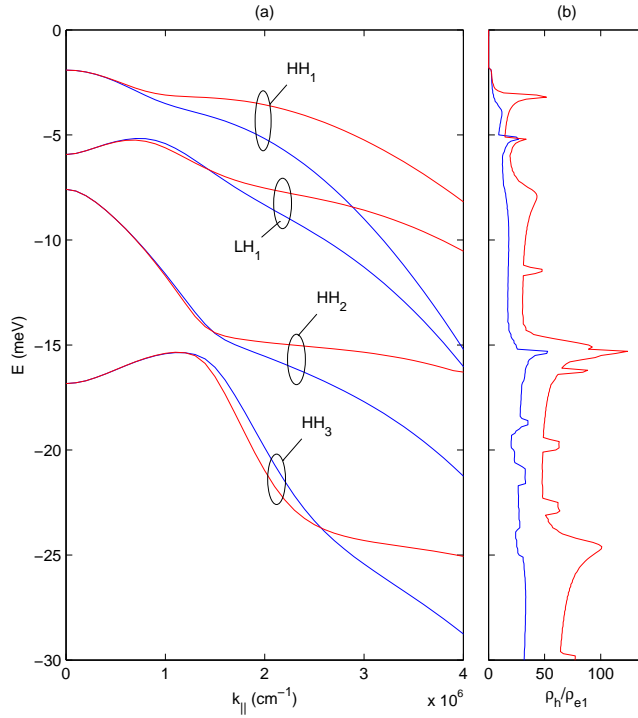


Figure 2.7: (a) Valence subbands dispersion relations calculated for a 200 Å wide GaAs/Al_{0.1}Ga_{0.9}As quantum well, for [100] (blue) and [110] (red) crystallographic directions at $T = 2\text{ K}$. The subbands are named after their dominant character at the zone center ($k_t = 0$). (b) The ratio between the density of states of the valence subbands and the first conduction subband, calculated for the same structure for both crystal directions.

Thus we have four unknown constants in each region, making a total of 12 unknowns over the three regions. The boundary conditions at the interfaces between the regions and the demand that the solutions be confined in the quantum well provide the necessary relations to solve the problem. In order to symmetrize the problem the following quantities have to be matched across the interfaces

$$F_{hh} \text{ and } (\gamma_1 - 2\gamma_2) \frac{dF_{hh}}{dz} + \sqrt{3}\gamma_3 k_t F_{lh}, \quad (2.2.65)$$

$$F_{lh} \text{ and } (\gamma_1 - 2\gamma_2) \frac{dF_{lh}}{dz} - \sqrt{3}\gamma_3 k_t F_{hh}. \quad (2.2.66)$$

These boundary conditions were obtained by symmetrizing the Hamiltonian (2.2.51). Caution should be issued however that the above boundary conditions only apply when the Bloch functions in both well materials and are similar, as is the case for the GaAs – AlGaAs system used throughout this thesis. The boundary conditions boil down to the continuity of the wave function and “generalized” continuity of its derivative, corresponding to current across the interface. The numerical implementation details of the two bands model are given in Appendix B.

As an illustration of the numerical method formulated in this section, we present in Fig. 2.7(a) the valence subband structure of a 200 Å GaAs/Al_{0.1}Ga_{0.9}As quantum well. The light and heavy holes are very heavily coupled, giving rise to highly non-parabolic subbands. The difference between the two crystallographic directions becomes clearly observable away from the zone center.

Particularly important is the *density of states* (DOS), which can be found from

$$\rho(E) = \frac{1}{\pi} \frac{dk}{dE}, \quad (2.2.67)$$

assuming the dispersion relationship is isotropic (using the axial approximation, see Appendix B). As an illustration,

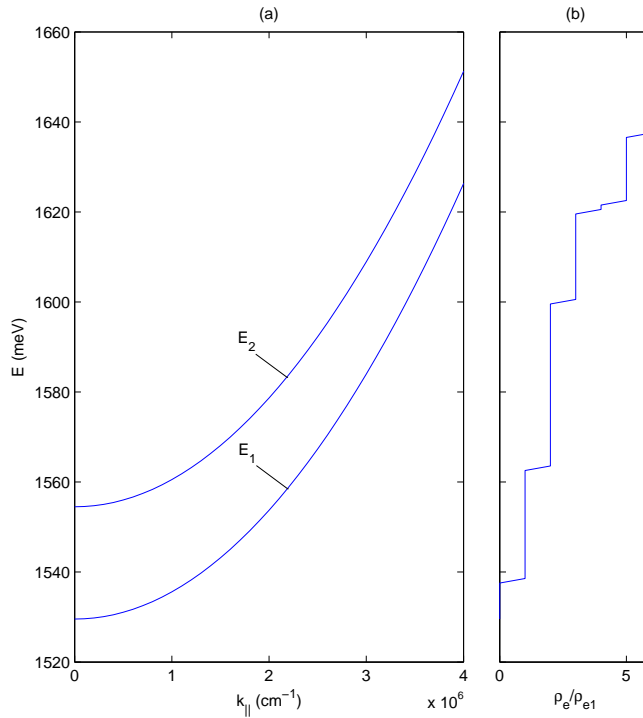


Figure 2.8: (a) Conduction subbands dispersion relations calculated for a 200 Å wide GaAs/Al_{0.1}Ga_{0.9}As quantum well at T = 2 K. (b) The ratio between the density of states of the conduction subbands and the first conduction subband, calculated for the same structure.

we plot in Fig. 2.7(b) the calculated ratio between the DOS of the valence subbands from 2.7(a) and the DOS of the first conduction subband. The spikes in the DOS are due to the band extrema away from the zone center.

As stated at the beginning of the section, the conduction subbands are calculated using the effective mass approximation, where the bands are assumed to be parabolic and the problem reduces to a one-dimensional Schrödinger equation of the form

$$\left(-\frac{\hbar^2}{2} \frac{d}{dz} \frac{1}{m^*(z)} \frac{d}{dz} + V(z) \right) \varphi_n(z) = E_n \varphi_n(z). \quad (2.2.68)$$

We can write down the conduction band wave function as

$$\Psi_n(\mathbf{r}) = \frac{1}{\sqrt{A}} e^{i\mathbf{k}_{\perp} \cdot \mathbf{r}} \varphi_n(z) (|S, \uparrow\rangle + |S, \downarrow\rangle), \quad (2.2.69)$$

where \$|S, \uparrow\rangle\$ and \$|S, \downarrow\rangle\$ are the conduction band wave functions for the bulk case. As an illustration, we plot in Fig. 2.8(a) the dispersion relation for the first two conduction subbands calculated for the same structure as in Fig. 2.7 above. Fig. 2.8(b) also presents the two-dimensional density of states for these subbands.

For the sake of completeness, we present in Fig. 2.9 the wavefunctions for first two conduction and first four valence subbands calculated at the the Brillouin zone center, for the 200 Å wide GaAs/Al_{0.1}Ga_{0.9}As quantum wells considered in the examples above. Here we separate the heavy and light hole subband wavefunctions into figures (b) and (c) for the sake of clarity. The dotted lines mark the energetic locations of these wavefuctions and the quantum well energetic profile is outlined by solid black curves.

2.3 Schrödinger-Poisson Model

In the discussion so far have concentrated solely on solving systems for a single charge carrier. In many devices such models would be inadequate as large numbers of charge carriers, e.g. electrons, can be present in the conduction

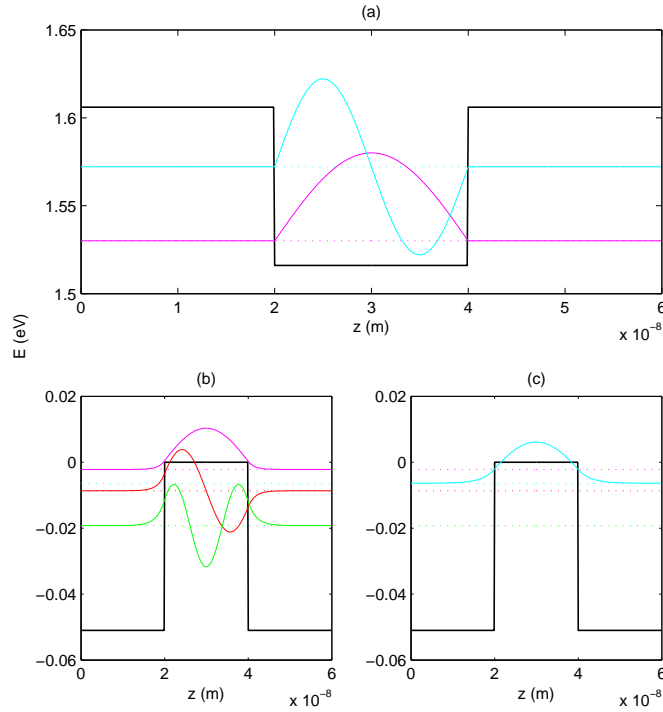


Figure 2.9: Wave functions for the (a) conduction, (b) valence heavy and (c) light hole subbands, calculated at the Brillouin zone center ($k_t = 0$) for a 200 Å wide GaAs/Al_{0.1}Ga_{0.9}As quantum well at $T = 2\text{ K}$.

band. In order to decide whether or not typical carrier densities would give rise to a significant additional potential on top of the usual band-edge potential terms (which will be labelled specifically as V_{CB} or V_{VB}), it then becomes necessary to solve the electrostatics describing the system.

2.3.1 Model Formulation

When considering the case of an n-type material, then (although obvious) it is worth stating that the number of free electrons in the conduction band is equal to the number of positively charged ionized donors in the heterostructure. As an example, we can point out the modulation doped system, where the doping is located in a position where the free carriers it produces will become spatially separated from the ion. The additional potential term $V_\rho(z)$ arising from this, or any other charge distribution ρ , can be expressed by using Poisson's equation

$$\nabla^2 V_\rho = -\frac{\rho}{\epsilon} \quad (2.3.1)$$

where ϵ is the permittivity of the material, i.e. $\epsilon = \epsilon_r \epsilon_0$. The solution is generally obtained via the electric field strength \mathbf{E} . Recalling that

$$\mathbf{E} = -\nabla V \quad (2.3.2)$$

the potential then follow in the usual way [1]

$$V_\rho(z) = - \int_{-\infty}^z \mathbf{E} \cdot d\mathbf{r}. \quad (2.3.3)$$

Given that the potential profiles, $V_{CB}(Z)$ for example, are one-dimensional, then they will also produce a one-dimensional charge distribution. In addition, remembering that the quantum wells are assumed infinite in the $x - y$ plane then any charge density $\rho(z)$ can be thought of as an infinite plane, i.e. a sheet, with areal charge density $\sigma(z)$ and thickness δz , as shown in Fig. 2.10(a). Such an infinite plane of charge produces an electric field perpendicular

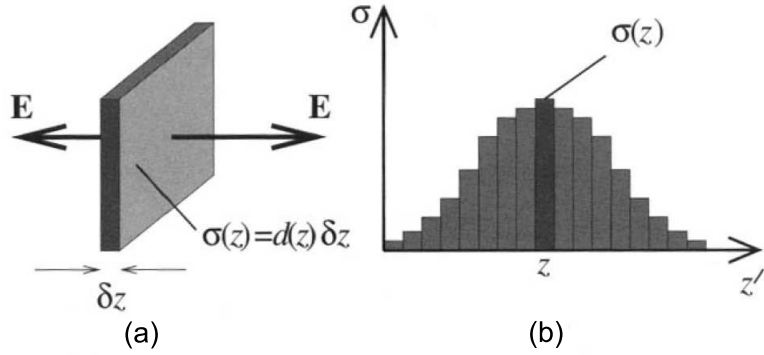


Figure 2.10: *Electric field strength from an infinite plane of charge of volume density $d(z)$ and thickness δz (after [25]).*

to it, and with a strength

$$\mathbf{E} = \frac{\sigma}{2\epsilon}. \quad (2.3.4)$$

Note that as the sheet is infinite in the plane, then the field strength is constant for all distances from the plane. The total electric field strength due to many of these planes of charge, as shown in Fig. 2.10(b), is then the sum of the individual contributions as follows

$$\mathbf{E}(z) = \sum_{z'=-\infty}^{\infty} \frac{\sigma(z')}{2\epsilon} \text{sign}(z - z') \quad (2.3.5)$$

where the function sign is defined as

$$\text{sign}(z) = \begin{cases} 1, & z \geq 0 \\ -1, & z \leq 0 \end{cases} \quad (2.3.6)$$

and has been introduced to account for the vector nature of \mathbf{E} , i.e. if a single sheet of charge is at a position z' , then for $z > z'$, $\mathbf{E}(z) = +\sigma/2\epsilon$, whereas for $z < z'$, $\mathbf{E}(z) = -\sigma/2\epsilon$. Note further that it is only the charge neutrality, there are as many ionized donors (or acceptors) in the system as there are electrons (or holes), or expressed mathematically

$$\sum_{z=-\infty}^{\infty} \sigma(z) = 0, \quad (2.3.7)$$

which ensures that the electric field, and hence the potential, go to zero at large distances from the charge distribution. For the case of a doped semiconductor, there would be two contributions to the charge density $\sigma(z)$, where the first would be the ionized impurities and the second the free charge carriers themselves. While the former would be known from the doping density in each semiconductor layer, as defined at growth time, the latter would be calculated from the probability distributions of the carriers in the heterostructure. Thus if $d(z)$ defines the volume density of the dopants at position z , where the planes are separated by the usual step length δz , then the total number of carriers, per unit cross-sectional area, introduced into the heterostructure is given by

$$N = \int_{-\infty}^{\infty} d(z) dz. \quad (2.3.8)$$

The net charge density in any of the planes follows as

$$\sigma(z) = q [N\psi^*(z)\psi(z) - d(z)] \delta z \quad (2.3.9)$$

where q is the charge on the extrinsic carriers. The step length δz selects the proportion of the carriers that are within that slab and converts the volume density of dopant, $d(z)$, into an areal density.

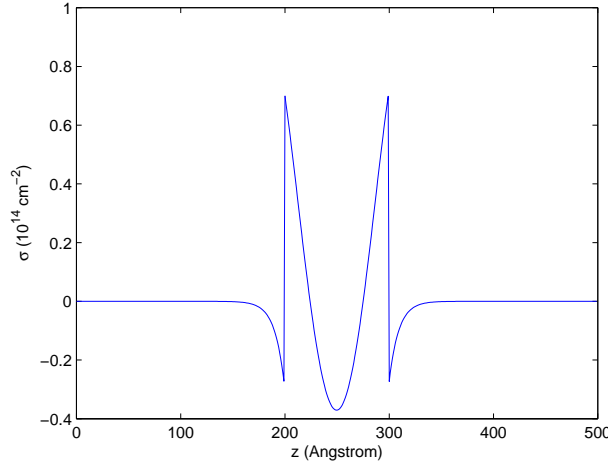


Figure 2.11: Areal charge density σ for a 100 \AA GaAs well, n -type doped to $2 \times 10^{18}\text{ cm}^{-3}$, surrounded by undoped $\text{Al}_{0.2}\text{Ga}_{0.8}\text{As}$ 4 meV barriers.

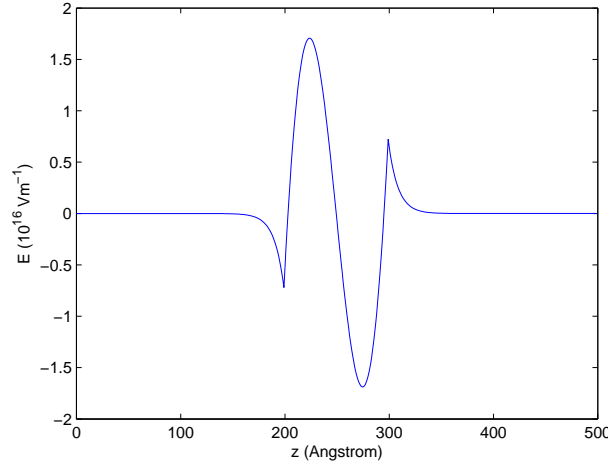


Figure 2.12: The electric field strength \mathbf{E} due to the charge distribution shown in Fig. 2.11.

If the charge carriers are distributed over more than one subband, then the contribution to the charge density $\sigma(z)$ would have to be summed over the relevant subbands

$$\sigma(z) = q \left[\sum_{i=1}^n N_i \psi_i^*(z) \psi_i(z) - d(z) \right] \delta z, \quad (2.3.10)$$

where $\sum_{i=1}^n N_i = N$.

Fig. 2.11 shows the areal charge density along the growth axis for a 100 \AA GaAs well, n -type doped to $2 \times 10^{18}\text{ cm}^{-3}$, surrounded by undoped $\text{Ga}_{0.8}\text{Al}_{0.2}\text{As}$ barriers. The ionized donors yield a constant contributions to σ within the well of $d(z)\delta z = 2 \times 10^{24}\text{ m}^{-3} \times 1\text{ \AA} = 2 \times 10^{14}\text{ m}^{-2}$, in each of the 1 \AA thick slabs. Hence, the total number N of electrons in the quantum well is $100 \times 2 \times 10^{14}\text{ m}^{-2} = 2 \times 10^{12}\text{ cm}^{-2}$. By assuming that the electrons introduced by such doping all occupy the ground state of the quantum well, then the curve on top of the ionized impurity background clearly resembles $-\psi^*\psi$, as expected from the mathematics. The discontinuities in σ occur at the edges of the doping profiles and are of magnitude $2 \times 10^{14}\text{ m}^{-2}$, again as expected.

There are a number of points to note about Fig. 2.12, which plots the electric field strength \mathbf{E} due to the charge distribution (as defined in equation (2.3.5)) along the growth axis of the heterostructure. First, the field

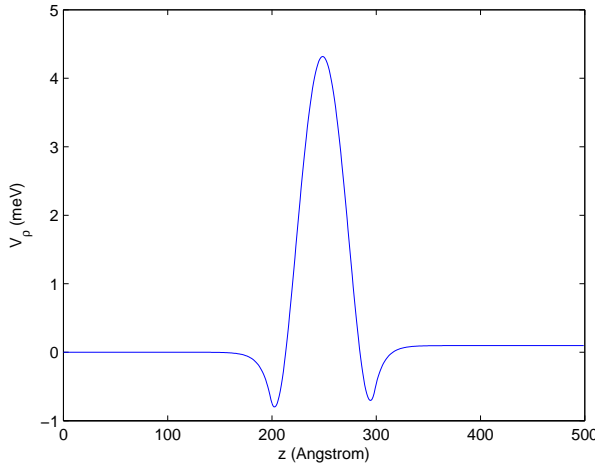


Figure 2.13: The potential due to the ionized donor/electron charge distribution shown in Fig. 2.11.

does reach zero at either end of the structure, which implies charge neutrality. In addition, the zero field point at the center of the structure reflects the symmetry of the charge distribution. The electric field strength itself is not an observable, merely an intermediate quantity which can be useful to plot from time to time; the quantity which is significant is the potential due to this charge distribution. Fig. 2.13 plots the potential as calculated from equation (2.3.3), defining the origin, in this case for the potential, at the effective infinity at the left-hand edge of the barrier-well-barrier structure. Again, the symmetry of the original heterostructure and doping profiles are reflected in the symmetric potential. The potential is positive at the center of the well since the system under consideration consists of electrons in the conduction band, so any test charge used to probe the potential is also an electron which would be repelled by the existing charge. The carrier density in this single quantum well is reasonably high at $2 \times 10^{12} \text{ cm}^{-2}$, and this produces a potential of up to 4 meV. While this is small compared to the conduction band offset, which is usually of the order of one or two hundred meV or more, it could still have a measurable effect on the energy eigenvalues of the quantum well.

The energy eigenvalues are calculated by considering the introduction of a further test electron into the system and incorporating the potential due to the carrier density already present into the standard Schrödinger equation, i.e. the potential term $V(z)$ in equations (2.2.55) becomes

$$V(z) \rightarrow V(z) + V_\rho(z), \quad (2.3.11)$$

where V represents the band edge potential at zero doping and the potential due to the non-zero number of carriers, the charge density ρ , represented by the function V_ρ . The numerical shooting method, described in detail in appendix B, can be used without alteration to solve for this new potential, which will thus yield new energies and wave functions. The latter is an important point since the potential due to the charge distribution is itself dependent on the wave functions. Therefore, it is necessary to form a closed loop solving Schrodinger's equation, calculating the potential due to the resulting charge distribution, adding it to the original bandedge potential, solving Schrödinger's equation again, and so on - a process illustrated schematically in Fig. 2.14. The process is repeated until the energy eigenvalues converge; at this point the wave functions are simultaneously solutions to both Schrodinger's and Poisson's equations—the solutions are described as *self-consistent*. The numerical implementation details of the self-consistent Schrödinger-Poisson model is presented in Appendix C.

Figure 2.15 shows the result of adding the potential due to the charge distribution V_ρ , as displayed in Fig. 2.13, to the original band-edge potential for the single quantum well. The perturbation, even at this relatively high carrier density of $2 \times 10^{12} \text{ cm}^{-2}$, is rather small compared to the barrier height, for instance. Nonetheless it is important to calculate the effect of this perturbation on the electron energy levels by continuing with the iterative process and looking for convergence of the resulting energy solutions.

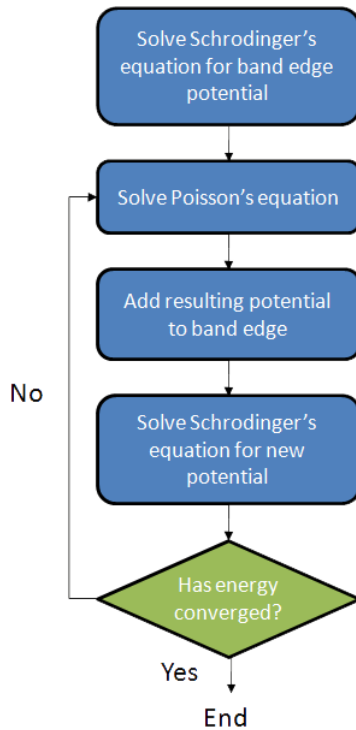


Figure 2.14: Block diagram illustrating the process of self-consistent iteration.

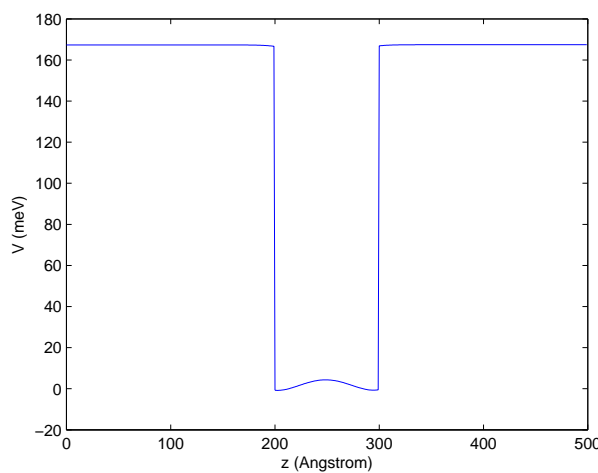


Figure 2.15: The sum of the band-edge potential V_{CB} and Poisson's potential V_ρ for single quantum well for the charge distribution shown in Fig. 2.11.

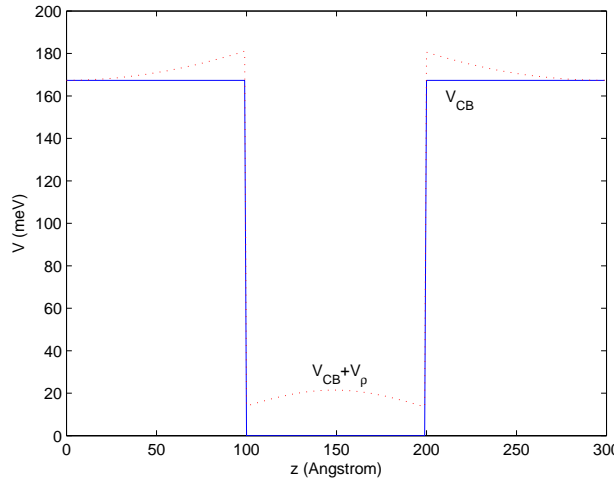


Figure 2.16: The band-edge potential (solid blue) and the self-consistent potential (dotted red) of a modulation-doped single quantum well.

2.3.2 Two-Dimensional Electron Gas

Although mention has been made of quantum well systems in which doping in the barriers leads to a spatial separations of the ions and charge carriers, which collect in a quantum well, quantitative calculations presented thus far have not considered these modulation-doped systems. Fig. 2.16 shows the band-edge potential, V_{CB} , and the self-consistent potential, $V_{CB} + V_p$, for a system with an undoped single quantum well surrounded by doped barriers with the full layer definition being: 100 Å $Ga_{0.8}Al_{0.2}As$ doped n -type to $2 \times 10^{17} cm^{-3}$; 100 Å $GaAs$ undoped; 100 Å $Ga_{0.8}Al_{0.2}As$ doped n -type to $2 \times 10^{17} cm^{-3}$. As the Fermi level in the doped $AlGaAs$ layer shifts from the middle of bandgap towards the donor levels, the electrons flow from the $AlGaAs$ layer to $GaAs$ in order to maintain a constant chemical potential throughout the two materials (see Fig. 2.17). The electrons introduced into the system are physically separated from the ionized donors, so therefore instead of an ion/charge carrier plasma, the mobile charge in this case is often referred to as a *two-dimensional electron gas* (2DEG). The physical separation leads to a reduction in the ionized impurity scattering and hence increased electron mobilities for in-plane ($x - y$) transport.

A similar method for introducing carrier plasma 2DEG at the material interface is to introduce dopings with high peak concentrations and narrow concentration width, which are effectively one-dimensional (1D) [26]. This can be achieved by confining the doping atoms to a single atomic layer of the host semiconductor (see Fig. 2.18). This doping is termed the δ -doping and its concentration profile can be written to be

$$N(z) = N_{2D}\delta(z - z_d), \quad (2.3.12)$$

where the 2D density, N_{2D} , us the number of doping atoms in the doping plane and z is the location of the dopant layer. Similarly to the modulation doped quantum well case considered earlier, we can introduce two symmetrical δ -doping layers into the two $AlGaAs$ barrier layers and compute the influence of this doping on the potential profile. We consider a 200 Å $GaAs$ quantum well with wide $AlGaAs$ barriers. The δ -doping layers are introduced symmetrically in the barriers at a distance of 1000 Å from the well-barrier interfaces. The charge distribution profile obtained from the self-consistent calculation is presented in Fig. 2.19. The doping level narrow contributions are clearly observable. The total electron-gas concentration inside the well area is computed to be $9 \times 10^{10} cm^{-2}$. The appropriate band-edge potential profiles for the conduction and valence bands are presented in Fig. 2.20. The substantial band-bending introduced by the doping levels is clearly seen at the well-barrier interfaces, and the 2DEG accumulation at these areas is evident from the location of the Fermi level energy, indicated by the dotted horizontal line in Fig. 2.20).

An alternative method for creating the 2DEG is photoexcitation by utilizing a mixed type I - type II quantum well (MTQW) structure, which consists of a wide QW cladded on both sides by narrow wells. In this structure, illustrated in Fig. 2.21, under laser photoexcitation with energy below the narrow QW bandgap, one generates

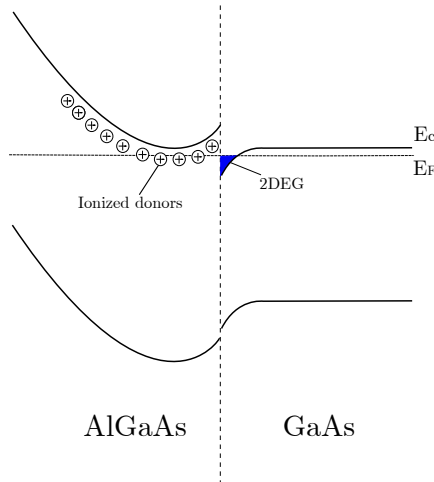


Figure 2.17: The structure and band diagram of a modulation-doped heterojunction between $GaAs$ and $n - AlGaAs$. E_c and E_F represent, respectively, the conduction band edge and the Fermi level energy.

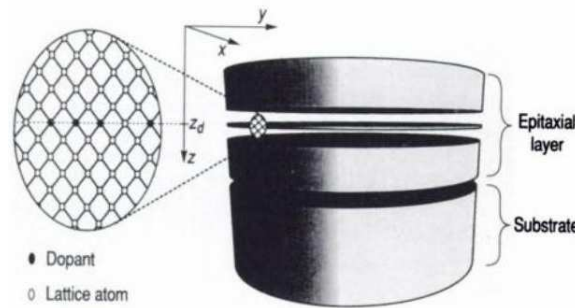


Figure 2.18: Schematic illustration of a semiconductor substrate and an epitaxial film containing a δ -doping layer. Also shown is a schematic lattice with the impurity atoms being confined to a single atomic plane (after [26]).

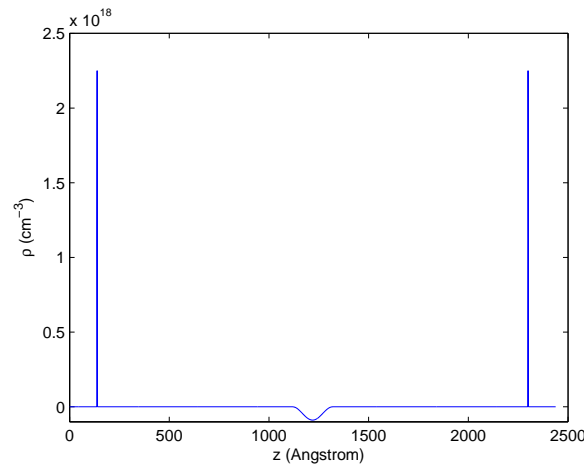


Figure 2.19: Volume charge density ρ for a 200 \AA $GaAs$ well, surrounded by $Ga_{0.9}Al_{0.1}As$ barriers, doped with two symmetrical δ -doping layers located 1000 \AA from the well. The achieved 2DEG inside the well is $9 \times 10^{10} \text{ cm}^{-2}$.

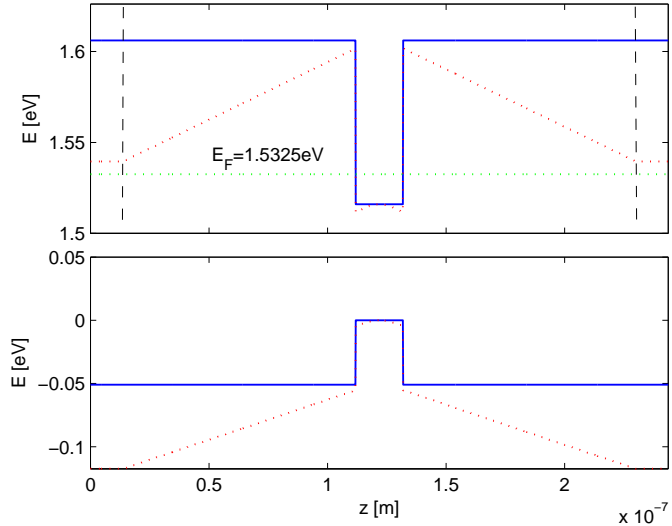


Figure 2.20: The band-edge potential (solid blue) and the self-consistent potential (dotted red) of a δ -doped single quantum well described in Fig. 2.19. The locations of the δ -doping layers are indicated by the vertical dashed lines.

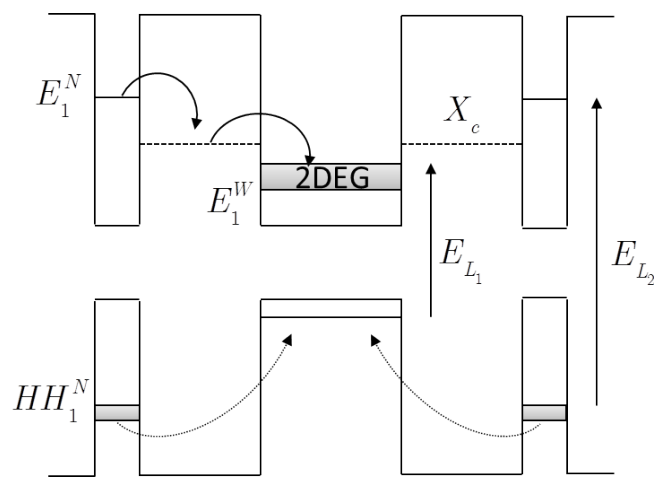


Figure 2.21: A schematic diagram of a GaAs/AlAs mixed type I - type II QWs structure. Photoexcitation with E_{L_1} creates electron-hole pairs in the wide QW, while photoexcitation with E_{L_2} creates a 2DEG in the wide QW and a 2DHG in the narrow QWs.

electron-hole pairs only in the wide QW. Photoexcitation with energy above the bandgap of the narrow well creates electron-hole pairs in both narrow and wide wells. Because of the large confinement energy in the narrow well its conduction band Γ minimum lies above the X-valley of the barrier, thus electrons created in the narrow well can relax rapidly into the wide well. In contrast, the holes have to tunnel through a $\approx 0.5\text{ eV}$ barrier and transfer very slowly. As a result, a spatial separation between electrons and holes is achieved and a stable 2DEG is formed in the wide QW while a two-dimensional hole gas (2DHG) remains in the narrow well. The photoexcitation created electron-hole bound pairs (excitons) in the wide QW have very short lifetimes ($\approx ns$) and thus their density is much smaller than the 2DEG concentration n_e . Selective excitation of the wide well can be used to create additional excitons in the wide wells. The 2DEG density n_e obtained in this structure is controlled starting at very low values, by changing the photoexcitation intensity. In contrast to the modulation doping, the 2DHG in the narrow wells is free, thus the electrons in the wide well are not subjected to random static Coulomb fields and remain free even at low densities.

Introducing electrons into a QW results in profound changes in the optical spectrum. As lower electron densities the effects of the electrons on the spectrum are related to their scattering with bound electron-hole pair (excitons) formed in the structure, and free-carrier screening [27]. At higher densities many-body effects such as bandgap renormalization and phase-space filling become important. The former effect appears as a decrease in the bandgap energy with increasing electron concentration (n_e) [28] while the latter results in a reduction of the exciton oscillator strength and binding energy [29]. We further discuss these effects in chapter 4.

We formulate the statistical distribution of 2DEG electrons. The free electrons occupy the energy levels in the quantum well according to the Fermi-Dirac distribution

$$f(E) = \frac{1}{1 + e^{\frac{E - E_F}{k_B T}}}, \quad (2.3.13)$$

where E_F is the chemical potential of the electrons, k_B is the Boltzman constant and T the temperature. In order to calculate the Fermi energy, the 2D density of states should be multiplied by this statistical distribution and integrated over all possible states. We concentrate on the low temperature regime ($T \rightarrow 0$), and assuming that all available states are occupied in the first conduction subband, the Fermi energy of the system equals the electron chemical potential

$$E_F = E_{E_1}(0) + \frac{\pi \hbar^2}{m_e^*} n_e, \quad (2.3.14)$$

where $E_{E_1}(0)$ denotes the bottom of the first conduction subband, k_B is the Boltzman constant and T the temperature. The wavevector of the top most occupied state thus becomes (assuming a parabolic dispersion)

$$k_F = \sqrt{\frac{2m_e^*}{\hbar^2} E_F} = \sqrt{2\pi n_e}. \quad (2.3.15)$$

To complete the discussion, we calculate using the Schrödinger-Poisson model the electronic properties of a 200 nm wide $GaAs/Al_{0.1}Ga_{0.9}As$ quantum well with δ -doped cladding layers presented in figures 2.19 and 2.20. In Fig. 2.22 we plot the dispersion relations obtained for the first conduction and first four valence subbands of this structure for various 2DEG concentrations. It is obvious from these curves that the change in the gas concentration influences the location of the subbands energies but not the functional dependence. With the rise of the concentration the subbands shift to lower energies due to the induced bending of the band-edge potential profiles, as seen in Fig. 2.20. Figures 2.23 and 2.24 present, respectively, the calculated wavefunctions for 2DEG concentrations of $1 \times 10^{10} \text{ cm}^{-2}$ and $1 \times 10^{11} \text{ cm}^{-2}$. The band-edge profile change can be clearly seen, but no noticeable change in the functional form of the function themselves can be seen compared to the undoped structure presented in Fig. 2.9.

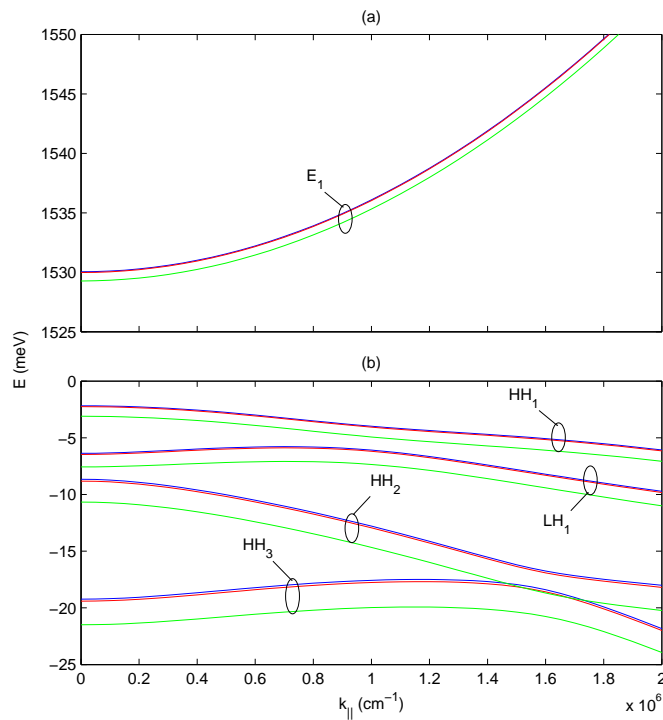


Figure 2.22: The calculated dispersion relations for the (a) conduction and (b) valence subbands, for a 200 Å wide GaAs/Al_{0.1}Ga_{0.9}As quantum well at T = 2 K, with 2DEG concentrations of 1 \times 10⁶ cm⁻² (blue), 1 \times 10¹⁰ cm⁻² (red) and 1 \times 10¹¹ cm⁻² (green).

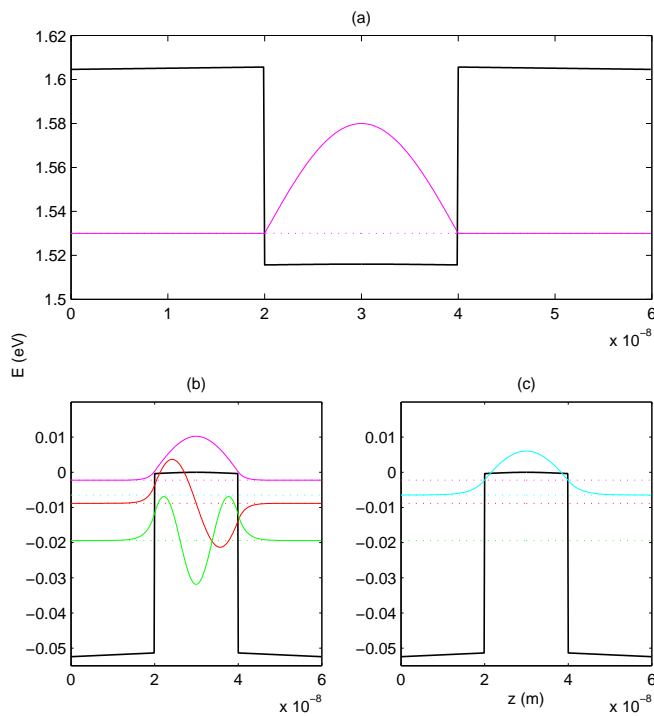


Figure 2.23: The calculated wavefunction for the (a) conduction, (b) valence heavy and (c) light hole subbands for 200 Å wide GaAs/Al_{0.1}Ga_{0.9}As quantum well at T = 2 K with $1 \times 10^{10} \text{ cm}^{-2}$ 2DEG concentration.

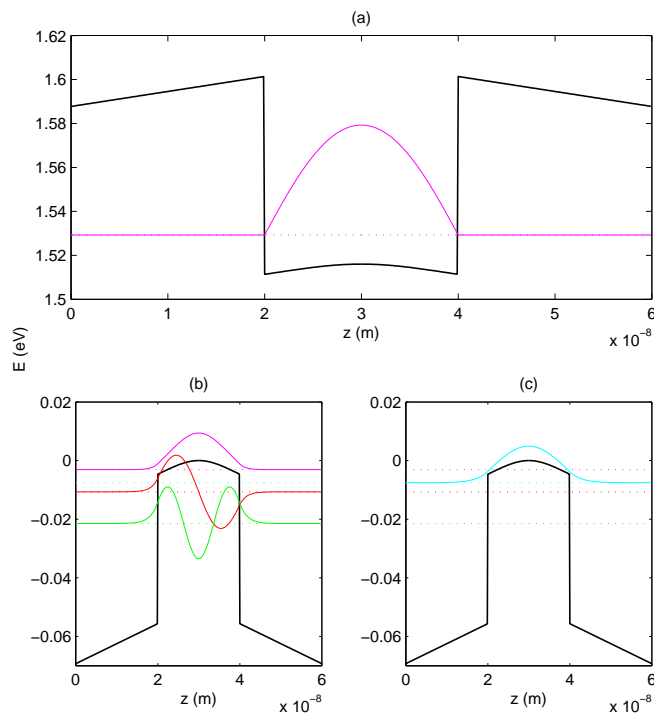


Figure 2.24: The calculated wavefunction for the (a) conduction, (b) valence heavy and (c) light hole subbands for 200 Å wide $\text{GaAs}/\text{Al}_{0.1}\text{Ga}_{0.9}\text{As}$ quantum well at $T = 2 \text{ K}$ with $1 \times 10^{11} \text{ cm}^{-2}$ 2DEG concentration.

Chapter 3

Free Carriers Optical Transitions

Absorption and emission of photons in semiconductors and semiconductor nanostructures is the result of the complex interaction between light and condensed matter, i.e. photons, electrons, and ions. In order to capture the physics behind these processes, electromagnetism and quantum mechanics have to be combined, leading to a multitude of physical phenomena. This thesis focuses on the static properties of nanostructures, such as the constant emission or absorption of light. Therefore, the theory will be treated within the time-independent limit. The theory here is formulated within the classical limit of optical transitions, where the quantum-mechanically treated carriers couple to a classical electromagnetic field. The resulting equations are famous and denoted as *semiconductor-Bloch equations* [30]. These equations have been used successfully over decades to describe optical properties within semiconductors. A fully consistent treatment of the light-emission would in principle require to work in a fully quantized picture (see [31]), leading to the *semiconductor-luminescence equations*. Such a treatment is beyond the scope of this thesis. The derivation presented here serves to illustrate the imposed approximations and to clearly document the implemented equations for nanostructures considered in this thesis using the electronic structure obtained using the methods outlined in chapter 2. This theory review is based mainly on [4, 1, 32, 30, 33].

The chapter is organized as follows. We start by introducing the transformation of the crystal Hamiltonian (2.1.8) into the second quantization. Then, the representation is rewritten in terms of the Bloch states, with a particular focus on the details arising when electronic states obtained using the $\mathbf{k} \cdot \mathbf{p}$ envelope function method are used. In the present chapter, the Coulomb interaction will be excluded and thereby, only transitions between free carriers will be considered. Coulomb-correlated transitions will be treated in Chapter 4. Then, we introduce the classical (monochromatic) light field and the self-consistent coupling to the electrons within the semiconductor nanostructure. The resulting equations allow the calculation the optical susceptibility and therefrom of the absorption, stimulated emission and refractive index change. In two final sections, we briefly explains how spontaneous emission can be obtained from optical susceptibility and cover the procedure to calculate required matrix elements from wavefunctions obtained using the $\mathbf{k} \cdot \mathbf{p}$ envelope equations.

3.1 Second Quantization

3.1.1 Introduction

The electrons are fermions and consequently their wavefunction must be antisymmetric to obey the Pauli exclusion principle. But instead of using a complicated expression for the antisymmetric wavefunction, restricted to a constant number of particles, the Hamiltonian can be formulated in the second quantization that allows to include a varying number of particles and maintain the antisymmetry of the wavefunction naturally. Starting with the Hamiltonian

(2.1.8) and separating the interaction with the external electromagnetic field leads to

$$\begin{aligned} H = & \underbrace{\sum_i \left(\frac{\mathbf{p}_i^2}{2m_0} + U(\mathbf{r}_i) \right)}_{H_1} + \underbrace{\sum_i \left(\frac{e}{m_0} \mathbf{A}_i \cdot \mathbf{p}_i + \frac{e^2}{2m_0} \mathbf{A}_i^2 \right)}_{H_{e-EM}} \\ & + \underbrace{\frac{1}{2} \sum_{i,j} \frac{e^2}{4\pi\epsilon_0 |\mathbf{r}_i - \mathbf{r}_j|}}_{H_2}. \end{aligned} \quad (3.1.1)$$

Here the pure electro-magnetic Hamiltonian H_{EM} has been dropped as it constitutes within the present theory only an additional energy. Let φ_n be the eigenstates of the single particle Hamiltonian H_1

$$H_1 \varphi_n = E \varphi_n \quad (3.1.2)$$

with resulting energies and wavefunctions. Next, the vacuum ground state $|0\rangle$ and creation and annihilation operators \hat{a}_n^\dagger and \hat{a}_n are introduced. These operators create and destroy a particle with φ_n and therefore act on the state

$$\hat{a}_n^\dagger |0\rangle = |1_n\rangle, \hat{a}_n |1_n\rangle = |0\rangle, \hat{a}_n |0\rangle = 0, \hat{a}_n^\dagger |1_n\rangle = 0. \quad (3.1.3)$$

The state span an Hilbert space of varying number of particles termed as the *Fock space*. The Fock space \mathcal{F} can be defined in terms of the direct sum of N -particle Hilbert spaces \mathcal{H}_N

$$\mathcal{F} = \mathcal{H}_0 + \mathcal{H}_1 + \mathcal{H}_2 + \dots$$

The antisymmetry of the state is preserved by the fermion commutation rule

$$[\hat{a}_n^\dagger, \hat{a}_{n'}]_+ = \hat{a}_n^\dagger \hat{a}_{n'} + \hat{a}_{n'} \hat{a}_n^\dagger = \delta_{nn'} \quad (3.1.4)$$

and

$$[\hat{a}_n, \hat{a}_{n'}]_+ = [\hat{a}_n^\dagger, \hat{a}_{n'}^\dagger]_+ = 0. \quad (3.1.5)$$

A valuable tool to transfer the Hamiltonian (3.1.1) (or any other operator) into second quantization representation is given by the electron field operator

$$\hat{\Phi}(\mathbf{r}, t) = \sum_n \varphi_n(\mathbf{r}) \hat{a}_n(t). \quad (3.1.6)$$

Here, we switch from the Schrödinger to the Heisenberg picture. For an operator A in the Schrödinger picture, the corresponding operator in the Heisenberg picture is given by

$$A_H = e^{iHt/\hbar} A e^{-iHt/\hbar}, \quad (3.1.7)$$

where H is the Hamilton operator. As the Heisenberg picture will be generally used, the time-dependence of the operators is dropped from now on.

3.1.1.1 Single Particle Hamiltonian

Using the field operator $\hat{\Phi}(\mathbf{r})$, the representation of the single-particle Hamiltonian H_1 in second quantization is given by

$$\begin{aligned} \hat{H}_1 &= \int d\mathbf{r} \hat{\Phi}^\dagger(\mathbf{r}) H_1 \hat{\Phi}(\mathbf{r}) \\ &= \sum_{j,k} \hat{a}_j^\dagger \hat{a}_k \int d\mathbf{r} \varphi_j^* H_1 \varphi_k \\ &= \sum_j \hat{a}_j^\dagger \hat{a}_j E_j, \end{aligned} \quad (3.1.8)$$

which is diagonal as φ_n is assumed to be an eigenfunction of H_1 . The representation in terms of second quantization could also be performed using another basis of the single-particle Hilbert space, but then (3.1.8) would not be diagonal in jk . Another detail is that here, the first quasi-particle, a particle occupying the eigenstates of the single particle Hamiltonian H_1 , has been introduced.

3.1.1.2 Two Particle Hamiltonian: Coulomb Interaction

The transformation of the two-particle interaction, the Coulomb term H_2 , is similar, but more complicated. The result of the expansion is

$$\hat{H}_2 = \frac{1}{2} \sum_{j,k,l,m} \langle jk | v | lm \rangle \hat{a}_j^\dagger \hat{a}_k^\dagger \hat{a}_l \hat{a}_m. \quad (3.1.9)$$

The matrix element $\langle jk | v | lm \rangle$ is given by

$$\langle jk | v | lm \rangle = \int d\mathbf{r} d\mathbf{r}' \varphi_j^*(\mathbf{r}) \varphi_k^*(\mathbf{r}') \frac{e^2}{4\pi\epsilon_0 |\mathbf{r} - \mathbf{r}'|} \varphi_m(\mathbf{r}) \varphi_l(\mathbf{r}'). \quad (3.1.10)$$

Note that the m and the l are swapped in the integral compared to the annihilation and creation operators and that in $\langle jk | v | lm \rangle$, the spin variable must be included, so

$$\langle jk | v | lm \rangle \rightarrow \delta_{s_j s_m} \delta_{s_k s_l} \langle jk | v | lm \rangle.$$

3.1.1.3 Particle – Electromagnetic Field Interaction Hamiltonian

The next Hamiltonian to quantize is the electron-EM field interaction Hamiltonian H_{e-EM} defined in (3.1.1). It is clear that H_{e-EM} is a one-particle Hamiltonian and therefore its representation in the second quantization is obtained by applying the field operators as in (3.1.8), with the difference that φ_n is diagonal in H_1 but not in H_{e-EM} . The resulting expression reads

$$\hat{H}_{e-EM} = \sum_{j,k} \left(\frac{e}{m_0} \langle j | \mathbf{A} \cdot \mathbf{p} | k \rangle + \frac{e^2}{2m_0} \langle j | \mathbf{A}^2 | k \rangle \right) \hat{a}_j^\dagger \hat{a}_k. \quad (3.1.11)$$

To simplify the Hamiltonian and in order to get rid of the vector potential \mathbf{A} in favor of the electric field $\mathbf{E} = -\frac{\partial}{\partial t} \mathbf{A}$ (Coulomb gauge assumed as before), the *dipole approximation* can be applied. As the crystal is a quasi-periodic structure, where the periodicity is much smaller than the photon wavelength of usual electromagnetic fields, the electric field can be assumed to be constant within the range of a lattice cell. This approximation removes the spatial dependence of \mathbf{A} and reduces the second term $\langle j | \mathbf{A}^2 | k \rangle$ to a contribution diagonal in j, k , and is therefore proportional to the number of electrons and does not contribute to any interband transitions. Therefore, it can be treated as an additional energy constant and thus be neglected. The remaining term, $\frac{e}{m_0} \langle j | \mathbf{A} \cdot \mathbf{p} | k \rangle$ is more difficult to simplify and thus a simplified argument is brought here, while the full justification can be found in [33]. The first step is to relate the momentum matrix element \mathbf{p} and the dipole transition matrix element \mathbf{r} . The relation is given by

$$[\mathbf{r}, H_1] = \frac{i\hbar}{m_0} \mathbf{p}, \quad (3.1.12)$$

where H_1 is the single particle Hamiltonian. Thus, the second term in (3.1.11) can be transformed into

$$\begin{aligned} \frac{e}{m_0} \langle j | \mathbf{A} \cdot \mathbf{p} | k \rangle &= \mathbf{A} \cdot \frac{e}{i\hbar} \langle j | [\mathbf{r}, H_1(\mathbf{r})] | k \rangle \\ &= \mathbf{A} \cdot \frac{e}{i\hbar} \langle j | \mathbf{r} H_1(\mathbf{r}) - H_1(\mathbf{r}) \mathbf{r} | k \rangle \\ &= \mathbf{A} \cdot \frac{e}{i\hbar} \langle j | \mathbf{r} | k \rangle (E_k - E_j) \\ &= -\frac{i}{\hbar} (E_k - E_j) \mathbf{A} \cdot \langle j | \mathbf{d} | k \rangle, \end{aligned} \quad (3.1.13)$$

where $\mathbf{d} = -e\mathbf{r}$ is the dipole moment. The last step involved adding the term $\mathbf{d}_{j,k} \cdot \mathbf{E} - \mathbf{d}_{j,k} \cdot \mathbf{E}$, which with the definition of \mathbf{E} gives

$$\frac{e}{m_0} \langle j | \mathbf{A} \cdot \mathbf{p} | k \rangle = -\mathbf{d}_{j,k} \cdot \mathbf{E} - \left(\frac{\hbar}{i} \frac{\partial}{\partial t} + E_j - E_k \right) \mathbf{A} \cdot \mathbf{d}_{j,k}. \quad (3.1.14)$$

If \mathbf{A} is given by a plane wave $\mathbf{A}_0 e^{i(\omega_0 t - k_0 r)}$ with center frequency ω_0 and the transition energies $E_k - E_j$ are ranged around $\hbar\omega_0$, the expression in the brackets vanished and the dipole approximation for the Hamiltonian is obtained,

$$\hat{H}_{e-EM} = - \sum_{j,k} \langle j | \mathbf{d} \cdot \mathbf{E} | k \rangle \hat{a}_j^\dagger \hat{a}_k. \quad (3.1.15)$$

The final Hamiltonian for the crystal electrons (3.1.1), can therefore be written as

$$\hat{H} = \sum_{j,k} \langle j \mid H_1 \mid k \rangle \hat{a}_j^\dagger \hat{a}_k + \frac{1}{2} \sum_{j,k,l,m} \langle jk \mid v \mid lm \rangle \hat{a}_j^\dagger \hat{a}_k^\dagger \hat{a}_l \hat{a}_m - \sum_{j,k} \langle j \mid \mathbf{d} \cdot \mathbf{E} \mid k \rangle \hat{a}_j^\dagger \hat{a}_k. \quad (3.1.16)$$

3.1.2 Bloch States Formulation

Up to now, we have ignored the specific form of the wavefunction φ_n . Here we consider the wavefunction to be a Bloch function, as presented in Chapter 2. Within a bulk crystal, the Bloch function is given by

$$\varphi_{n\mathbf{k}}(\mathbf{r}) = u_{n\mathbf{k}}(\mathbf{r}) e^{i\mathbf{k}\cdot\mathbf{r}}, \quad (3.1.17)$$

where $u_{n\mathbf{k}}(\mathbf{r})$ is lattice periodic and the exponential term is slowly varying. The current section aims now to transform (3.1.16) into Bloch states, which needs some clarifications and definitions.

The Bloch-functions are required to be orthonormalized over the crystal domain Ω

$$\int_{\Omega} d\mathbf{r} \varphi_{n'\mathbf{k}'}^* \varphi_{n\mathbf{k}} = \delta_{n',n} \delta_{\mathbf{k}',\mathbf{k}}. \quad (3.1.18)$$

The goal now is to represent the Hamiltonian (3.1.16) using the field operator

$$\hat{\Phi}(\mathbf{r}, t) = \sum_{n,\mathbf{k}} \varphi_{n\mathbf{k}} \hat{a}_{n\mathbf{k}}(t) \quad (3.1.19)$$

in terms of the Bloch-functions. As the Bloch-states are not localized, the Fourier transform of certain quantities (such as the electromagnetic field or the Coulomb interaction) in the translational invariant directions will be used to simplify the Hamiltonian. For the spatial Fourier transform, the conventions are given by

$$w(\mathbf{r}) = \sum_{\mathbf{q}} w(\mathbf{q}) e^{i\mathbf{q}\cdot\mathbf{r}}, \quad (3.1.20)$$

$$w(\mathbf{q}) = \frac{1}{A} \int_A d\mathbf{r} w(\mathbf{r}) e^{-i\mathbf{q}\cdot\mathbf{r}}. \quad (3.1.21)$$

3.1.2.1 Normalization

In the case of a quantum nanostructure, the Bloch function loses its plane wave dependence in the quantized direction and is therefore expressed as

$$\varphi_{n\mathbf{k}}(\mathbf{r}, z) = |n\mathbf{k}\rangle = u_{n\mathbf{k}}(\mathbf{r}, z) e^{i\mathbf{k}\cdot\mathbf{r}} F_{n\mathbf{k}}(z). \quad (3.1.22)$$

The free direction is represented by the plane-wave and the symmetry broken part by $F(z)$. The indices n now include the subbands. In the following, the coordinate z will be used for the symmetry broken direction while \mathbf{r} will denote the translational invariant direction.

Regarding the normalization, it is assumed that A is the volume of the translational invariant direction and L is the volume of the quantized direction. Obviously, $\Omega = L A$. (3.1.18) is still required to hold, but the normalization over the translational invariant direction is distributed into the lattice periodic part $u_{n\mathbf{k}}(\mathbf{r}, z)$. The envelope function $F(z)$ is then normalized over the quantized direction. Therefore, for a system quantized in d dimensions, the units of the wavefunction parts are given by

$$\underbrace{\varphi_{n\mathbf{k}}(\mathbf{r}, z)}_{\frac{1}{\sqrt{m^3}} = \frac{1}{\sqrt{\Omega}}} = \underbrace{u_{n\mathbf{k}}(\mathbf{r}, z)}_{\frac{1}{\sqrt{m^{3-d}}} = \frac{1}{\sqrt{A}}} e^{i\mathbf{k}\cdot\mathbf{r}} \underbrace{F_{n\mathbf{k}}(z)}_{\frac{1}{\sqrt{m^d}} = \frac{1}{\sqrt{L}}}. \quad (3.1.23)$$

3.1.2.2 Lattice-Cell Average

A general problem of the approach using wavefunctions of the $\mathbf{k} \cdot \mathbf{p}$ envelope equation is that the lattice-periodic functions $u_{n\mathbf{k}}(\mathbf{r}, z)$ are not given in an explicit form. Only their symmetry properties, the fact that they are orthogonal to each other and some measurable quantities are available. Nevertheless, these properties are sufficient for building the Hamiltonian and calculating desired matrix elements, within the approximation that lattice-cell averaged quantities are used. In the $\mathbf{k} \cdot \mathbf{p}$ method, the envelopes and plane waves are assumed to vary little over a crystal cell. If an operator A mainly acts on the lattice-periodic part, a matrix element between two wavefunctions (3.1.22) can be simplified as

$$\langle n'\mathbf{k}' | A | n\mathbf{k} \rangle \approx \frac{\mathcal{A}}{V_c} \langle u_{n'\mathbf{k}'} | A | u_{n\mathbf{k}} \rangle_{V_c} \delta_{k', k} \int dz F_{n'\mathbf{k}'}^*(z) F_{n\mathbf{k}}(z). \quad (3.1.24)$$

Here the operator A is replaced with its lattice averaged quantity

$$V_c^{-1} \langle u_{n'\mathbf{k}'} | A | u_{n\mathbf{k}} \rangle_{V_c}.$$

V_c denotes the crystal cell and $\langle \rangle_{V_c}$ the integration over it. The matrix elements found in the literature are related by

$$\frac{\mathcal{A}}{V_c} \langle u_{n'\mathbf{k}'} | A | u_{n\mathbf{k}} \rangle_{V_c} = \langle \tilde{u}_{n'\mathbf{k}'} | A | \tilde{u}_{n\mathbf{k}} \rangle \quad (3.1.25)$$

where \tilde{u}_i is the Bloch function normalized with respect to a single crystal cell. Therefore to determine values for the short-range operator $\langle n'\mathbf{k}' | A | n\mathbf{k} \rangle$, only the envelope function $F_{n\mathbf{k}}(z)$ and the experimental value for $\langle \tilde{u}_{n'\mathbf{k}'} | A | \tilde{u}_{n\mathbf{k}} \rangle$ for the from bulk measurements are required.

The other case is given by the long-range operator B , such as the Coulomb potential. In that case, the operator is constant over a lattice cell and the integral of the matrix element can be reduced using the orthogonality of the Bloch functions. The lattice-cell average reads

$$\begin{aligned} \langle n'\mathbf{k}' | B | n\mathbf{k} \rangle &= \int_{\Omega} d\mathbf{r} dz u_{n'\mathbf{k}'}^*(\mathbf{r}, z) e^{-i\mathbf{k}' \cdot \mathbf{r}} F_{n'\mathbf{k}'}^*(z) B u_{n\mathbf{k}}(\mathbf{r}, z) e^{i\mathbf{k} \cdot \mathbf{r}} F_{n\mathbf{k}}(z) \\ &\approx \int_{\Omega} d\mathbf{r} dz \frac{1}{V_c} \langle u_{n'\mathbf{k}'} | u_{n\mathbf{k}} \rangle_{V_c} e^{-i\mathbf{k}' \cdot \mathbf{r}} F_{n'\mathbf{k}'}^* B u_{n\mathbf{k}}(\mathbf{r}, z) e^{i\mathbf{k} \cdot \mathbf{r}} F_{n\mathbf{k}}(z). \end{aligned} \quad (3.1.26)$$

A further simplification depends on the actual form of the considered operator. We return to this relation further in section 3.4.

3.1.2.3 The Kinetic Term

To transform the kinetic part into the Bloch states, the eigenfunctions $\varphi_{n\mathbf{k}}(\mathbf{r}, z)$ of the single particle Hamiltonian are inserted into the field operator. Using that particular field operator, the kinetic term (3.1.16) is given by

$$\hat{H}_1 = \sum_{n, \mathbf{k}} \hat{a}_{n\mathbf{k}}^\dagger \hat{a}_{n\mathbf{k}} E_{n, \mathbf{k}}. \quad (3.1.27)$$

3.1.2.4 The Interaction Term

The remaining step is to quantize the electron - electromagnetic field interaction Hamiltonian H_{e-EM} within the dipole approximation. The Fourier representation of the electric field $\mathbf{E}(\mathbf{r}, t)$ is given by

$$\mathbf{E}(\mathbf{r}, t) = \sum_{\mathbf{q}} \mathbf{E}(\mathbf{q}, t) e^{i\mathbf{q} \cdot \mathbf{r}}. \quad (3.1.28)$$

As it is assumed that $\mathbf{E}(\mathbf{r}, t)$ is slowly-varying, the relevant contributions to the sum will be around very small values of \mathbf{q} . This allows to pull the $e^{i\mathbf{q} \cdot \mathbf{r}}$ factor out of the dipole integral in the calculation below. The resulting

Hamiltonian then reads

$$\begin{aligned} & \int_{\Omega} d\mathbf{r} dz \hat{\Phi}^\dagger H_{e-EM} \hat{\Phi} \\ = & - \sum_{n', \mathbf{k}', n, \mathbf{k}} \hat{a}_{n' \mathbf{k}'}^\dagger \hat{a}_{n \mathbf{k}} \int_{\Omega} d\mathbf{r} dz \varphi_{n' \mathbf{k}'}^* \mathbf{d} \cdot \left(\sum_{\mathbf{q}} \mathbf{E}(\mathbf{q}, t) e^{i \mathbf{q} \cdot \mathbf{r}} \right) \varphi_{n \mathbf{k}} \\ = & - \sum_{n', \mathbf{k}', n, \mathbf{k}} \sum_{\mathbf{q}} \delta_{\mathbf{k}' \mathbf{k}} \boldsymbol{\mu}_{n' n, \mathbf{k}} \cdot \mathbf{E}(\mathbf{r}, t) e^{i \mathbf{q} \cdot \mathbf{r}}, \end{aligned}$$

where the dipole matrix element between two states n and n' with same crystal momentum \mathbf{k} is given by

$$\boldsymbol{\mu}_{n' n, \mathbf{k}} = \mathcal{A} \int_{\mathcal{L}} dz u_{n' \mathbf{k}}^* F_{n' \mathbf{k}}^* \mathbf{d} u_{n \mathbf{k}} F_{n \mathbf{k}}. \quad (3.1.29)$$

The delta function $\delta_{\mathbf{k}' \mathbf{k}}$ results from the plane wave and ensures momentum conservation. In other words, only direct transitions are allowed. Using the dipole matrix element, the Hamiltonian can finally be written as

$$\hat{H}_{e-EM} = -\mathbf{E}(\mathbf{r}, t) \sum_{n', n, \mathbf{k}} \boldsymbol{\mu}_{n' n, \mathbf{k}} \hat{a}_{n' \mathbf{k}}^\dagger \hat{a}_{n \mathbf{k}}. \quad (3.1.30)$$

The transformation of the two particle Hamiltonian H_2 is presented in the next chapter. For the moment, it is assumed that the carriers are *uncorrelated* and their coulomb interaction is included in the single particle Hamiltonians. Collecting all single particle interactions, the Hamiltonian in the Bloch basis is given as

$$\hat{H} = \sum_n E_n(\mathbf{k}) \hat{a}_{n \mathbf{k}}^\dagger \hat{a}_{n \mathbf{k}} - \mathbf{E}(\mathbf{r}, t) \sum_{n', n, \mathbf{k}} \boldsymbol{\mu}_{n' n, \mathbf{k}} \hat{a}_{n' \mathbf{k}}^\dagger \hat{a}_{n \mathbf{k}}. \quad (3.1.31)$$

3.1.3 Introduction of Holes

In a semiconductor at $T = 0K$, the valence band is fully occupied while the conduction band is empty. With increasing temperature, electrons in the valence band get excited into the conduction band and leave behind holes. Consequently, it is common to use for the valence band the absence of an electron, the hole, as a quasi particle. Therefore, if an electron with momentum $-\mathbf{k}$ is created ($= \hat{a}_{-\mathbf{k}}^\dagger$), a hole with momentum \mathbf{k} is annihilated ($= \hat{b}_{\mathbf{k}}$) and vice versa. The sign is switched by convention. In order to introduce the concept of holes into the Hamiltonian, the commutator rules (3.1.4) and (3.1.5) are used to reestablish the normal ordering of creation and annihilation operators. One obtains for the kinetic and dipole Hamiltonian

$$\begin{aligned} \hat{H} = & \sum_{c, \mathbf{k}} E_c(\mathbf{k}) \hat{a}_{c \mathbf{k}}^\dagger \hat{a}_{c \mathbf{k}} - \sum_{v, \mathbf{k}} E_v(\mathbf{k}) \hat{b}_{v \mathbf{k}}^\dagger \hat{b}_{v \mathbf{k}} \\ & - \mathbf{E}(\mathbf{r}, t) \left(\underbrace{\sum_{c, v, \mathbf{k}} \boldsymbol{\mu}_{cv, \mathbf{k}} \hat{a}_{c \mathbf{k}}^\dagger \hat{b}_{v - \mathbf{k}}^\dagger}_{\hat{p}_{vc, \mathbf{k}}^\dagger} + \underbrace{\boldsymbol{\mu}_{cv, \mathbf{k}}^* \hat{b}_{v - \mathbf{k}} \hat{a}_{c \mathbf{k}}}_{\hat{p}_{vc, \mathbf{k}}} \right). \end{aligned} \quad (3.1.32)$$

Note that from now on, the summation is distinguished between summation over conduction bands indicated with c and valence bands indicated using the index v . In (3.1.32), transitions between conduction subbands and transitions between valence subbands have been neglected.

One important point is that in the Hamiltonian (3.1.32), some terms can already be identified: $\hat{n}_{c \mathbf{k}} = \hat{a}_{c \mathbf{k}}^\dagger \hat{a}_{c \mathbf{k}}$ is the number operator counting the number of electrons in the band c with crystal momentum \mathbf{k} , while $\hat{n}_{v \mathbf{k}} = \hat{b}_{v - \mathbf{k}}^\dagger \hat{b}_{v - \mathbf{k}}$ is the number operator counting the holes in the valence band v . The term $\hat{p}_{vc, \mathbf{k}} = \hat{b}_{v - \mathbf{k}} \hat{a}_{c \mathbf{k}}$ is named *microscopic polarization* and is given by the off-diagonal density matrix element, giving the correlation between a particle in one band and an empty state in the other. In a simplistic view, the dipole matrix element $\boldsymbol{\mu}_{cv, \mathbf{k}}$ gives the coupling strength of such a correlation to an electric field.

3.1.4 Carrier Statistics

The main interest of the current work is the continuous emission of light of a semiconductor, which is given in the steady state of the system. In the limit of small light intensity and therefore absence of spectral-hole burning, it can be assumed that the carriers relax into their quasi-equilibrium distributions, given by the Fermi distributions for the electrons in the conduction band

$$n_{c\mathbf{k}} = \langle \hat{n}_{c\mathbf{k}} \rangle = f_{c\mathbf{k}} = \frac{1}{1 + e^{(E_c(\mathbf{k}) - E_{F,c})/k_B T}} \quad (3.1.33)$$

and the holes in the valence band

$$n_{v\mathbf{k}} = \langle \hat{n}_{v\mathbf{k}} \rangle = f_{v\mathbf{k}} = \frac{1}{1 + e^{(E_{F,v} - E_v(\mathbf{k}))/k_B T}}. \quad (3.1.34)$$

Here, $E_{F,c}$ and $E_{F,v}$ denote the quasi-Fermi levels of the electrons and holes, k_B is Boltzmann's constant and T denotes the temperature. The Fermi levels can be calculated from the 3D carrier density N

$$N = \frac{1}{\Omega} \sum_{c\mathbf{k}} f_{c\mathbf{k}} \quad (3.1.35)$$

for electrons and P

$$P = \frac{1}{\Omega} \sum_{v\mathbf{k}} f_{v\mathbf{k}} \quad (3.1.36)$$

for holes. Here Ω denotes the volume of the system, which is usually unknown. When the sum over \mathbf{k} is transformed into an integral

$$\sum_{\mathbf{k}} \rightarrow \frac{2\mathcal{A}}{(2\pi)^d} \int d\mathbf{k} \quad (3.1.37)$$

the unknown Ω volume is removed and one ends up with known quantities ($\mathcal{L} = \Omega/\mathcal{A}$). d denotes the dimensionality of the \mathbf{k} -space. Note the factor 2 which stems from the implicit summation over the spin states. For an ideal 2D quantum well, the electrons are free to move only in the plane of the active layer, so that the summation over \mathbf{k} is restricted to two dimensions according to

$$\sum_{\mathbf{k}} \rightarrow \frac{2\mathcal{A}}{(2\pi)^2} \int dk 2\pi k, \quad (3.1.38)$$

where we assume that the function summed over is cylindrically symmetric (which is a reasonable assumption for the subband structure near the zone center $\mathbf{k} = 0$). As the \mathbf{k} dependence of the distributions for general band structures is quite evolved, an analytical inversion of (3.1.35) and (3.1.36) is not feasible. Therefore, the simplest way to calculate the quasi-Fermi levels is to perform a numerical Newton procedure to find the roots of $N_0 - N(E_F) = 0$.

3.2 Transitions Calculation

3.2.1 Introduction

Classically, an electric field \mathbf{E} in a semiconductor induces dipoles. These dipoles create a macroscopic polarization \mathbf{P} . The induced polarization $\mathbf{P}(t)$ at time t depends on the electric field $\mathbf{E}(t')$ at time $t' < t$. Their relation is defined in terms of a time-dependent susceptibility $\chi(t - t')$ (in this case a scalar)

$$\mathbf{P}(t) = \epsilon_b \int_{-\infty}^t \chi(t - t') \mathbf{E}(t') dt'. \quad (3.2.1)$$

Taking the Fourier transform of (3.2.1) leads to the more convenient form

$$\mathbf{P}(\omega) = \epsilon_b \chi(\omega) \mathbf{E}(\omega). \quad (3.2.2)$$

The polarization influences the electric field via the electric displacement

$$\mathbf{D} = \epsilon \mathbf{E} = \epsilon_b \mathbf{E} + \mathbf{P}. \quad (3.2.3)$$

Therefore, the creation of dipoles and the amplification of an electric field needs to be treated self-consistently. The aim is therefore to calculate the polarization quantum-mechanically in the presence of an electric field and obtain a self-consistent formula for the steady state.

As a first step, Maxwell's equations are rewritten to give a single relation between the electric field \mathbf{E} and the macroscopic polarization \mathbf{P} . Taking the curl of

$$\nabla \times \mathbf{H} - \frac{\partial \mathbf{D}}{\partial t} = \mathbf{j} \quad (3.2.4)$$

and using

$$\nabla \times \mathbf{E} = -\frac{\partial \mathbf{B}}{\partial t}, \quad (3.2.5)$$

ones obtains

$$\nabla \times \nabla \times \mathbf{E} = -\nabla \times \frac{\partial \mu_0 \mathbf{H}}{\partial t}, \quad (3.2.6)$$

$$\nabla (\nabla \cdot \mathbf{E}) - \nabla^2 \mathbf{E} = -\mu_0 \frac{\partial}{\partial t} (\nabla \times \mathbf{H}). \quad (3.2.7)$$

On the left hand side, the term $\nabla \cdot \mathbf{E} = 0$ vanishes, assuming charge neutrality and homogeneous media. On the right hand side, using (3.2.4), $\nabla \times \mathbf{H}$ is replaced by the electric displacement \mathbf{D}

$$\nabla (\nabla \cdot \mathbf{E}) - \nabla^2 \mathbf{E} \approx -\nabla^2 \mathbf{E} = -\mu_0 \frac{\partial^2 \mathbf{D}}{\partial t^2}, \quad (3.2.8)$$

which now allows to introduce the macroscopic polarization \mathbf{P} using (3.2.3)

$$-\nabla^2 \mathbf{E} + \mu_0 \epsilon_b \frac{\partial^2 \mathbf{E}}{\partial t^2} = -\mu_0 \frac{\partial^2 \mathbf{P}}{\partial t^2}. \quad (3.2.9)$$

This equation is the *inhomogeneous Helmholtz equation*. The next step is to assume a monochromatic electrical field \mathbf{E} (traveling into z -direction) given by

$$\mathbf{E}(z, t) = \frac{1}{2} \hat{e}_i E(z) e^{i(k_0 z - \nu t - \phi(z))} + \text{c.c}, \quad (3.2.10)$$

where $k_0 = \nu n/c$ is the photo wavenumber and \hat{e}_i is a unit vector orthogonal to \hat{e}_z . $\phi(z)$ us the real phase shift and $E(z)$ is the real field amplitude, varying little within an optical wavelength. ν denotes the field frequency. It is assumed that the spacial strong oscillatory part is properly described by the plane wave. The electric field induces a polarization

$$\mathbf{P}(z, t) = \frac{1}{2} \hat{e}_i P(z) e^{i(k_0 z - \nu t - \phi(z))} + \text{c.c.} \quad (3.2.11)$$

The next step is to insert (3.2.10) and (3.2.11) into (3.2.9) and neglect all terms containing $\partial_z^2 E(z)$, $\partial_z^2 \phi(z)$ and $\partial_z E(z) \partial_z \phi(z)$. This approach is denoted as the *slowly varying envelope approximation* and one ends up with an equation for the amplitudes $E(z)$ and $P(z)$,

$$\partial_z E(z) - i E(z) \partial_z \phi(z) = i \frac{\mu_0 \nu^2}{2 k_0} \chi(z) E(z). \quad (3.2.12)$$

Splitting into real and imaginary parts and using (3.2.2), the self consistent equations are obtained as

$$\partial_z E(z) = -\frac{\nu}{2 \epsilon_0 n c} \Im \{P(z)\} = -\frac{k_0}{2} \chi''(z) E(z), \quad (3.2.13)$$

$$\partial_z \phi(z) = -\frac{1}{E(z)} \frac{\nu}{2 \epsilon_0 n c} \Re \{P(z)\} = -\frac{k_0}{2} \chi'(z), \quad (3.2.14)$$

where $\chi = \chi' + i\chi''$ is the electrical susceptibility of the system. Consequently, the intensity gain (amplitude is half of it) is defined by

$$G = -k_0\chi'', \quad (3.2.15)$$

and the change of refractive index (via a continuous phase change) is given by the real part of the susceptibility

$$\frac{\delta n}{n} = \frac{\chi'}{2}. \quad (3.2.16)$$

The absorption can be obtained from the intensity gain through $\alpha = -G$.

3.2.2 Quantum Microscopic Polarization

The second step is to couple quantum mechanical observables to the solids properties. The dipole interaction between electrons and the electric field is given by

$$H_{e-EM} = -V\mathbf{P} \cdot \mathbf{E}, \quad (3.2.17)$$

where V is the volume of the system and \mathbf{P} is defined as the macroscopic polarization density

$$\mathbf{P} = \frac{1}{V} \sum_{n,n',\mathbf{k}} \boldsymbol{\mu}_{n'n,\mathbf{k}} \left\langle \hat{a}_{n'\mathbf{k}}^\dagger \hat{a}_{n\mathbf{k}} \right\rangle = \frac{1}{V} \sum_{c.v.\mathbf{k}} \boldsymbol{\mu}_{cv,\mathbf{k}} p_{vc,\mathbf{k}}^\dagger + \boldsymbol{\mu}_{cv,\mathbf{k}}^* p_{vc,\mathbf{k}} \quad (3.2.18)$$

from which the optical properties (3.2.15) and (3.2.16) can be obtained. Here, the expectation value $p_{vc,\mathbf{k}} = \langle \hat{p}_{vc,\mathbf{k}} \rangle$ has been used. The amplitude $P(z)$ of the macroscopic polarization $\mathbf{P}(z, t)$ used for the optical properties is given by

$$P(z) = 2e^{-i(k_0 z - \nu t - \phi(z))} \frac{1}{V} \sum_{c.v.\mathbf{k}} \boldsymbol{\mu}_{cv,\mathbf{k}}^* p_{vc,\mathbf{k}} \quad (3.2.19)$$

The other term of the polarization containing $p_{vc,\mathbf{k}}^\dagger$ is related to the complex conjugate part of (3.2.11) and is not required to determine the macroscopic amplitude $P(z)$.

3.2.3 Heisenberg's Equation of Motion

In order to calculate the expectation value $p_{nm,\mathbf{k}}$, the equation of motion of the microscopic polarization operator $\hat{p}_{nm,\mathbf{k}}$ has to be solved. Here the index m is used for the conduction band and n for the valence band of interest. The indices c and v will be used for the summation over remaining conduction and valence bands. The Heisenberg equation of motion for a time dependent operator \hat{O} is given by [32]

$$\frac{d}{dt} \hat{O} = \frac{i}{\hbar} [\hat{H}, \hat{O}]. \quad (3.2.20)$$

Applying to the microscopic polarization operator, one obtains

$$\frac{d}{dt} \hat{p}_{nm,\mathbf{k}} = \frac{i}{\hbar} [\hat{H}_1, \hat{p}_{nm,\mathbf{k}}] + \frac{i}{\hbar} [\hat{H}_{e-EM}, \hat{p}_{nm,\mathbf{k}}]. \quad (3.2.21)$$

The evaluation of the first commutator gives

$$-\frac{i}{\hbar} (E_c(\mathbf{k}) - E_v(\mathbf{k})) \hat{p}_{nm,\mathbf{k}}. \quad (3.2.22)$$

For the second operator

$$\frac{1}{V} \sum_{c,v,\mathbf{k}'} \boldsymbol{\mu}_{cv,\mathbf{k}'} \hat{p}_{vc,\mathbf{k}'}^\dagger + \boldsymbol{\mu}_{cv,\mathbf{k}'}^* \hat{p}_{vc,\mathbf{k}'}, \quad (3.2.23)$$

the second term containing $\hat{p}_{vc,\mathbf{k}}$ vanishes because four anticommuting exchanges are required (leading to no sign change) to obtain $\hat{p}_{nm,\mathbf{k}} \hat{H} - \hat{p}_{nm,\mathbf{k}} \hat{H} = 0$. Therefore, one is left with the first term, where operators are exchanged

to transform $\hat{H}\hat{p}$ into $\hat{p}\hat{H}$

$$\begin{aligned} \hat{a}_{c\mathbf{k}'}^\dagger \hat{b}_{c-\mathbf{k}'}^\dagger \hat{b}_{n\mathbf{k}} \hat{a}_{m\mathbf{k}} &\rightarrow \hat{a}_{c\mathbf{k}'}^\dagger \hat{a}_{m\mathbf{k}} \delta_{v,n} \delta_{\mathbf{k}',\mathbf{k}} \\ &+ \hat{b}_{v-\mathbf{k}'}^\dagger \hat{b}_{n-\mathbf{k}} \delta_{c,m} \delta_{\mathbf{k}',\mathbf{k}} \\ &- \delta_{\mathbf{k}',\mathbf{k}} \delta_{n,v} \delta_{m,c} + \hat{p}\hat{H}. \end{aligned} \quad (3.2.24)$$

The delta functions of the remaining terms lead in the sum over c, v and \mathbf{k}' to

$$\sum_c \hat{a}_{c\mathbf{k}}^\dagger \hat{a}_{m\mathbf{k}} + \sum_v \hat{b}_{v-\mathbf{k}} \hat{b}_{n-\mathbf{k}} - 1. \quad (3.2.25)$$

Here, the sums over c and v except for $c = m$ and $v = n$ will vanish when later the expectation value $\langle \hat{a}_{c\mathbf{k}}^\dagger \hat{a}_{m\mathbf{k}} \rangle$ is taken. Therefore, the sums are neglected from now on. This approximation scheme is called the *random phase approximation*. The hand waving argument is that the expectation value $\langle \hat{a}_{n'\mathbf{k}'}^\dagger \hat{a}_{n\mathbf{k}} \rangle$ has a dominant time-dependence

$$\langle \hat{a}_{n'\mathbf{k}'}^\dagger \hat{a}_{n\mathbf{k}} \rangle \propto e^{i(\omega_{n'\mathbf{k}'} - \omega_{n\mathbf{k}})t} \quad (3.2.26)$$

and therefore rapidly oscillates for $\omega_{n'\mathbf{k}'} \neq \omega_{n\mathbf{k}}$ and then averages out over time.

The terms with $c = m$ and $v = n$ are the density operators $\hat{n}_{m\mathbf{k}}$ and $\hat{n}_{n\mathbf{k}}$. Collecting everything and taking the expectation values, the equation of motion of the free carrier microscopic polarization is

$$\begin{aligned} \frac{d}{dt} \hat{p}_{nm,\mathbf{k}} &= -\frac{i}{\hbar} (E_m(\mathbf{k}) - E_n(\mathbf{k})) \hat{p}_{nm,\mathbf{k}} \\ &- \frac{i}{\hbar} \mathbf{E}(z, t) \cdot \boldsymbol{\mu}_{mn,\mathbf{k}} (\hat{n}_{m\mathbf{k}} + \hat{n}_{n\mathbf{k}} - 1) \\ &+ \left. \frac{\partial}{\partial t} \hat{p}_{nm,\mathbf{k}} \right|_{col.}. \end{aligned} \quad (3.2.27)$$

Similar equations can be formulated for the carriers density operators $\hat{n}_{m\mathbf{k}}$ and $\hat{n}_{n\mathbf{k}}$

$$\begin{aligned} \frac{d\hat{n}_{n\mathbf{k}}}{dt} &= -\frac{2}{\hbar} \Im \{ \mathbf{E}(z, t) \cdot \boldsymbol{\mu}_{\mathbf{k}} \hat{p}_{nm,\mathbf{k}}^* \} \\ &+ \left. \frac{\partial}{\partial t} \hat{n}_{n\mathbf{k}} \right|_{col.}, \end{aligned} \quad (3.2.28)$$

$$\begin{aligned} \frac{d\hat{n}_{m\mathbf{k}}}{dt} &= -\frac{2}{\hbar} \Im \{ \mathbf{E}(z, t) \cdot \boldsymbol{\mu}_{\mathbf{k}} \hat{p}_{nm,\mathbf{k}}^* \} \\ &+ \left. \frac{\partial}{\partial t} \hat{n}_{m\mathbf{k}} \right|_{col.}. \end{aligned} \quad (3.2.29)$$

These equations constitute the *semiconductor Bloch equations* [30], for the free-carrier case. These semiconductor Bloch equations contain the basis for most of our understanding of the optical properties of semiconductors and semiconductor microstructures. Depending on the strength and time dynamics of the field, one can distinguish several relevant regimes:

- the low excitation regime in which the exciton resonances - sometimes accompanied by exciton molecule (biexciton) resonances - dominate the optical properties. The interaction with phonons provides the most important relaxation and dephasing mechanism. As the density increases gradually, scattering between electron-hole excitations also becomes important.
- the high excitation regime in which an electron-hole plasma is excited. Here, the screening of the Coulomb interaction by the optically excited carriers and the collective plasma oscillations are the relevant physical phenomena. The main dissipative mechanism is the carrier-carrier Coulomb scattering.
- the quasi-equilibrium regime which can be realized on relatively long time scales. Here, the excitations have relaxed into a quasi-equilibrium and can be described by thermal distributions. The relatively slow approach to equilibrium can be described by a semi-classical relaxation and dephasing kinetics.

- the ultrafast regime in which quantum coherence and the beginning dissipation determine the optical response. The process of decoherence, of the beginning relaxation and the build-up of correlations, e.g., by a time-dependent screening are governed by the quantum kinetics with memory structure of the carrier-carrier and carrier-phonon scattering.

Throughout this thesis, the high-excitation and quasi-equilibrium regimes dominate the theoretical analysis of the discussed quantum structures. Generally, the scattering terms in the semiconductor Bloch equations describe all the couplings of the polarizations and populations, i.e., of the single-particle density matrix elements to higher-order correlations, such as two-particle and phonon- or photon-assisted density matrices. However, in many cases one can identify specific physical mechanisms that dominate the scattering terms in some of the excitation regimes listed above. For example, in the low excitation regime often the coupling of the excited carriers to phonons determines relaxation and dephasing, whereas at high carrier densities carrier-carrier scattering dominates. For relatively long pulses, Markov approximations for the scattering processes are often justified, and the scattering terms can be described by Boltzmann-like scattering rates due to carrier-phonon or carrier-carrier scattering, respectively [30].

In all situations, the semiconductor Bloch equations are a very suitable theoretical framework which, however, has to be supplemented with an appropriate treatment of the scattering terms in order to describe the various aspects of the rich physics which one encounters in pulse excited semiconductors. In general, the semiconductor Bloch equations have to be treated together with the Maxwell equations for the light field in order to determine the optical response. This self consistent coupling of Maxwell and semiconductor Bloch equations (for shortness also called Maxwell-semiconductor-Bloch equations) is needed as soon as spatially extended structures are analyzed where light propagation effects become important. Relevant examples are the polariton effects, as well as semiconductor lasers or the phenomenon of optical bistability [30]. In optically thin samples, however, where propagation effects are unimportant, the transmitted light field is proportional to the calculated polarization field. Under these conditions one can treat the semiconductor Bloch equations separately from Maxwell's equations to calculate the optical response.

The first term in (3.2.28) and (3.2.29) describes the generation of electrons and holes pairs by the absorption of light. As long as the scattering terms are ignored, the rate of change of the hole population (3.2.29) is identical to the rate of change of the electron population (3.2.28). The scattering terms require a more sophisticated treatment and some of these will be addressed in chapter 4. For the moment, scattering is approximated using a simple phenomenological decay rate model given by

$$\left. \frac{\partial}{\partial t} \hat{p}_{nm,\mathbf{k}} \right|_{col.} \approx -\gamma \hat{p}_{nm,\mathbf{k}}, \quad (3.2.30)$$

3.2.4 Solving the Equation for Free Carriers

To solve (3.2.27) one could use the approach given in [32] and formally integrate the differential equation. A simpler way is to replace the oscillating microscopic polarization $p_{nm,\mathbf{k}}$ by its slowly varying envelope

$$s_{nm,\mathbf{k}} = p_{nm,\mathbf{k}} e^{-i(k_0 z - \nu t - \phi(z))}, \quad (3.2.31)$$

where ν is the frequency of the optical field, and solve for the steady state of

$$\frac{d}{dt} s_{nm,\mathbf{k}} = 0. \quad (3.2.32)$$

Inserting (3.2.31) and (3.2.10) into (3.2.27), and skipping all fast oscillating parts (as they should average out over time), leads to

$$p_{nm,\mathbf{k}} = -\frac{i}{\hbar} \frac{E(z)}{2} \mu_{mn,\mathbf{k}} \frac{n_{m\mathbf{k}} + n_{n\mathbf{k}} - 1}{i(\omega_{n,m}(\mathbf{k}) - \nu) + \gamma} e^{-i(k_0 z - \nu t - \phi(z))}, \quad (3.2.33)$$

where $\omega_{n,m}(\mathbf{k})$ is defined by

$$\hbar \omega_{n,m}(\mathbf{k}) = E_m(\mathbf{k}) - E_n(\mathbf{k}). \quad (3.2.34)$$

Inserting this equation into (3.2.15) we obtain the expression for the absorption spectrum

$$\alpha_{FCT}(\nu) = k_0 \chi'' = -\frac{\nu}{\epsilon_0 n_b c} \frac{1}{\hbar} \frac{1}{\Omega} \sum_{n,m,\mathbf{k}} |\mu_{nm,\mathbf{k}}|^2 (n_{n\mathbf{k}} + n_{m\mathbf{k}} - 1) \frac{\gamma}{(\omega_{n,m}(\mathbf{k}) - \nu)^2 + \gamma^2}. \quad (3.2.35)$$

Here, the $\mu_{nm,\mathbf{k}}$ denotes the dipole matrix element, between the subbands n and m , along the polarization of the light field, resulting from the scalar product between the monochromatic light field \mathbf{E} and the dipole $\boldsymbol{\mu}_{nm,\mathbf{k}}$.

In order to evaluate numerically the absorption spectrum we make the following assumptions:

- The system under discussion is 2 dimensional and all \mathbf{k} -vector dependencies are cylindrically symmetric. Thus, we can use (3.1.38) transformation from summation to integration for the \mathbf{k} -vector.
- The system undergoes a rapid equilibration of electrons and holes into Fermi-Dirac distributions, which, assuming that the conduction band and the valence band are two carrier reservoirs, leads to $n_{e\mathbf{k}} = f_{e\mathbf{k}}$ and $n_{h\mathbf{k}} = f_{h\mathbf{k}}$.

Under these assumptions, (3.2.35) becomes

$$\alpha_{FCT}(\nu) = -\frac{\nu}{\hbar c \epsilon_0 n_b \pi \mathcal{L}} \sum_{n,m} \int_0^\infty dk k |\mu_{nm,\mathbf{k}}|^2 (f_{e\mathbf{k}}^n + f_{h\mathbf{k}}^m - 1) \frac{\gamma}{(\omega_{n,m}(\mathbf{k}) - \nu)^2 + \gamma^2}, \quad (3.2.36)$$

where \mathcal{L} is the length of the 2D quantum system.

3.3 Spontaneous Emission

The spontaneous emission within a semiconductor nanostructure can be obtained from the amplification G of the photon field, i.e. the complex part of the optical susceptibility χ'' . Using a phenomenological approach, (3.2.35) can be divided into an emitting and an absorbing part, $G = G_e - G_a$. The term $n_{e\mathbf{k}} + n_{v\mathbf{k}} - 1$ is the inversion of the electron-hole population in the semiconductor, which can be rewritten to

$$n_{e\mathbf{k}} + n_{v\mathbf{k}} - 1 = n_{e\mathbf{k}} n_{v\mathbf{k}} - (1 - n_{e\mathbf{k}})(1 - n_{v\mathbf{k}}). \quad (3.3.1)$$

The first term on rhs denotes the probability of a photon emission, i.e. electron and hole is occupied, while the second term denotes the probability of a photon absorption. Therefore, by evaluating (3.2.35) including only the emission probability term $G_e \sim n_{e\mathbf{k}} n_{v\mathbf{k}}$, the spontaneous emission probability per unit length is obtained. As the velocity of a photon in the semiconductor is given by c/n_b , the spontaneous emission probability per second is given by $G_e c / n_b$. Neglecting the existence of a cavity, the photon density of states (of photons with energy $\hbar\omega$) is given by

$$N(\hbar\omega) = \frac{n_b^3(\hbar\omega)^2}{\pi^2 \hbar^3 c^3} \quad (3.3.2)$$

and therefore the spontaneous emission ($s^{-1} m^{-3} eV^{-1}$) per second per unit volume per unit energy is given by

$$r_{sp}(\hbar\omega) = \frac{n_b^3(\hbar\omega)^2}{\pi^2 \hbar^3 c^2} G_e \quad (3.3.3)$$

where as the spontaneous emission intensity ($s^{-1} m^{-3}$) is given by

$$I_{sp}(\hbar\omega) = \hbar\omega r_{sp}(\hbar\omega). \quad (3.3.4)$$

Note that the result can be related to the Kubo-Martin-Schwinger (KMS) [34] relation. The relation between emission and inversion gives

$$\frac{f_{e\mathbf{k}} f_{v\mathbf{k}}}{f_{e\mathbf{k}} + f_{v\mathbf{k}} - 1} = \frac{1}{1 - \exp((E_c(\mathbf{k}) - E_v(\mathbf{k}) - (E_{Fc} - E_{Fv})) / k_B T)}. \quad (3.3.5)$$

Due to the Lorentzian in (3.2.35), the transition energy $E_c(\mathbf{k}) - E_v(\mathbf{k})$ is close to the photon energy. Consequently, it may be replaced with $\hbar\omega$ on the r.h.s of (3.3.5), which allows to pull the factor (3.3.5) out of the k -sum in (3.2.35), leading to the KMS relation

$$r_{sp}(\hbar\omega) = \frac{n_b^2(\hbar\omega)^2}{\pi^2 \hbar^3 c^2} \frac{1}{1 - \exp((\hbar\omega - (E_{Fc} - E_{Fv})) / k_B T)} G(\hbar\omega) \quad (3.3.6)$$

between gain and spontaneous emission.

Another aspect to consider is the dependence of the dipole matrix element $\mu_{cv,\mathbf{k}}$ on the polarization of the light field. Therefore, the average of all possible transitions is usually taken for the spontaneous emission

$$\mu_{cv,\mathbf{k}}^{sp} = \frac{1}{3} \sum_{i=x,y,z} \mu_{cv,\mathbf{k}}^i. \quad (3.3.7)$$

The spontaneous emission rate per unit volume ($s^{-1}m^{-3}$) is given by integrating $r_{sp}(\hbar\omega)$ over the energy

$$R_{sp} = \int_0^\infty r_{sp}(\hbar\omega) d\hbar\omega = Bnp \quad (3.3.8)$$

which defines another figure of merit, the spontaneous emission B coefficient ($m^3 s^{-1}$).

There is an obvious pathological feature when such a relation is used to obtain the spontaneous emission: if the electric field is zero, then no spontaneous emission would exist. The root of this misbehavior is due to the fact that the quantization of the electro-magnetic field is not included. Including this, spontaneous emission would occur - spontaneously. Nevertheless, the spontaneous emission of a two level system treated using quantized electro-magnetic fields does not differ from dipole radiation, therefore the error of the classical treatment may be small enough for the present purpose.

3.4 Dipole Matrix Element

The evaluation of the interband dipole matrix element $\mu_{mn,\mathbf{k}}$ between the solutions of the $\mathbf{k} \cdot \mathbf{p}$ band structure calculation is not straight-forward. In the general case, the envelope functions are given by

$$\varphi_{m\mathbf{k}} = \sum_i F_{m,i\mathbf{k}} u_{i0}, \quad (3.4.1)$$

where u_{i0} are again zone-center Bloch functions. Using this expansion, the dipole matrix element between two states is given by

$$\mu_{n'n,\mathbf{k}} = \mathcal{A} \int_{\mathcal{L}} dz \sum_{i,j} u_{i0}^* F_{m,i\mathbf{k}}^* \mathbf{d}u_{j0} F_{n,j\mathbf{k}}. \quad (3.4.2)$$

The question to answer is to whether the dipole operator is acting on the lattice periodic part u_{j0} or on the envelope part F_i . The issue has been addressed by Burt and others [35, 36], concluding that the expression is dominated by

$$\mu_{n'n,\mathbf{k}} \approx \frac{\mathcal{A}}{V_c} \sum_{i,j} \langle u_{i0} | u_{j0} \rangle_{V_c} \int_{\mathcal{L}} dz F_{m,i\mathbf{k}}^* \mathbf{d}F_{n,j\mathbf{k}}. \quad (3.4.3)$$

But, within a $\mathbf{k} \cdot \mathbf{p}$ calculation involving only single-band models for both, conduction and valence band, the last expression evaluates due to the orthogonality of u_{c0} and u_{v0} to zero¹. Therefore, no transition between conduction and valence subbands in such models would exist. The reason lies in the single-band approximation. While the wavefunction of e.g. conduction subbands is dominated by the envelope modulating u_{c0} , the interband dipole moment is dominated by the admixture of u_{v0} into the conduction subbands and u_{c0} into the valence subbands. Working within the 8×8 model would therefore resolve the problem.

A simpler solution, allowing to use non- 8×8 models without the pathological feature of vanishing transition probabilities, is to use the momentum- instead of the dipole matrix element. The relation can be derived using the Heisenberg equation of motion for the position operator r , given by

$$\frac{\partial}{\partial t} \mathbf{r} = \frac{i}{\hbar} [H, \mathbf{r}]. \quad (3.4.4)$$

Assuming that n and m are eigenfunctions of the Hamiltonian H with corresponding eigenenergies E_n and E_m , replacing the derivative of the position operator by the momentum operator and $H|m\rangle$ by $E_m|m\rangle$, one obtains

$$\langle n | \mathbf{p} | m \rangle = \frac{im}{\hbar} (E_n - E_m) \langle n | \mathbf{r} | m \rangle. \quad (3.4.5)$$

¹This fact also applies to 4×4 and 6×6 $\mathbf{k} \cdot \mathbf{p}$ valence band models.

The electron dipole operator (electrons are negatively charged) is related to the position operator by $\mathbf{d} = e\mathbf{r}$ leading to

$$\langle n | \mathbf{d} | m \rangle = e \frac{\hbar}{im} \frac{\langle n | \mathbf{p} | m \rangle}{(E_n - E_m)}. \quad (3.4.6)$$

Within direct transitions, the energy difference $E_n - E_m$ can be replaced by the photon energy $\hbar\omega$, leading to the simple expression for $\mu_{mn,\mathbf{k}}$ in terms of the momentum matrix element

$$\mu_{mn,\mathbf{k}} = \frac{e}{im\omega} \mathbf{p}_{mn,\mathbf{k}}. \quad (3.4.7)$$

In the approximation of slowly varying envelopes, the derivatives of the envelopes are small and the momentum matrix element is dominated by

$$\mathbf{p}_{mn,\mathbf{k}} \approx \frac{\mathcal{A}}{V_c} \sum_{i,j} \langle u_{i0} | \mathbf{p} | u_{j0} \rangle_{V_c} \int_{\mathcal{L}} dz F_{m,i\mathbf{k}}^* F_{n,j\mathbf{k}}. \quad (3.4.8)$$

The momentum matrix elements are related via (3.1.25) to band structure parameters P , defined e.g. in (2.2.10). This approximation is commonly applied and is also used in the remainder of the thesis.

Beside the neglected derivatives of the envelopes, the approximation (3.4.8) neglects the effect of remote bands. (3.4.8) considers only transitions between zone-center functions u_{i0} included explicitly in the Hamiltonian. In the $\mathbf{k} \cdot \mathbf{p}$ envelope equations, the effect of remote bands is included using Löwdins perturbation theory. Therefore, beside the mixing of the explicitly considered states in the Hamiltonian, the zone-center functions away from k include remote contributions. Consequently, transitions between remote contributions have to be included in a consistent definition of the momentum matrix elements [20].

We can now formulate the transition matrix elements calculation for the special case of the 2 band model presented in section 2.2.4. When calculating μ_t , all possible transitions between the involved conduction and valence subbands (HH or LH) have to be taken into consideration, yielding

$$|\mu_{\mathbf{k}}|^2 = \frac{1}{2} \sum_{u_c, \bar{u}_c} \sum_{u_v, \bar{u}_v} |\langle u_c | \hat{\mathbf{e}} \cdot \mathbf{p} | u_v \rangle \langle F_c | F_v \rangle|^2. \quad (3.4.9)$$

The factor $\frac{1}{2}$ compensates for the spin degeneracy. It is customary to express $|\mu_{\mathbf{k}}|$ as a function of $|\mu_0| = \langle u_c | \hat{\mathbf{e}} \cdot \mathbf{p} | u_i \rangle$, where $i = x, y, z$. $|\mu_0|$ can be determined from measurements of the band curvature [4]. By expressing the valence bands u_v as linear combinations of the basis functions, the expression for $|\mu_{\mathbf{k}}|^2$ can be much simplified. We assume the envelope function overlap integral to be unity, because of the moment we will be interested in is a transition between two bulk plane wave states. We find for the normalized transition strength in bulk material

$$\frac{|\mu_{\mathbf{k}}|^2}{|\mu_0|^2} = \begin{cases} \frac{1}{2} \left(1 - \left| \hat{\mathbf{k}} \cdot \hat{\mathbf{e}} \right|^2 \right), & HH \\ \frac{1}{2} \left(\frac{1}{3} + \left| \hat{\mathbf{k}} \cdot \hat{\mathbf{e}} \right|^2 \right), & LH \end{cases}. \quad (3.4.10)$$

$\hat{\mathbf{k}}$ is a unit vector pointing along the electron \mathbf{k} -vector.

As shown in Fig. 3.1, the strength of interaction between each electron plane wave and the incident photon is highly polarization dependent. However, in bulk material this dependence doesn't reveal itself as the incident field interacts with many electrons with different wave vectors, effectively averaging out the polarization dependence. In bulk, the relative interaction strength is equal in all the three principal directions, i.e., $\frac{|\mu_{\mathbf{k}}|^2}{|\mu_0|^2} = \frac{1}{3}$.

In quantum well structures, we can no longer work with simple plane wave states, but have to take into account the envelope functions. As a general valence band wave function consists of both HH and LH components, equation (3.4.9) can be replaced by:

1. For the TE polarization ($E_z = 0$, for beam propagation in z -direction):

$$M_{nm}^{\sigma} = \frac{|\mu_{\mathbf{k}}|}{|\mu_0|} = \begin{cases} \frac{3}{4} \left(|\langle \varphi_n(z) | g_{1,m}(k, z) \rangle|^2 + \frac{1}{3} |\langle \varphi_n(z) | g_{2,m}(k, z) \rangle|^2 \right), & \sigma = Up \\ \frac{3}{4} \left(|\langle \varphi_n(z) | g_{3,m}(k, z) \rangle|^2 + \frac{1}{3} |\langle \varphi_n(z) | g_{4,m}(k, z) \rangle|^2 \right), & \sigma = Down \end{cases}. \quad (3.4.11)$$

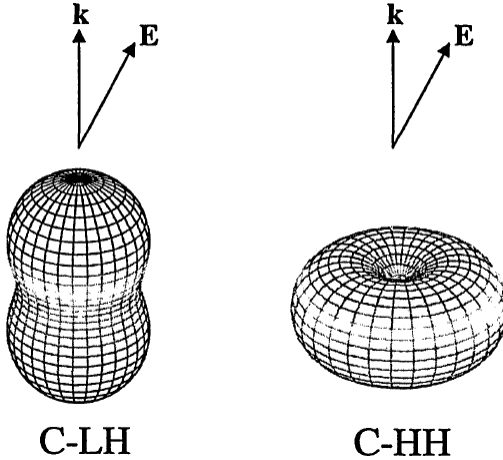


Figure 3.1: Dependence of the transition strength $|\mu_{\mathbf{k}}|$ on the angle between the electron \mathbf{k} -vector and the electric field polarization vector \mathbf{E} .

2. For the TM polarization ($H_z = 0$):

$$M_{nm}^{\sigma} = \frac{|\mu_{\mathbf{k}}|}{|\mu_0|} = \begin{cases} |\langle \varphi_n(z) | g_{2,m}(k, z) \rangle|, & \sigma = Up \\ |\langle \varphi_n(z) | g_{4,m}(k, z) \rangle|, & \sigma = Down \end{cases} \quad (3.4.12)$$

The term $|\mu_0|$ can be written as

$$|\mu_0| = \frac{eP}{\sqrt{3}\hbar\omega}, \quad (3.4.13)$$

where P is the dipole matrix element and ω is the transition wavelength.

As an illustration, we plot in Fig. 3.2 the calculated dipole matrix elements (for both polarities) of a 200 Å wide $GaAs/Al_{0.1}Ga_{0.9}As$ quantum well at $T = 2 K$ obtained using equations (3.4.11) and (3.4.12), where the wavefunctions from Fig. 2.9 are used in the matrix element calculations. The various conduction and valence subbands are indicated. If we add 2DEG into the simulated quantum structure the matrix element are altered, as shown in Fig. 3.3. Here we use the results of the calculations from section 2.3.2 to plot the matrix element change with 2DEG concentration from $1 \times 10^9 cm^{-2}$ to $1 \times 10^{11} cm^{-1}$, where the curves are ordered according the rising value of the concentration. As can be seen for both polarities, the concentration dependence of the matrix element is negligible close to the Brillouin zone center, while for $k_t \approx 5 \times 10^6 cm^{-1}$ the matrix elements start to diverge as the concentration rises.

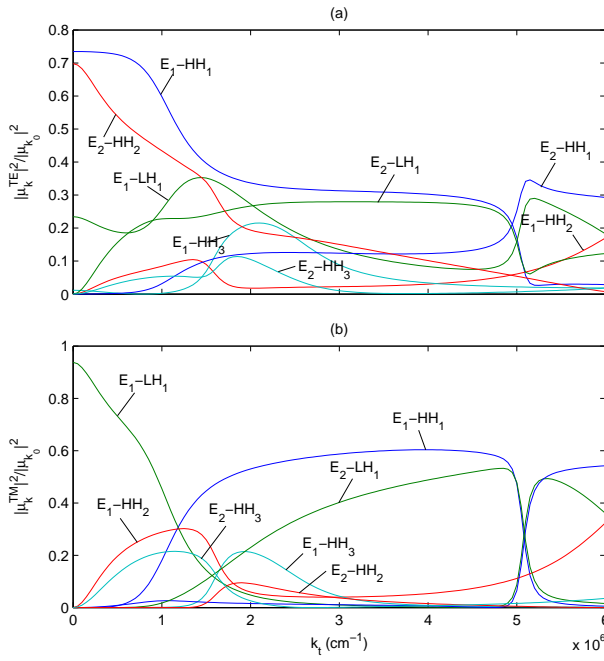


Figure 3.2: (a) TE and (b) TM dipole matrix elements calculated for 200 Å wide GaAs/Al_{0.1}Ga_{0.9}As quantum well at T = 2 K, without additional doping.

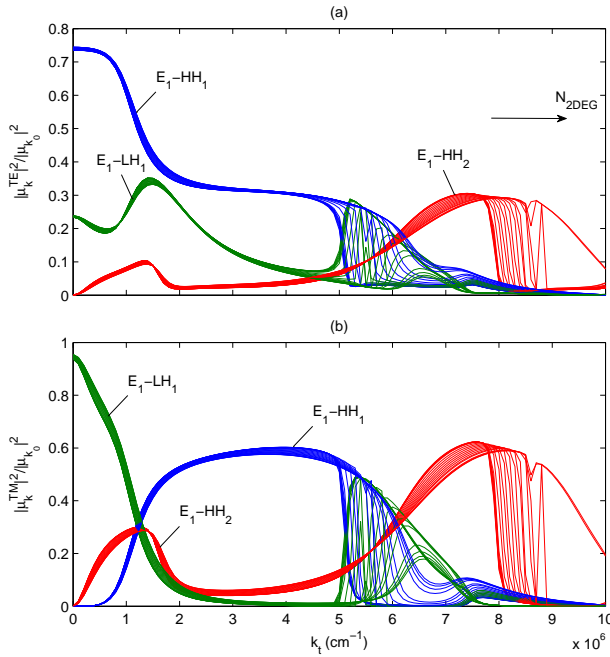


Figure 3.3: (a) TE and (b) TM dipole matrix elements calculated for 200 Å wide GaAs/Al_{0.1}Ga_{0.9}As quantum well at T = 2 K, containing 2DEG with various concentrations in the range of $1 \times 10^9 \text{ cm}^{-2}$ to $1 \times 10^{11} \text{ cm}^{-2}$.

Chapter 4

Coulomb Correlated Optical Transitions

The preceding chapter only considered free carriers and omitted their Coulomb interaction. The Coulomb interaction leads to the formation of electron-hole pairs, also known as *excitons*. Due to their bound nature, the transition energy is lowered, leading to absorption below the fundamental band gap, while the correlated movement of the electron-hole pair increases the transition probability and consequently the transitions strengths. As in the previous chapter, the theory review is based mainly on [4, 1, 32, 30, 33].

The present chapter therefore focuses on the inclusion of such many body effects in the evaluation of optical properties. A large part of the theory presented in the preceding chapter can be recycled. In general, only the omitted two-particle interaction Hamiltonian H_2 in (3.1.9) needs to be added to the equation of motion for the microscopic polarization (3.2.27). The chapter is therefore structured as follows: first, the Coulomb Hamiltonian is derived for Bloch functions and transformed into the electron-hole picture. Then the Coulomb Hamiltonian is included into the equation of motion, and the so called Hartree-Fock (HF) approximation is performed along with the introduction of screening. This leads to the formulation of the Coulomb enhancement of the absorption spectrum of the system. In order to utilize these observations, a numerical formulation of the HF model is outlined in detail facilitating a numerical calculation of the relevant optical characteristics. Finally, this formulation is applied to an actual quantum well structure, with and without the presence of 2DEG in the well region, and the results and discussed in detail.

4.1 Second Quantization

4.1.1 Introduction

If n_i, \mathbf{k}_i denote the quantum number of a Bloch state, then the Coulomb Hamiltonian (3.1.9) can be written as

$$\hat{H}_2 = \frac{1}{2} \sum_{\substack{n_1 \mathbf{k}_1, n_2 \mathbf{k}_2, \\ n_3 \mathbf{k}_3, n_4 \mathbf{k}_4}} \langle n_1 \mathbf{k}_1 n_2 \mathbf{k}_2 | v | n_3 \mathbf{k}_3 n_4 \mathbf{k}_4 \rangle \hat{a}_{n_1 \mathbf{k}_1}^\dagger \hat{a}_{n_2 \mathbf{k}_2}^\dagger \hat{a}_{n_3 \mathbf{k}_3} \hat{a}_{n_4 \mathbf{k}_4} \quad (4.1.1)$$

and the matrix element of the Coulomb operator reads

$$\begin{aligned} \langle n_1 \mathbf{k}_1 n_2 \mathbf{k}_2 | v | n_3 \mathbf{k}_3 n_4 \mathbf{k}_4 \rangle &= \frac{e^2}{4\pi\epsilon_0} \int_{\Omega} \int_{\Omega} dr dz dr' dz' \varphi_{n_1 \mathbf{k}_1}^*(\mathbf{r}, z) \varphi_{n_2 \mathbf{k}_2}^*(\mathbf{r}', z') \\ &\cdot \frac{1}{|(\mathbf{r}, z) - (\mathbf{r}', z')|} \varphi_{n_4 \mathbf{k}_4}(\mathbf{r}, z) \varphi_{n_3 \mathbf{k}_3}(\mathbf{r}', z'). \end{aligned} \quad (4.1.2)$$

The Coulomb-potential is mainly long-range and therefore more or less constant within a lattice cell. Consequently, the lattice periodic part can be averaged over a single crystal cell. The integration is then performed over lattice averaged quantities, as suggested in (3.1.26). Therefore, rewriting (4.1.2) into a more suitable form including lattice

cell averages, yields

$$\langle n_1 \mathbf{k}_1 n_2 \mathbf{k}_2 | v | n_3 \mathbf{k}_3 n_4 \mathbf{k}_4 \rangle = \frac{e^2}{4\pi\epsilon_0} \int_{\Omega} \int_{\Omega} d\mathbf{r} dz d\mathbf{r}' dz' \frac{1}{\mathcal{A}^2} e^{i(\mathbf{k}_4 - \mathbf{k}_1) \cdot \mathbf{r}} e^{i(\mathbf{k}_3 - \mathbf{k}_2) \cdot \mathbf{r}'} \\ \cdot g_{n_1 \mathbf{k}_1, n_4 \mathbf{k}_4}(z) g_{n_2 \mathbf{k}_2, n_3 \mathbf{k}_3}(z') \frac{1}{|(\mathbf{r}, z) - (\mathbf{r}', z')|}, \quad (4.1.3)$$

where $g_{n_1 \mathbf{k}_1, n_4 \mathbf{k}_4}(z) \approx \sum_i F_{n_1 \mathbf{k}_1, i}^*(z) F_{n_4 \mathbf{k}_4, i}(z)$ and $g_{n_2 \mathbf{k}_2, n_3 \mathbf{k}_3}(z')$ is defined accordingly. The next step is to get rid of the free directions \mathbf{r} and \mathbf{r}' , where the slowly varying part of the Bloch-function is given by the plane wave. The first step is to rewrite the term $\frac{1}{|(\mathbf{r}, z) - (\mathbf{r}', z')|}$ as $\frac{1}{\sqrt{(\mathbf{r} - \mathbf{r}')^2 + (z - z')^2}}$. Then, the integration over \mathbf{r}' is transformed into the integration over the distance between \mathbf{r} and \mathbf{r}' , $\mathbf{s} = \mathbf{r} - \mathbf{r}'$. So, instead of performing for every point \mathbf{r} the integration over \mathbf{r}' , one integrates for every point \mathbf{r} over all possible distances \mathbf{s} . This approach leads to several simplifications

$$\langle n_1 \mathbf{k}_1 n_2 \mathbf{k}_2 | v | n_3 \mathbf{k}_3 n_4 \mathbf{k}_4 \rangle = \frac{e^2}{4\pi\epsilon_0} \int_{\mathcal{L}} \int_{\mathcal{L}} dz dz' \frac{1}{\mathcal{A}^2} g_{n_1 \mathbf{k}_1, n_4 \mathbf{k}_4}(z) g_{n_2 \mathbf{k}_2, n_3 \mathbf{k}_3}(z') \\ \cdot \int_{\mathcal{A}} \int_{\mathcal{A}} d\mathbf{r} d\mathbf{s} \left[\frac{1}{\sqrt{|\mathbf{s}|^2 + (z - z')^2}} \right. \\ \left. \cdot e^{i(\mathbf{k}_4 + \mathbf{k}_3 - \mathbf{k}_1 - \mathbf{k}_2) \cdot \mathbf{r}} e^{i(\mathbf{k}_2 - \mathbf{k}_3) \cdot \mathbf{r}'} \right]. \quad (4.1.4)$$

The integration over \mathbf{r} and \mathbf{s} is decoupled and therefore the plane-wave leads to a delta function

$$\int_{\mathcal{A}} d\mathbf{r} e^{i(\mathbf{k}_4 + \mathbf{k}_3 - \mathbf{k}_1 - \mathbf{k}_2) \cdot \mathbf{r}} = \mathcal{A} \delta_{\mathbf{k}_4 + \mathbf{k}_3, \mathbf{k}_1 + \mathbf{k}_2}. \quad (4.1.5)$$

The remaining integration over z, z' and \mathbf{s} depends on the dimensionality of the system.

The Fourier transformation along the free direction \mathcal{A} defined in (3.1.20) is used to expand $\frac{1}{\mathbf{r}}$

$$\vartheta(\mathbf{s}, z, z') = \frac{1}{\sqrt{|\mathbf{s}|^2 + (z - z')^2}} = \sum_{\mathbf{q}} \vartheta_{\mathbf{q}}(z, z') e^{i\mathbf{q} \cdot \mathbf{s}} \quad (4.1.6)$$

in terms of its Fourier representation. Taking the integral over \mathbf{s}

$$\int_{\mathcal{A}} d\mathbf{s} \sum_{\mathbf{q}} \vartheta_{\mathbf{q}}(z, z') e^{i\mathbf{q} \cdot \mathbf{s}} e^{i(\mathbf{k}_2 - \mathbf{k}_3) \cdot \mathbf{s}} = \mathcal{A} \sum_{\mathbf{q}} \vartheta_{\mathbf{q}}(z, z') \delta_{\mathbf{k}_3 - \mathbf{k}_2, \mathbf{q}} \quad (4.1.7)$$

leads to another delta function, which can together with (4.1.5) be used to simplify (4.1.1) into

$$\hat{H}_2 = \frac{1}{2} \sum_{n_1, n_2} \sum_{\mathbf{k}, \mathbf{k}' \neq \mathbf{q}} \Theta_{\mathbf{q}, \mathbf{k}, \mathbf{k}'}^{n_1, n_2, n_3, n_4} \hat{a}_{n_1 \mathbf{k} + \mathbf{q}}^\dagger \hat{a}_{n_2 \mathbf{k}' - \mathbf{q}}^\dagger \hat{a}_{n_3 \mathbf{k}'} \hat{a}_{n_4 \mathbf{k}}. \quad (4.1.8)$$

Here, \mathbf{k}_4 has been relabeled to \mathbf{k} and \mathbf{k}_3 to \mathbf{k}' . The term $\Theta_{\mathbf{q}, \mathbf{k}, \mathbf{k}'}^{n_1, n_2, n_3, n_4}$ contains all parts of (4.1.2) depending on actual wavefunctions and on the dimensionality of the nanostructure. It is given by

$$\Theta_{\mathbf{q}, \mathbf{k}, \mathbf{k}'}^{n_1, n_2, n_3, n_4} = \frac{e^2}{4\pi\epsilon_0} \int_{\mathcal{L}} \int_{\mathcal{L}} dz dz' g_{n_1 \mathbf{k} + \mathbf{q}, n_4 \mathbf{k}}(z) g_{n_2 \mathbf{k}' - \mathbf{q}, n_3 \mathbf{k}'}(z') \vartheta_{\mathbf{q}}(z, z'). \quad (4.1.9)$$

In the case of a bulk crystal, there is no integration over z, z' . Then, $\vartheta_{\mathbf{q}}^{3D}$ is given by the 3D Fourier transform of the Coulomb potential

$$\vartheta_{\mathbf{q}}^{3D} = \frac{4\pi}{\Omega q^2}. \quad (4.1.10)$$

The quantum well case has a 2D plane as the translational invariant directions and a 1D axis where symmetry is broken. The 2D Fourier transformation of (4.1.6) gives

$$\vartheta_{\mathbf{q}}^{2D}(z, z') = \frac{2\pi}{Aq} e^{-q|z-z'|}. \quad (4.1.11)$$

Hereby, the factor $\frac{2\pi}{Aq}$ denotes the Fourier transform of an ideal quantum well with no extension in the symmetry broken direction, while the exponential factor comprises of the finite extension of the quantum well wavefunctions.

For the sake of convenience, we define the form factor term to be

$$G_{\mathbf{q}, \mathbf{k}, \mathbf{k}'}^{n_1, n_2, n_3, n_4} = \int_{\mathcal{L}} \int_{\mathcal{L}} dz dz' g_{n_1 \mathbf{k} + \mathbf{q}, n_4 \mathbf{k}}(z) g_{n_2 \mathbf{k}' - \mathbf{q}, n_3 \mathbf{k}'}(z') e^{-q|z-z'|}, \quad (4.1.12)$$

in terms of which $\Theta_{\mathbf{q}, \mathbf{k}, \mathbf{k}'}^{n_1, n_2, n_3, n_4}$ can be written as

$$\Theta_{\mathbf{q}, \mathbf{k}, \mathbf{k}'}^{n_1, n_2, n_3, n_4} = G_{\mathbf{q}, \mathbf{k}, \mathbf{k}'}^{n_1, n_2, n_3, n_4} V_{\mathbf{q}}. \quad (4.1.13)$$

For the 2D case we can write

$$\Theta_{\mathbf{q}, \mathbf{k}, \mathbf{k}'}^{n_1, n_2, n_3, n_4} = G_{\mathbf{q}, \mathbf{k}, \mathbf{k}'}^{n_1, n_2, n_3, n_4} \frac{e^2}{2\epsilon_r q A}. \quad (4.1.14)$$

Inspecting the Coulomb terms, it is clear that these terms diverge in the limit of $\mathbf{q} = 0$. The divergence can be resolved within the *Jellium model* [30], where the semiconductor is assumed to be intrinsically charge free. As a result, the diverging term of the electron-electron interaction at $\mathbf{q} = 0$ is canceled by the diverging term of the interaction of electrons with the homogeneous positive charge background. Hence, terms $\mathbf{q} = 0$ within the summation over \mathbf{q} are discarded.

4.1.2 Diagonal Approximation

The next approximation performed aims to remove two of the four subband indices in (4.1.8) by assuming that Coulomb interactions will not cause interband transitions. Then, $n_1 = n_4$ and $n_2 = n_3$, which is called here diagonal Coulomb approximation. This assumption is for example justified at an approximate level in symmetrical quantum wells, as the diagonal Coulomb matrix elements are due to the symmetry of the wavefunctions, two orders of magnitude larger than the off-diagonal [37]. Also, for single-band effective mass wavefunctions, only the diagonal terms remain, while others vanish due to the orthogonality of the zone-center functions. Using this approximations, the Coulomb Hamiltonian reads

$$\hat{H}_2 = \frac{1}{2} \sum_{m,n} \sum_{\mathbf{k}, \mathbf{k}' \neq \mathbf{q}} \Theta_{\mathbf{q}, \mathbf{k}, \mathbf{k}'}^{m, n, n, m} \hat{a}_{m \mathbf{k} + \mathbf{q}}^\dagger \hat{a}_{n \mathbf{k}' - \mathbf{q}}^\dagger \hat{a}_{n \mathbf{k}'} \hat{a}_{m \mathbf{k}}. \quad (4.1.15)$$

Consequently, the notation $\Theta_{\mathbf{q}, \mathbf{k}, \mathbf{k}'}^{m, n, n, m}$ can be reduced to $\Theta_{\mathbf{q}, \mathbf{k}, \mathbf{k}'}^{m, n}$.

4.1.3 Introduction of Holes

The next step is to transform the Coulomb Hamiltonian into the electron-hole picture. In the diagonal approximation (4.1.15), one distinguishes between electron states in the conduction bands c, d and hole states in the valence bands v, w . Therefore, the following four combinations are possible

$$n = c, m = d \quad n = c, m = v \quad n = v, m = c \quad n = v, m = w. \quad (4.1.16)$$

As next, hole operators are inserted for electrons in the valence band. Further, a natural ordering is reestablished by propagating the creation operators to the left and the annihilation operators to the right and setting the hole creation operator before, the hole annihilation operator after the one of the electron. The terms involving the sum $\sum_{n=c, m=d}$ are already in that ordering. Permuting the hole terms in the sum $\sum_{n=v, m=w}$ introduces a new two-operator term while the sums $\sum_{n=c, m=v}$ and $\sum_{n=v, m=c}$ can be summed together. Hence, the final Hamiltonian

which will be used to calculate the microscopic equation of motion is obtained as

$$\hat{H} = \sum_{c,\mathbf{k}} E_c(\mathbf{k}) \hat{a}_{c\mathbf{k}}^\dagger \hat{a}_{c\mathbf{k}} - \sum_{v,\mathbf{k}} E_v(\mathbf{k}) \hat{b}_{v\mathbf{k}}^\dagger \hat{b}_{v\mathbf{k}} \quad (4.1.17)$$

$$- \mathbf{E}(\mathbf{r}, t) \cdot \sum_{c,v,\mathbf{k}} \boldsymbol{\mu}_{cv,\mathbf{k}} \hat{a}_{c\mathbf{k}}^\dagger \hat{b}_{v-\mathbf{k}}^\dagger + \boldsymbol{\mu}_{cv,\mathbf{k}}^* \hat{b}_{v-\mathbf{k}} \hat{a}_{c\mathbf{k}} \quad (4.1.18)$$

$$+ \frac{1}{2} \sum_{c,d} \sum_{\mathbf{k}\mathbf{k}'\mathbf{q}} \Theta_{\mathbf{q},\mathbf{k},\mathbf{k}'}^{c,d} \hat{a}_{c\mathbf{k}+\mathbf{q}}^\dagger \hat{a}_{d\mathbf{k}'-\mathbf{q}}^\dagger \hat{a}_{d\mathbf{k}'} \hat{a}_{c\mathbf{k}} \quad (4.1.19)$$

$$+ \frac{1}{2} \sum_{v,w} \sum_{\mathbf{k}\mathbf{k}'\mathbf{q}} \Theta_{-\mathbf{q},-\mathbf{k}'+\mathbf{q},-\mathbf{k}-\mathbf{q}}^{w,v} \hat{b}_{v\mathbf{k}+\mathbf{q}}^\dagger \hat{b}_{v\mathbf{k}'-\mathbf{q}}^\dagger \hat{b}_{w\mathbf{k}'} \hat{b}_{v\mathbf{k}} \quad (4.1.20)$$

$$\sum_{v,\mathbf{k}',\mathbf{q}} \Theta_{-\mathbf{q},-\mathbf{k}'+\mathbf{q},-\mathbf{k}}^{v,v} \hat{b}_{v\mathbf{k}'}^\dagger \hat{b}_{v\mathbf{k}'} \quad (4.1.21)$$

$$- \frac{1}{2} \sum_{\mathbf{k}\mathbf{k}'\mathbf{q}} \left\{ \left(\Theta_{-\mathbf{q},-\mathbf{k}'+\mathbf{q},\mathbf{k}}^{v,c} + \Theta_{\mathbf{q},\mathbf{k},\mathbf{q}-\mathbf{k}'}^{c,v} \right) \hat{a}_{c\mathbf{k}+\mathbf{q}}^\dagger \hat{b}_{v\mathbf{k}'-\mathbf{q}}^\dagger \hat{b}_{v\mathbf{k}'} \hat{a}_{c\mathbf{k}} \right\}. \quad (4.1.22)$$

The indices \mathbf{k} and \mathbf{k}' have in some cases been swapped, shifted by \mathbf{q} and occasionally changed sign.

4.2 Transitions Calculation

4.2.1 Equations of Motion

The next task is to evaluate the equation of motion (3.2.20) for $\hat{p}_{nm,\mathbf{k}}$, as it has already been done in previous chapter, excluding the Coulomb interaction. Therefore, the remaining task is to evaluate the commutator of the microscopic polarization and the Coulomb Hamiltonian,

$$\frac{d}{dt} \hat{p}_{nm,\mathbf{k}} = \frac{i}{\hbar} \left[\hat{H}_2 \hat{p}_{nm,\mathbf{k}} \right] + \text{rest} \quad (4.2.1)$$

where \hat{H}_2 are the Coulomb terms in (4.1.17). The evaluation is straight forward but lengthy: For each four-operator term, one writes $\hat{H}_2 \hat{p}_{nm,\mathbf{k}} - \hat{p}_{nm,\mathbf{k}} \hat{H}_2$ and then permutes $\hat{p}_{nm,\mathbf{k}}$ in the first term to the left to obtain the remaining terms which do not cancel finally. The remaining terms are resorted at the end into the natural ordering. The resulting equation of motion is given by

$$\frac{d}{dt} \hat{p}_{nm,\mathbf{k}} = - \frac{i}{\hbar} \left\{ E_m(\mathbf{k}) - \left(E_n(\mathbf{k}) - \sum_{\mathbf{q}} \Theta_{-\mathbf{q},-\mathbf{k}+\mathbf{q},\mathbf{k}}^{n,n} \right) \right\} \hat{p}_{nm,\mathbf{k}} \quad (4.2.2)$$

$$- \frac{i}{\hbar} \mathbf{E}(z, t) \cdot \boldsymbol{\mu}_{mn,\mathbf{k}} \left(\sum_c \hat{a}_{c\mathbf{k}}^\dagger \hat{a}_{m\mathbf{k}} + \sum_v \hat{b}_{v\mathbf{k}}^\dagger \hat{b}_{n\mathbf{k}} - 1 \right) \quad (4.2.3)$$

$$+ \frac{i}{2\hbar} \sum_{c,\mathbf{k}',\mathbf{q}} \left(\Theta_{-\mathbf{q},\mathbf{k}+\mathbf{q},\mathbf{k}'}^{m,c} + \Theta_{\mathbf{q},\mathbf{k}',\mathbf{k}+\mathbf{q}}^{c,m} \right) \hat{a}_{c\mathbf{k}'+\mathbf{q}}^\dagger \hat{b}_{n-\mathbf{k}} \hat{a}_{c\mathbf{k}'} \hat{a}_{m\mathbf{k}+\mathbf{q}} \quad (4.2.4)$$

$$+ \frac{i}{2\hbar} \sum_{v,\mathbf{k}',\mathbf{q}} \left(\Theta_{-\mathbf{q},-\mathbf{k}'+\mathbf{q},\mathbf{k}}^{v,n} + \Theta_{\mathbf{q},\mathbf{k},-\mathbf{k}'+\mathbf{q}}^{n,v} \right) \hat{b}_{v\mathbf{k}'-\mathbf{q}}^\dagger \hat{b}_{v\mathbf{k}'} \hat{a}_{m\mathbf{k}} \hat{b}_{n-\mathbf{k}-\mathbf{q}} \quad (4.2.5)$$

$$- \frac{i}{2\hbar} \sum_{c,\mathbf{k}',\mathbf{q}} \left(\Theta_{-\mathbf{q},\mathbf{k},\mathbf{k}'}^{n,c} + \Theta_{\mathbf{q},\mathbf{k}',\mathbf{k}}^{c,n} \right) \hat{a}_{c\mathbf{k}'+\mathbf{q}}^\dagger \hat{b}_{n-\mathbf{k}+\mathbf{q}} \hat{a}_{c\mathbf{k}'} \hat{a}_{m\mathbf{k}} \quad (4.2.6)$$

$$- \frac{i}{2\hbar} \sum_{v,\mathbf{k}',\mathbf{q}} \left(\Theta_{-\mathbf{q},-\mathbf{k}'+\mathbf{q},\mathbf{k}-\mathbf{q}}^{v,m} + \Theta_{\mathbf{q},\mathbf{k}-\mathbf{q},-\mathbf{k}'+\mathbf{q}}^{m,v} \right) \hat{b}_{v\mathbf{k}'-\mathbf{q}}^\dagger \hat{b}_{n-\mathbf{k}} \hat{b}_{v\mathbf{k}'} \hat{a}_{m\mathbf{k}-\mathbf{q}} \quad (4.2.7)$$

$$+ \frac{i}{2\hbar} \sum_{\mathbf{q}} \left(\Theta_{-\mathbf{q},\mathbf{k},\mathbf{k}-\mathbf{q}}^{n,m} + \Theta_{\mathbf{q},\mathbf{k}-\mathbf{q},\mathbf{k}}^{m,n} \right) \hat{b}_{n-\mathbf{k}+\mathbf{q}} \hat{a}_{m\mathbf{k}-\mathbf{q}}. \quad (4.2.8)$$

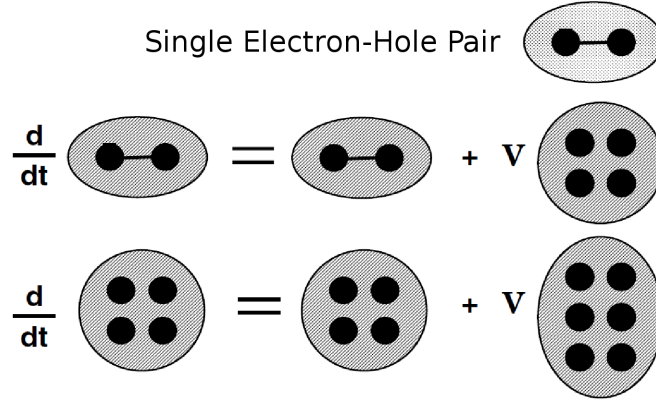


Figure 4.1: *Infinite hierarchy of operator products for the equations of motion.*

Figure 4.2: *Schematic representation of the Hartree-Fock approximation operator product in the equation of motion.*

Taking the two-band approximation of this particular equation and ignoring the \mathbf{k} dependence of the Coulomb matrix element results in Eq. (3.9) of ref. [32]. Comparing this equation with the free-carrier result (3.2.27) reveals that in (4.2.2), the valence band energy is shifted to

$$E_n(\mathbf{k}) \rightarrow E_n(\mathbf{k}) - \sum_{\mathbf{q}} \Theta_{-\mathbf{q}, -\mathbf{k} + \mathbf{q}, \mathbf{k}}^{n,n}. \quad (4.2.9)$$

The values usually inserted into $E_v(\mathbf{k})$ are results of a preceding band structure calculation, where parameters are obtained from low excitation experiments, where the valence band is full [32]. Therefore, the $E_v(\mathbf{k})$ actually already holds the Coulomb energy of the full valence band. The free-carrier calculation implicitly included this energy within the band structure result, while it appears here explicitly.

Similar equations of motion can be obtained for the carrier population operators

The terms (4.2.4) and (4.2.5) are the result of the equation of motion of the conduction-conduction and valence-valence terms (4.1.19), (4.1.20) and (4.1.21). The terms (4.2.6)-(4.2.8) are the results of the commutator with the conduction-valence terms (4.1.22). The term (4.2.8) is obtained at the end when (4.2.7) is brought into proper order.

The obtained equation of motion for the two-particle operator term $\hat{p}_{nm,\mathbf{k}}$ obviously depends on the four-particle operator terms. Therefore, it would be necessary to calculate the equation of motion of the four-particle operator term which would couple to a six-particle operator term: one obtains an infinite hierarchy of equations, as demonstrated in Fig. 4.1. For this reason, one usually truncates the hierarchy at a certain order [32]. Factorizing the four-particle operator into two two-particle operators yields the *Hartree-Fock approximation*, which is considered in the next section.

4.2.2 Hartree-Fock Approximation

In the next step, all four-particle operators are factorized into all possible products of two-particle operators, of which the expectation values are taken. While permuting these operators, the correct sign due to the anti-commutation relations has to be tracked. Due to the random-phase approximation (3.2.26), all expectation values of two-particle operators reduce either to microscopic polarizations $p_{nm,\mathbf{k}}$, particle densities $n_{n,\mathbf{k}}$ or to zero. We summarize this approach for a two-operator expectation value

$$\begin{aligned}\frac{d}{dt} \langle AB \rangle &= \frac{d}{dt} \langle AB \rangle_{HF} + \left(\frac{d}{dt} \langle AB \rangle - \frac{d}{dt} \langle AB \rangle_{HF} \right) \\ &= \frac{d}{dt} \langle AB \rangle_{HF} + \frac{d}{dt} \langle AB \rangle_{col.}\end{aligned}\quad (4.2.10)$$

where $\langle AB \rangle_{HF}$ is the Hartree-Fock contribution to the equation of motion which will be treated in this chapter (see Fig. 4.2). The term $\langle AB \rangle_{col.}$ is a higher-order contribution containing four-operator expectation values and they will be discussed briefly later in this chapter. Here, we only mention that with the full many-body Hamiltonian (3.1.1), the Heisenberg equation of motion gives the equation of motion for $\langle ABCD \rangle$ as

$$\frac{d}{dt} \langle ABCD \rangle = \frac{d}{dt} \langle ABCD \rangle_F + \left(\frac{d}{dt} \langle ABCD \rangle - \frac{d}{dt} \langle ABCD \rangle_F \right), \quad (4.2.11)$$

where $\frac{d}{dt} \langle ABCD \rangle$ contains expectation values of products of up to six operators. The label F is used to indicate the result from a Hartree-Fock factorization of the four and six operator expectation values. We can continue by deriving the equation of motion for

$$\langle ABCDEF \rangle \equiv \left(\frac{d}{dt} \langle ABCD \rangle - \frac{d}{dt} \langle ABCD \rangle_F \right) \quad (4.2.12)$$

and so on. The result is a hierarchy of equations, where each succeeding equation describes a correlation contribution that is of higher order than the one before. In practice, we truncate the hierarchy at some point.

As an example, the factorization of (4.2.4) leads to

$$\begin{aligned}\left\langle \hat{a}_{c\mathbf{k}'+\mathbf{q}}^\dagger \hat{b}_{n-\mathbf{k}} \hat{a}_{c\mathbf{k}'} \hat{a}_{m\mathbf{k}+\mathbf{q}} \right\rangle_{HF} &= \left\langle \hat{a}_{c\mathbf{k}'+\mathbf{q}}^\dagger \hat{b}_{n-\mathbf{k}} \right\rangle \left\langle \hat{a}_{c\mathbf{k}'} \hat{a}_{m\mathbf{k}+\mathbf{q}} \right\rangle \\ &\quad - \left\langle \hat{a}_{c\mathbf{k}'+\mathbf{q}}^\dagger \hat{a}_{c\mathbf{k}'} \right\rangle \left\langle \hat{b}_{n-\mathbf{k}} \hat{a}_{m\mathbf{k}+\mathbf{q}} \right\rangle \\ &\quad + \left\langle \hat{a}_{c\mathbf{k}'+\mathbf{q}}^\dagger \hat{a}_{m\mathbf{k}+\mathbf{q}} \right\rangle \left\langle \hat{b}_{n-\mathbf{k}} \hat{a}_{c\mathbf{k}'} \right\rangle \\ &= 0 - \delta_{\mathbf{q}0} + \delta_{\mathbf{k}'\mathbf{k}} \delta_{cm} n_{m,\mathbf{k}+\mathbf{q}} p_{nm,\mathbf{k}}.\end{aligned}$$

Other terms are factorized accordingly. The factorized terms of (4.2.4) and (4.2.5) can be added to the transition energy, while the remaining terms are proportional to the inversion factor. Finally, the equation for the microscopic polarization in the Hartree-Fock approximation is obtained as

$$\begin{aligned}\frac{d}{dt} p_{nm,\mathbf{k}} &= -\frac{i}{\hbar} \hbar \tilde{\omega}_{mn}(\mathbf{k}) p_{nm,\mathbf{k}} \\ &\quad - \frac{i}{\hbar} \left\{ \mathbf{E}(z, t) \cdot \boldsymbol{\mu}_{mn,\mathbf{k}} + \sum_{\mathbf{q}} \Theta_{-\mathbf{q},\mathbf{k},\mathbf{k}-\mathbf{q}}^{n,m} p_{nm,\mathbf{k}-\mathbf{q}} \right\} (n_{m\mathbf{k}} + n_{n\mathbf{k}} - 1) \\ &\quad + \frac{\partial}{\partial t} p_{nm,\mathbf{k}}|_{col.},\end{aligned}\quad (4.2.13)$$

and the renormalized transition energy is given as

$$\begin{aligned}\hbar \tilde{\omega}_{mn}(\mathbf{k}) &= E_m(\mathbf{k}) - \left(E_n(\mathbf{k}) - \sum_{\mathbf{q}} \Theta_{-\mathbf{q},-\mathbf{k}+\mathbf{q},\mathbf{k}}^{n,n} \right) \\ &\quad - \sum_{\mathbf{q}} \left(\Theta_{\mathbf{q},\mathbf{k},\mathbf{k}+\mathbf{q}}^{m,m} n_{m,\mathbf{k}+\mathbf{q}} + \Theta_{\mathbf{q},\mathbf{k},\mathbf{k}+\mathbf{q}}^{n,n} n_{n,\mathbf{k}+\mathbf{q}} \right).\end{aligned}\quad (4.2.14)$$

The sum term in (4.2.14) is called the *exchange shift* term. Inspecting (4.2.13) reveals that the microscopic polarization $p_{nm,\mathbf{k}}$ at \mathbf{k} is now coupled to the one at \mathbf{k}' by the Coulomb interaction, while in the free-carrier expression, the microscopic polarization was entirely determined by the momentum matrix element and the inversion. This coupling introduces the excitonic effects such as enhancing gain or absorption. The higher-order correlation (collisions) contributions are denoted similarly to previous chapter with the subscript col. The expressions for the carrier distribution operators $\hat{n}_{n\mathbf{k}}$ and $\hat{n}_{m\mathbf{k}}$ can be obtained similarly. By introducing *renormalized Rabi frequency*

$$\Omega_{\mathbf{k}}(z, t) = \mathbf{E}(z, t) \cdot \boldsymbol{\mu}_{mn,\mathbf{k}} + \sum_{\mathbf{q}} \Theta_{-\mathbf{q},\mathbf{k},\mathbf{k}-\mathbf{q}}^{n,m} p_{nm,\mathbf{k}-\mathbf{q}}, \quad (4.2.15)$$

we can rewrite the semiconductor Bloch equations as

$$\frac{d}{dt} p_{nm,\mathbf{k}} = -i\tilde{\omega}_{mn}(\mathbf{k})p_{nm,\mathbf{k}} - i\Omega_{\mathbf{k}}(z,t)(n_{m\mathbf{k}} + n_{n\mathbf{k}} - 1) + \frac{\partial}{\partial t} p_{nm,\mathbf{k}}|_{col.}, \quad (4.2.16)$$

$$\frac{d}{dt} n_{n\mathbf{k}} = i[\Omega_{\mathbf{k}}(z,t)p_{nm,\mathbf{k}}^* - \Omega_{\mathbf{k}}^*(z,t)p_{nm,\mathbf{k}}] + \frac{\partial}{\partial t} n_{n\mathbf{k}}|_{col.}, \quad (4.2.17)$$

$$\frac{d}{dt} n_{m\mathbf{k}} = i[\Omega_{\mathbf{k}}(z,t)p_{nm,\mathbf{k}}^* - \Omega_{\mathbf{k}}^*(z,t)p_{nm,\mathbf{k}}] + \frac{\partial}{\partial t} n_{m\mathbf{k}}|_{col.}. \quad (4.2.18)$$

The second term in (4.2.15) is called the *Coulomb field renormalization*.

The semiconductor Bloch equations look like the two-level Bloch equations, with the exceptions that the transition energy and the electric-dipole interaction are renormalized, and the carrier probabilities $n_{n\mathbf{k}}$ enter instead of the probability difference between upper and lower levels. The renormalizations are due to the many-body Coulomb interactions, and they couple equations for different \mathbf{k} states. This coupling leads to significant complications in the evaluation of (4.2.16)-(4.2.18) in comparison to the corresponding free-carrier equations, (3.2.27)-3.2.29. If all Coulomb-potential contributions are dropped, the semiconductor Bloch equations reduce to the undamped inhomogeneously broadened two-level Bloch equations [32]. Of course, this limit is unacceptable for semiconductors.

4.2.3 Many-Body Effects

There are two important many-body effects that do not appear in the Hartree-Fock limit of the equation of motion, the collisions between particles and the plasma screening. They occur at high carrier densities. The main consequences of the collisions between particles are:

- A decay of the microscopic polarization $p_{nm,\mathbf{k}}$ that we can model with a relaxation time γ . This implies $\frac{\partial}{\partial t} p_{nm,\mathbf{k}}|_{col.} = -\gamma p_{nm,\mathbf{k}}$.
- A rapid equilibration of electrons and holes into Fermi-Dirac distributions. We can model this, assuming that the conduction band and the valence band are two carrier reservoirs, which are Fermi-distributed, i.e. $n_{e\mathbf{k}} = f_{e\mathbf{k}}$ and $n_{h\mathbf{k}} = f_{h\mathbf{k}}$.

It is more difficult to include the plasma screening effect into (4.2.16)-(4.2.18). The procedure is outlined in this subsection.

4.2.3.1 Background Screening

In the crystal electron Hamiltonian (2.1.8), the interaction between ion cores and the interaction between electrons and ion cores is merged into the potential $U(\mathbf{r})$, while the Coulomb energy between electrons has been retained and later transformed into the Bloch states. With the introduction of $\mathbf{k} \cdot \mathbf{p}$ states, only a restricted number of valence electrons are considered, while core electrons are included implicitly. These implicitly included core electrons and ion cores screen the Coulomb interaction between explicitly included electrons. The effect can be considered by replacing the dielectric permittivity of the vacuum ϵ_0 with the static semiconductor crystal background permittivity ϵ_b in the Coulomb matrix element (4.1.2).

4.2.3.2 Plasma Screening

A profound weakness of the Hartree-Fock approximation is the lack of screening of Coulomb interactions at elevated carrier densities. The presence of unbound carriers of the electron-hole plasma leads to an adjustment of the carriers to a charge, effectively screening it and thereby reducing the Coulomb interaction energy. The lack of screening in the Hartree-Fock equations is caused by the early truncation of the infinite hierarchy of equations of motion. One therefore introduces the screening effect phenomenologically using a dynamic dielectric function $\epsilon(\mathbf{q}, \omega)$

$$V_{s\mathbf{q}} = \frac{V_{\mathbf{q}}}{\epsilon(\mathbf{q}, \omega)}, \quad (4.2.19)$$

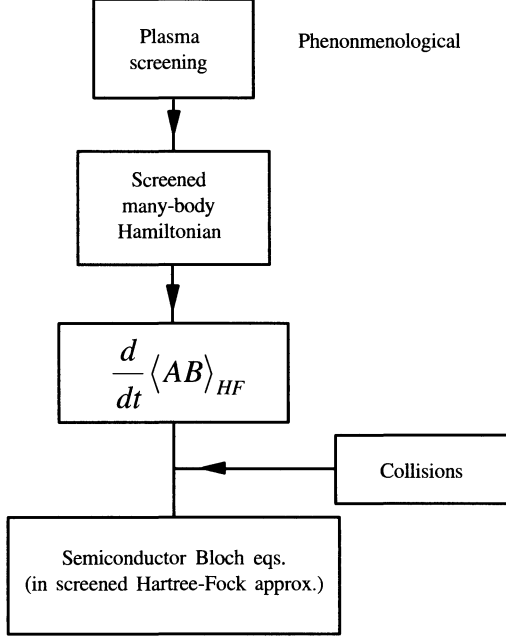


Figure 4.3: Outline of an approach that takes advantage of a phenomenological derivation of plasma screening, which is incorporated directly into the many-body Hamiltonian to give the screened Hartree-Fock equations (after [32]).

where $V_{s\mathbf{q}}$ denotes the screened potential and $V_{\mathbf{q}}$ the unscreened one¹. There are several model dielectric functions, where all have their strengths, limitations and weaknesses. One standard approach is the *Lindhard's formula* [32, 30],

$$\epsilon(\mathbf{q}, \omega) = 1 - V_{\mathbf{q}} \sum_{n\mathbf{k}} \frac{n_{n,\mathbf{k}-\mathbf{q}} - n_{n,\mathbf{k}}}{E_n(\mathbf{k} - \mathbf{q}) - E_n(\mathbf{k}) + \hbar\omega + \hbar i\delta}, \quad (4.2.20)$$

also denoted as randomphase approximation. The Lindhard formula can be derived using the self-consistent field (SCF) approach [38], or more profound, by neglecting vertex corrections in the equation of motion for the Green's function [39] of the designated system and using the Kadanoff-Baym formalism [39]. The derivation using the SCF approach involves the reaction of a homogeneous electron gas to a test charge (see detailed derivation in Appendix D). To use Lindhard's formula in optical calculations, the test charge potential $V_{\mathbf{q}}$ is replaced with the Coulomb potential $\Theta_{\mathbf{q},\mathbf{k},\mathbf{k}'}^{n_1,n_2,n_3,n_4}$ defined in (4.1.13), including the factor due to the finite extend of the wavefunctions.

There are several far better models [40] for the dielectric screening but the Lindhard formula is still popular and commonly used in optoelectronic modeling [32] due to its simple structure. For many practical applications, the damped response of the screening is ignored, therefore setting $(\omega + i\delta)$ to zero. Once $\epsilon(\mathbf{q}, 0)$ is obtained, one replaces the Coulomb potential within all equations with

$$\Theta_{s,\mathbf{q},\mathbf{k},\mathbf{k}'}^{n_1,n_2,n_3,n_4} = \frac{1}{\epsilon(\mathbf{q}, 0)} \Theta_{\mathbf{q},\mathbf{k},\mathbf{k}'}^{n_1,n_2,n_3,n_4}. \quad (4.2.21)$$

Beside its physical importance, the screening introduces the desired effect of removing the divergence of the Coulomb potential with $\mathbf{q} \rightarrow 0$, thereby facilitating the numerical evaluation.

The outline of the screened Hartree-Fock approach is presented in Fig. (4.3).

¹Note that the Coulomb interaction Hamiltonian with the bare Coulomb potential already contains the mechanism for plasma screening. Therefore, one should be concerned that an *ad hoc* replacement of $V_{\mathbf{q}}$ with $V_{s\mathbf{q}}$ might count some screening effects twice. Such problems can only be avoided within a systematic many-body approach.

4.2.3.3 Coulomb Hole Self Energy

By replacing the electron operators with hole operators in (4.2.2), the valence band energy was shifted by a constant value,

$$E_n(\mathbf{k}) \rightarrow E_n(\mathbf{k}) - \sum_{\mathbf{q}} \Theta_{-\mathbf{q}, -\mathbf{k} + \mathbf{q}, \mathbf{k}}^{n,n}. \quad (4.2.22)$$

This shift is already implicitly included in the band structure. In the high density limit, the Coulomb interaction is screened

$$\Theta_{s,-\mathbf{q}, -\mathbf{k} + \mathbf{q}, \mathbf{k}}^{n,n} = \frac{\Theta_{-\mathbf{q}, -\mathbf{k} + \mathbf{q}, \mathbf{k}}^{n,n}}{\epsilon(\mathbf{q}, 0)} \quad (4.2.23)$$

and the difference between the unscreened and the screened Coulomb interaction leads to a density dependent shift

$$\Delta E_{CH,n} = \sum_{\mathbf{q}} \Theta_{-\mathbf{q}, -\mathbf{k} + \mathbf{q}, \mathbf{k}}^{n,n} \left(\frac{1}{\epsilon(\mathbf{q})} - 1 \right). \quad (4.2.24)$$

The shift is denoted as *Debye shift* or *Coulomb-hole self energy*.

4.2.3.4 Screened Exchange Energy

Beside the Coulomb-hole self energy, the transition energy (4.2.14) is, compared to the free carrier result, reduced by the density dependent *screened exchange shift*,

$$\Delta E_{SX,mn}(\mathbf{k}) = \sum_{\mathbf{q}} \left(\Theta_{\mathbf{q}, \mathbf{k}, \mathbf{k} + \mathbf{q}}^{m,m} n_{m,\mathbf{k}+\mathbf{q}} + \Theta_{\mathbf{q}, \mathbf{k}, \mathbf{k} + \mathbf{q}}^{n,n} n_{n,\mathbf{k}+\mathbf{q}} \right). \quad (4.2.25)$$

where the screened Coulomb potentials are used.

In conclusion, within the screened Hartree-Fock limit, the transition energy is therefore renormalized

$$\hbar \tilde{\omega}_{mn}(\mathbf{k}) = \Delta E_{mn}(\mathbf{k}) + \Delta E_{CH,n} - \Delta E_{SX,mn}(\mathbf{k}). \quad (4.2.26)$$

Note that both contributions 4.2.24 and 4.2.25 reduce the transition energy and can lead to a significant red shift.

4.2.4 Solving the Correlated Equation

In order to solve the equation of motion (4.2.13), the collision term is approximated using a decay rate $-\gamma p_{mn,\mathbf{k}}$. As equation (4.2.13) couples microscopic polarizations $p_{mn,\mathbf{k}}$ of different \mathbf{k} values, the equation system has to be solved self-consistently. Therefore, the equation is transformed using the same ansatz as in Chapter 3. The fast oscillating $p_{mn,\mathbf{k}}$ is replaced with its slowly-varying envelope

$$s_{nm,\mathbf{k}} = p_{mn,\mathbf{k}} e^{-i(k_0 z - \nu t - \phi(z))}. \quad (4.2.27)$$

Inserting (4.2.27) into (4.2.13), taking the time derivative, using the plane wave expression for the electrical field (3.2.10), skipping the fast oscillating parts (as they should average out to zero) and solving for the steady state leads to

$$\begin{aligned} s_{nm,\mathbf{k}} &= -\frac{1}{i(\tilde{\omega}_{mn}(\mathbf{k}) - \nu) + \gamma} \frac{i}{\hbar} \\ &\cdot \left\{ \mu_{mn,\mathbf{k}} \frac{E(z)}{2} + \sum \Theta_{\mathbf{q}, \mathbf{k}, \mathbf{k} + \mathbf{q}}^{n,m} s_{nm,\mathbf{k} + \mathbf{q}} \right\} \\ &\cdot (n_{m\mathbf{k}} + n_{n\mathbf{k}} - 1). \end{aligned} \quad (4.2.28)$$

The polarization envelope still depends on the intensity of the considered field. Therefore, the field independent solution variable is introduced, given by

$$\lambda_{nm,\mathbf{k}} = \frac{2s_{nm,\mathbf{k}}}{E(z)}. \quad (4.2.29)$$

In order to obtain a practicable expression, the lineshape and the inversion factor are combined into

$$\Lambda_{nm,\mathbf{k}} = \frac{i}{\hbar} \frac{(n_{m\mathbf{k}} + n_{n\mathbf{k}} - 1)}{i(\tilde{\omega}_{mn,\mathbf{k}} - \nu) + \gamma}. \quad (4.2.30)$$

Inserting (4.2.29) and (4.2.30) into (4.2.28), yields

$$\Lambda_{nm,\mathbf{k}} \sum_{\mathbf{q},\mathbf{k}+\mathbf{q}} \Theta_{\mathbf{q},\mathbf{k}+\mathbf{q}}^{n,m} \lambda_{nm,\mathbf{k}+\mathbf{q}} + \lambda_{nm,\mathbf{k}} = -\mu_{mn,\mathbf{k}} \Lambda_{nm,\mathbf{k}}. \quad (4.2.31)$$

This equation is the self-consistency equation for $\lambda_{nm,\mathbf{k}}$. Once solved, the elelctrical susceptibility is calculated using

$$\chi(\nu) = \frac{1}{n_b^2 \epsilon_0} \frac{P(z)}{E(z)} = \frac{1}{n_b^2 \epsilon_0} \frac{1}{V} \sum_{n,m,\mathbf{k}} \mu_{mn,\mathbf{k}}^* \lambda_{nm,\mathbf{k}}. \quad (4.2.32)$$

Absorption, refractive index change and spontaneous emission can therefrom be calculated as already presented in the preceding Chapter 3. In the next section we present the numerical implementation details of the solution.

4.2.5 Implementation Considerations

As a consequence of the collisions between particles in the assumed equilibrium state, we consider the conduction band and the valence band as two carriers reservoirs with Fermi-Dirac distributions for the electrons and holes. Thus, we only need to solve the equation of motion for the polarization $\hat{p}_{nm,\mathbf{k}}$. Using the decay model for the microscopic polarization we obtain

$$\frac{d}{dt} p_{nm,\mathbf{k}} = -i\tilde{\omega}_{mn}(\mathbf{k}) p_{nm,\mathbf{k}} - i\Omega_{\mathbf{k}}(z,t) (f_{e\mathbf{k}}^n + f_{h\mathbf{k}}^m - 1) - \gamma p_{nm,\mathbf{k}}, \quad (4.2.33)$$

where n and m denote the conduction and valence subbands, respectively, involved in the transition. As for the free carrier model, the electron and hole densities are given as input parameters, and the chemical potentials, E_{Fc} and E_{Fv} , are calculated as described in section 3.1.4.

As the first step for the calculation, the dielectric function $\epsilon(\mathbf{q})$, the Coulomb-hole self energy $\Delta E_{CH,n}$ and the screened exchange shift energy $\Delta E_{SX,mn}(\mathbf{k})$ must be evaluated. Here we elaborate on the practical numerics for the calculation of these terms (and others), and illustrate the results for a 200 nm wide *GaAs* well, surrounded by *Ga_{0.9}Al_{0.1}As* barriers with δ-doped layers introduced at 1000 nm away from the barrier-well boundaries.

- It is more convenient to evaluate $q\epsilon(\mathbf{q})$ than only $\epsilon(\mathbf{q})$. With Fermi-Dirac electron and hole distributions, we have from (4.2.20)

$$q\epsilon(\mathbf{q}) = q - \frac{e^2}{2\epsilon_r A} \sum_{n\mathbf{k}} \frac{f_{n,\mathbf{k}-\mathbf{q}} - f_{n,\mathbf{k}}}{E_n(\mathbf{k}-\mathbf{q}) - E_n(\mathbf{k})}. \quad (4.2.34)$$

Converting the sum over the \mathbf{k} -states into an integral, adding the sum over the spin, choosing θ as the angle between \mathbf{k} and \mathbf{q} and assuming no angular dependence for the subband structure, we obtain

$$q\epsilon(q) = q - \frac{e^2}{4\pi^2 \epsilon_r} \sum_n \int_0^\infty dk k \int_0^{2\pi} d\theta \frac{f_{n,|\mathbf{k}-\mathbf{q}|} - f_{n,|\mathbf{k}|}}{E_n(|\mathbf{k}-\mathbf{q}|) - E_n(|\mathbf{k}|)}. \quad (4.2.35)$$

with

$$|\mathbf{k}'| = |\mathbf{k} - \mathbf{q}| = (k^2 + q^2 - 2kq \cos \theta)^{\frac{1}{2}}. \quad (4.2.36)$$

The integrals can be evaluated here, as before, using the trapezoidal method for integration. As an illustration, Fig. 4.4 presents result of the calculation for the toy structure presented above with variable 2DEG concentration $n_e = 1 \times 10^9 \div 1 \times 10^{11} \text{ cm}^{-2}$. As can be seen, the screening effect mainly influential at low wavevector values, influence which extends with higher gas concentrations.

- For the Coulomb-hole self energy with Fermi-Dirac distributions we can write

$$\begin{aligned} \Delta E_{CH,n} &= \sum_{\mathbf{q} \neq 0} \Theta_{-\mathbf{q},-\mathbf{k}+\mathbf{q},\mathbf{k}}^{n,n} \left(\frac{1}{\epsilon(\mathbf{q})} - 1 \right) \\ &= \frac{e^2}{4\pi\epsilon_r} \int_{0^+}^\infty dq G_{\mathbf{q}}^{n,n} \left(\frac{1}{\epsilon(q)} - 1 \right), \end{aligned} \quad (4.2.37)$$

where the parameter n denotes the hole subband.

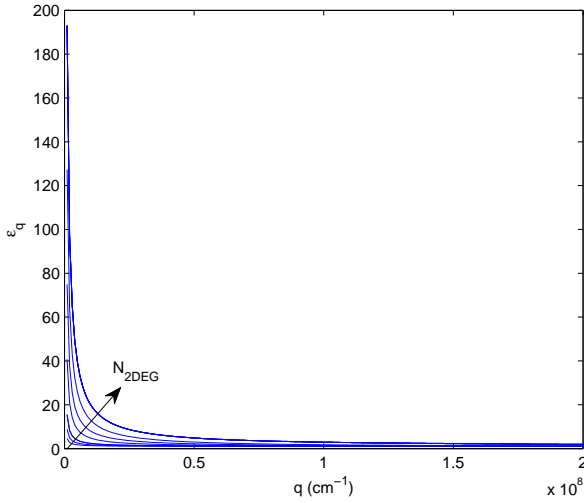


Figure 4.4: The screening dielectric function $\epsilon(q)$ calculated for the 200 Å wide GaAs/Ga_{0.9}Al_{0.1}As well with $n_e = 1 \times 10^9 \div 1 \times 10^{11} \text{ cm}^{-2}$ at $T = 2\text{K}$.

- The screened-exchange shift energy becomes

$$\Delta E_{SX,nm}(\mathbf{k}) = \sum_{\mathbf{k}' \neq \mathbf{k}} (\Theta_{s,\mathbf{q}}^{n,n} f_{e,\mathbf{k}'}^n + \Theta_{s,\mathbf{q}}^{m,m} f_{h,\mathbf{k}'}^m). \quad (4.2.38)$$

The band indices m and n are defined as before for the interacting subbands. If we convert the sum over \mathbf{k}' into an integral with θ' defining the angle between \mathbf{k} and \mathbf{k}' and we assume a rotationally symmetric band structure, we obtain

$$\Delta E_{SX,nm}(\mathbf{k}) = \frac{e^2}{8\pi^2\epsilon_r} \int_0^\infty dk' \int_0^{2\pi} d\theta' \frac{k'}{q\epsilon(q)} (G_{\mathbf{q}}^{n,n} f_{e,\mathbf{k}'}^n + G_{\mathbf{q}}^{m,m} f_{h,\mathbf{k}'}^m) \quad (4.2.39)$$

where

$$|\mathbf{q}| = |\mathbf{k} - \mathbf{k}'| = (k^2 + k'^2 - 2kk' \cos \theta')^{\frac{1}{2}}. \quad (4.2.40)$$

Fig. 4.5 presents the calculated values of the Coulomb-hole self energy and screened-exchange energy shifts for various 2DEG concentrations. As predicted, both shifts are negative in nature and their values increase (in an absolute value) with the rise in the gas concentration. Fig. 4.6 presents the dispersion relation of the total bandgap renormalization (BGR) energy, $\Delta E_{CH,m} - \Delta E_{SX,nm}(\mathbf{k})$, calculated for the 200 Å wide GaAs/Ga_{0.9}Al_{0.1}As well with 2DEG concentration of $n_e = 1 \times 10^{11} \text{ cm}^{-2}$. In this calculation we consider the transitions between the first conduction subband and first four valence subbands. Fig. 4.7 presents the total bandgap renormalization for the same structure for various 2DEG concentrations for ambient temperatures $T = 2\text{K}$ and $T = 77\text{K}$ (respectively in (a) and (b)). The renormalization value grown (in absolute value) with the concentration because of the state filling in the conduction subband. The exponential fit of the calculated values is also presented for $T = 2\text{K}$ (red dashed curve in (a)), where the expected [41] $\sim 1/3$ exponential dependence is clearly seen.

In all the expressions above we use (4.1.14) to describe the coulomb interaction for the 2D case. The form factor is explicitly calculated using

$$G_{\mathbf{q}}^{n,m} = \int_{-\infty}^{\infty} dz \int_{-\infty}^{\infty} dz' |F_{n,\mathbf{k}}(z)|^2 |F_{m,\mathbf{k}}(z')|^2 e^{-q|z-z'|}, \quad (4.2.41)$$

where $F_{n,\mathbf{k}}(z)$ is the envelope function of the specific subband considered. Fig. 4.8 presents the calculated form factors used throughout the examples presented above.

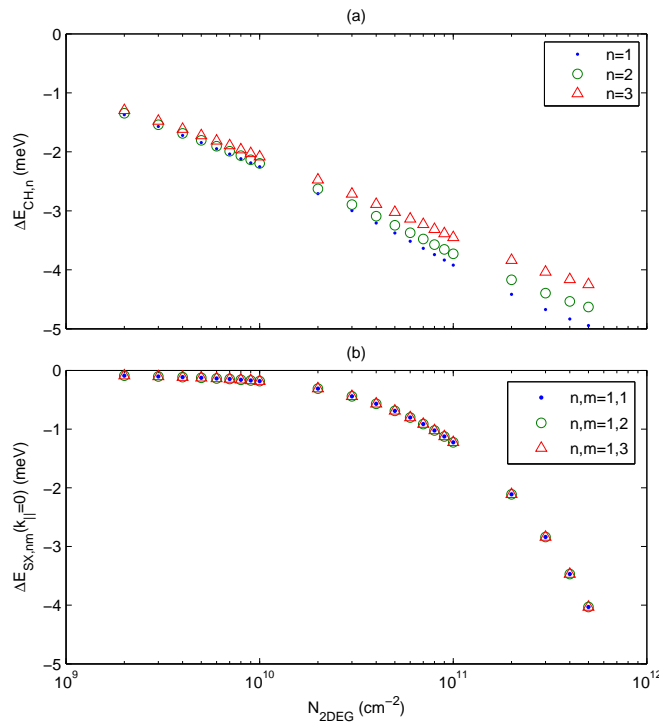


Figure 4.5: Calculated (a) Coulomb-hole self energy and (b) screened-exchange shift energy at the Brillouin zone center ($k_t = 0$), for the 200 \AA wide $\text{GaAs}/\text{Ga}_{0.9}\text{Al}_{0.1}\text{As}$ well with various 2DEG concentrations for various conduction and valence subbands.

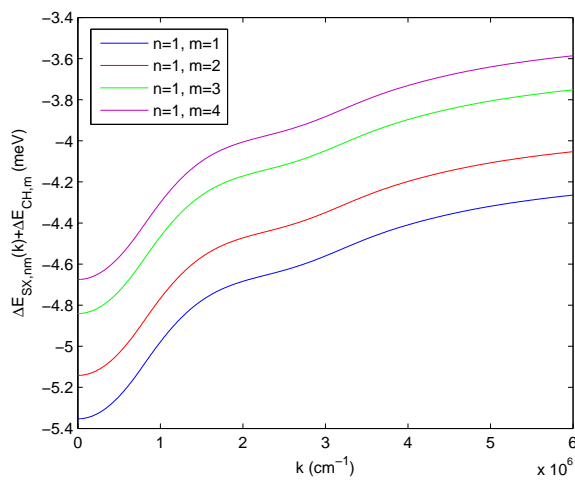


Figure 4.6: The bandgap renormalization dispersion for the various subband transitions calculated for the 200 \AA wide $\text{GaAs}/\text{Ga}_{0.9}\text{Al}_{0.1}\text{As}$ well with $n_e = 1 \times 10^{11} \text{ cm}^{-2}$.

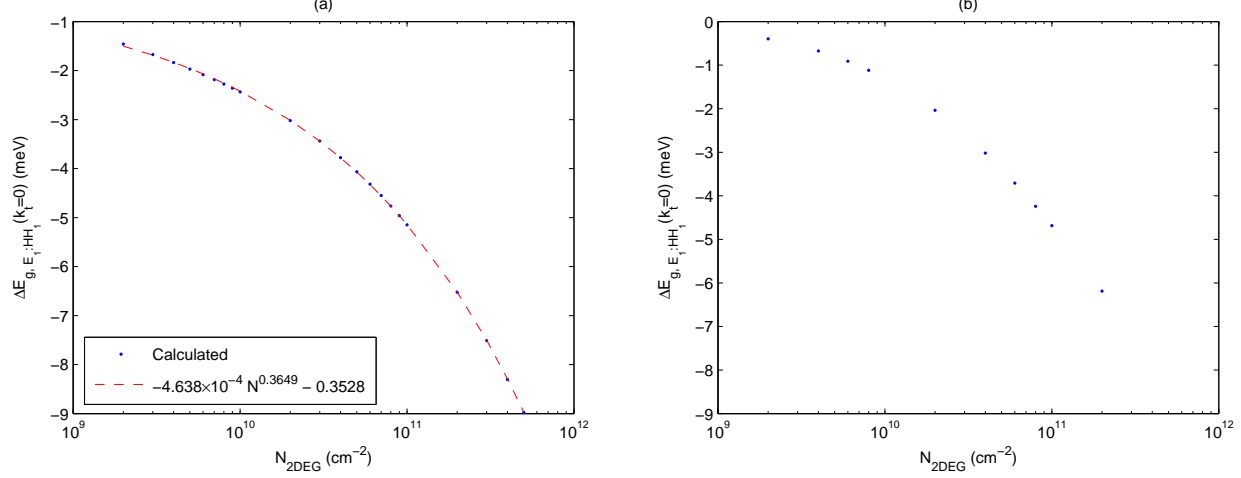


Figure 4.7: The total bandgap renormalization at the Brillouin zone center ($k_t = 0$), for the 200\AA wide $\text{GaAs}/\text{Ga}_{0.9}\text{Al}_{0.1}\text{As}$ well with various 2DEG concentrations for the $E_1 - \text{HH}_1$ transition for (a) $T = 2\text{ K}$ and (b) $T = 77\text{ K}$ ambient temperatures. The blue dots denote the calculated values while the red dashed curve in (a) is the result of an exponential fit (where the fitted function is given in the legend box).

With the knowledge of these terms, we can now concentrate on (4.2.33). The last difficulty resides in $\Omega_{\mathbf{k}}(z, t)$. The first step is to eliminate the rapidly varying phase factor from $p_{nm,\mathbf{k}}$ and to work with $s_{nm,\mathbf{k}}$ as in (4.2.28)

$$\begin{aligned} \frac{d}{dt}s_{nm,\mathbf{k}} &= -(i(\tilde{\omega}_{n,m}(\mathbf{k}) - \nu) + \gamma)s_{nm,\mathbf{k}} - \frac{i}{\hbar}\mu_{\mathbf{k}}\frac{E(z)}{2}w_{\mathbf{k}} \\ &\quad - \frac{i}{\hbar}w_{\mathbf{k}}\sum_{\mathbf{k} \neq \mathbf{k}'}\Theta_{s,\mathbf{q}}^{n,m}s_{nm,\mathbf{k}'}, \end{aligned} \quad (4.2.42)$$

where we defined $w_{\mathbf{k}} = f_{ek}^n + f_{hk}^m - 1$. To obtain susceptibility spectrum of a medium, (4.2.42) is solved for the steady state (as in the previous section), which leads to

$$s_{nm,\mathbf{k}} = -\frac{i}{\hbar}\frac{w_{\mathbf{k}}\mu_{\mathbf{k}}}{i(\tilde{\omega}_{n,m}(\mathbf{k}) - \nu) + \gamma}\left(\frac{E(z)}{2} + \frac{1}{\mu_{\mathbf{k}}}\sum_{\mathbf{k} \neq \mathbf{k}'}\Theta_{s,\mathbf{q}}^{n,m}s_{nm,\mathbf{k}'}\right). \quad (4.2.43)$$

We define two new variables, the \mathbf{k} -dependent complex susceptibility function

$$\chi_{\mathbf{k}}^0 = -\Lambda_{nm,\mathbf{k}}\mu_{\mathbf{k}}, \quad (4.2.44)$$

and the Coulomb enhancement factor

$$\Gamma_{\mathbf{k}}^{n,m} = \frac{\lambda_{nm,\mathbf{k}}}{\chi_{\mathbf{k}}^0}, \quad (4.2.45)$$

where $\Lambda_{nm,\mathbf{k}}$ and $\lambda_{nm,\mathbf{k}}$ where defined in the previous section. Substituting these two expressions into (4.2.43) we obtain

$$\Gamma_{\mathbf{k}}^{n,m}(\nu) = 1 + \frac{1}{\mu_{\mathbf{k}}}\sum_{\mathbf{k} \neq \mathbf{k}'}\Theta_{s,\mathbf{q}}^{n,m}\chi_{\mathbf{k}'}^0\Gamma_{\mathbf{k}'}^{n,m}(\nu). \quad (4.2.46)$$

We consider the last part of this equation and transfor the sum over \mathbf{k}' into an integral as before. Furthermore, we assume that the microscopic polarization $p_{nm,\mathbf{k}}$ has no angular dependence

$$\frac{1}{\mu_{\mathbf{k}}}\sum_{\mathbf{k} \neq \mathbf{k}'}\Theta_{s,\mathbf{q}}^{n,m}\chi_{\mathbf{k}'}^0\Gamma_{\mathbf{k}'}^{n,m}(\nu) = \frac{1}{\mu_{\mathbf{k}}}\int_0^\infty dk' \varepsilon_{k,k'}\chi_{k'}^0\Gamma_{k'}^{n,m}(\nu), \quad (4.2.47)$$

where

$$\varepsilon_{k,k'} = \frac{e^2}{2\pi^2\epsilon_r}k' \int_0^{2\pi} d\theta' \frac{G_{\mathbf{q}}^{n,m}}{q\epsilon(q)}. \quad (4.2.48)$$

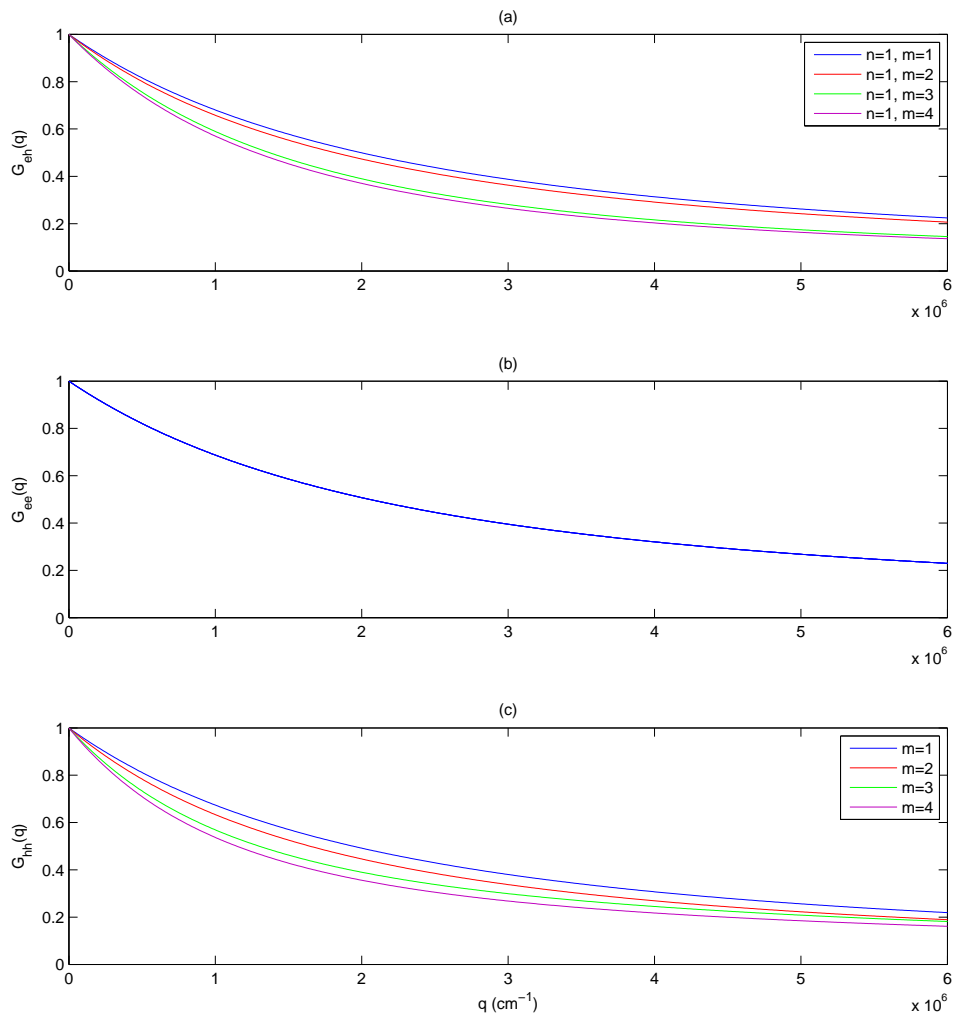


Figure 4.8: Calculated form factors for the (a) electron-hole, (b) electron-electron and (c) hole-hole combinations.

Inserting (4.2.47) into (4.2.46), we obtain

$$\Gamma_k^{n,m}(\nu) = 1 + \frac{1}{\mu_k} \int_0^\infty dk' \varepsilon_{k,k'} \chi_{k'}^0 \Gamma_{k'}^{n,m}(\nu). \quad (4.2.49)$$

Various approaches exist in the literature to solve this self-consistent equation [30, 42]. We choose to use the most general matrix inversion method, in-spite of its tendency to be rater resource consuming, as apposed to various approximate methods (such as Pade and the dominant momentum methods). To this end we approximate the integral over the k space by a sum of trapezoidal areas and discretize k and k' with n values and constant step size Δk^2 . Eq. (4.2.49) can thus be written in a matrix form

$$\mathbf{M} \cdot \Gamma_{\mathbf{k}}^{n,m} = \mathbf{1}, \quad (4.2.50)$$

with

$$\Gamma_{\mathbf{k}}^{n,m} = (\Gamma_{k_1}^{n,m}, \Gamma_{k_2}^{n,m}, \dots, \Gamma_{k_n}^{n,m})^T \quad (4.2.51)$$

and

$$\mathbf{M} = \begin{pmatrix} 1 - \frac{\Delta_k}{\mu_{k_1}} \varepsilon_{k_1, k'_1} \chi_{k'_1}^0 & -\frac{\Delta_k}{\mu_{k_1}} \varepsilon_{k_1, k'_2} \chi_{k'_2}^0 & \cdots & -\frac{\Delta_k}{\mu_{k_1}} \varepsilon_{k_1, k'_n} \chi_{k'_n}^0 \\ -\frac{\Delta_k}{\mu_{k_1}} \varepsilon_{k_1, k'_1} \chi_{k'_1}^0 & 1 - \frac{\Delta_k}{\mu_{k_2}} \varepsilon_{k_2, k'_2} \chi_{k'_2}^0 & \cdots & -\frac{\Delta_k}{\mu_{k_2}} \varepsilon_{k_2, k'_n} \chi_{k'_n}^0 \\ \vdots & \vdots & \ddots & \vdots \\ -\frac{\Delta_k}{\mu_{k_n}} \varepsilon_{k_n, k'_1} \chi_{k'_1}^0 & -\frac{\Delta_k}{\mu_{k_n}} \varepsilon_{k_n, k'_2} \chi_{k'_2}^0 & \cdots & 1 - \frac{\Delta_k}{\mu_{k_n}} \varepsilon_{k_n, k'_n} \chi_{k'_n}^0 \end{pmatrix}. \quad (4.2.52)$$

Eq. (4.2.50) can now be solved using standard mathematical methods to obtain $\Gamma_{\mathbf{k}}^{n,m}$. The microscopic polarization can be obtain using

$$p_{nm,\mathbf{k}} = \frac{1}{2} e^{-i(k_0 z - \nu t - \phi(z))} E(z) \chi_k^0 \Gamma_k^{n,m}. \quad (4.2.53)$$

Inserting (4.2.53) into (4.2.32) and using the definitions in chapter 3, (3.2.15) and (3.3.6), we can write the expressions for the absorption (or the gain amplitude) and spontaneous emission spectra

$$\begin{aligned} \alpha_{HF}(\nu) &= -\Im \left\{ \frac{i\nu}{\hbar c \epsilon_0 n_b \pi \mathcal{L}} \sum_{n,m,\mathbf{k}} |\mu_{nm,\mathbf{k}}|^2 \frac{w_{\mathbf{k}}}{i(\tilde{\omega}_{n,m}(\mathbf{k}) - \nu) + \gamma} \Gamma_{\mathbf{k}}^{n,m}(\nu) \right\} \\ &= -\Im \left\{ \frac{i\nu}{\hbar c \epsilon_0 n_b \pi \mathcal{L}} \sum_{n,m} \int_0^\infty dk k |\mu_{nm,\mathbf{k}}|^2 \frac{w_k}{i(\tilde{\omega}_{n,m}(\mathbf{k}) - \nu) + \gamma} \Gamma_{\mathbf{k}}^{n,m}(\nu) \right\} \end{aligned} \quad (4.2.54)$$

and

$$r_{sp,HF}(\nu) = -\frac{n_b^2 (\hbar \nu)^2}{\pi^2 \hbar^3 c^2} \frac{1}{1 - \exp((\hbar \nu - (E_{Fc} - E_{Fv})) / k_B T)} \alpha_{HF}(\nu), \quad (4.2.55)$$

where $\Gamma_{\mathbf{k}}^{n,m}(\nu)$ are the solution of (4.2.50), $\tilde{\omega}_{n,m}(\mathbf{k})$ is the renormalized bandgap defined in (4.2.26), and \mathcal{L} is the length if the 2D quantum structure.

In this chapter we have discussed the screened Hartree-Fock approximation and its consequences for the absorption spectra. It represents a simple model which accounts for the plasma screening but not for the particle collisions. As a next level of complication, next higher level of approximations can be computed referred to as Coulomb correlations. The main advantage of this model is the elimination of the phenomenological modeling of the microscopic polarization decay through the use of γ parameter. On the other hand, this model much more demanding computationally and thus ineffective for our purposes.

4.3 Numerical Results

In this section we present the results of the numerical modeling of sample structures using the models presented in this and previous chapters. As before, we investigate the optical properties of a 200 Å wide *GaAs* well, surrounded by *Al_{0.1}Ga_{0.9}As* barriers with δ-doped layers introduced at 1000 Å away from the barrier-well boundaries. We investigate elelctrical susceptibility, refractive index, absorption and spontaneous emission properties of this structure

²An alternative choice for Δk is to take the elements of the k vector as the support of a Gaussian quadrature [30].

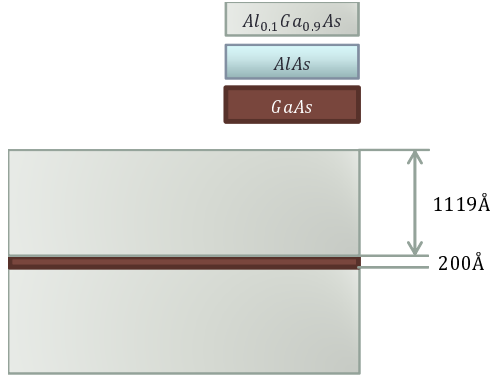


Figure 4.9: Schematic structure of the undoped QW examined in the numerical calculations. The legend for the coloring of the various layers is also given.

at various ambient temperatures and doping conditions. Along with the variation of the physical parameters of the discussed models, we investigate the influence of the various phenomenological parameters of the models on the optical properties.

For all the considered calculations throughout this chapter and the entire thesis, unless noted otherwise, the materials are assumed to have a circularly symmetric crystallographic structure along the [100] orientation. In addition, only the first conduction subband (E_1) and the first three valence subbands (HH_1 , LH_1 and HH_2) are used throughout the calculations. Finally, unless noted otherwise, the phenomenological broadening factor γ is taken to be $1 \times 10^{11} \text{ sec}^{-1}$ for all calculations. The chosen value was obtained from a comparison of the calculated spectra to the experimental linewidths for similar structures.

4.3.1 Bare Quantum Well

We start by considering the optical properties of an undoped structure, i.e. without a 2DEG presence in the well region. We model this situation by introducing holes and electrons of equal and low concentrations ($n_e = n_h = 1 \times 10^6 \text{ cm}^{-2}$) into the well region. The schematic depiction of the structure is given in fig. 4.9. We perform the susceptibility calculation for this structure for two ambient temperatures, $T = 2 \text{ K}$ and $T = 77 \text{ K}$, using the free-carrier (FCT) model, presented in chapter 3, and the screened Hartree-Fock (HF) model, presented earlier in this chapter.

Fig. 4.10 presents the calculation of the complex susceptibility χ , using equations (3.2.13), (3.2.14) and (3.2.33) of the FCT model. Calculation results for both TE and TM polarities are shown (figures (a) and (b), respectively), and for each of these the real and imaginary parts of the complex susceptibility are plotted on separate axis. The dashed vertical line marks the energetic bottom of the first conduction subband at this temperature. Fig. 4.11 present the same calculation of χ performed using equations 3.2.13, 3.2.14 and 4.2.53 of the HF model. The most striking difference between the results of the two models is the appearance of strong transition lines below and above the bandgap for the HF case. This transition lines are the direct consequence of the incorporation of Coulombic interactions into the calculation. Another prominent feature of the HF model results is the energetic shift towards the lower energies brought by the renormalization effect discussed earlier in this chapter.

Fig. 4.12 presents the calculated absorption spectra for the two polarizations. Here, the results of both models are plotted in the same scale for comparison (using equations (3.2.35) and 4.2.54 respectively for the FCT and HF models), while the insets are given to show a zoomed-in view of the high energy region of the spectra. As before, the dashed vertical lines mark the bottom of the first conduction subband. The interaction strength enhancement is clearly seen by comparing the absolute value of the absorption spectra calculated using the two models. The relative energetic shift can be also clearly seen. We can compare these results to the simplified excitonic spectral

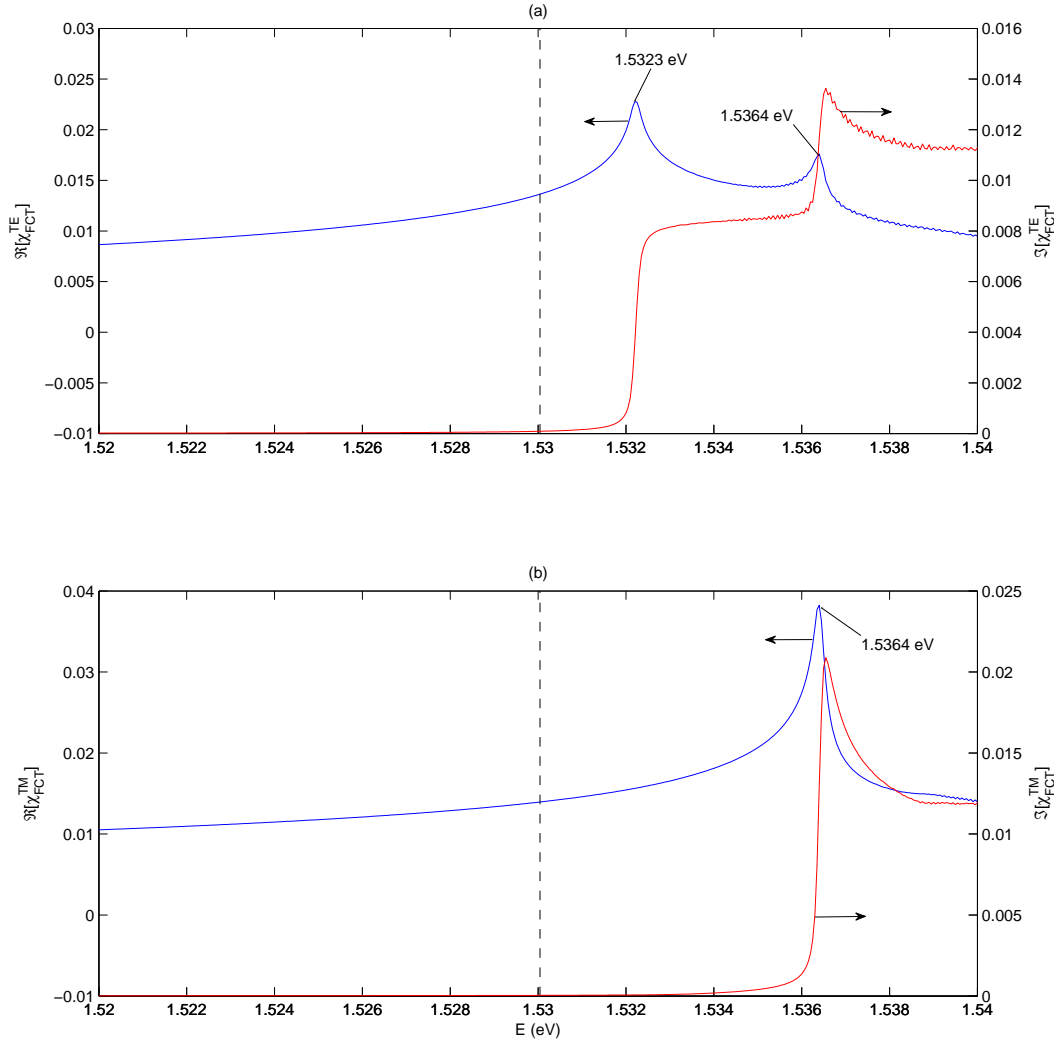


Figure 4.10: The complex elelctrical susceptibility, χ , real (blue) and imaginary (red) parts, calculated using the FCT model for the undoped well at $T = 2K$. The two plots are the (a) TE and (b) TM polarization calculations.

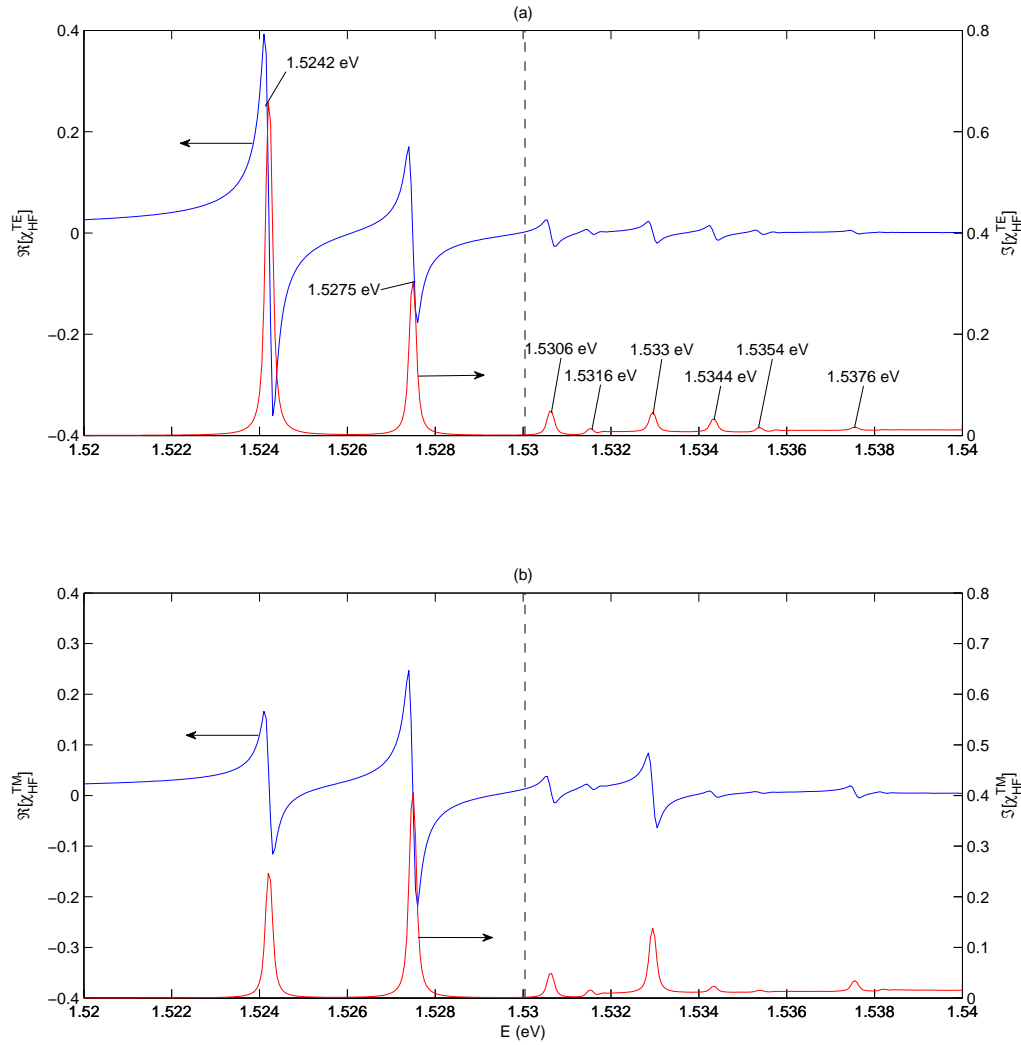


Figure 4.11: The complex eleclctrical susceptibility, χ , real (blue) and imaginary (red) parts, calculated using the HF model for the undoped well at $T = 2K$. The two plots are the (a) TE and (b) TM polarization calculations.

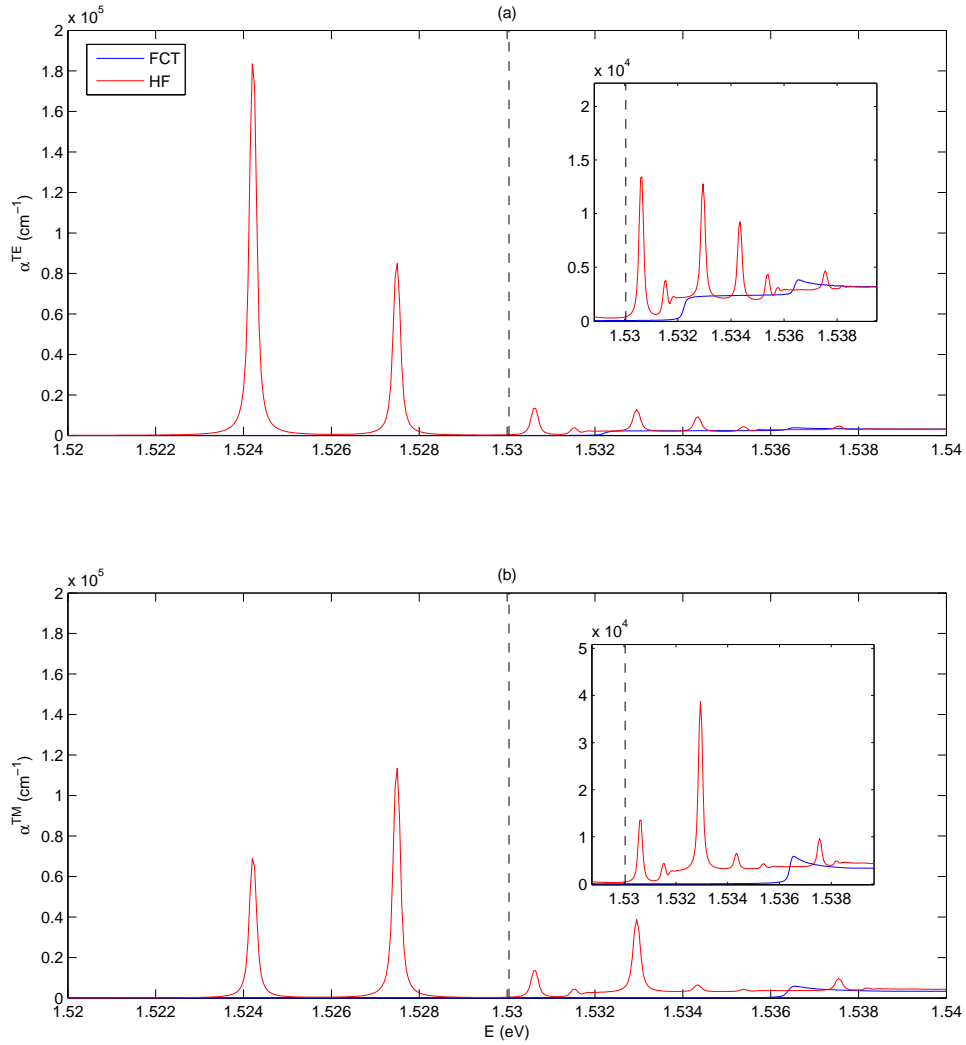


Figure 4.12: The absorption spectra for the (a) TE and (b) TM polarizations, calculated using the FCT (blue) and HF (red) models for the undoped well at $T = 2\text{K}$.

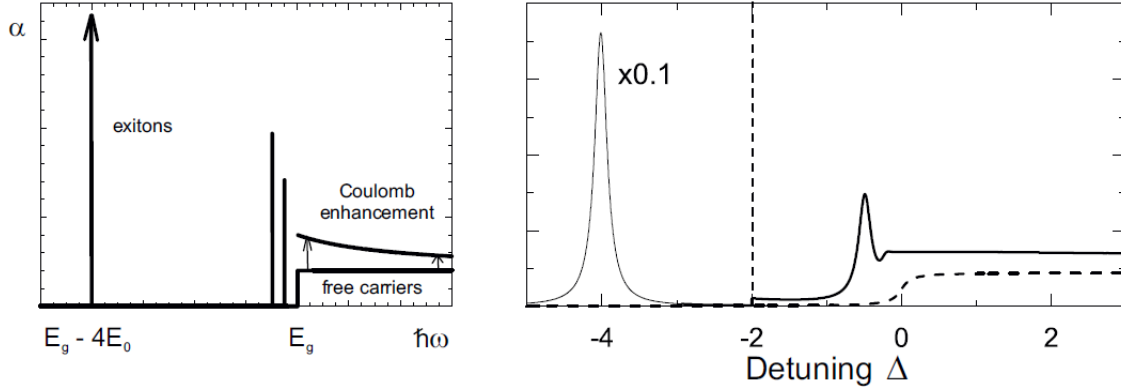


Figure 4.13: Schematic (left) and calculated (right) band edge absorption spectrum for a 2D semiconductor. Shown are the results obtained with and without including the Coulomb interaction. The first exciton in the computed absorption spectra has been scaled by a factor of 0.1 (after [30]).

theory presented extensively in literature. For the 2D case, the electrical susceptibility can be written as [30]

$$\begin{aligned} \chi(\nu) &= -\frac{|\mu_{eh}|^2}{\mathcal{L}\pi a_0^2 E_0} \left[\sum_{n=0}^{\infty} \frac{2}{(n+1/2)^3} \frac{E_0}{\hbar(\nu+i\delta)-E_g-E_n} \right. \\ &\quad \left. + \int dx \frac{xe^{\pi/x}}{\cosh(\pi/x)} \frac{E_0}{\hbar(\nu+i\delta)-E_g-E_0 x^2} \right], \end{aligned} \quad (4.3.1)$$

and the resulting absorption spectrum is given by the *Elliot formula*

$$\alpha(\nu) = \alpha_0^{2D} \frac{\hbar\nu}{E_0} \left[\sum_{n=0}^{\infty} \frac{4}{(n+1/2)^3} \delta\left(\Delta + \frac{1}{(n+1/2)^2}\right) + \Theta(\Delta) \frac{e^{\pi/\sqrt{\Delta}}}{\cosh(e^{\pi/\sqrt{\Delta}})} \right]. \quad (4.3.2)$$

where

$$\alpha_0^{2D} = \frac{4\pi^2}{\hbar n_b c} |\mu_{eh}|^2 \frac{1}{(2\pi a_0)^2} \mathcal{A}. \quad (4.3.3)$$

The term

$$C(\nu) = \frac{e^{\pi/\sqrt{\Delta}}}{\cosh(e^{\pi/\sqrt{\Delta}})} \quad (4.3.4)$$

is the Coulomb enhancement factor, which shows that the attractive Coulomb interaction not only creates the bound states but has also a pronounced influence on the ionization continuum compared to the free carrier case. A schematic and calculated absorption spectra obtained using the results above are plotted in Fig. 4.13. The influence of the Coulomb enhancement term is clearly seen in the calculated plot, when comparing the dashed (free carrier) to the solid (elliot formula) curves. The similarity between this result to our results in figure 4.12(a) can be easily seen.

The curves presented thus far are all given for both light polarizations, TE and TM, and we can easily detect the differences between the two cases. For the FC model case, the main difference is the appearance of low energy (near 1.532 eV) transition peak in the TE absorption spectrum (see figure 4.10 and 4.12) compared to the TM case. This additional transition is a result of the difference between allowed transitions for the two polarizations, as seen in figures 3.2. For the TE polarization both $E_1 - HH_1$ and $E_1 - LH_1$ are dominant for the low k_t values (which is region relevant for our calculations) compared to the single $E_1 - LH_1$ transition dominant for the TM case. In the HF model results the differences between the polarizations are mainly exhibited in the transition strength of the various lines, where the most noticeable example is the difference between the sub-bandgap transition lines. Here the energetically lowest lying line at 1.4811 eV (attributed to the $E_1 - HH_1$ transition) and the next line at 1.4843 eV (the $E_1 - LH_1$ transition) exchange their relative strength between the two polarities. This effect can be

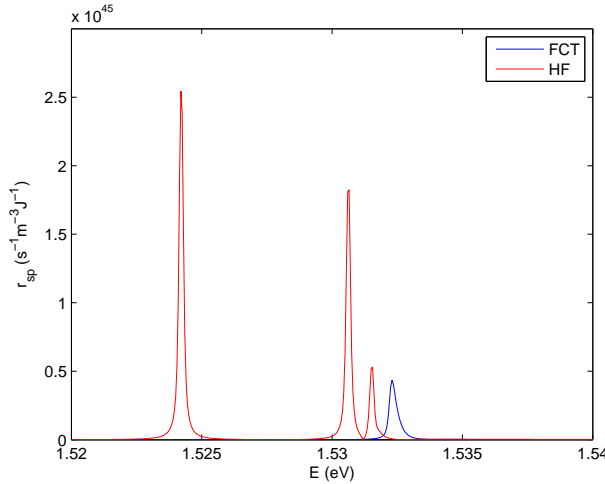


Figure 4.14: Spontaneous emission spectra calculated using the FCT (blue) and HF (red) models for the considered undoped structure at $T = 2K$.

seen also in the higher energy lines, most vividly in the insets of figure 4.12. The cause for these variations in the relative line strengths is, again, the difference between the respective inter-subband transition probabilities seen in figures 3.2 and 3.3.

Fig. 4.14 presents the calculated spontaneous emission spectra using the two models from the discussed structure. As for the absorption spectra, the results of the two discussed models are quite different. Again, the energetic shift due to the large bandgap renormalization can be seen for the HF model spectrum, together with the sharp transition peak. The results of the HF model reveal the stronger transitions compared to the FCT model results.

We now present the results of a similar calculation, performed at higher ambient temperature of $T = 77 K$, which can be seen in figures 4.15, 4.16, 4.17 and 4.18. It can be easily seen that the results are similar to the $T = 2 K$ case, but for the considerable energetic shift due to the lowering of the bandgap with temperature (see figure E.1 in appendix E). We also observe here, as for the $T = 2 K$ case, the bandgap renormalization and transition peak difference between the two discussed models.

4.3.2 Doped Quantum Well

In the previous section we have discussed in detail the calculated susceptibility and spontaneous emission spectra of a 200 \AA wide quantum wells devoid of delta doping, i.e. of two-dimensional gas. In this section we introduce a delta-doping into the cladding layers of the discussed bare quantum, which results in the introduction of 2DEG into the well. This structure is schematically described in fig. 4.19. We investigate the influence of this gas on the optical characteristics of the structure for several concentrations of the gas using the same two theoretical models. We perform the simulation for two ambient temperatures, $T = 2K$ and $T = 77K$, for 2DEG concentrations of $n_e = 2 \times 10^9 \div 4 \times 10^{11} \text{ cm}^{-2}$.

Figures 4.22 and 4.23 present the absorption spectra from the structure for the various 2DEG concentrations, respectively, for the TE and TM polarizations, calculated using the two discussed models, FCT (in blue) and HF (in red). The spectra are presented in a waterfall chart style to effectively illustrate the influence of the 2DEG. To facilitate the comparison, the curves are scaled to unity, and the scaling factor for each is indicated in the plots. As can be seen, for both models in the introduction of electron gas into the well leads to an energetic shift of towards higher energies. This phenomenon can be attributed to the phase space filling due to the introduced electrons, causing the Fermi level to shift toward higher energies. This shift can be seen clearly from fig. 4.21(a), where we present the calculated and theoretical Fermi level energy as the function of the introduces electron concentration. The absorption, occurring above the Fermi edge energy, thus moves according to this shift. Another major consequence of the rise the 2DEG concentration is the reduction of the absorption intensity, revealed best for the HF model calculations, for both polarizations. The reason of for this reduction in the strength of the resonances present in the structure is the enhanced screening effect of the 2DEG, reducing the Coulombic interaction between

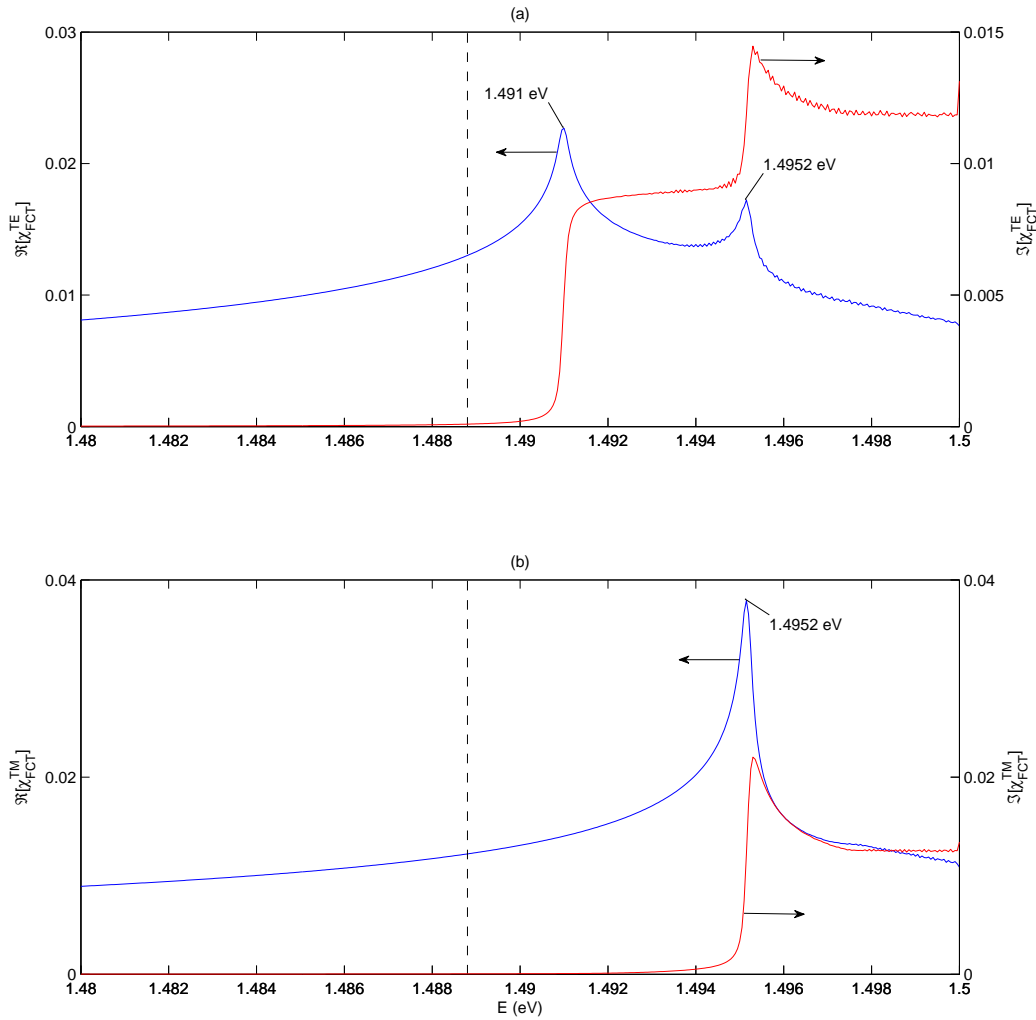


Figure 4.15: The complex elelctrical susceptibility, χ , real (blue) and imaginary (red) parts, calculated using the FCT model for the undoped well at $T = 77\text{K}$. The two plots are the (a) TE and (b) TM polarization calculations.

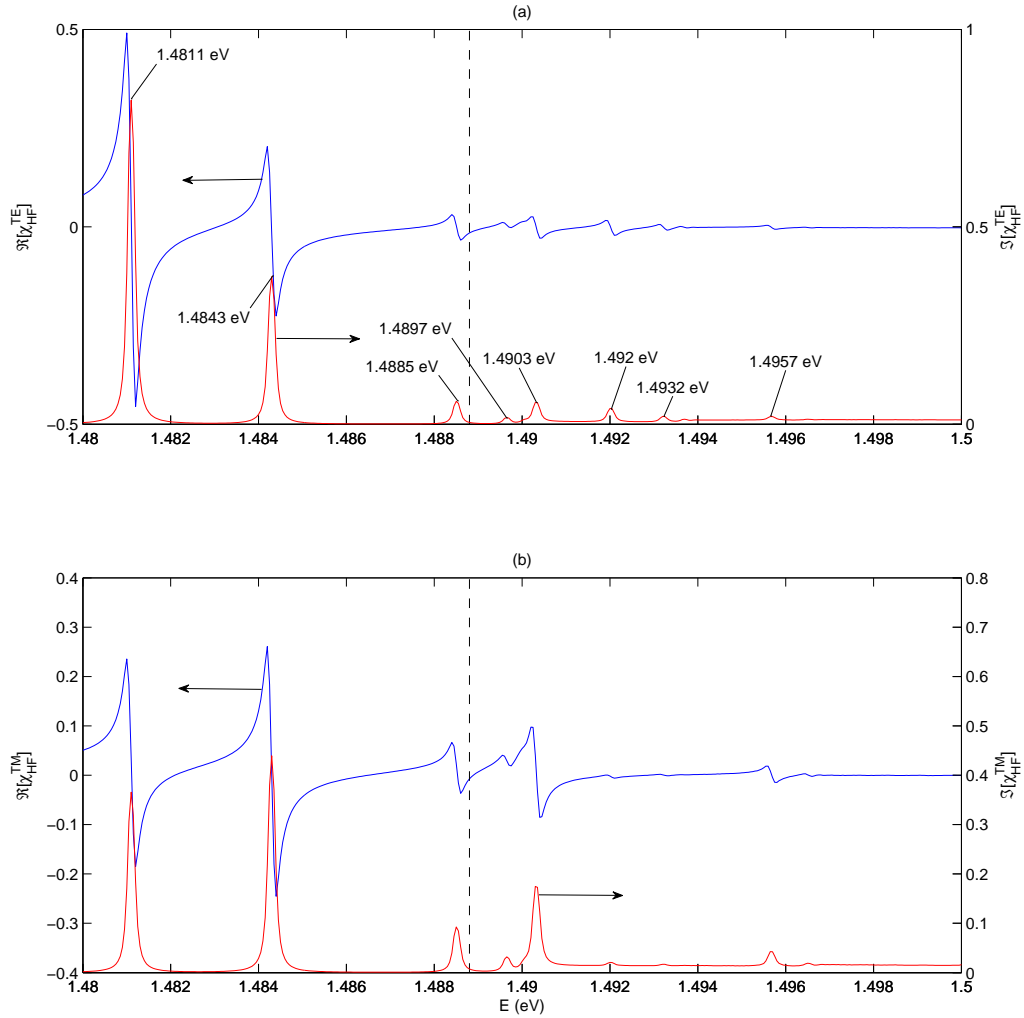


Figure 4.16: The complex elelctrical susceptibility, χ , real (blue) and imaginary (red) parts, calculated for the undoped structure using the HF mode for the undoped well at $T = 77\text{K}$. The two plots are the (a) TE and (b) TM polarization calculations.

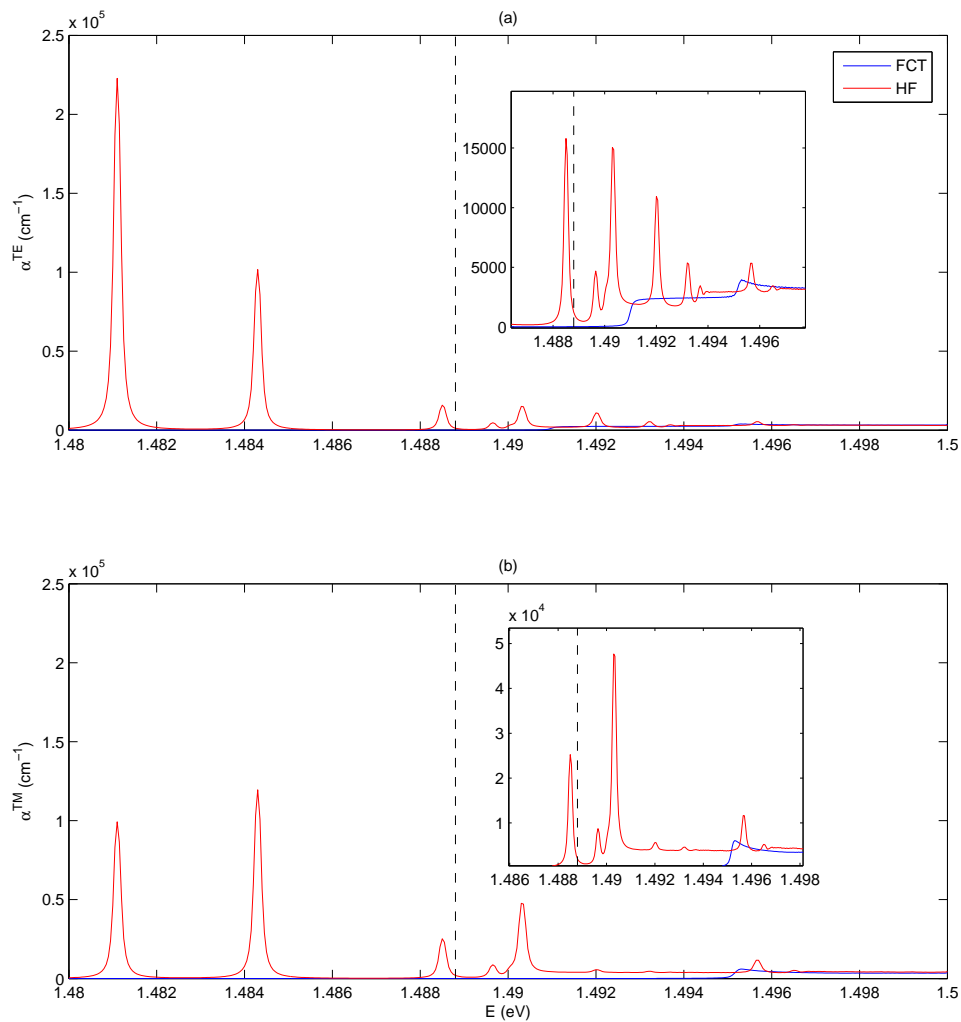


Figure 4.17: The absorption spectra for the (a) TE and (b) TM polarizations, calculated using the FCT (blue) and HF (red) models for the undoped well at $T = 77\text{K}$.

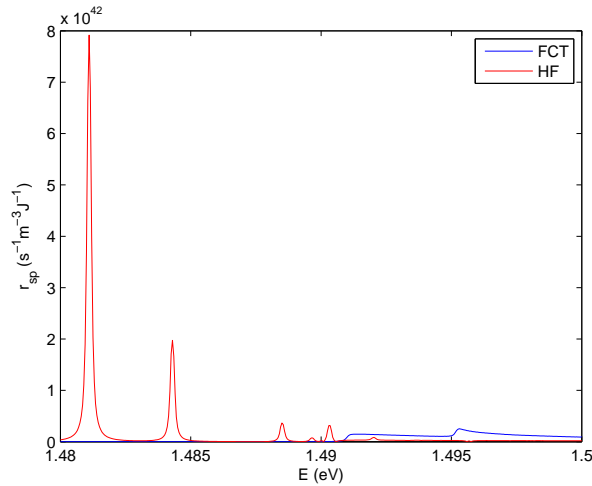


Figure 4.18: Spontaneous emission spectra calculated using the FCT (blue) and HF (red) models for the considered undoped structure at $T = 77K$.

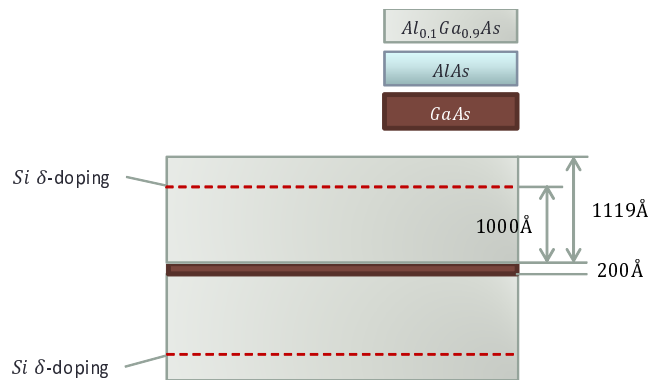


Figure 4.19: Schematic structure of the doped QW examined in the numerical calculations. The δ-doping Si atom layers are marked with the red dashed lines on the cladding layers of the structure.

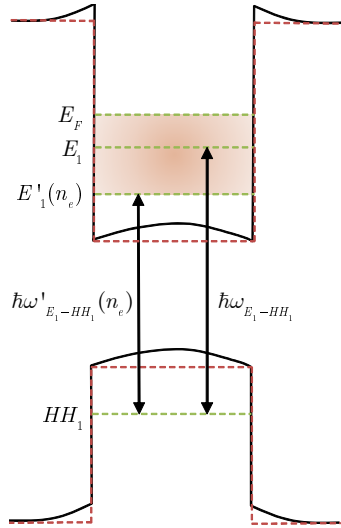


Figure 4.20: A schematic depiction of the bandgap renormalization due to the introduction of 2DEG into the well region of the structure. The band bending due to the internal electrical field is also shown. E_F stands for the Fermi level energy, E_1 is the first conduction subband of the undoped structure, $E'_1(n_e)$ is the renormalized effective first conduction subband and HH_1 is the first heavy-hole subband. The shaded blue area marks the energetic region occupied by the 2DEG.

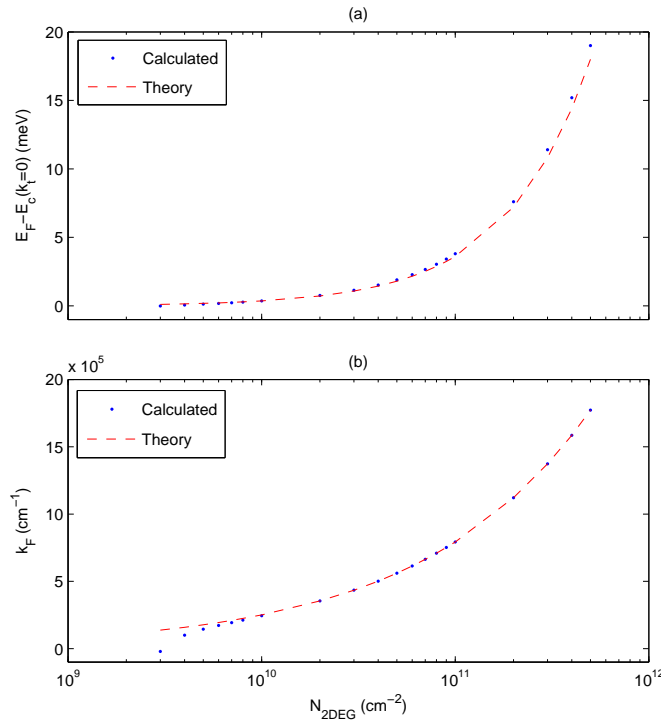


Figure 4.21: (a) The energetic gap between the Fermi energy and the bottom of the conduction band and (b) the Fermi wavevector, both as a function of the 2DEG concentration obtained using numerical calculation and the simple theoretical model presented in section 2.3.2.

the interacting conduction band electrons and valence band holes. Another contributing factor to the observed diminishing interaction are the inter-carrier collisions, introduced in both models via the phenomenological factor γ , though its influence is much weaker compared to the screening. This can be best seen for the results of the FCT calculations for which this effect is most dominant because of the absence Coulombic interaction between carriers. Here, we can clearly see a milder reduction of the interaction strength compared to the HF results. This reduction in the strength of the absorption resonance peaks, or the disappearance of the exciton transition lines, is most noticeable for 2DEG concentrations above $\sim 6 \times 10^{10} \text{ cm}^{-2}$.

The differences between the absorption spectra for the two polarizations are to the description in the previous section. For the HF model results, the main differentiating feature is the relative strength of the two dominant peaks between the two polarizations, while for the FCT model the main difference is the presence of a single peak in the TM spectrum (fig. 4.23) compared to the additional lower energy peak for the TE polarization (fig. 4.22). Finally, we can note that as for the undoped case, the Coulomb enhancement causes the spectra obtained from the HF model to be much stronger than the FCT ones, an effect not seen in the presented plots because of the relative scaling. Similar analysis may be applied to the refractive index change spectra, δn , shown for the same structure in figures 4.24 and 4.25, respectively for both polarities.

Figures 4.26 and 4.27 present a comparison between the absorption and spontaneous emission spectra, both obtained using the HF model calculation, for both polarities. We can investigate the influence of the 2DEG concentration on the spontaneous emission and compare it to the absorption. We can see that the spontaneous emission, as the absorption, changes its energetic position with the rise of the doping concentration. We have attributed the absorption peaks movement to the Fermi edge translation due to the phase space filling in the conduction band. For an undoped QW, the spontaneous emission peak location coincides with the energetic location of the first conduction subband [41]. As we can see in fig. 4.20, the bandgap renormalization, caused by the introduction of electrons inside the well, shifts this subband towards lower energies, an effect proportional to the carrier concentrations (n_e). This causes the spontaneous emission and the absorption spectra to diverge with the added carriers' concentration, an effect known as the Burstein-Moss shift (BMS) [41].

Along with the energetic shift in the peak location, there is a noticeable alteration of the lineshape and the linewidth of the spontaneous emission spectra. In these figures two noticeable spontaneous emission peaks (marked 1 and 2) are present and the change in their position and shape should be addressed. The lineshape profile of the peak together with the energetic shift pattern can be explained by considering two types of emission from the structure using fig. 4.20. It is a well known fact [43] that the emission due to the introduced external electrons (the 2DEG) stretches from the effective bandgap, denoted $E'_1(n_e)$, to the Fermi edge energy, E_F . In fig. 4.21(a) we can see the shift of the Fermi edge towards high energies, while fig. 4.7(a) shows an opposite trend of the bandgap renormalization, leading to the shift of the effective bandgap towards low energies. The combined influence of these two trends leads to an asymmetric broadening of the emission line, as is observed for peak 2 in our simulations. Here the overall shift to the lower energies can be clearly seen, together with the asymmetric broadening. Along with the energetic shift, the relative intensity of this emission peak intensified compared to peak 1, which eventually disappears for high 2DEG concentrations. Peak 1, for the entire diapason of the simulated gas concentrations, retains its symmetric lineshape and also closely follows the lower most absorption spectrum peak. Thus, we may attribute this peak to the strong excitonic resonance present for lower 2DEG concentrations, which loses its intensity because of the screening effect of the introduced electrons.

In figures 4.28 and 4.29 we give a detailed zoomed in view of the absorption and spontaneous emission spectra for 2DEG concentrations in range of $n_e = 3 \times 10^{10} \div 8 \times 10^{10} \text{ cm}^{-2}$, respectively for the TE and TM polarizations. These figures present a detailed view of the intercrossing region of the broad 2DEG induced peak and the excitonic line of the spontaneous emission. The relative intensity change can be clearly seen, where the strong excitonic line attains its dominance up to $n_e = 5.5 \times 10^{10} \text{ cm}^{-2}$, after which the 2DEG emission retains the lead. These plots also give a clear picture of the 2DEG emission asymmetric broadening, becoming larger with the 2DEG concentration. Along with the broadening, these spectra also attain a characteristic curve close to the Fermi edge energy, marked by the dotted circle at the $n_e = 6 \times 10^{10} \text{ cm}^{-2}$ curve in figure 4.28.

Figures 4.30 and 4.31 present the absorption spectra calculation using the FCT and HF models at ambient temperature $T = 77 \text{ K}$, respectively for the TE and TM polarizations. As for the $T = 2 \text{ K}$ case discussed earlier, the FCT and HF differ greatly in the lineshapes and intensities of the resonances. For both polarizations, the HF model calculation leads to the appearance of two strong spectral lines, which can be attributed to excitonic transitions. These lines maintain their form and amplitude for much of the considered 2DEG concentration values, indicating on the minor influence of the screening effect of the introduced electrons on the excitonic bonds in the

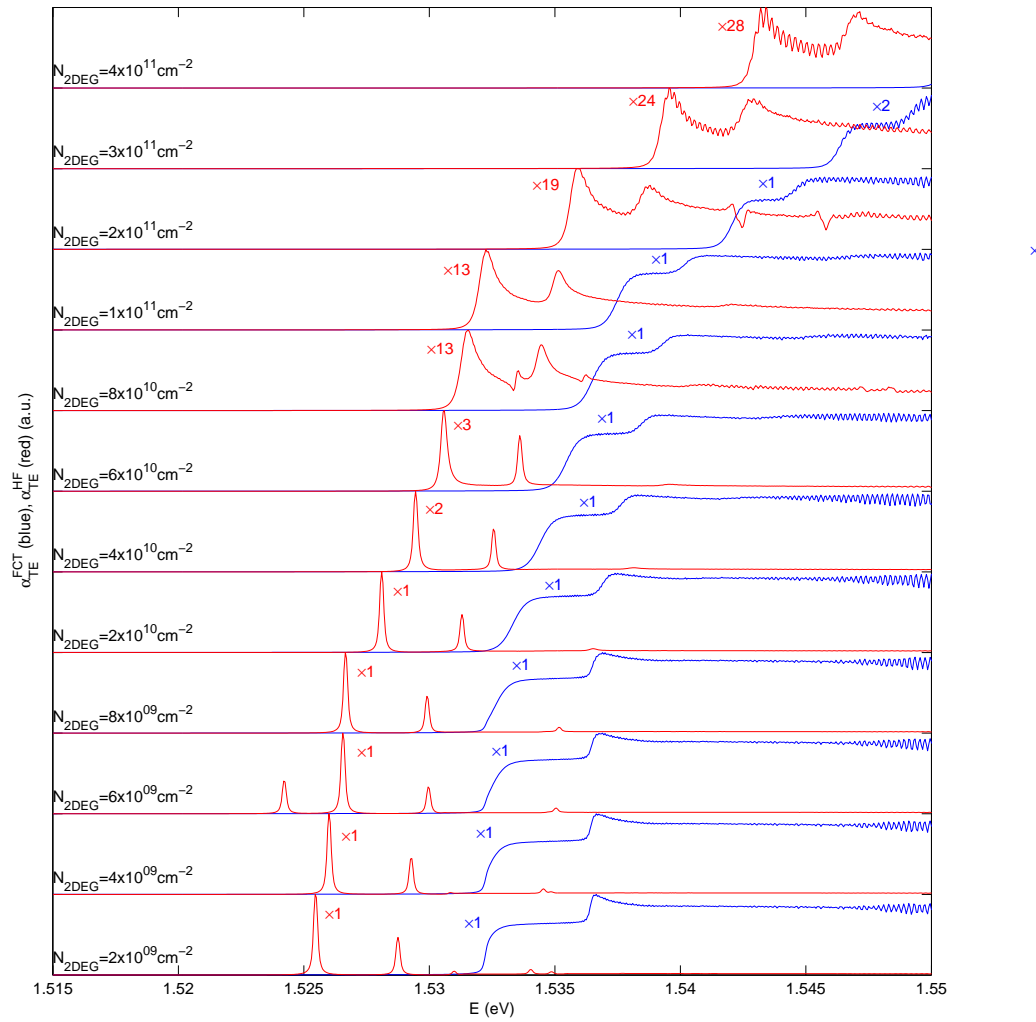


Figure 4.22: The TE polarization absorption spectra calculated for the doped structure for various gas concentrations n_e using the FCT (blue) and HF (red) models at $T = 2\text{K}$. The scaling factor is indicated in the respective color.

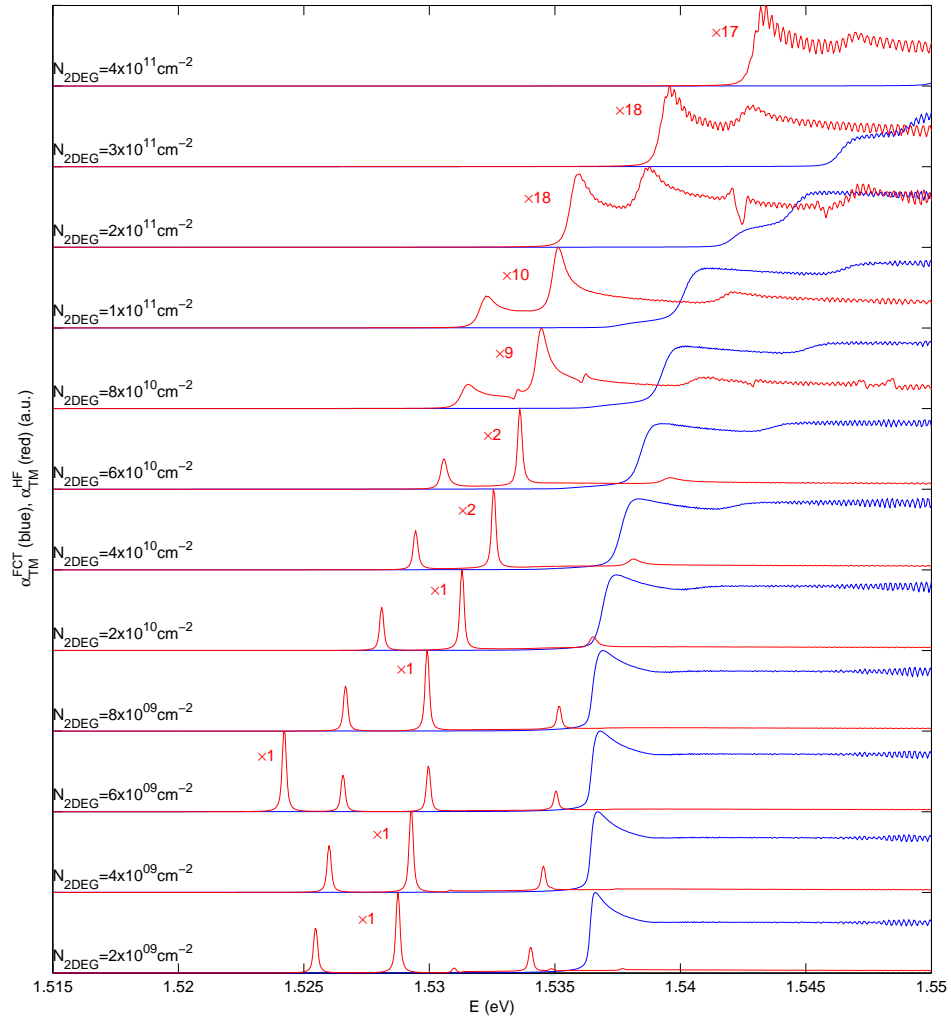


Figure 4.23: The TM polarization absorption spectra calculated for the doped structure for various gas concentrations n_e using the FCT (blue) and HF (red) models at $T = 2K$.

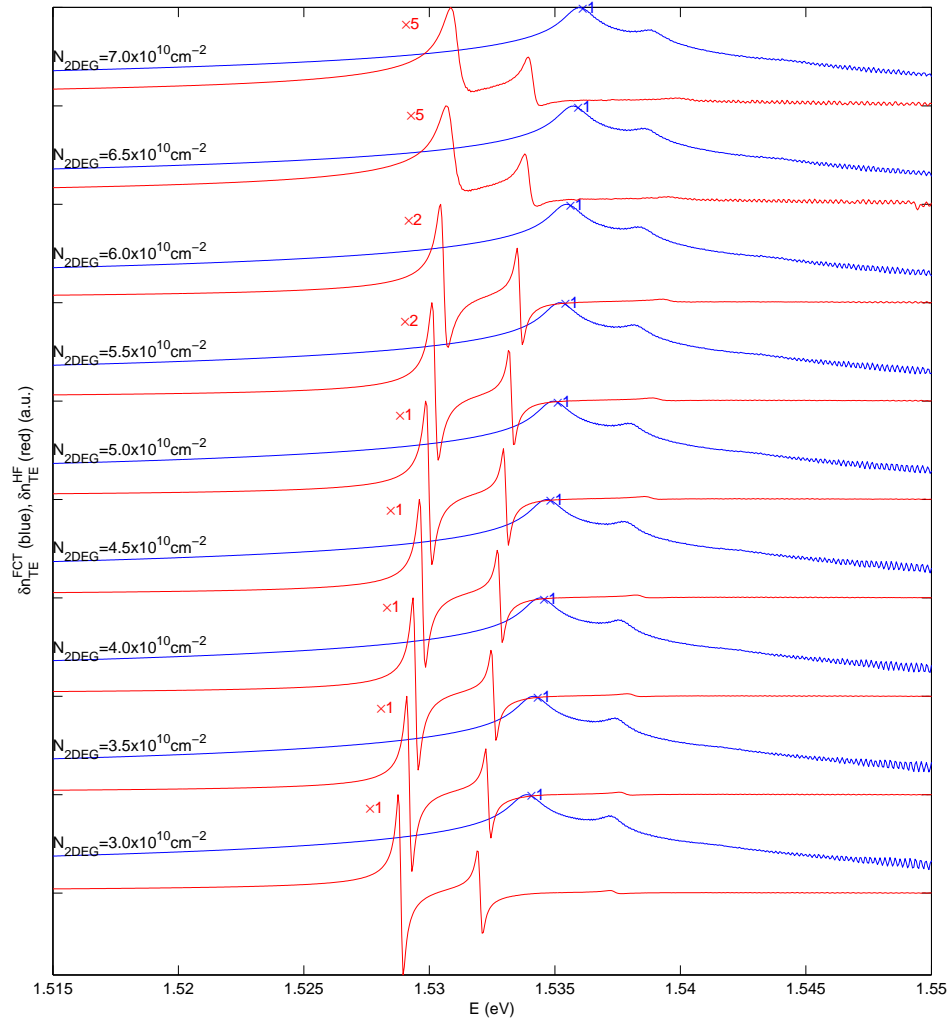


Figure 4.24: The TE refractive index change spectra calculated for the doped structure for various gas concentrations n_e using the FCT (blue) and HF (red) models at $T = 2K$.

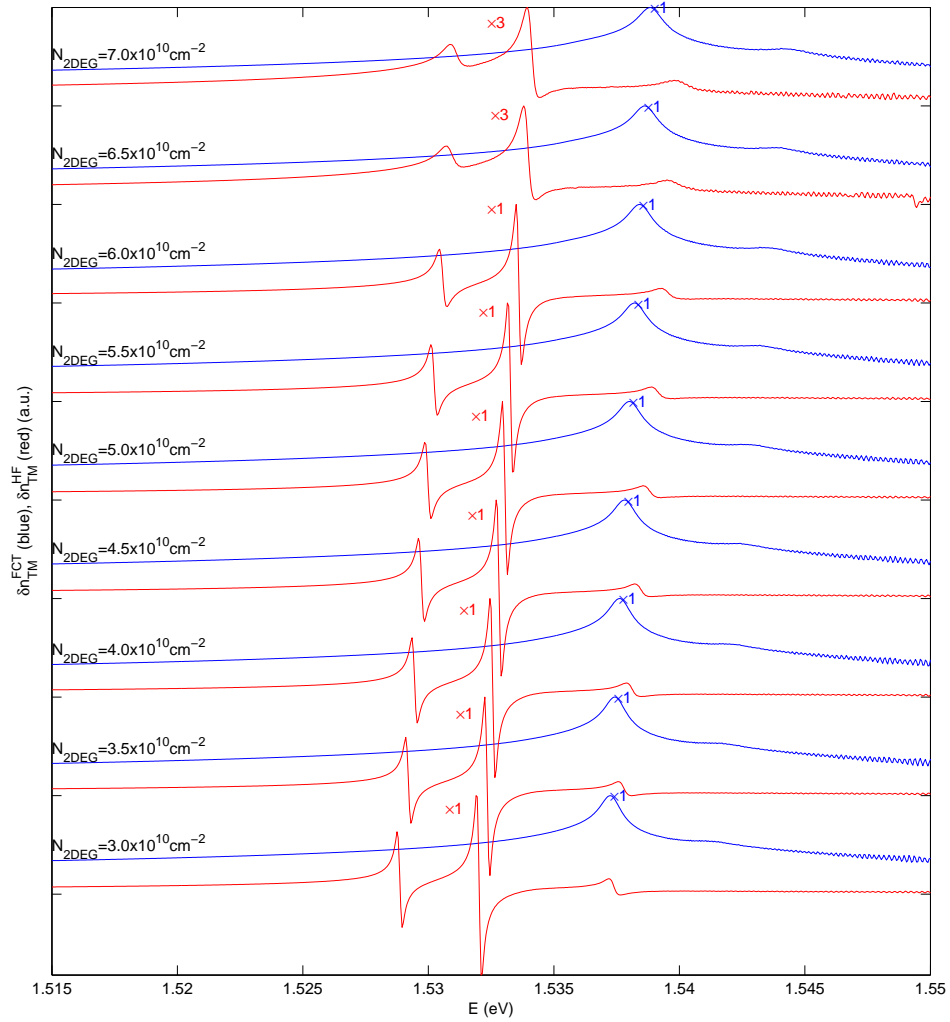


Figure 4.25: The TM refractive index change spectra calculated for the doped structure for various gas concentrations n_e using the FCT (blue) and HF (red) models at $T = 2K$.

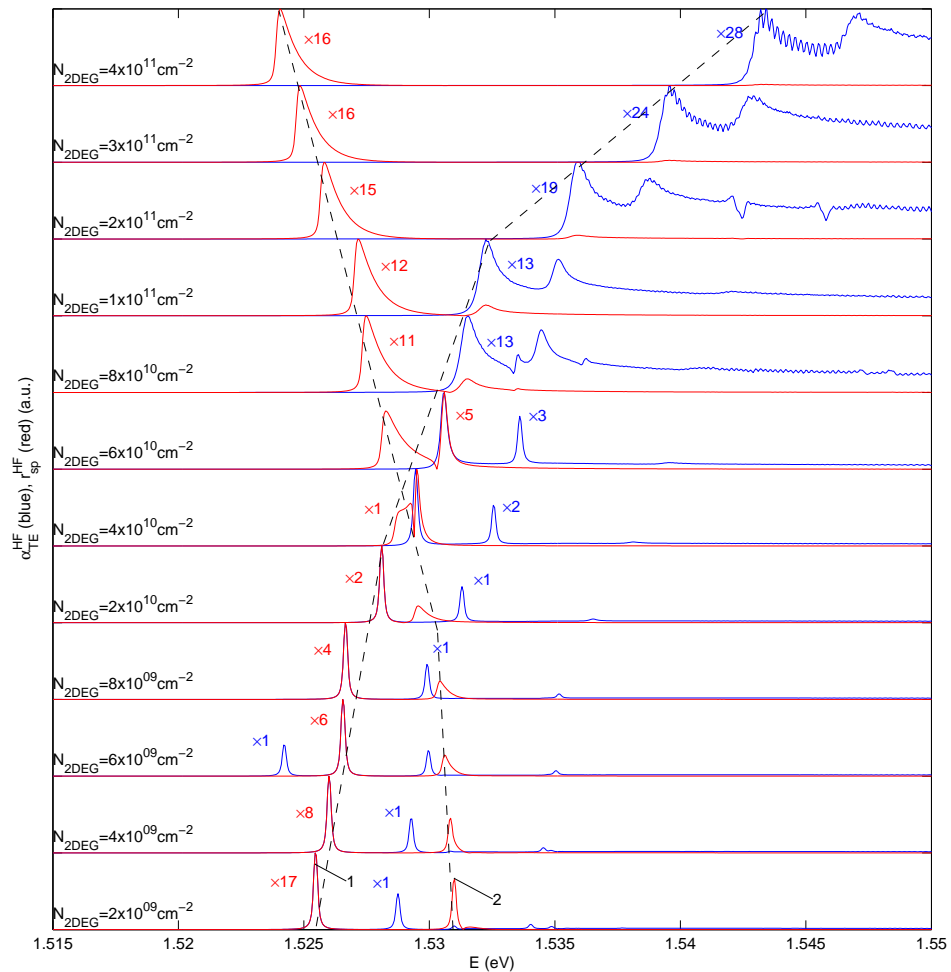


Figure 4.26: The TE polarization absorption (blue) and spontaneous emission (red) spectra calculated for the doped structure for various gas concentrations n_e using the HF model at $T = 2\text{K}$.

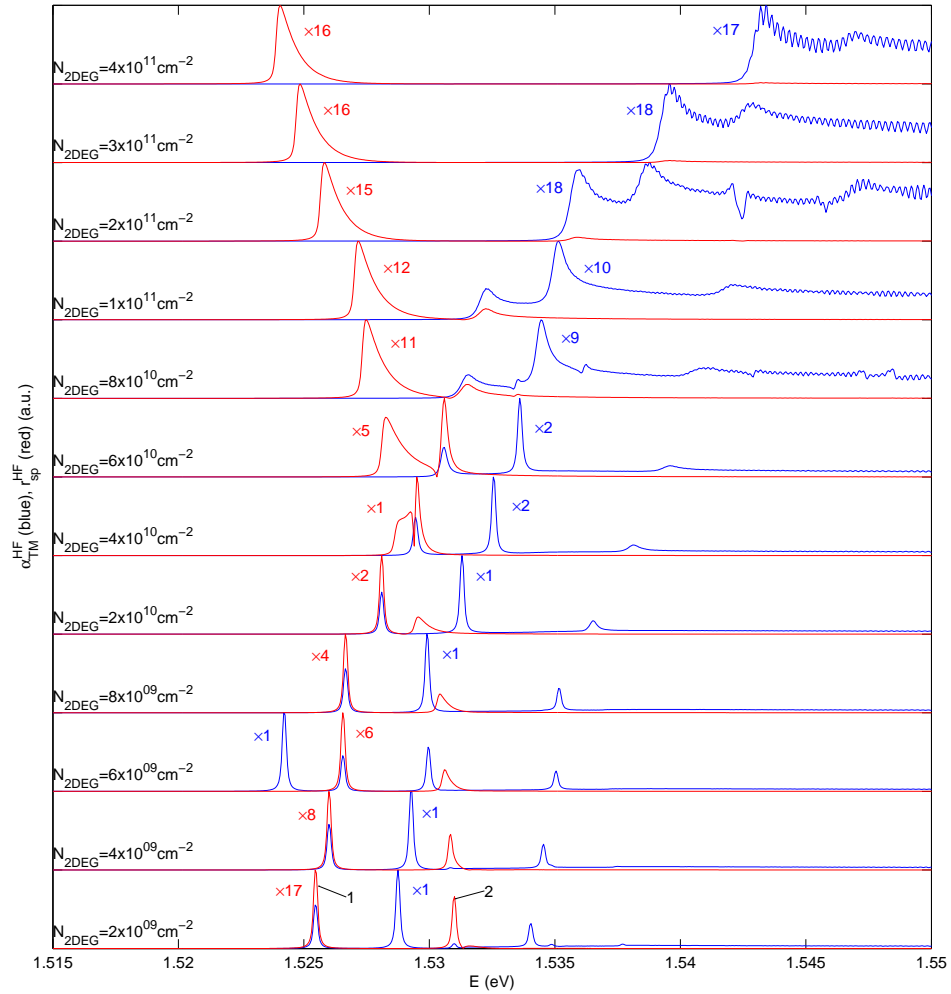


Figure 4.27: The TM polarization absorption (blue) and spontaneous emission (red) spectra calculated for the doped structure for various gas concentrations n_e using the HF model at $T = 2\text{K}$.

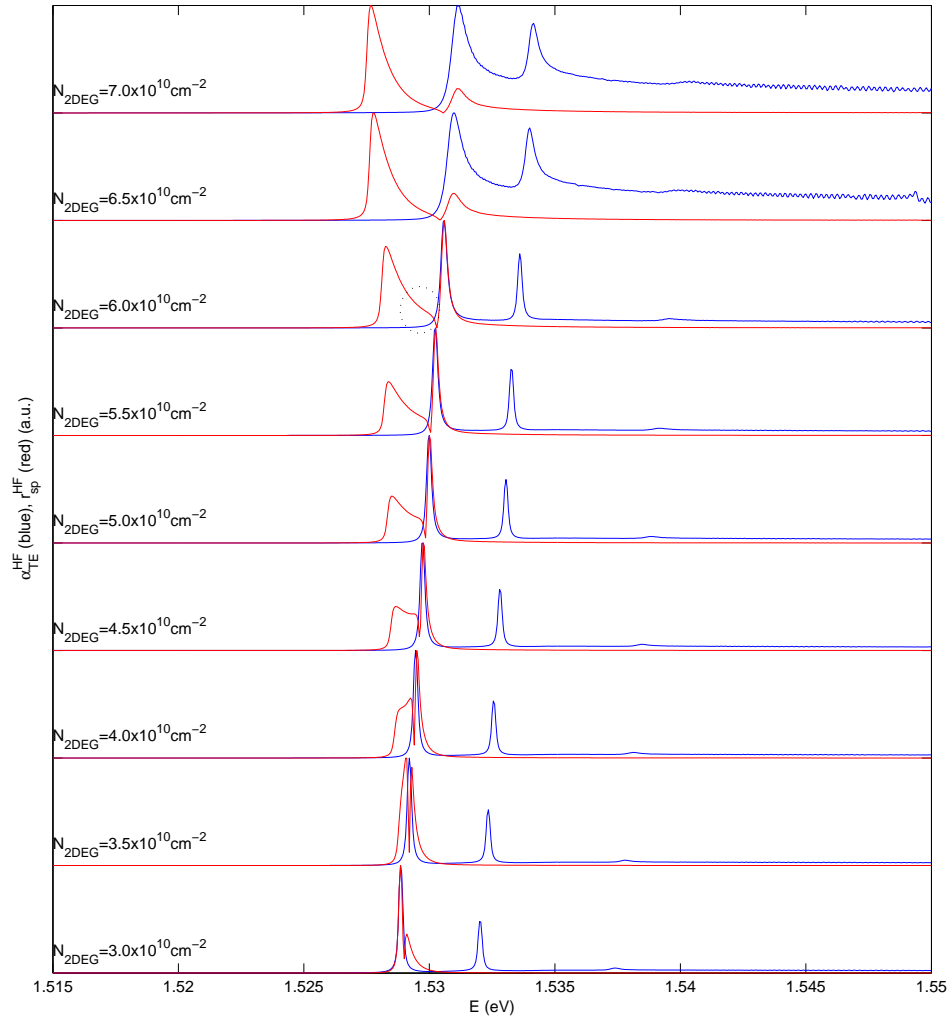


Figure 4.28: Detailed view of the transition region in the absorption (blue) and spontaneous emission (red) spectrum for the TE polarization using the HF model at $T = 2\text{K}$.

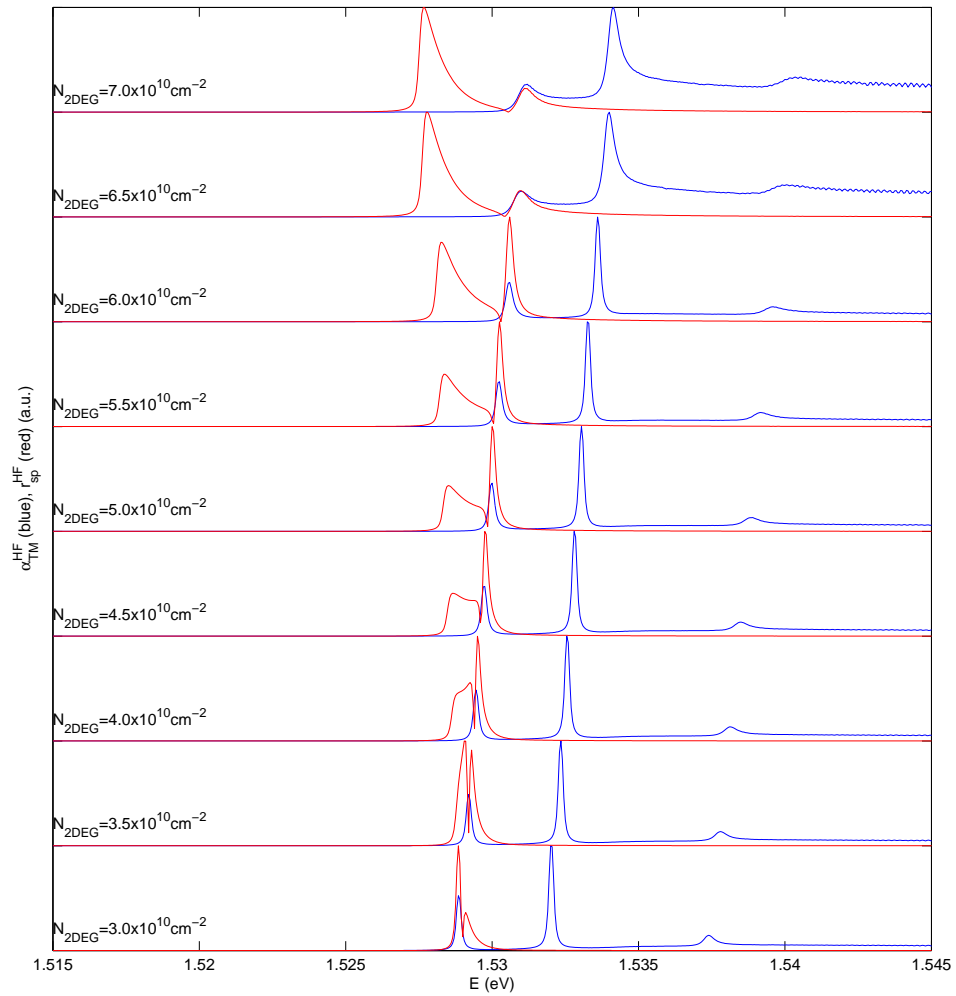


Figure 4.29: Detailed view of the transition region in the absorption (blue) and spontaneous emission (red) spectrum for the TM polarization using the HF model at $T = 2\text{K}$.

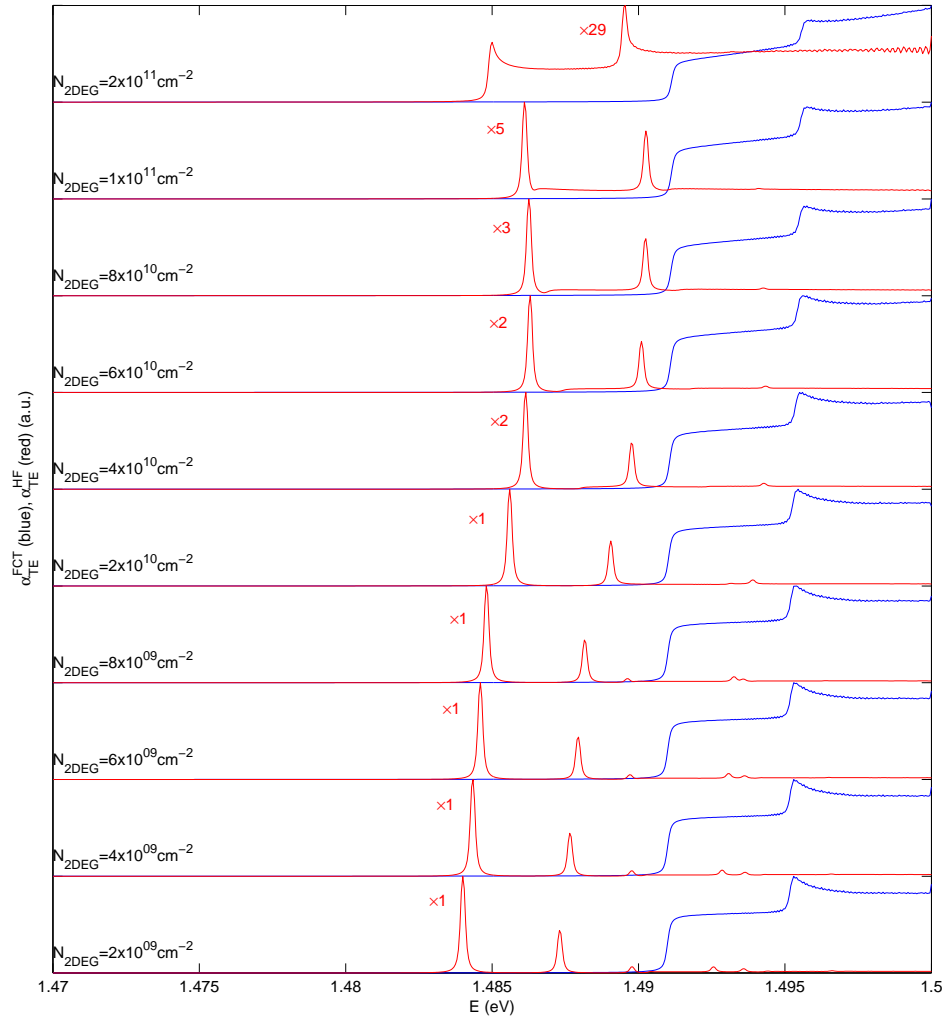


Figure 4.30: The TE polarization absorption spectra calculated for the doped structure for various gas concentrations n_e using the FCT (blue) and HF (red) models at $T = 77\text{K}$.

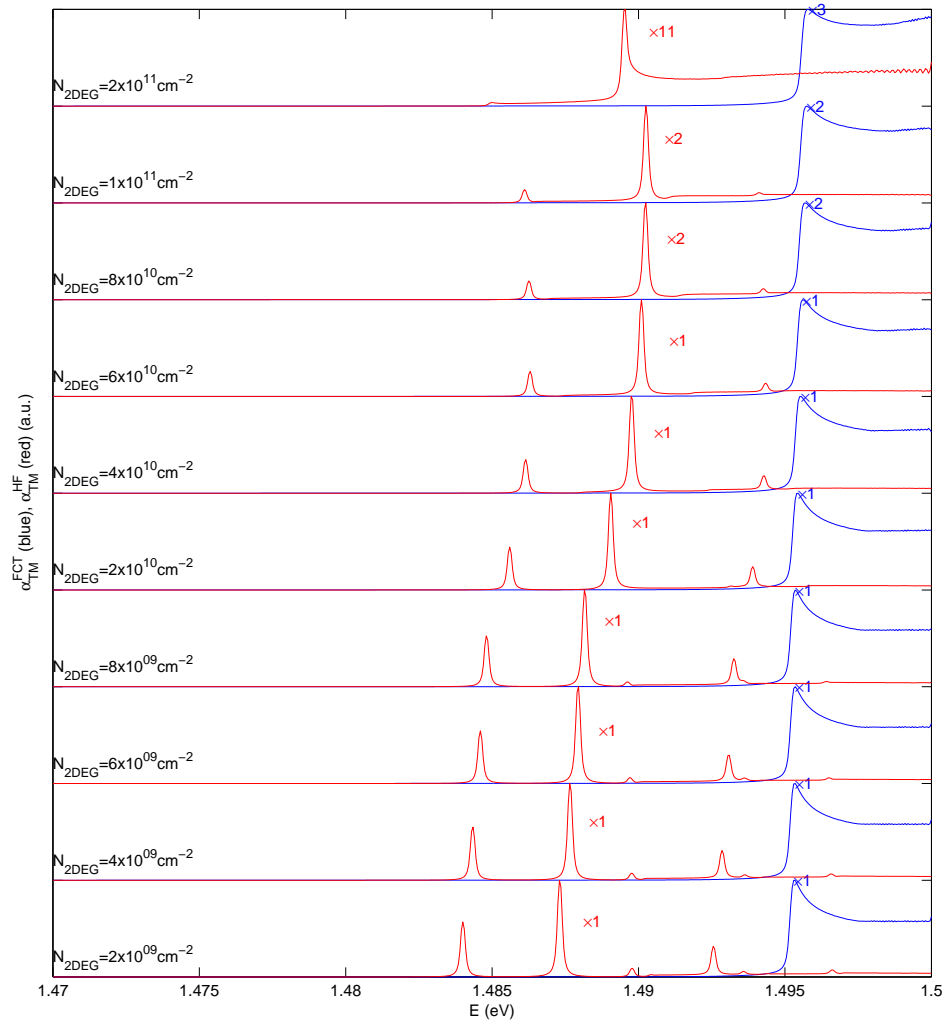


Figure 4.31: The TM polarization absorption spectra calculated for the doped structure for various gas concentrations n_e using the FCT (blue) and HF (red) models at $T = 77\text{K}$.

well, especially compared to the $T = 2\text{ K}$ case discussed earlier. Another striking difference of these curves from the $T = 2\text{ K}$ case is the relative energetic immobility of the spectral lines with 2DEG concentration, indicating to a milder effect of introduced electron on the bandgap renormalization.

Figures 4.32 and 4.33 present the absorption and spontaneous emission spectra calculated using the HF model respectively for the TE and TM polarization at ambient temperature of $T = 77\text{ K}$. The spontaneous emission spectra, like the absorption spectra, differ greatly from the results for $T = 2\text{ K}$ discussed earlier in this section. Here, two strong emission peaks are noticeable, which follow closely the excitonic absorption resonances. These line amplitudes intensify considerably with 2DEG concentration, reaching peak intensity for $n_e = 1 \times 10^{11} \text{ cm}^{-2}$, maintaining approximately the same linewidth for this entire stretch of 2DEG concentrations. At $n_e = 2 \times 10^{11} \text{ cm}^{-2}$ both the absorption and spontaneous emission spectra change in both linewidth and lineshape, indicating to a drastic reduction of the excitonic interaction.

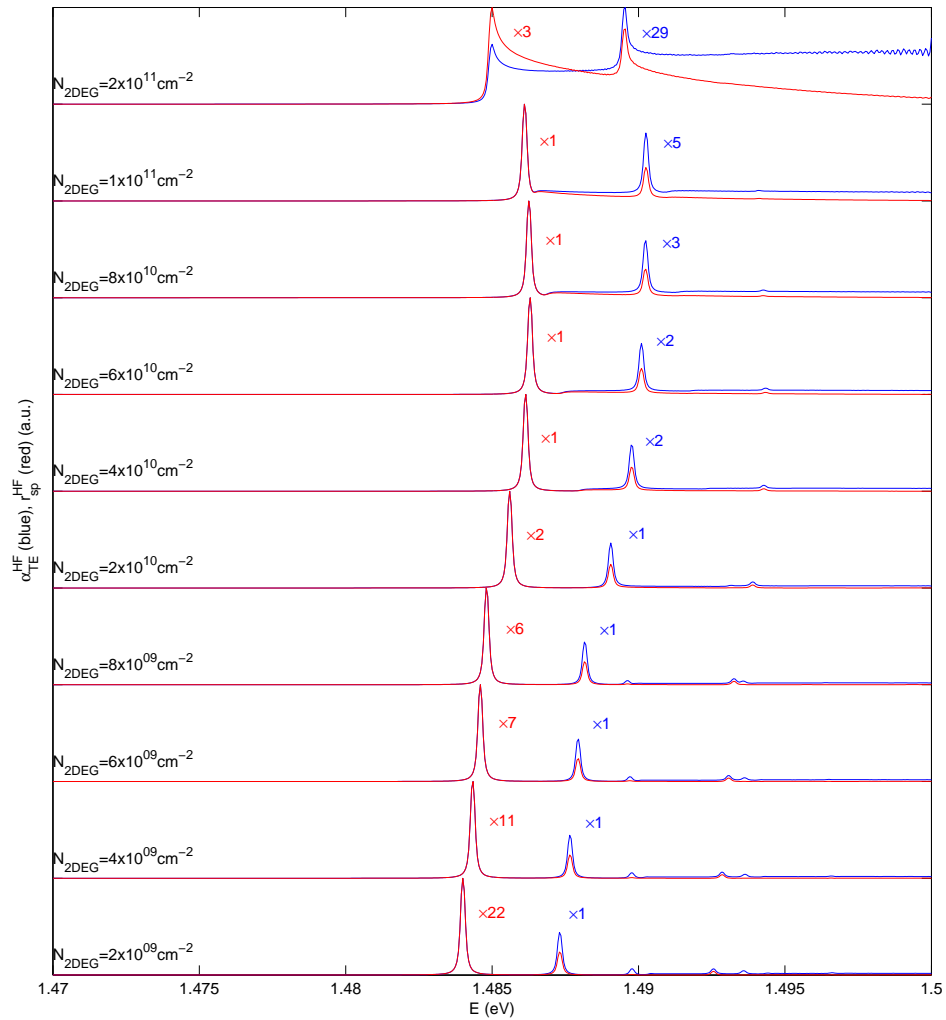


Figure 4.32: The TE polarization absorption (blue) and spontaneous emission (red) spectra calculated for the doped structure for various gas concentrations n_e using the HF model at $T = 77K$.

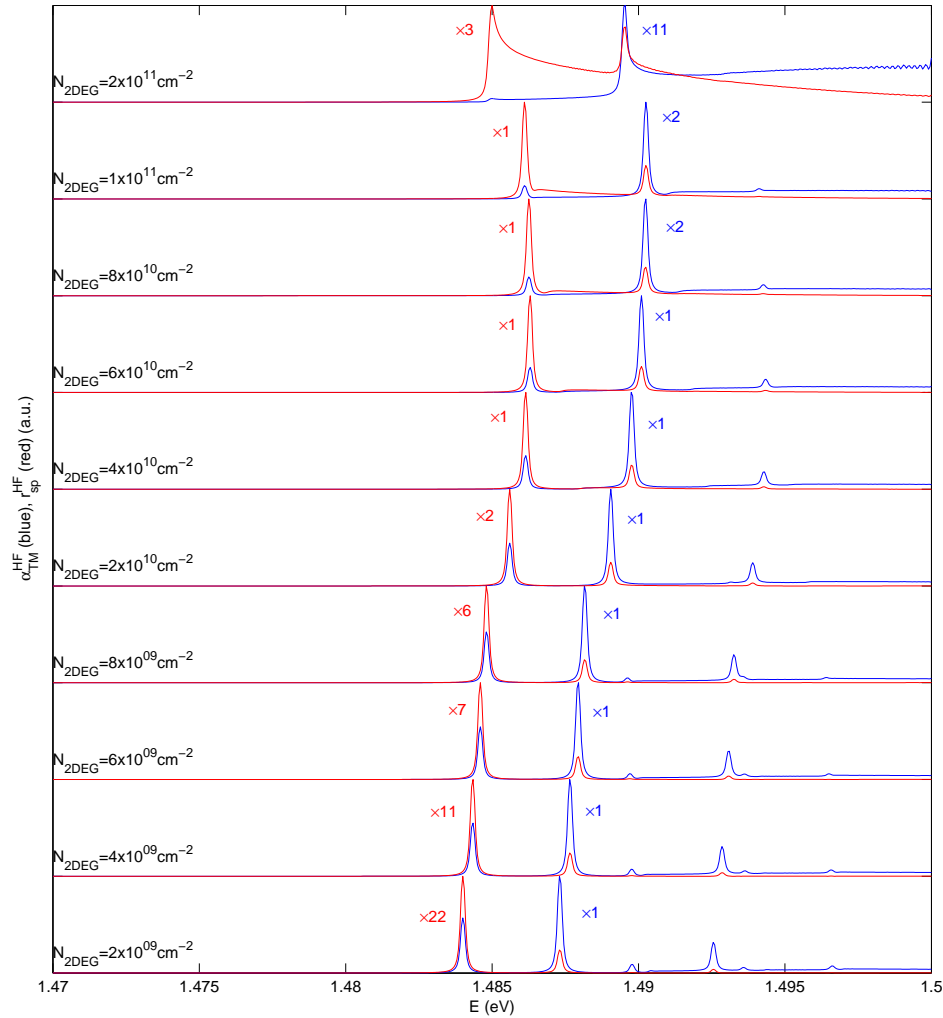


Figure 4.33: The TM polarization absorption (blue) and spontaneous emission (red) spectra calculated for the doped structure for various gas concentrations $N_{2\text{DEG}}$ using the HF model at $T = 77\text{K}$.

Chapter 5

Semiconductor Microcavities and Polaritonic Effect

In the previous two chapters, we have considered the optical properties of bare quantum wells, and the influence of the introduced 2DEG inside the cavity region. As we have seen, these structures allow efficient confinement of charge carriers in a defined region of the structure, which allows us to easily probe their electronic and optical properties. In this chapter we explore another form of confinement, namely that of electromagnetic radiation, through the use of microcavity structures consisting of a cavity layer cladded by a distributed Bragg reflector on each side. A heterostructure, such as quantum well or heterojunctions, can be embedded within the MC. Inside such a structure, the photon mode is spatially confined inside the cavity region, and when the cavity width is comparable to the wavelength of the QW resonant modes (excitons), a resonant interaction takes place. These interaction modes are termed *polaritons*, and the examination of their optical properties constitute the main objective of this chapter.

We start our discussion by giving a brief introduction to the classical theory of microcavities, by describing the optical properties of Fabri-Perot resonators, followed by a description of a distributed Bragg reflector (DBR) mirrors, and finally the introduction of semiconductor resonator built of a cavity layer cladded with two DBR mirrors. The method for the calculation of optical reflection and transmission of such structures is presented, together with the characterization of electromagnetic distribution inside the cavity region and the dispersion properties of the confined photonic mode.

Next, in order to introduce the interaction of electromagnetic field mode with a QW confine electron-hole resonance, we present simple idealized models for the interaction of a two-level electronic system with a photon mode. We complicate the model by considering multiple two-level systems interacting with the photon field mode, and then apply them to the case of semiconductor microcavities and the polaritonic modes. Here we put a special emphasis on the coupled oscillator model to describe the polariton dispersion relations.

In the last part of this chapter, we present a unified framework for the calculation of the optical properties of MCs with embedded QWs in the cavity region, obtained by combining the numerical approaches formulate in this and previous chapters. We also discuss the influence of the introduction of 2DEG into the well region of the embedded QWs and compare the results to the optical properties of bare QWs, presented in chapter 4.

5.1 Optical Resonator

An optical resonator is a device used for confining light at certain frequencies. The classical resonator (such as the Fabri-Perot etalon seen in Fig. 5.1) consists of two planar mirrors, separated by a distance l . The region between the two mirror is called the spacer layer and its refractive index is denoted by n . For now we assume that the medium outside the structure is plain air. The transmission spectrum of this structure exhibits a pattern of repetitive peaks of large transmission corresponding to resonances of the etalon. This varying transmission function is caused by an interference between the multiple reflections of light between the two reflecting surfaces (see Fig. 5.1). Constructive interference occurs if the transmitted beams are in phase, which corresponds to a high-transmission peak. For transmitted beams that are out-of-phase a destructive interference occurs, which corresponds to a minimum in the

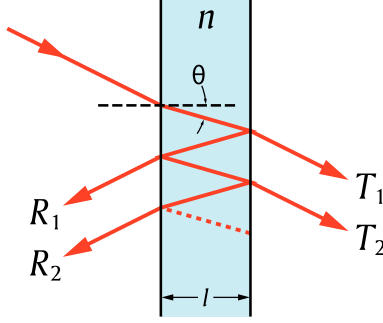


Figure 5.1: *Fabri-Perot etalon multiple reflections.*

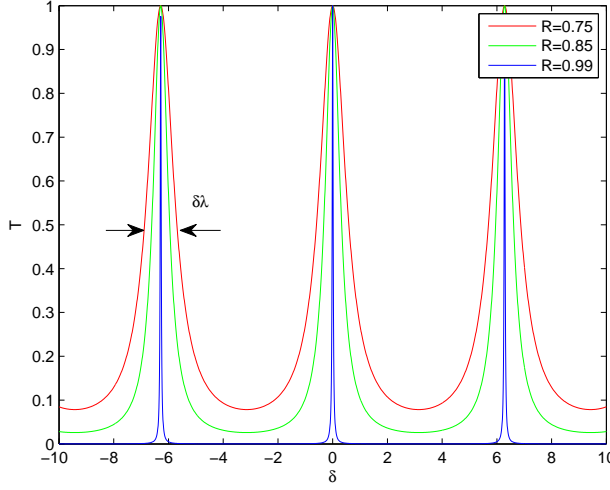


Figure 5.2: *Resonator transmittance function for various values of mirror reflectance R . $\delta\lambda$ is the full-width half-maximum of the transmission band.*

transmission spectrum. The multiple-reflected beams' phase matching depends in the wavelength λ of the light, the beam incidence angle θ , the etalon thickness l and the refractive index of the spacer material n .

The phase between each successive reflection is [44]

$$\delta = \left(\frac{2\pi}{\lambda} \right) 2nl \cos(\theta) \quad (5.1.1)$$

If both surfaces have reflectance R , the transmittance function of the entire structure is given by

$$T = \frac{(1-R)^2}{1+R^2-2R \cos(\delta)} = \frac{1}{1+F \sin^2(\frac{\delta}{2})}, \quad (5.1.2)$$

where $F = \frac{4R}{(1-R)^2}$ is the finesse coefficient. Fig. 5.2 shows the dependence of the transmittance on the phase parameter δ , for various values of R (or equivalently of F). The maximum transmission occurs when the optical path length difference $2nl \cos(\theta)$ between each transmitted beam is an integer multiple of the wavelength. In the absence of absorption, the reflectance of the structure R is the complement of the transmittance, i.e. $R + T = 1$. The maximum reflectivity is given by

$$R_{max} = 1 - \frac{1}{1+F}, \quad (5.1.3)$$

which occurs when the path-length difference is equal to half an odd multiple of the wavelength.

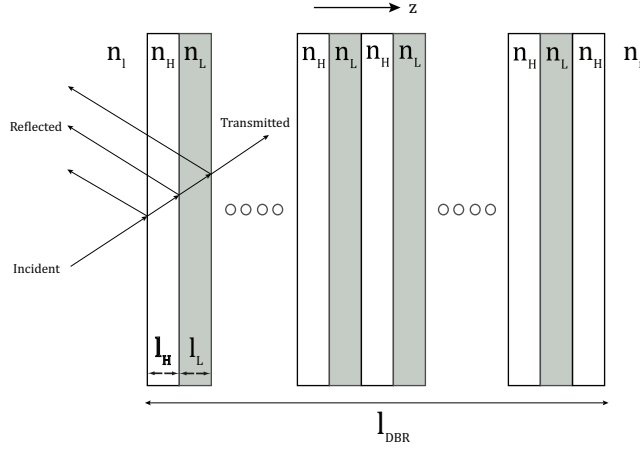


Figure 5.3: Schematic illustration of a Distributed Bragg Reflector (DBR). z represents the growth direction of the layered structure.

The wavelength separation between adjacent transmission peaks or free spectral range (FSR) of the etalon, $\Delta\lambda$, is given by

$$\Delta\lambda = \frac{\lambda_0^2}{2nl \cos(\theta) + \lambda_0}, \quad (5.1.4)$$

where λ_0 is the central wavelength of the nearest transmission peak. The FSR is related to the full-width half-maximum (FWHM) $\delta\lambda$ of any one transmission band by a quantity known as the *finesse*

$$\mathcal{F} = \frac{\Delta\lambda}{\delta\lambda} = \frac{\pi}{2 \arcsin(1/\sqrt{F})} \quad (5.1.5)$$

5.2 Distributed Bragg Reflector

The reflecting surfaces (or mirrors) modeled in previous section by a reflectivity parameter R are realized in practice by a stack of multiple layers of alternating semiconductor materials with varying refractive indices called Distributed Bragg Reflector (DBR) (see Fig. 5.3). The alternating high and low indices, denoted respectively by n_H and n_L , and the semiconductor layer thicknesses satisfy the following condition

$$n_L l_L = n_H l_H = \frac{\lambda_c}{4}, \quad (5.2.1)$$

where λ_c is the center wavelength of the high reflectivity region of the structure. The two indices n_l and n_r are, respectively, the left- and right-hand cladding material refractive indices.

The principle of operation can be understood as follows. Each interface between the two materials contributes a Fresnel reflection. For the design wavelength λ_c , the optical path length difference between reflections from subsequent interfaces is half the wavelength; in addition, the reflection coefficients for the interfaces have alternating signs. Therefore, all reflected components from the interfaces interfere constructively, which results in a strong reflection. The reflectivity achieved is determined by the number of layer pairs and by the refractive index contrast between the layer materials. The reflection bandwidth is determined mainly by the index contrast, $n_H - n_L$.

In order to analyze the reflection and transmittance of the DBR, we use the Transfer Matrix formalism [45], as is described in the next section.

5.2.1 Transfer Matrix Method (TMM)

A monochromatic electric field of frequency ω propagating in a dielectric medium, assuming a frequency independent dielectric function, can be shown to satisfy the following wave equation

$$\nabla^2 \mathbf{E}(\mathbf{r}) + \frac{\omega^2}{c^2(r)} \mathbf{E}(\mathbf{r}) = 0, \quad (5.2.2)$$

where

$$\mathbf{E}(\mathbf{r}, t) = \Re \{ \mathbf{E}(\mathbf{r}) e^{i\omega t} \},$$

the speed of light in the dielectric $c(r) = c_0/n(r)$, c_0 being the speed of light in the vacuum and $n(r)$ the location dependent refractive index.

A medium consisting of pairs of two different dielectric materials with different refraction indices has a growth axis, \hat{z} , dependent refraction index, i.e. $n(r) = n(z)$. Therefore equation (5.2.2) can be written as

$$\nabla^2 \mathbf{E}(\rho, z) + \frac{\omega^2}{c^2(z)} \mathbf{E}(\rho, z) = 0. \quad (5.2.3)$$

Because of the translational invariance along the in-plane, the solution of Eq. (5.2.3) consists of plane waves along the in-plane direction. For a given in-plane wave vector k_t (parallel to the dielectric layer plane) we can make the following ansatz for the solution

$$\mathbf{E}_{\mathbf{k}_t} = E_{\mathbf{k}_t, \omega}(z) e^{i\mathbf{k}_t \cdot \rho}. \quad (5.2.4)$$

Substituting into Eq. (5.2.3) yields the following one-dimensional equation

$$\frac{d^2 E_{\mathbf{k}_t, \omega}(z)}{dz^2} + \left(\frac{\omega^2}{c^2(z)} - k_t^2 \right) E_{\mathbf{k}_t, \omega}(z) = 0. \quad (5.2.5)$$

This equation can be solved separately for each layer of the stack. The solution for a homogeneous layer with a constant refractive index is of the form

$$\begin{aligned} E_{\mathbf{k}_t, \omega}(z) &= E^+ e^{ik_z z} + E^- e^{-ik_z z}, \\ k_z &= \sqrt{\frac{\omega^2}{c^2} - \mathbf{k}_t^2}. \end{aligned} \quad (5.2.6)$$

The solution is a linear combination of two traveling waves in opposite direction along the \hat{z} axis. A non-evanescent wave solution exist only if $\frac{\omega}{c} > \mathbf{k}_t$. The complex amplitudes of the forward (E^+) and backward (E^-) propagating waves are determined from the boundary conditions at each interface between two adjacent layers of the stack.

The relation between the two complex amplitudes between two point along the propagation direction, z_1 and z_2 , can be expressed as a 2×2 matrix transfer matrix. From here on we assume the non-unique basis for the transfer matrix is (E^+, E^-) . The transfer matrix takes into account the propagation through the dielectric media and the boundary conditions at each interface between two adjacent layers. The boundary conditions resulting from Maxwell's equations state that tangential components of the electric and magnetic fields are continuous across the interface. The boundary conditions for the field components can be written as

$$\begin{aligned} D_{\perp 1} &= D_{\perp 2} \\ B_{\perp 1} &= B_{\perp 2} \\ E_{\parallel 1} &= E_{\parallel 2} \\ H_{\parallel 1} &= H_{\parallel 2} \end{aligned} \quad (5.2.7)$$

For simplicity we assume propagation only in the \hat{z} direction and normal incidence of the light waves on the dielectric interfaces. The boundary conditions for the electric field become (see Fig. 5.4(a))

$$E_1^+ + E_1^- = E_2^+ + E_2^- \quad (5.2.8)$$

$$n_2 (E_2^+ - E_2^-) = n_1 (E_1^+ - E_1^-) \quad (5.2.9)$$

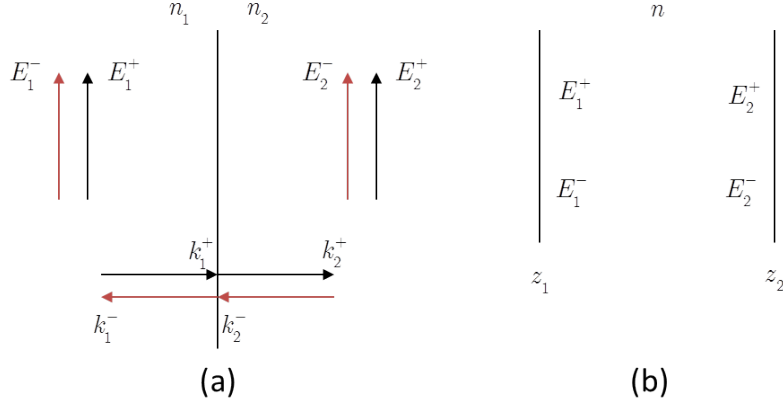


Figure 5.4: Schematic description of (a) light propagation through an interface between two adjacent dielectric layers and (b) light propagation in a homogeneous medium.

The interface transfer matrix \$M_i\$, for both linear polarizations of the field, TE and TM, can be written as

$$\begin{pmatrix} E_2^+ \\ E_2^- \end{pmatrix} = \frac{1}{2n_2} \begin{pmatrix} n_2 + n_1 & n_2 - n_1 \\ n_2 - n_1 & n_2 + n_1 \end{pmatrix} \begin{pmatrix} E_1^+ \\ E_1^- \end{pmatrix} \equiv M_i \begin{pmatrix} E_1^+ \\ E_1^- \end{pmatrix} \quad (5.2.10)$$

or a wave propagating from layer 1 to layer 2. The in-layer propagation transfer matrix \$M_p\$, which relates different vectors at \$z_1\$ and \$z_2\$ in the same layer can be written as (Fig. 5.4(b))

$$\begin{pmatrix} E_2^+ \\ E_2^- \end{pmatrix} = \begin{pmatrix} e^{ikl} & 0 \\ 0 & e^{-ikl} \end{pmatrix} \begin{pmatrix} E_1^+ \\ E_1^- \end{pmatrix} \equiv M_p \begin{pmatrix} E_1^+ \\ E_1^- \end{pmatrix}, \quad (5.2.11)$$

where \$k = (\omega/c_0)n\$.

This amplitude propagation approach can be applied to the entire multilayer structure, for which the transfer matrix is simply the multiplication of \$M_i\$ and \$M_p\$ matrices for each boundary and layer

$$M_{DBR} = \prod_m M_{i,m} M_{p,m}, \quad (5.2.12)$$

where \$m\$ is the dielectric layer index. The explicit relation between the amplitudes of the incident electric field in the DBR structure and the transmitted field on the other side can be written as

$$\begin{pmatrix} E_{out}^+ \\ 0 \end{pmatrix} = \begin{pmatrix} M_{11} & M_{12} \\ M_{21} & M_{22} \end{pmatrix} \begin{pmatrix} E_{in}^+ \\ E_{in}^- \end{pmatrix}. \quad (5.2.13)$$

The reflection and transmission coefficients of the entire structure can thus be written as

$$r_{DBR} = -\frac{M_{21}}{M_{22}} \quad (5.2.14)$$

$$t_{DBR} = \frac{\det(M_{DBR})}{M_{22}} \quad (5.2.15)$$

The reflection coefficient can be expressed as \$r_{DBR}(\lambda) = |r|e^{i\alpha_r}\$. It can be shown that for a structure containing \$2N + 1\$ layers of high and low refractive indices (as in Fig. 5.3), so that the outermost layers are of high refractive index, \$n_H\$, and for the case of \$k_l l_i = \frac{\pi}{2}\$

$$|r| = \left(\frac{1 - \left(\frac{n_H}{n_L} \right)^{2N} \frac{n_H^2}{n_r n_l}}{1 + \left(\frac{n_H}{n_L} \right)^{2N} \frac{n_H^2}{n_r n_l}} \right)^2. \quad (5.2.16)$$

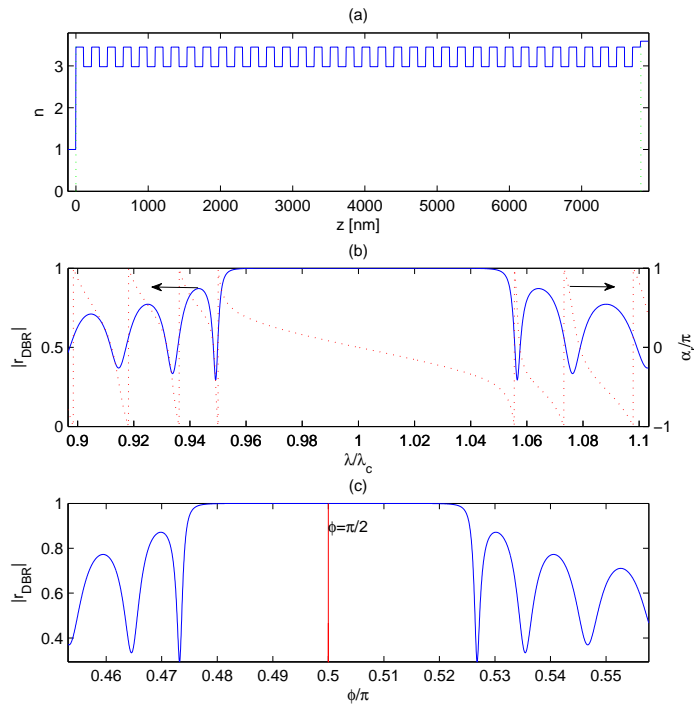


Figure 5.5: *Simulation of a DBR structure with 35 alternating high and low refraction index layers, where (a) is the refractive index profile as a function of the growth axis, (b) the amplitude and phase of the normal incidence reflection function this structure as a function of normalized wavelength, λ/λ_c , and (c) the same amplitude as a function of the phase acquired by the EM field at each layer, $\phi = \frac{2\pi l_i n_i}{\lambda}$.*

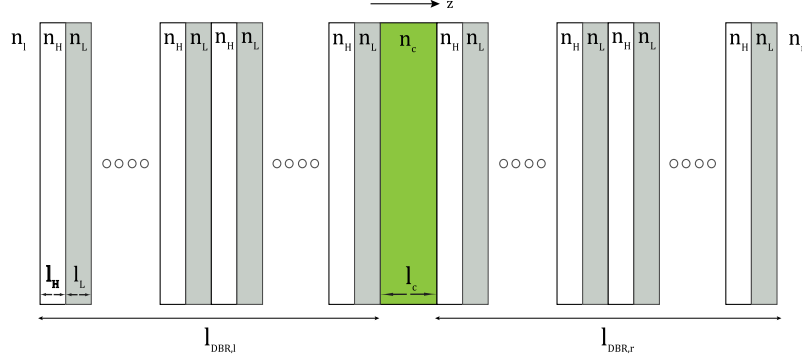


Figure 5.6: A microcavity schematic structure.

As an illustration, we present in Fig. 5.5 an exact calculation of the reflection coefficient of a DBR containing 35 pairs of alternating high and low refractive index layers. The refractive indices for the simulation are $n_l = 1$ (air), $n_H = 3.45$ ($Al_{0.2}Ga_{0.8}As$), $n_L = 2.98$ ($AlAs$) and $n_r = 3.59$ ($GaAs$) (the structure refractive index profile is presented in (a)). In subplots (b) and (c) we plot the reflection coefficient as a function of the normalized wavelength, λ/λ_c , and the phase acquired by the electromagnetic field at each layer, $\phi = \frac{2\pi l_i n_i}{\lambda}$. The stop-band, as can be clearly seen from these plots, is centered at $\phi = \frac{\pi}{2}$, which corresponds to λ_c . In subplot (b) we also present the reflectivity phase α_r , where the zero-phase crossing is observed at λ_c as expected for the left-face reflection.

5.3 Microcavity Optical Characteristics

5.3.1 Microcavity Reflection Spectrum

A microcavity (MC) is a Fabry-Perot resonator, whose mirrors are two DBRs and the spacer material is a semiconductor layer with refractive index n_c and of length $l_c = \frac{\lambda_c}{2n_c} m$ (m is a positive integer). The microcavity can be analyzed similarly to the DBR using the transfer matrix formalism. The MC's transfer matrix for a wave traveling from left to right can be written as

$$M_{MC} = M_{DBR}^r M_c M_{DBR}^l, \quad (5.3.1)$$

where M_c is the transfer matrix of the spacer (cavity) layer. We can write the these three transfer matrices in their most general form as

$$M_{DBR}^r = \frac{n_c}{n_r} \begin{pmatrix} \frac{1}{t_r^*} & -\frac{r_r^*}{t_r^*} \\ -\frac{r_r}{t_r} & \frac{1}{t_r} \end{pmatrix}, \quad (5.3.2)$$

$$M_{DBR}^l = \frac{n_l}{n_c} \begin{pmatrix} \frac{1}{t_l^*} & \frac{r_l}{t_l} \\ \frac{r_l^*}{t_l^*} & \frac{1}{t_l} \end{pmatrix}, \quad (5.3.3)$$

$$M_c = \begin{pmatrix} e^{ikl_c} & 0 \\ 0 & e^{-ikl_c} \end{pmatrix}, \quad (5.3.4)$$

where (r_l, t_l) and (r_r, t_r) are, respectively, the reflection and transmission coefficients of the left- and right-hand DBR mirrors (see Fig. 5.6) and n_l and n_r are the left- and right-hand cladding material refractive indices, respectively.

Inserting these matrices into Eq. (5.3.1) yields

$$M_{MC} = \left(\frac{n_L}{n_H} \right)^2 \begin{pmatrix} \frac{e^{ikl_{eff}} - R^* e^{-ikl_{eff}}}{T^*} & \frac{r_l e^{ikl_{eff}} - r_r^* e^{-ikl_{eff}}}{t_l t_r^*} \\ \frac{r_l^* e^{-ikl_{eff}} - r_r e^{ikl_{eff}}}{t_l^* t_r} & \frac{e^{-ikl_{eff}} - R e^{ikl_{eff}}}{T} \end{pmatrix}, \quad (5.3.5)$$

where $T = t_l t_r$ and $R = r_l r_r$. l_{eff} is not equal to l_c but rather to $l_{eff} = l_c + l_p$, where l_p is the penetration depth

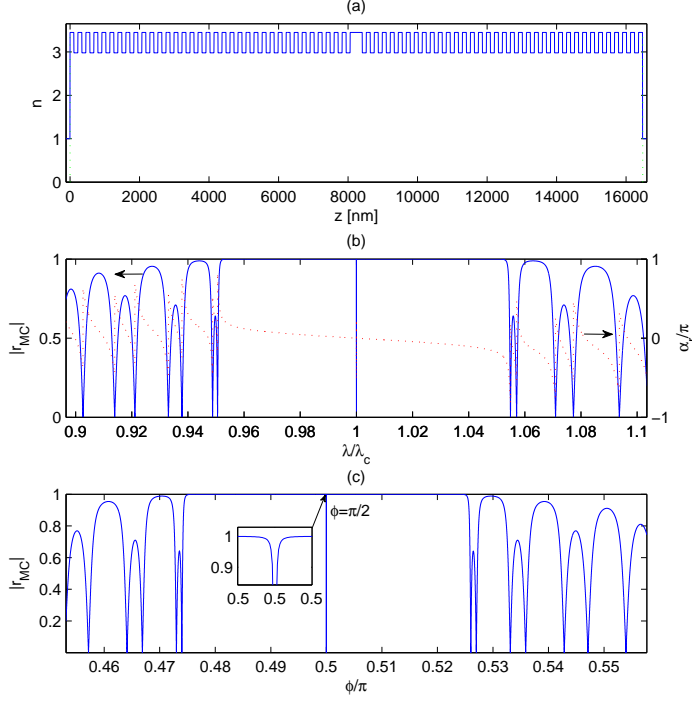


Figure 5.7: *Simulation of a microcavity with two DBR's with 35 alternating high and low refractive index layers each, where (a) is the refractive index profile as a function of the growth axis, (b) the amplitude and phase of the normal incidence reflection function this structure as a function of normalized wavelength, λ/λ_c , and (c) the same amplitude as a function of the phase acquired by the EM field at each layer, $\phi = \frac{2\pi l_i n_i}{\lambda}$. The inset in (c) shows the reflection profile in the vicinity of $\phi = \frac{\pi}{2}$.*

of the cavity field into the DBR [46] and is given by

$$l_p = \frac{\lambda_c}{2} \frac{n_L n_H}{n_c (n_H - n_L)}. \quad (5.3.6)$$

The reflectance and transmittance of the MC can thus be written as

$$T_{MC} = \frac{1}{\det(M_{MC}) |M_{MC}^{22}|^2} = \frac{T}{(1-R)^2 + 4R \sin^2(k_z l_{eff})} \quad (5.3.7)$$

$$R_{MC} = \frac{|M_{MC}^{21}|^2}{|M_{MC}^{22}|^2} = \frac{(|r_r| - |r_l|)^2 + 4R \sin^2(k_z l_{eff})}{(1-R)^2 + 4R \sin^2(k_z l_{eff})} \quad (5.3.8)$$

It is clear that there are several modes which satisfy the condition $k_z l_{eff} = m\pi$. As we increase the number of layers in the DBR mirrors the stop-band reflectivity approaches unity and the cavity field reflection line becomes narrower. Because of the finite transmission probability of the DBR, the MC mode has a FWHM which can be shown to be [46]

$$2\gamma_c = \frac{1 - R_{MC}}{\sqrt{R_{MC}}} \frac{c}{n_c l_{eff}}. \quad (5.3.9)$$

γ_c is a homogeneous lifetime broadening of the confined cavity mode, caused by the decay through the mirrors.

As an illustration, we present in Fig. 5.7 the simulation results of a sample microcavity with two DBR mirrors with 35 alternating layers of high and low refractive index each and cavity length of $l_c = \frac{\lambda_c}{2n_c}$. This calculation was performed using the direct TMM calculation of the entire the structure, similarly to the DBR simulation

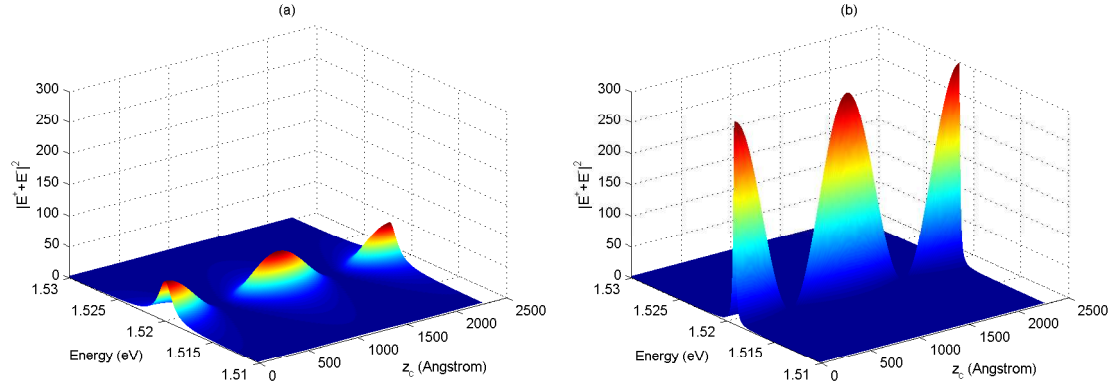


Figure 5.8: Simulation the electric field amplitude of a microcavity with DBR mirrors made of (a) 15 left and 25 right alternating layers and (b) 22 left and right alternating layers. The cavity in this calculation is λ -wide and the layer materials are the same as in previous calculations.

presented above. The DBR parameters are the same as in Fig. 5.5, while for the cavity we choose $n_c = n_H = 3.45$ ($Al_{0.2}Ga_{0.8}As$).

Using the same procedure, the electric field buildup can be calculated inside the cavity. This is obtained by plugging the accumulated transfer matrix (5.3.1) for each layer of the structure into (5.2.13), with the use of appropriate initial electric field amplitudes. As an illustration we plot in Fig. 5.8 the electric field profile inside a λ -wide microcavity for two configurations of the cavity DBR mirrors. The spatial and spectral localization of the electric field intensity and its enhancement (from (a) to (b)) is clearly seen.

5.3.2 Microcavity Confined Photon

The dispersion of the MC modes is defined as the k_t dependence of the MC-mode energy. As we have seen in the previous section, it is obtained from the resonance condition $k_z l_{eff} = m\pi$, where $k_z = \sqrt{\frac{\omega^2}{c^2} - k_t^2}$. Combining this condition with the condition for a propagating wave inside the cavity, $k_t^2 < \frac{\omega^2}{c^2}$, we can write the MC-mode dispersion relation of the form [47]

$$E_{ph}(k_t) = \frac{\hbar c k}{n_c} = \frac{\hbar c}{n_c} \sqrt{\left(\frac{2\pi m}{l_c}\right)^2 + k_t^2}, \quad (5.3.10)$$

where m is a positive integer. For small k_t we approximate the dispersion relation to a parabola

$$E_{ph}(k_t) \approx \frac{2\pi\hbar c}{n_c l_c} \left(1 + \frac{\hbar^2 k_t^2}{2m_{ph}}\right). \quad (5.3.11)$$

The parabolic dispersion can be interpreted as a cavity photon that carries a very small in-plane effective mass $m_{ph} = \frac{\hbar n_c}{cl_c} \approx 10^{-5} m_0$, where m_0 is the free electron mass. We plot the confined photon dispersion, for various values of m , in Fig. 5.9 and compare it to the free photon dispersion. For high k_t values, the confined photon dispersion coincides with the free photon dispersion for all the modes.

5.4 Microcavity Polaritons

As we have seen in previous sections, a MC is used to sort out a single mode of the electromagnetic field that is confined in one direction. Semiconductor microcavities with embedded QWs are of particular interest as they exhibit a one-dimensional confinement of both the electronic states and the electromagnetic field [48]. The resonant transitions (excitons) in QWs behave like a two-level absorber system due to their enhanced oscillator strength and the large binding energy resulting from the quantum confinement [49]. The interaction of the MC-photon with

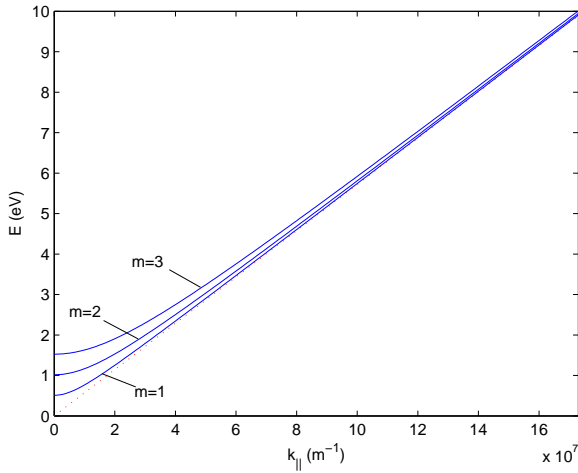


Figure 5.9: Microcavity confined photon dispersion curves for various resonance modes (solid blue) compared to a free photon dispersion curve $E_{ph,f}(k_t) = \frac{\hbar c k_t}{n_c}$ (dotted red).

the QW-exciton leads to several new effects that can generally be divided into two classes: (a) the enhancement or inhibition of the spontaneous emission rate in the weak coupling regime [50] and (b) the observation of new eigen-modes with a Rabi splitting (normal mode splitting) between them, in the strong coupling regime [51, 52].

The coupled exciton-photon eigenstates of the QW embedded in a MC are called *cavity polaritons*, by analogy with the exciton-polariton modes of the bulk material [53]. Various theoretical models have been proposed to describe the exciton-cavity polariton such as a semi-classical linear dispersion model, in which the active medium is represented by a Lorentzian oscillator [54, 52, 51], and a quantum mechanical model representing the MC-photon and the QW exciton as two coupled harmonic oscillators [55, 47, 56]. The semi-classical model has the advantage of using the realistic MC parameters and it gives the reflectivity, transmission and absorption spectra. The coupled oscillators model is more suitable for the description of the dynamics of the MC-polaritons. A full quantum mechanical treatment developed in [57] is out of the scope of this thesis. In this section we elaborate on the quantum mechanical model for the two-level absorber and extend the analog to a microcavity polariton. The presented review is primarily based on [58].

5.4.1 Strong Absorber-Photon Coupling

5.4.1.1 Single Two-Level System

To understand the interaction of a single photon mode with two-level absorber we employ the Jaynes-Cummings model [59, 60, 61], where a single photon mode is described by the Fock Hamiltonian

$$H_F = \hbar\omega \left(p^\dagger p + \frac{1}{2} \right). \quad (5.4.1)$$

Here p^\dagger and p are, respectively, the creation and annihilation operators that connect different photon Fock states, defined in analogy to (3.1.3), as

$$p |n\rangle = \sqrt{n} |n-1\rangle, \quad (5.4.2)$$

$$p^\dagger |n\rangle = \sqrt{n+1} |n+1\rangle. \quad (5.4.3)$$

p^\dagger and p obey the bosonic commutation relation $[p, p^\dagger] = 1$. The field operator of the photon field $\mathbf{E}(\mathbf{r})$ is given by

$$\mathbf{E}(\mathbf{r}) = \sqrt{\frac{\hbar\omega}{2\epsilon_0 V}} [pf(\mathbf{r}) + p^\dagger f^\dagger(\mathbf{r})], \quad (5.4.4)$$

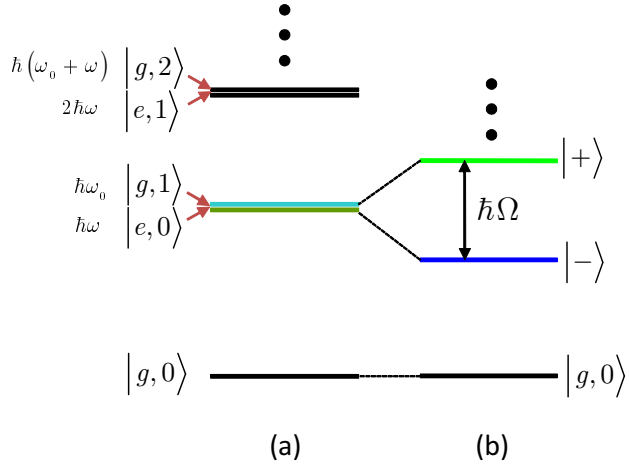


Figure 5.10: (a) Energy levels of the uncoupled absorber and field modes and (b) the dressed energy levels of the coupled system.

where $f(\mathbf{r})$ is a complex vector function that describes the polarization and relative amplitude of the cavity mode at the position \mathbf{r} . The effective cavity mode volume V is defined as $V = \int |f(\mathbf{r})|^2 d^3\mathbf{r}$. The atomic two-level system is described by a two-level Hamiltonian

$$H_A = \frac{1}{2}\hbar\omega\hat{\sigma}_z, \quad (5.4.5)$$

where σ_z is a spin 1/2 like operator. We also define two additional operators

$$\sigma_+ |g\rangle = |e\rangle, \quad (5.4.6)$$

$$\sigma_- |e\rangle = |g\rangle, \quad (5.4.7)$$

where $|g\rangle$ and $|e\rangle$ represent, respectively, the ground and excited states. These operators obey the fermionic commutation relations $[\sigma_+, \sigma_-] = 2\sigma_z$. The atom-field interaction is once again the dipole interaction (as in 3.1.1.3) and is given by

$$H_I = \mathbf{d} \cdot \mathbf{E} = -\hbar\Omega f(r) [p\sigma_+ + p^\dagger\sigma_-]. \quad (5.4.8)$$

Here, \mathbf{d} is the electric dipole matrix element between the ground and excited states of the atom and Ω , the coupling term, is given by

$$\Omega = \frac{d}{\hbar} \sqrt{\frac{\hbar\omega}{2\epsilon_0 V}}. \quad (5.4.9)$$

The ground state of the entire system is $|g; 0\rangle$ with the atom is the ground state and the optical cavity is devoid of photons. At the resonance, i.e. $\omega = \omega_0$, and without the atom-field interaction, all the excited states of the entire system are grouped into doubly degenerate level groups (see Fig. 5.10(a)) $|g; n+1\rangle$ and $|e; n\rangle$. The atom-field interaction H_I couples only the doublet states within each group and doesn't couple states from different level groups. The interaction then lifts the degeneracy within each group and new states are formed which are merely a linear combination of the doublets. These new states are termed “dressed states” or the “dressed atom basis”, seen in Fig. 5.10(b).

From (5.4.8), the eigenstates of the system are

$$|\pm, n\rangle = \frac{1}{\sqrt{2}} [|e, n\rangle \mp |g, n+1\rangle], \quad (5.4.10)$$

constituting symmetric and anti-symmetric combinations of the uncoupled states. The eigenenergies are given by

$$E_{\pm, n} = (n+1)\hbar\omega_0 \pm \hbar\Omega f(r)\sqrt{n+1}. \quad (5.4.11)$$

The double degeneracy is lifted by the interaction and the separation between the dressed states within each group is $2\hbar\Omega f(r)\sqrt{n+1}$, termed the Rabi splitting.

We now assume the initial state of the system to be

$$|\psi(t=0)\rangle = |e, 1\rangle = \frac{1}{\sqrt{2}} [|+\rangle + |-\rangle]. \quad (5.4.12)$$

after a finite period of time t the system will be in the state

$$|\psi(t)\rangle = \frac{1}{\sqrt{2}} [|+\rangle e^{-iE_+t/\hbar} + |-\rangle e^{-iE_-t/\hbar}]. \quad (5.4.13)$$

The probability that the field mode is excited and the absorber is in its ground state is not stationary but rather of the form

$$|\langle e, n | \psi(t) \rangle|^2 = \frac{1}{2} (1 + \cos \Omega t), \quad (5.4.14)$$

termed the Rabi oscillations. If the absorber is in its excited states and it emits a photon, then it will subsequently reabsorb the photon. There is no irreversible decay in this model since there is only one photon mode. In reality, the cavity damping Q factor is finite leading to a cavity damping γ_{cav} . In the strong coupling regime, the vacuum Rabi splitting must be greater than the cavity damping and the absorber damping, i.e., $\hbar\Omega > \gamma_{cav}, \gamma_{abs}$.

5.4.1.2 Multiple Two-Level Systems

An extension of the former system is a setting of multiple two level atoms interacting with a single photon mode. This system is of relevance to the semiconductor MCs, since it involves a large ensemble of absorbers (or QW excitations). We consider a set of N identical two level atoms, where we assume that the atoms interact only through their coupling to the radiation field. Thus, the atomic Hamiltonian as well as the atom-field interaction are sums of the individual atomic Hamiltonians. Since all the atoms are coupled to the field in a similar fashion, the excitation of the atomic system is equally shared among all atoms, and the coupled atom-radiation system has $N + 1$ non-degenerate, equidistant energy levels. This description is valid also for QWs in resonant structures since typical exciton size is much smaller than the optical wavelength ($a_0 \ll \lambda$) [30]. The atomic Hamiltonian and the atom-field interaction can be then expressed in terms of collective operators defined by

$$\sigma_z = \sum_i \sigma_{z,i}, \quad \sigma_+ = \sum_i \sigma_{+,i}, \quad \sigma_- = \sum_i \sigma_{-,i}. \quad (5.4.15)$$

The atom-field interaction Hamiltonian is

$$H_I = \hbar\Omega [a\sigma_+ + a^\dagger\sigma_-], \quad (5.4.16)$$

where Ω is the single atom single photon Rabi frequency, defined by (5.4.9) and assuming $f(r)$ is unity for all the atoms. Due to the symmetrical form of the raising and lowering operators, the excitation is equally shared among the atoms. The atomic Hamiltonian has $N + 1$ non-degenerate levels $|J, M\rangle$ with $J = N/2$ and $-J \leq M \leq J$.

The two lowest states of the atomic system are the ground state $|G\rangle = |J, -J\rangle$ and the first excited state $|E\rangle = |J, -J + 1\rangle$. The ground state of the coupled system of atoms and cavity atoms is $|G, 0\rangle$, which describes an atomic ground state with an empty cavity. The two degenerate states in the first group under resonant condition are $|G, 1\rangle$ and $|E, 0\rangle$. These two states are coupled by the atom-field interaction to form two dressed states exactly as for the single atom case

$$|\pm, 0\rangle = \frac{1}{\sqrt{2}} [|E, 0\rangle \mp |G, 1\rangle]. \quad (5.4.17)$$

The eigenenergies of these states are given by

$$E_\pm = \hbar\omega_0 \pm \hbar\Omega\sqrt{N}. \quad (5.4.18)$$

The splitting energy in this case becomes larger by the factor \sqrt{N} than the isolated atom, i.e., there is an enhancement of the splitting because of the collective coupling of the atoms with the field.

This discussion results hold only for weak light intensities, when there is only one photon in the cavity. The structure of higher dressed state groups is quite different from lowest state groups and thus it is different from the single atom case. For example, there are three equally spaced dressed levels in the second group, four in the third

and so on. The spectra corresponding to these excitations are therefore very complicated. In the limit of very large N , it was shown [60] that the dressed state ladder consist of levels remaining nearly equidistant over a large energy range, with a spacing between nearby levels being of the order of $2m\hbar\Omega\sqrt{N}$, where m is the photon number. As a result, the spectra of all the state groups will have only two distinct lines with an energy separation of $2\hbar\Omega\sqrt{N}$. This system of many atoms where $m \ll N$, is similar to the dressed boson case described by the coupled oscillator model described in the next section.

5.4.1.3 Coupled Harmonic Oscillator

When two harmonic oscillators interact resonantly, the coupled system can be represented by new normal modes, which are eigenstates of the total system Hamiltonian of the form

$$H = \hbar\omega_0 \left(a^\dagger a + \frac{1}{2} \right) + \hbar\omega_0 \left(b^\dagger b + \frac{1}{2} \right) + \hbar\Omega (a^\dagger b + b^\dagger a). \quad (5.4.19)$$

Here both field operators satisfy the boson commutation relation. As we have mentioned before, in the case of $N \gg 1$ identical atoms with m photons ($m \ll N$) that are resonantly coupled to a single mode, the above dressed boson is a valid concept. The coupling constant Ω is then not the single atom Rabi frequency Ω_s , but the enhanced $\Omega_s\sqrt{N}$ collective coupling of all the atoms. An exciton in a semiconductor QW is in fact similar to such an assembly of N identical atoms, namely each lattice site having a unit dipole moment corresponds to a single two level atom.

The dressed bosons spectrum for $m = 1$ is identical to that of the corresponding dressed fermions. The $m = 2$ excitation state group has three degenerate bare states $|2\rangle_a |0\rangle_b$, $|1\rangle_a |1\rangle_b$ and $|0\rangle_a |2\rangle_b$, that split into three non-degenerate dressed states

$$|2, -\rangle = \frac{1}{2} |2\rangle_a |0\rangle_b - \frac{1}{\sqrt{2}} |1\rangle_a |1\rangle_b + \frac{1}{2} |0\rangle_a |2\rangle_b, \quad (5.4.20)$$

$$|2, +\rangle = \frac{1}{2} |2\rangle_a |0\rangle_b + \frac{1}{\sqrt{2}} |1\rangle_a |1\rangle_b + \frac{1}{2} |0\rangle_a |2\rangle_b, \quad (5.4.21)$$

$$|2, 0\rangle = -\frac{1}{\sqrt{2}} |2\rangle_a |0\rangle_b + \frac{1}{\sqrt{2}} |0\rangle_a |2\rangle_b, \quad (5.4.22)$$

with a frequency separation of 2Ω . The emission spectrum from the $m = 2$ to $m = 1$ state groups is, however, identical to that from $m = 1$ to $m = 0$ consisting of only two separate lines. This is because of the six possible transitions, two are forbidden and two pairs are degenerate. In general, the emission spectrum always has only two lines irrespective of the excitation state group. The dressed boson is then a perfectly linear system. Note that there is no difference between the fermion and boson cases for the first state group, thus in order to observe the differences a very high light intensity must be employed.

5.4.2 Strong Coupling in a Semiconductor Microcavity

As mentioned in the previous sections, excitons are similar to the two-level systems since only coupling between excitons and photon states of the same in-plane wave vector are allowed. This coupling mixes the exciton and the photon modes and the normal modes are similar to a dressed boson, and thus in analogy this modes are called dressed excitons. When this splitting is significantly greater than both the exciton and the cavity linewidths the system is said to be in the strong coupling regime. Two different models are usually used to describe such a system [54, 57, 55]. The first is a coupled quantum oscillators and the second is the semiclassical linear dispersion model (LDM). A brief summary of these two models is given and a new approach to the cavity polariton modeling is presented.

5.4.2.1 Coupled Oscillator Model

In the coupled oscillator model, we treat both the exciton transition and the photon mode as two quantum harmonic oscillators that are coupled together via their dipole interaction. The simplest Hamiltonian that describes this system can be written as

$$H = (E_X(\mathbf{k}_t) + \gamma_X) b^\dagger b + (E_C(\mathbf{k}_t) + \gamma_C) a^\dagger a + \hbar\Omega (a^\dagger b + b^\dagger a), \quad (5.4.23)$$

where we assume a single MC mode interacting with one electron-hole (exciton) mode. γ_X is the phenomenological linewidth of the exciton and γ_C is the cavity photon mode linewidth given by eq. (5.3.9). b and b^\dagger are the exciton creation and annihilation operators. $E_C(\mathbf{k}_t)$ is the photon in-plane dispersion inside the cavity given by eq. (5.3.10). This Hamiltonian can be written in a matrix form as

$$H = \begin{pmatrix} E_X(k_t) + i\gamma_X & \frac{\hbar\Omega}{2} \\ \frac{\hbar\Omega}{2} & E_C(k_t) + i\gamma_C \end{pmatrix}. \quad (5.4.24)$$

For this simple model, the diagonalization of this Hamiltonian for each k_t gives the polariton eigenenergies

$$E_{\pm}(k_t) = \frac{E_X(k_t) + E_C(k_t)}{2} \pm \sqrt{\left[E_X(k_t) - E_C(k_t) + i\left(\frac{\gamma_X - \gamma_C}{2}\right) \right] + \left(\frac{\hbar\Omega}{2}\right)^2}. \quad (5.4.25)$$

We denote the eigenvalues of this. This model can be extended to include larger number of exciton modes and the same single cavity mode, in which case the Hamiltonian matrix to be diagonalized becomes $(N_X + 1) \times (N_X + 1)$, where N_X is the number of strongly interacting excitons present in the system. For example, for $E_1 - HH_1$ and $E_1 - LH_1$ excitons the Hamiltonian becomes

$$H = \begin{pmatrix} E_C(k_t) + i\gamma_C & \frac{\hbar\Omega_{X_{LH}}}{2} & \frac{\hbar\Omega_{X_{HH}}}{2} \\ \left(\frac{\hbar\Omega_{X_{LH}}}{2}\right)^* & E_{X_{LH}}(k_t) - i\gamma_{X_{LH}} & 0 \\ \left(\frac{\hbar\Omega_{X_{HH}}}{2}\right)^* & 0 & E_{X_{HH}}(k_t) + i\gamma_{X_{HH}} \end{pmatrix}. \quad (5.4.26)$$

In order to simplify the coupled oscillator Hamiltonian 5.4.23 and present a more particle-like picture of the polariton, we apply the Bogoliubov's transformation [53] to obtain

$$H_{Pol} = \sum_i (E_{p,i} - i\gamma_{p,i}) p_i^\dagger p_i, \quad (5.4.27)$$

where p_i^\dagger and p_i are, respectively, the i -th polariton branch creation and annihilation operators, $E_{p,i}$ is the eigenenergy of this polariton branch and $\gamma_{p,i}$ is its linewidth. The eigenstates of this Hamiltonian can be written as

$$|P_i\rangle = |\alpha_C|^2 |C\rangle + \sum_j |\alpha_{i,j}|^2 |X_j\rangle, \quad (5.4.28)$$

where $|C\rangle$ and $|X_j\rangle$ are, respectively, the cavity mode and the j -th bare exciton wavefunctions, α_C and $\alpha_{i,j}$ are the admixing coefficients of the polariton.

5.4.2.2 Linear Dispersion Model and Beyond

Another description for the optical response of QW excitons inside a MC structure within the linear regime can be given in the framework of the semiclassical linear dispersion model [57, 55]. In this model, the transfer matrix formalism is used to describe the light propagation inside the MC layers (as explained earlier in this chapter). In the typical formulation of the model, the QW resonances (excitons) are treated as a resonant Lorentzian dispersive term in the dielectric response function of the QW material. The advantage of the LDM approach in calculating the absorption, transmission and reflection spectra is that it takes into account the geometry of the MC including all the DBR's.

We propose an altered version of the LDM approach, in which the results of the calculations presented in chapters 3 and 4 are used to model the dielectric response of the QW material. The use of this fully theoretical approach enables us to examine the optical properties of varieties of quantum structures, especially and specifically those of MC with embedded QWs in the cavity region. Fig. 5.11 presents a schematic outline of the proposed numerical approach. The computational starts with the definition of several inputs:

- The physical parameters: ambient temperature T , 2DEG concentration n_e and a phenomenological broadening parameter γ (set using a fit to experimental results, as discussed in section 4.3).

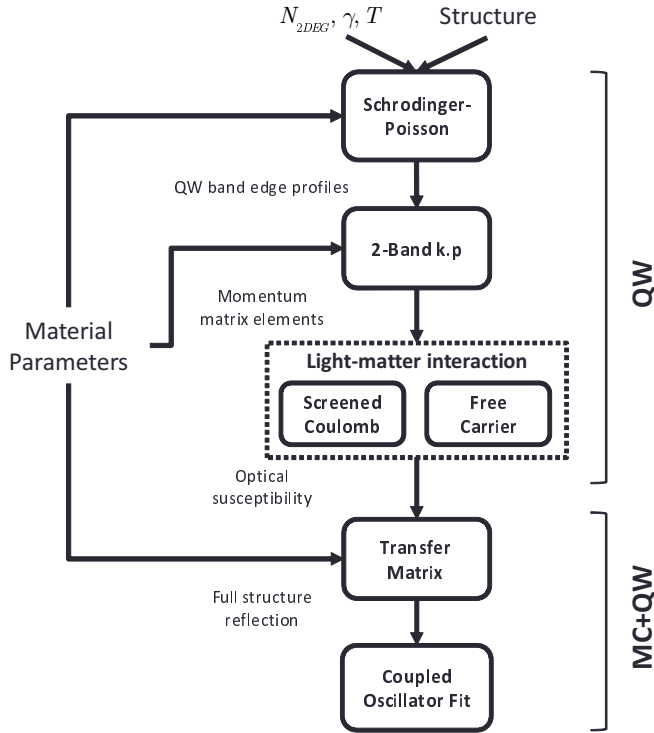


Figure 5.11: Schematic description of the proposed computation model.

- The quantum structure definition, namely the material composition and width of the epitaxial layers comprising the investigated structures.
- The common physical parameters used throughout the calculations.
- Various numerical calculation parameters, such as the maximal value and quantization of transverse wave vector k_t grid, the energy diapason for the spectra calculations etc..

The calculation is built of two separate phases. First, the cavity region of the full MC structure is considered as it contains the active section of the structure, namely the QW and its cladding layers (marked as the QW region of the calculation in figure 5.11). As can be seen in the figure, first the Schrödinger-Poisson model, formulated in section 2.3, is utilized to measure the influence of the introduced 2DEG on the band edges of the structure. Once the band edges are calculated, the two-band $\mathbf{k}.\mathbf{p}$ model, formulated in section 2.2.4, is used to calculate the conduction and valence subband dispersions up to k_t values far away from the Brillouin zone center. Once the dispersion relations are calculated, the momentum (or dipole) matrix elements can be calculated for each subband transition combination, as formulated in section 3.4. Once the electronic properties of the QW are calculated the optical properties can be addressed. To this end, the two models for the light-matter interaction presented in chapters 3 and 4 are used to calculate the optical susceptibility, absorption and spontaneous emission spectra of the structure at hand.

The second phase of the proposed approach considers the MC as a whole, and uses the results of the first bare QW phase results as an input (marked as the MC+QW phase in figure 5.11). The optical parameters of the bare QW are used to model the complex refractive indices of the cavity region of the MC, which facilitates in the reflection spectrum calculation using the TMM described in section 5.2.1. The reflection spectra represent the ultimate goal of this calculation and can be analyzed much like experimental results. To facilitate further analysis the minima of the reflection spectra are extracted and afterwards are fitted using the coupled oscillator model.

In the next section we present an application of the second phase of the above elaborated approach, and discuss the result and their analysis.

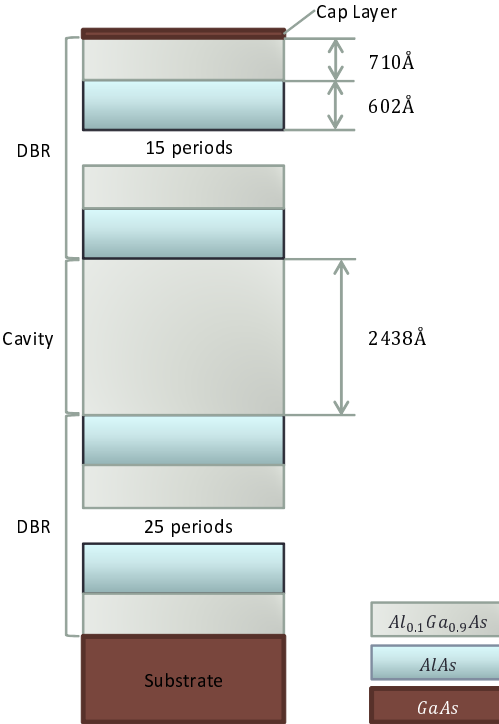


Figure 5.12: Schematic profiles of the simulated microcavity devoid of the embedded QW in the cavity region.

5.5 Numerical Results

In this section we present the results of the theoretical approach outlined in the previous section. We start by presenting a sample structure of a bare MC used throughout this section, and calculate its reflection spectrum. Next we present the reflection spectra of the same MC structures but with embedded QW structures in the cavity region. As in the discussion of the optical parameters of bare QW in chapter 4, we consider separately the doped and undoped QW structures. The reflection spectra, for both cases, are analyzed using the coupled oscillator model and various extracted parameters are presented and discussed.

5.5.1 Bare Microcavity

We now present the structure of a sample used extensively in our experimental studies, and thus is an ideal candidate for theoretical modeling. Figure 5.12 presents a schematic cross-sectional picture of the epitaxial semiconductor layers, including their composition and physical width. The considered structure is deposited upon a *GaAs* thick substrate layer, followed by 25 alternating 602 Å and 710 Å wide *AlAs* and *Al_{0.1}Ga_{0.9}As* layers, respectively. This collection of layers comprises the first of a pair of DBR mirrors of the MC. Atop of this structure a 2438 Å wide *Al_{0.1}Ga_{0.9}As* layer is deposited, plays the role of the cavity region, which is immediately followed by another structure of 15 alternating 602 Å and 710 Å wide *AlAs* and *Al_{0.1}Ga_{0.9}As* layers, respectively, being the second DBR mirror of the structure. Finally, atop of the entire MC a thin *GaAs* cladding is placed. Figure 5.13(a) presents the top and side views of a wafer from which a sample is cloven for actual experimental measurements. The side view of the wafer presents the varying width profile along the radius, which is uniform across all the epitaxial layers of the structure, i.e. the thickness of each layer described in figure 5.12 changes by the same amount along the wafer radius. All samples for experimental investigation have a nonlinear width profile, presented in figure 5.13(b), where the width detuning parameter δ is defined as the ratio between the width along the wafer radius $W(r)$ and the width at the wafer center $W(r = 0)$. Note that the widths of the epitaxial layers presented in figure 5.12 are in fact the wafer center values, i.e. the widths along the radius diminish in a direct proportion to the detuning parameter profile. In order to simplify result analysis, all calculations in this thesis assume a linear $\delta - r$ dependence.

Figure 5.14 presents the reflection spectrum of the discussed bare MC structure calculated at $T = 2 K$ using

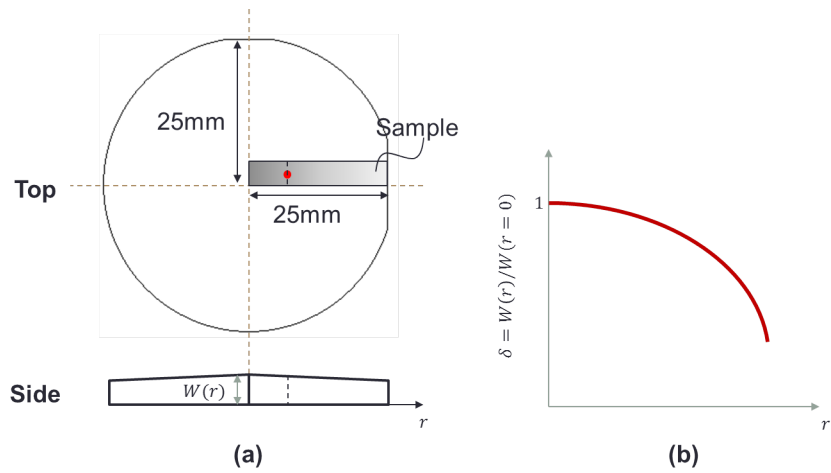


Figure 5.13: Schematic description of (a) a typical sample wafer and (b) the cross-sectional width profile of such a wafer.

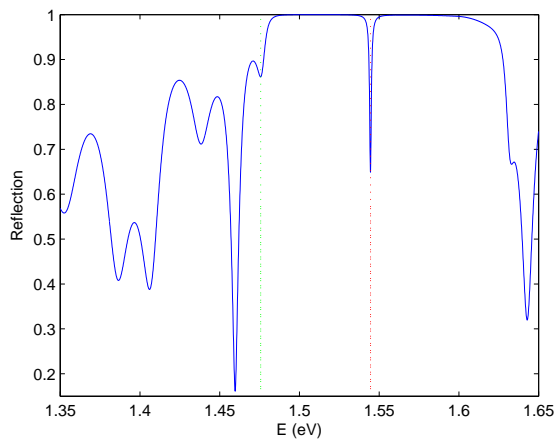


Figure 5.14: The reflection spectrum of the simulated microcavity structure (from figure 5.12), calculated using the transfer matrix method for width detuning $\delta = 0.94$ at $T = 2\text{ K}$. The red and green dashed lines mark, respectively, the location of the cavity mode and the first low energy side-band.

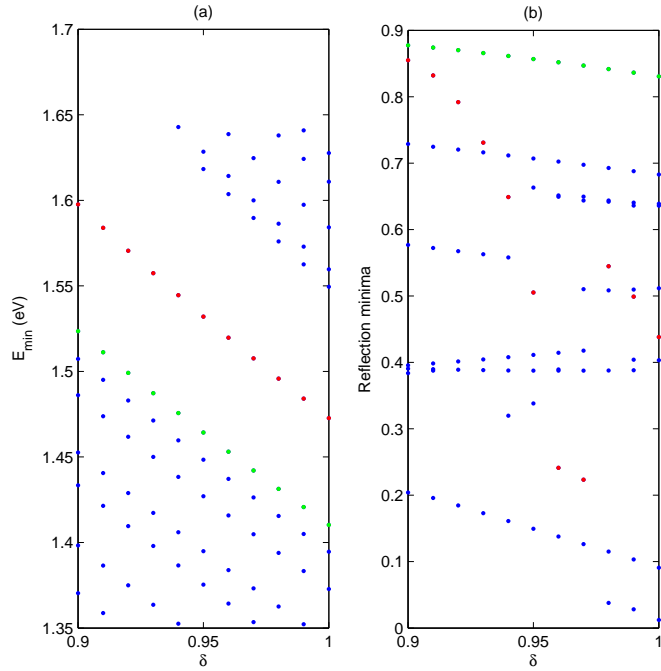


Figure 5.15: The reflection spectrum minima (a) energies and (b) values, calculated for the simulated structure (from figure 5.12) for various detunings.

the TMM, presented in section 5.2.1, for width detuning $\delta = 0.94$, i.e. the epitaxial layers widths shrink by 6% compared to the wafer center values. As an input to the calculation the layers and the refractive indices of the various epitaxial layers are used. The refractive indices are obtained by using empirical results presented in chapter F for the $Ga_xAl_{1-x}As$ alloys. The red dashed line marks the location of the low reflectivity cavity mode location, while the green dashed line marks the location of the first low energy side-band. This calculation can be performed for various values of width detuning parameter δ and ambient temperature T . Figures 5.15(a) and (b) present, respectively, the energetic locations of the reflection spectrum minima and the respective reflection values as a function of wafer width detuning δ , calculated for $T = 2 K$. The cavity mode and the side-band are again marked, respectively, in red and green. It can be easily seen that the cavity mode moves to higher energies as we probe the reflection away from the wafer center ($\delta = 1$), a phenomenon reflecting the linear change of the epitaxial layers widths mentioned above.

5.5.2 Embedded Undoped QW

As we have seen in the previous section, the reflection spectrum of the discussed microcavity structure has a characteristic high reflectivity wide window with a narrow deep trench at the cavity mode energy. We have also seen that the energetic location of this mode follows linearly the change in the structure width detuning, δ . In this section we examine the consequences of introducing a single undoped QW into the cavity region of the MC on the reflection of the entire structure. Figure 5.16 presents such a structure, with the physical dimensions of the various epitaxial layers and their composition, together with the width detuning parameter radial profile (shown in the inset). In order to use the TMM method in the reflection spectrum calculation, the refractive indices of the added QW layers have to be considered. While the cladding $Al_{0.1}Ga_{0.9}As$ layers complex refractive index spectrum can be modeled using the semi-empirical results of appendix F, the well layer index should be separately addressed being the active layer of the structure. As we have seen in chapter 3, the refractive index can be linked to the complex

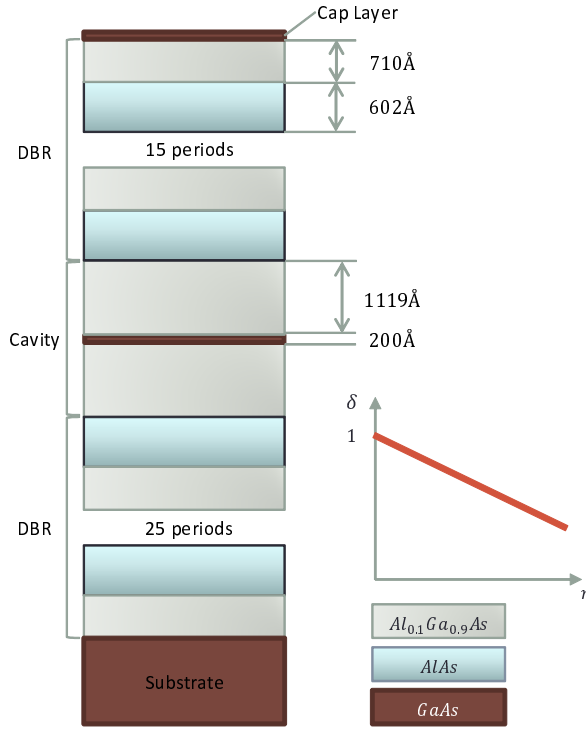


Figure 5.16: Schematic profiles of the simulated microcavity with embedded undoped QW in the cavity region. The linear width detuning parameter δ profile is given as an inset.

electrical susceptibility of the medium through

$$n(\omega) = \sqrt{1 + 4\pi\chi(\omega)}. \quad (5.5.1)$$

In our case, the complex electrical susceptibility spectrum is a superposition of the intrinsic *GaAs* susceptibility, obtained using the empirical data of appendix F, and the results of the theoretical model presented in the previous chapter, namely the HF model, so that $\chi = \chi_{GaAs} + \chi_{QW}^{HF}$. Fig. 5.17 presents an example for such a calculation of $n(\omega)$ for a 200 Å wide *GaAs* QW surrounded by *Al_{0.1}Ga_{0.9}As* barriers with δ -doped layers introduced at 1000 Å away from the barrier-well boundaries, inducing a 2DEG with concentration of $n_e = 1 \times 10^{11} \text{ cm}^{-2}$ in the well region. The obvious similarities to the results of the susceptibility calculation of section 4.3.2 for this concentration are clear.

Now that the refractive index spectra are known for each of the epitaxial layers of the structure, the reflection spectra can be obtained using a standard TMM calculation. Moreover, this calculation can be performed for multiple values of the width detuning parameter δ of the structure in order to trace the influence of the layers width alteration of the reflection spectra of the entire structure. Results of such a calculation at $T = 2 \text{ K}$, performed for $\delta = 0.94 \div 1$, are presented in figure 5.18 for the two light polarizations as a waterfall chart. The inset in figure 5.18(a) shows the reflection spectrum at $\delta = 0.98$ as an illustration. As we have seen in the previous section, the alteration of the detuning parameter δ leads to an energetic shift in the cavity mode location, thereby causing it to interact with the excitonic resonances present in the QW. These strong interactions lead to a characteristic splittings in the cavity mode location seen clearly in these figures for both polarizations. The location of the noninteracting cavity mode is marked by the diagonal red dashed line. This interaction region splitting can be better seen by plotting the reflection spectra minima as a function of the cavity mode energy E_C , as shown in figure 5.19 (for both polarizations), where each set of points along the vertical represents a single δ value. Again, the red diagonal dashed line marks the cavity mode dispersion. The obtained dispersion plots are conventionally termed the reflection anti-crossing curves, reflecting the interaction region splittings in the dispersion curves (circled areas in figure 5.19), and each branch represents a polariton mode. The most striking feature of these representation of the data is the plethora of resonances present, most of which are hardly recognizable in the reflection spectra

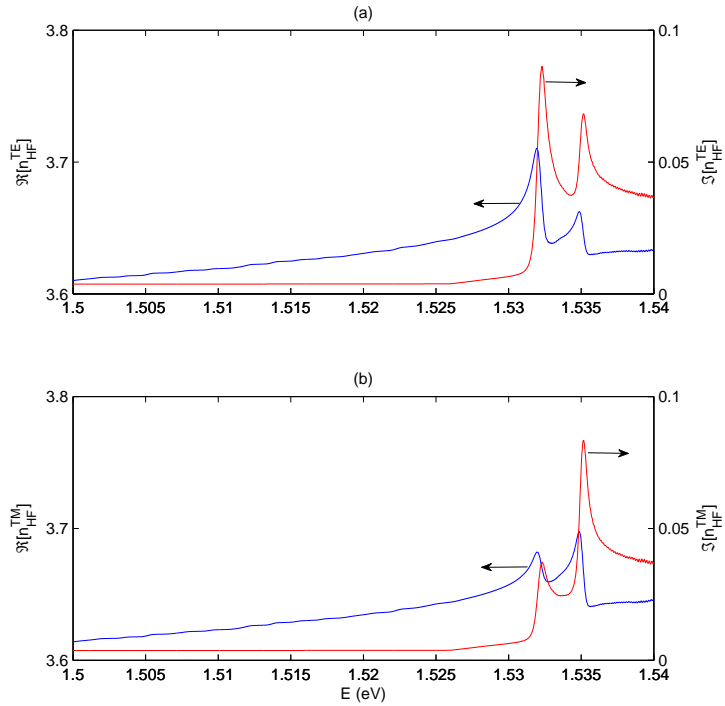


Figure 5.17: The real (blue) and imaginary (red) parts of the total refractive index spectrum of a bare 200\AA wide GaAs QW, surrounded by $\text{Al}_{0.1}\text{Ga}_{0.9}\text{As}$ barriers with δ -doped layers introduced at 1000\AA away from the barrier-well boundaries, inducing a 2DEG with concentration of $n_e = 1 \times 10^{11} \text{ cm}^{-2}$ in the well region. These results were obtained using the HF model for (a) TE and (b) TM polarizations for $T = 2\text{ K}$.

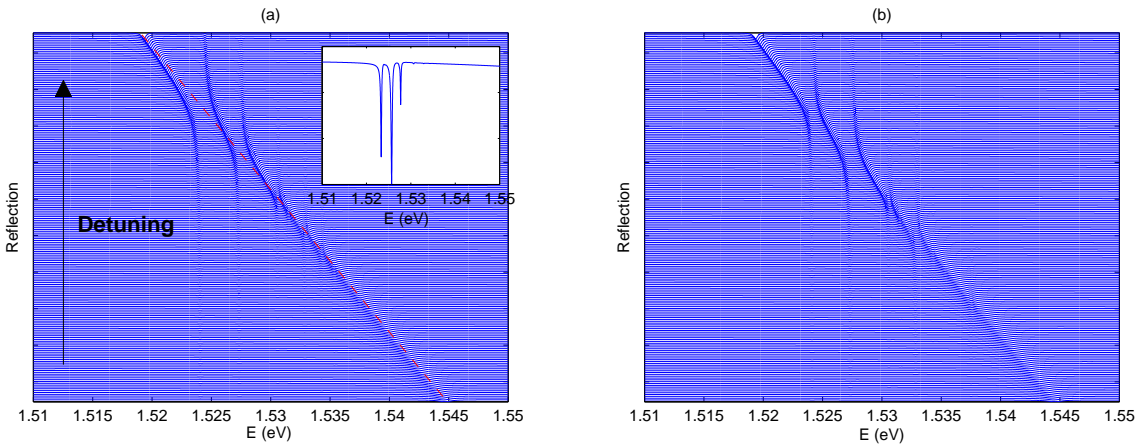


Figure 5.18: The reflection spectra for various width detuning values ($\delta = 0.94 \div 1$) calculated for normal incident light of (a) TE and (b) TM polarizations, at $T = 2\text{ K}$. The inset in (a) shows a zoomed-in view on one of the reflection spectra comprising the waterfall plot (for $\delta = 0.97$), and the red dashed diagonal line in (a) marks the location of the cavity mode.

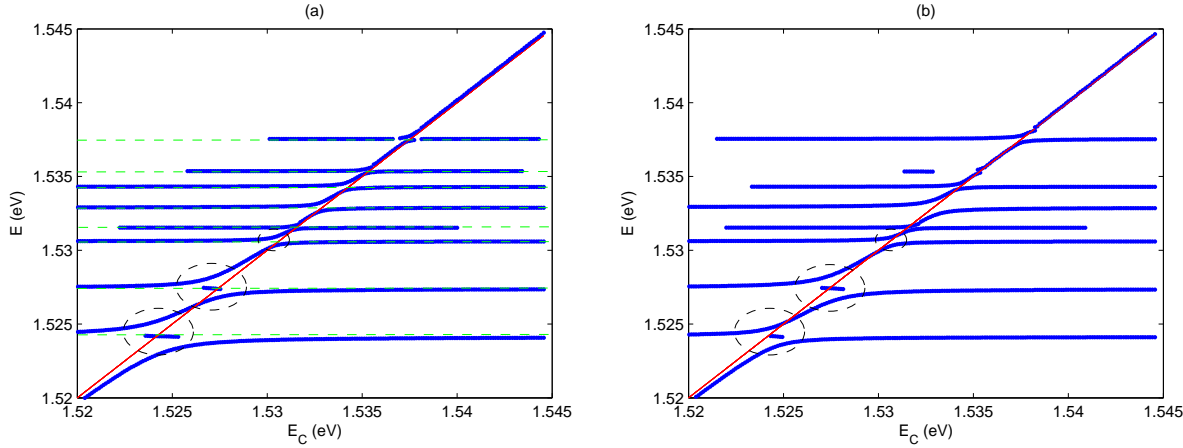


Figure 5.19: *Reflection minima anticrossing curves, extracted from figure 5.18, for (a) TE and (b) TM polarizations of incident light, calculated at $T = 2\text{ K}$. The red dashed line represents the location of the bare MC cavity mode while the horizontal green dashed lines in (a) mark the location of the electronic resonances. The black dashed circles in both figures mark the interactions areas of the cavity mode and the first three excitons.*

Table 5.1: *The extracted parameters of the simulated structure for each of the seven resonances X_i marked in figure 5.20. The second column from the left lists the energetic location of the resonances extracted manually from the figure, while the next three columns contain the coupled oscillator fit parameters.*

	Manual		Coupled oscillator	
	E_X (eV)	E_X (eV)	$\hbar\Omega_X$ (meV)	γ_X (10^{-3} meV)
X_1	1.5242	1.5241	1.4	3.66
X_2	1.5275	1.5274	1.8	3.09
X_3	1.5306	1.5306	0.626	3.23
X_4	1.5315	1.5315	0.28	1.66
X_5	1.5328	1.5329	1.1	19.1
X_6	1.5343	1.5243	0.377	2.03
X_7	1.5376	1.5375	0.765	607
CM	-	-	-	1.7109

in figure 5.18, marked by green horizontal dashed lines. By comparing these curves to the bare QW complex susceptibility calculations in figure 4.11 we can make several observations. First, the locations of the resonance lines in the reflection anti-crossing curves are unsurprisingly similar to the susceptibility resonances. Furthermore, the amount of splitting in the interaction regions and relative strengths of the resonance lines, expressed mainly by the depth of the particular reflection spectrum minima, coincide with the relative amplitudes of the susceptibility spectra resonances. The lowest-most resonance in figure 5.19(a) exhibits the largest splitting, in correlation with the largest absolute amplitude of this particular resonance for the TE and TM susceptibility spectra of 4.11. We thus state the direct connection between the amplitude of the electronic resonance of the bare QW to the amount of splitting in the reflection spectrum, i.e. the interaction strength of light-matter interaction in the cavity.

Fig. 5.20 presents the calculated TM polarization reflection anti-crossing curves (blue dots, as in figure 5.19(b)) with a superimposed coupled oscillator model fit results (red curves). The fitting was performed using the model presented in section (5.4.2.1) with 7 excitons (denoted X_i) corresponding to the seven resonances observed in the calculation results. The fit parameters E_X , $\hbar\Omega_X$ and γ_X are listed in table 5.1 together with a list of manually obtained energetic locations of these resonances. The fitting curves lie very close to the calculated anti-crossing data. The fitting model energy parameter E_X values are almost identical to the manually obtained values and the fitted coupling constant, $\hbar\Omega_X$, reflect the coupling strength in the interaction regions between the photon and the excitonic fields, and their size is in direct correlation to the observed splitting between adjacent branches of the anti-crossing dispersion curves. Using this data we can also convince ourselves that the strong interaction condition,

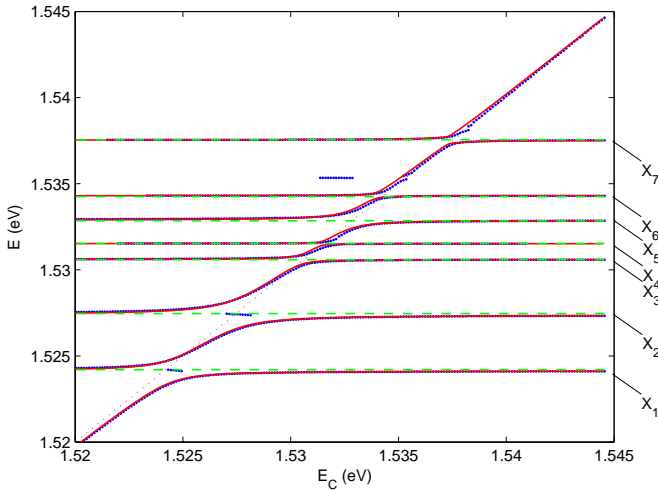


Figure 5.20: The TM polarization reflection minima anticrossing curves fitted using the coupled oscillator model, calculated at $T = 2\text{ K}$. The blue dotted lines are the simulation results, while the red solid lines represent the coupled oscillator fitting curves. The various resonance energies are marked by the green dashed horizontal lines and are denoted as X_i , where $i = 1 - 7$.

namely that $\hbar\Omega_X > \gamma_X, \gamma_C$, is satisfied for each one of the polaritonic branches.

Now we have performed the data coupled oscillator fit to the calculated reflection spectra, the polariton admixing coefficients can be extracted by a simple diagonalization of the obtained Hamiltonian. The results of this procedure for the TM polarization are presented in figure 5.21, where in the left panel we replot the anti-crossing polariton curves, already shown in figure 5.20, and on the right panel we present the admixing coefficients spectra. The numbering on the left is of the polaritonic branches, while on the right we enumerate the bare cavity mode (1) and the bare excitons (2-8). The red dashed line, shown in the $|\alpha_{i,j}|^2$ plot, marks the location of the interaction region and is omitted for the other seven subplots. The presence of the cavity mode (curve 1) in each one of the polariton branches can be clearly seen, together with two dominant excitonic contributions. The strong cavity mode interaction with the bare excitonic modes leads to relatively large admixing of elementary electronic excitations that are very different in nature.

5.5.3 Embedded Doped QW

Now we turn to the case of the doped QWs embedded inside the cavity region of the MC structure. We present such a structure in figure 5.22, together with the physical dimensions of the various epitaxial layers and the width detuning profile (as an inset). As for the undoped structure case, we perform a reflection spectrum calculation using the TMM approach, but now we use the calculated bare QW electrical susceptibility to obtain the well layer refractive index for each of the considered 2DEG concentrations. For the sake of continuity, we use the results presented in section 4.3.2 in the previous chapter for ambient temperature of $T = 2\text{ K}$, i.e. the calculation parameters are $n_e = 1 \times 10^9 \div 5 \times 10^{11} \text{ cm}^{-2}$, $\gamma = 1 \times 10^{11} \text{ sec}^{-1}$.

Figures 5.23 and 5.24 present a collection of calculated reflection spectra in a waterfall plot style (similar to figure 5.14), respectively for the TE and TM normal incident light polarizations, where each subplot in both figures corresponds to a certain n_e value. As before, the width detuning parameter δ values rise from the bottom up for each of the subplots. Figures 5.25 and 5.26 show the appropriate reflection anti-crossing curves for each 2DEG concentration, respectively for the TE and TM polarizations, extracted from the individual reflection spectra by registering the reflection dip minima. Figure 5.26 also presents the results of the coupled oscillator model fitting in the form of superimposed red curves.

These reflection spectra and the derivative anti-crossing dispersion curves present several dominant effects. First, the characteristic strong coupling splitting in the cavity mode and bare exciton interaction regions can be clearly seen, i.e. the presence of polaritons is verified. Moreover, these polaritonic branches remain visible in the structure

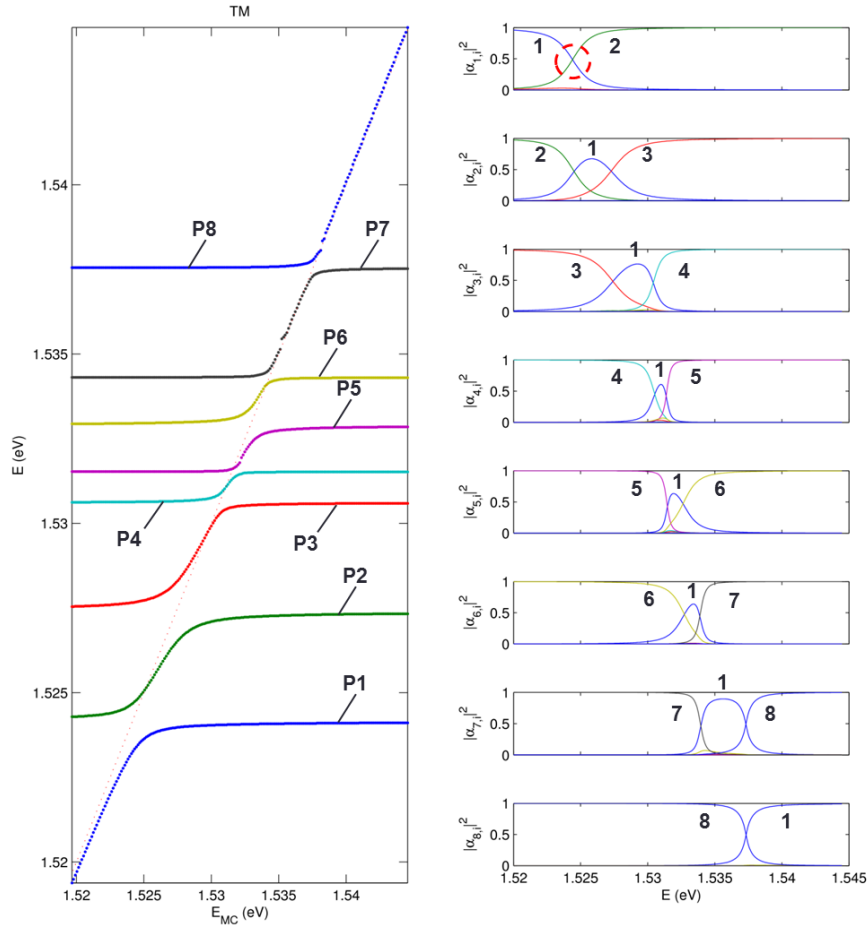


Figure 5.21: The TM polarization reflection minima anticrossing curves (left panel) together with respective polariton admixing coefficients $|\alpha_{i,j}|^2$ (right panel). An example of the interaction region is marked by the dashed red line and the cavity mode is marked by C.

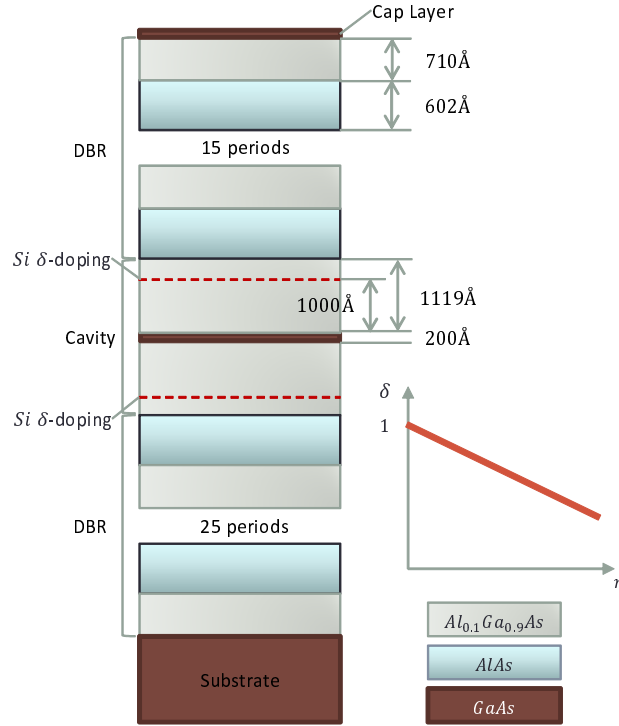


Figure 5.22: Schematic profiles of the simulated microcavity with embedded doped QW in the cavity region.

Table 5.2: The calculated intersubband transition energies for a bare doped QW with $n_e = 7 \times 10^{10} \text{ cm}^{-2}$ and the difference between them.

k_t	$\Delta E_{E_1-HH_1}$ (E ₁) (eV)	$\Delta E_{E_1-LH_1}$ (E ₂) (eV)	$\Delta E_{E_1-HH_2}$ (E ₃) (eV)	$E_2 - E_1$ (meV)	$E_3 - E_1$ (meV)	$E_3 - E_2$ (meV)
0	1.5323	1.5367	1.5396	4.4	6.7	2.3
k_F	1.536	1.5389	1.5443	2.9	8.3	5.4

along much of the discussed 2DEG concentrations diapason (up to $n_e = 2 \times 10^{11} \text{ cm}^{-2}$), contrary to the excitonic lines disappearance for high 2DEG concentrations observed in section 4.3.2 for the bare doped QW. This can be seen clearly for both polarizations of the incident light. We can thus deduce that the strong interaction of the QW resonances with the cavity mode photon delays the effect of the introduced free electrons on these bound resonances. Another noticeable effect present in these figures is the gradual shift in the location of the bare excitonic resonance line, seen especially well in figure 5.26. This shift can be attributed to the shift in the Fermi energy with the rise of the electron concentration, as was discussed in section 4.3.2 for the bare doped QW. It can be also seen that while the shift is not linear for each of the three resonances, marked by green dashed lines in figure 5.26, the distance between these line remains approximately costant along the whole investigated diapason of 2DEG concentrations.

Fig. 5.27 presents the energetic locations of the reflection anti-crossing resonances, E_{X_i} , extracted manually (red empty circles) and obtained from the coupled oscillator fit (blue dots) of the reflection spectra presented previously as a function of the 2DEG concentrations (in a semi logarithmic scale). As we have already seen for the undoped well case in table 5.1, the coupled oscillator model fit gives very similar results to the manually extracted points. Now we can identify each of the resonance lines in the reflection anti-crossing plots. To that end, we examine the energetic transitions present in a bare doped QW for a specific 2DEG concentration, say $n_e = 7 \times 10^{10} \text{ cm}^{-2}$. Fig. 5.28 presents the results of a QW conduction and valence subbands dispersion relations calculation for this particular case using the $\mathbf{k} \cdot \mathbf{p}$ method outlined in chapter 2. We present only the first conduction and three valence subbands, together with the Fermi edge energy for this particular 2DEG concentration. The possible transitions at k_F are explicitly marked. In table 5.2 we summarize the intersubband transition energies at $k_t = 0, k_F$ and

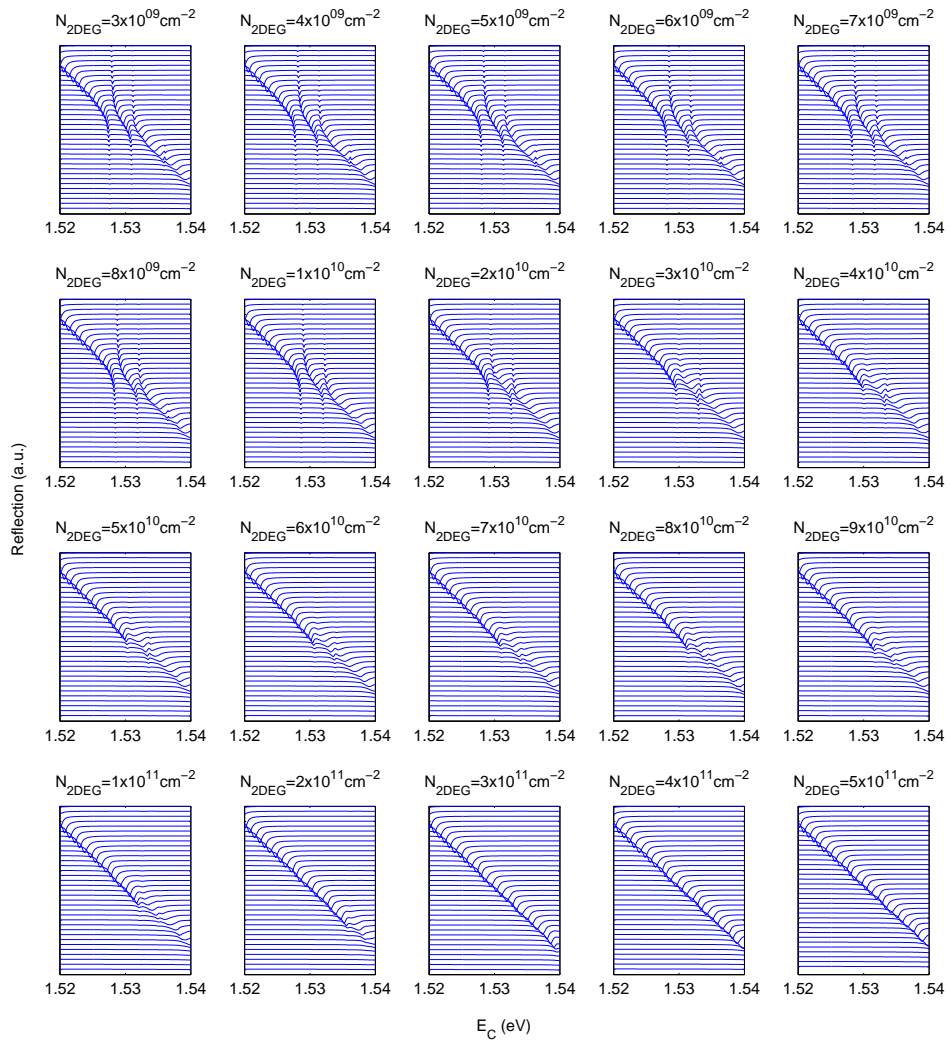


Figure 5.23: The TE reflection spectra as a function of the cavity mode energy, calculated for each of the considered 2DEG concentrations for various width detunings, at T = 2 K.

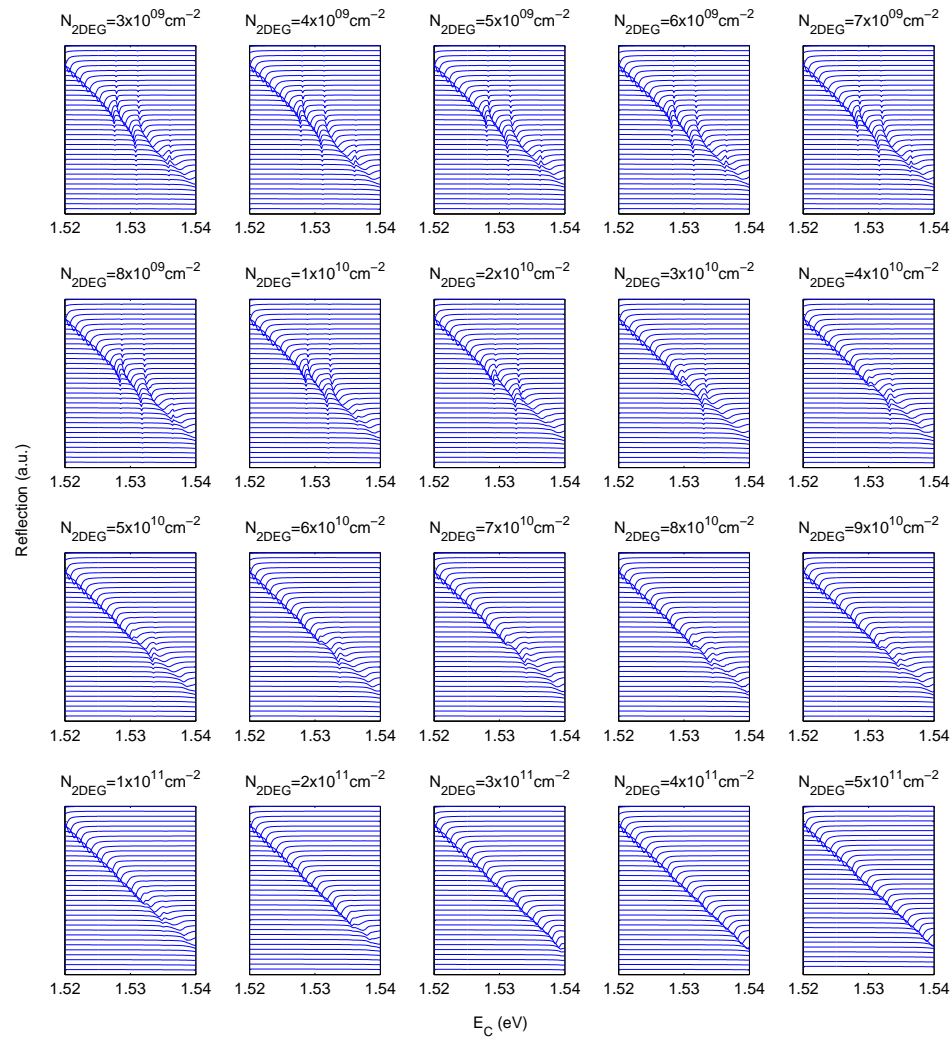


Figure 5.24: The TM reflection spectra as a function of the cavity mode energy, calculated for each of the considered 2DEG concentrations for various width detunings, at T = 2 K.

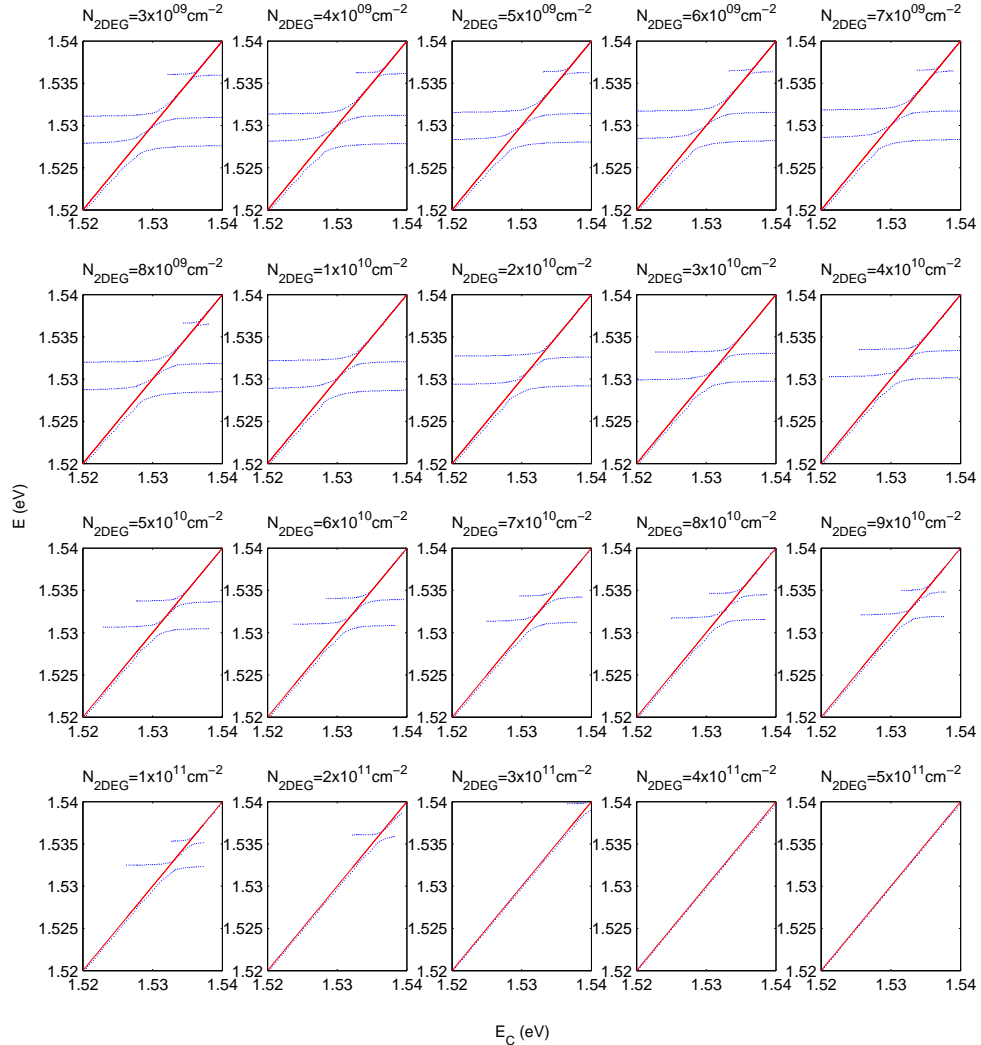


Figure 5.25: The TE reflection minima anticrossing curves (dotted blue) extracted for each 2DEG concentration from the reflection curves in figure 5.23. The cavity mode location is marked by the diagonal red line in each subplot. The suitable 2DEG concentration is shown above each subplot.

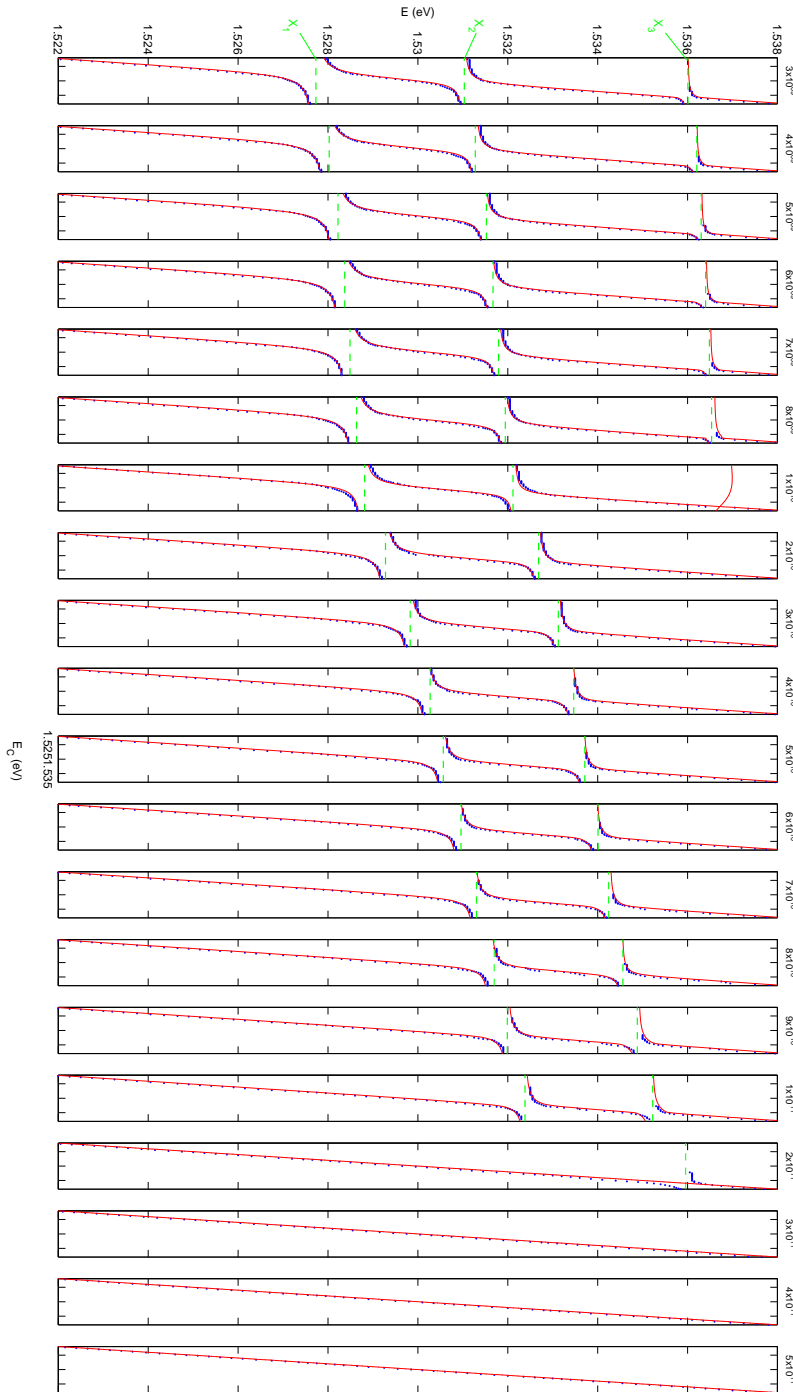


Figure 5.26: The TM reflection minima anticrossing curves (blue dots) extracted for each 2DEG concentration from the reflection curves in figure 5.23, with the superimposed coupled oscillator fitted curves (solid red). The respective 2DEG concentration is shown above each subplot in units of cm^{-2} and the three visible resonances (green dashed lines) are marked as X_i , $i = 1 - 3$.

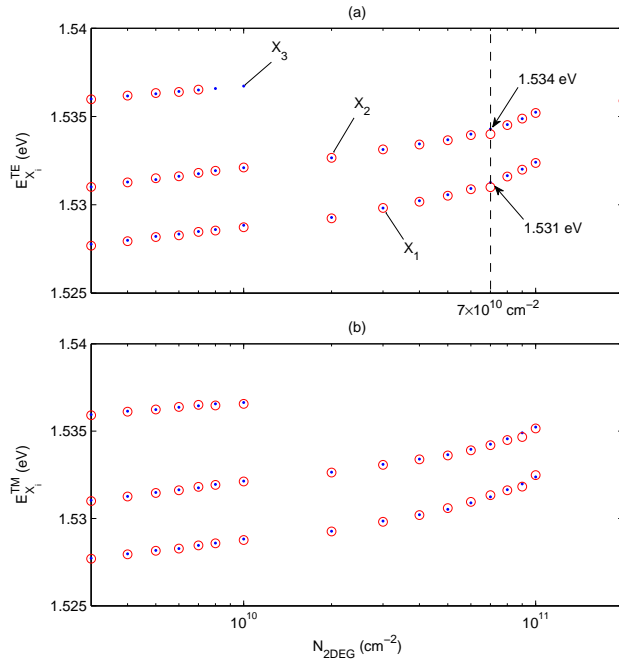


Figure 5.27: The reflection anti-crossing resonance energies as a function of 2DEG concentrations, obtained manually (red circles) and from the coupled oscillator fit results (blue dots) for (a) TE and (b) TM polarizations.

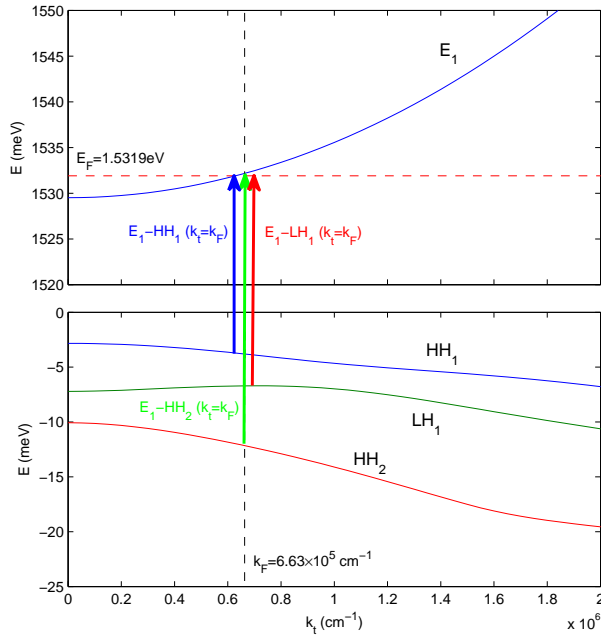


Figure 5.28: Calculated first conduction (E_1) and first three valence (HH_1 , LH_1 and HH_2) subbands dispersion relations for a bare doped QW with $n_e = 7 \times 10^{10} \text{ cm}^{-2}$, for $T = 2 \text{ K}$. The Fermi edge energy E_F and wavevector k_F are marked, respectively red and black dashed lines, together with intersubband transition energies.

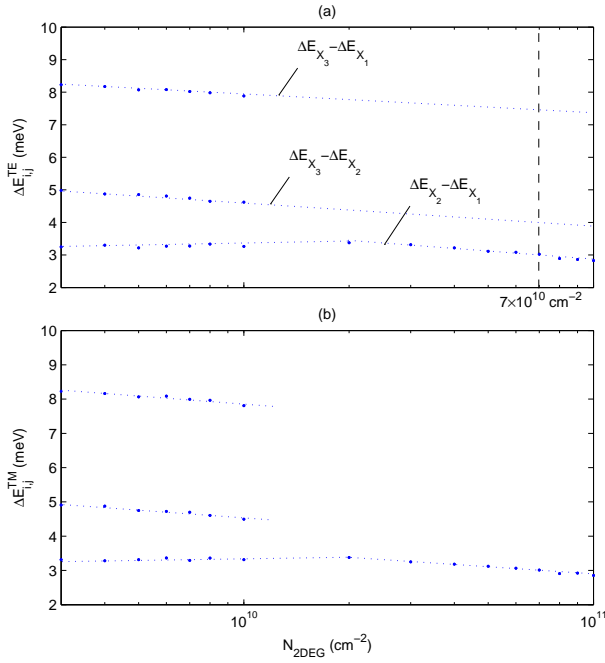


Figure 5.29: The energetic distance between the anticrossing resonance lines as a function of 2DEG concentrations for the (a) TE and (b) TM polarizations. The vertical dashed line marks the location of the $n_e = 7 \times 10^{10} \text{ cm}^{-2}$ concentration values.

the energetic difference between them. It is not surprising that the calculated transition energies do not match the values marked in figure 5.27 for this 2DEG concentration, as these transition energies do not take into consideration the bandgap renormalization effect inherent to the electrical susceptibility calculation. Granted that the estimate for this renormalization energy, obtained from figure 4.7(a), is $\approx -4.5 \text{ meV}$ for $n_e = 7 \times 10^{10} \text{ cm}^{-2}$, the actual transition energy for the two examined resonances in figure 5.27 are 1.5356 eV and 1.5386 eV, respectively for X_1 and X_2 . These values are very close to the values of the Fermi edge transition energies, i.e. at $k_t = k_F$. In order to verify this observation, we calculate the differences between the resonance energies in figure 5.27 for various 2DEG concentrations, and plot them graphically in figure 5.29. For the considered 2DEG concentration, the energetic differences between X_1 and X_2 resonances is 3 meV, a value very close to the 2.9 meV obtained from the intersubband transitions calculation in table 5.2. By performing the same procedure for the all other 2DEG concentration values, we can state that the observed X_1 , X_2 and X_3 resonances in the reflection anti-crossing curves are, respectively, the $E_1 - HH_1$, $E_1 - LH_1$ and $E_1 - HH_2$ intersubband transitions at the Fermi edge energy.

Now that we have identified the nature of the various resonances present in the reflection anti-crossing curves, we discuss their various other properties. Fig. 5.30 presents the coupling coefficients obtained for each resonance from the coupled oscillator model as a function of the 2DEG concentration. We can draw several conclusions from these plots. First, the general trends of the coupling coefficients can be clearly seen (marked by the respective dashed lines). It is clear that the $E_1 - HH_1$ resonance is much more susceptible to the change in the 2DEG concentration than the $E_1 - LH_1$ resonance. Second, the cavity mode coupling to the $E_1 - HH_1$ resonance (or exciton) is stronger than to the $E_1 - LH_1$ resonance for the TE polarization, while the situation is the other way around for the TM polarization. This switch in the coupling strength can be traced back to the relative amplitudes of the lowest two resonance of the bare QW absorption (and thus of the complex susceptibility) spectra in figures 4.26 and 4.27, where the for the TE polarization (fig. 4.26) the lowest resonance is the dominant one, and visa versa for the TM polarization (fig. 4.27). Finally, by comparing the absolute values of these coupling coefficients to those obtained earlier for the MC structure with the undoped QW (using the values listed in table 5.1), we can state that the introduction of 2DEG inside the cavity region doesn't impact substantially the coupling strength of the cavity mode photon to the electronic resonances present in the QW.

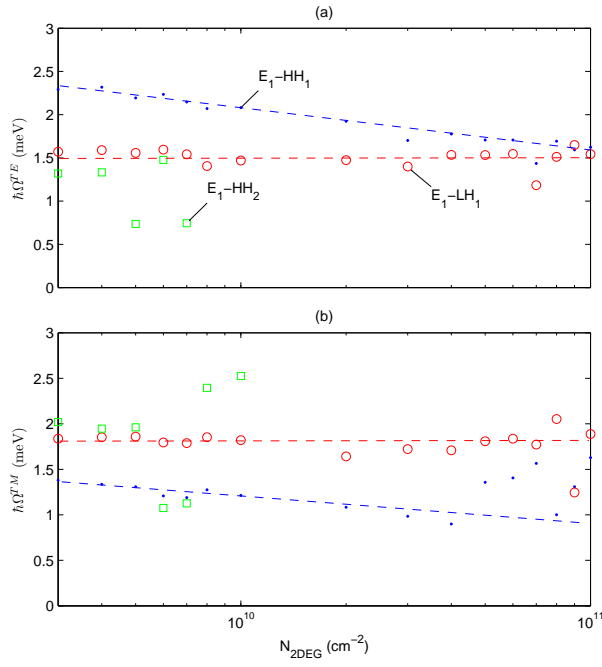


Figure 5.30: The coupling parameters extracted from the coupled oscillator fit of the reflection anti-crossing curves, for the (a) TE and (b) TM polarizations, as a function of the 2DEG concentration. The dashed lines mark the general trend of the various collections of data points.

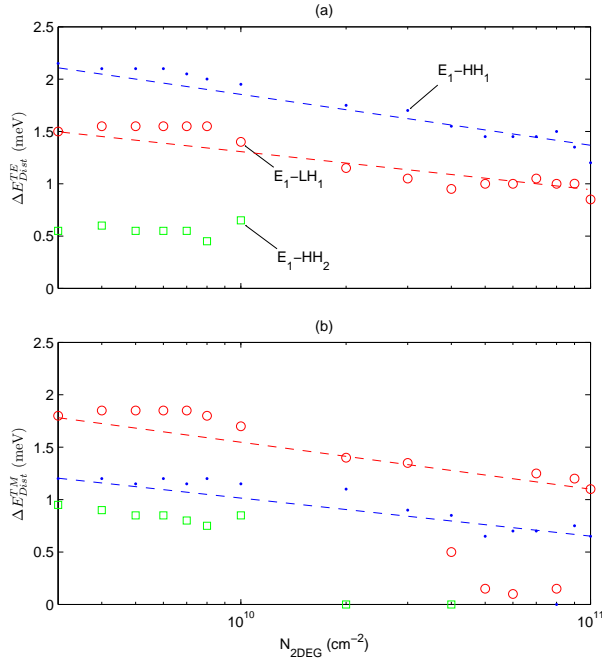


Figure 5.31: The energetic distance between adjacent anti-crossing curves near resonance lines as a function of the 2DEG concentration for (a) TE and (b) TM polarizations.

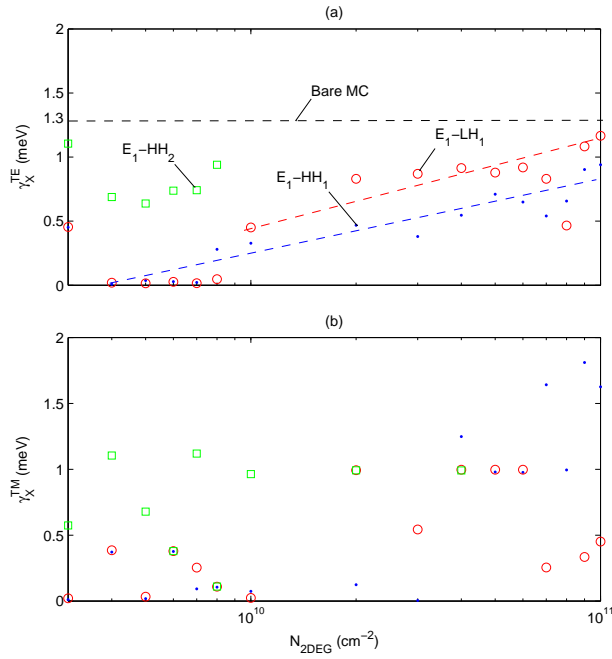


Figure 5.32: The resonance interaction linewidths extracted for various resonances using the coupled oscillator model fit of the anti-crossing curves as a function of the 2DEG concentration, for (a) TE and (b) TM polarizations. The dashed line mark the general trend of the appropriate resonance linewidth parameter.

Fig. 5.31 presents the Euclidean distances between the various polaritonic branches in the reflection anti-crossing curves in figures 5.25 and 5.26, respectively for the TE and TM polarizations. By comparing the obtained plots to figure 5.30, we can convince ourselves that this, in fact, can be an alternative method for the calculation of the cavity mode photon coupling to the QW excitons. We can claim this based on the similarity of the absolute values of the respective curves in the two figures, and the appearance of the discussed switch of the $E_1 - HH_1$ and $E_1 - LH_1$ coupling strength between the two polarizations.

Now we turn to discuss the linewidth properties of the calculated reflection spectra. Fig. 5.32 presents the coupled oscillator linewidth parameter, γ_X , dependence on the 2DEG concentration, obtained from the fit to the reflection spectra presented earlier. We can clearly see that the TM polarization fitting parameters in figure 5.32(b) are unintelligible and thus should be ignored. The TE polarization fitted parameters in figure 5.32(a) exhibit a clear trends (marked by the dashed lines) towards rising linewidths of all three visible resonances, reflecting the dephasing of the bound excitonic states due to the rising 2DEG electron concentrations. For comparison, we plot the bare MC cavity mode linewidth, found to be during the calculations in section 5.5.1 to be 1.3 eV. In order to further validate these results, we perform a manual calculation of the FWHM of the reflection spectra along multiple values of the 2DEG concentration, for a single value of the width detuning parameter δ . Fig. 5.33 presents the reflection spectra calculated at $\delta = 0.9528$ for the full diapason of the 2DEG concentrations for both polarizations. Here, the broadening of the resonance lines be clearly seen from the low concentrations up to the higher ones. These figures reveal two additional effects, discussed earlier in this thesis. The first is the gradual disappearance of the excitonic resonances due to the lowering of the coupling strength, and the second is the gradual shift of these fading resonance lines towards higher energies with the rising 2DEG concentrations. Fig. 5.34 presents the results of the FWHM calculation of the three major resonances present in figure 5.33 plotted as a function of the 2DEG concentration. As expected, the obtained plots are somewhat similar to the coupled oscillator fitting linewidth parameters in figure 5.32, but there are also several differences. First of all, the there is a consistency between the results for both light polarizations. Furthermore, the most dominant resonances, namely $E_1 - HH_1$ and $E_1 - LH_1$, exhibit quite different behavior. While $E_1 - HH_1$ linewidths rise almost monotonically with the 2DEG concentration, the $E_1 - LH_1$ linewidths have a somewhat more complex trajectory, where we first we observe a declining trend up

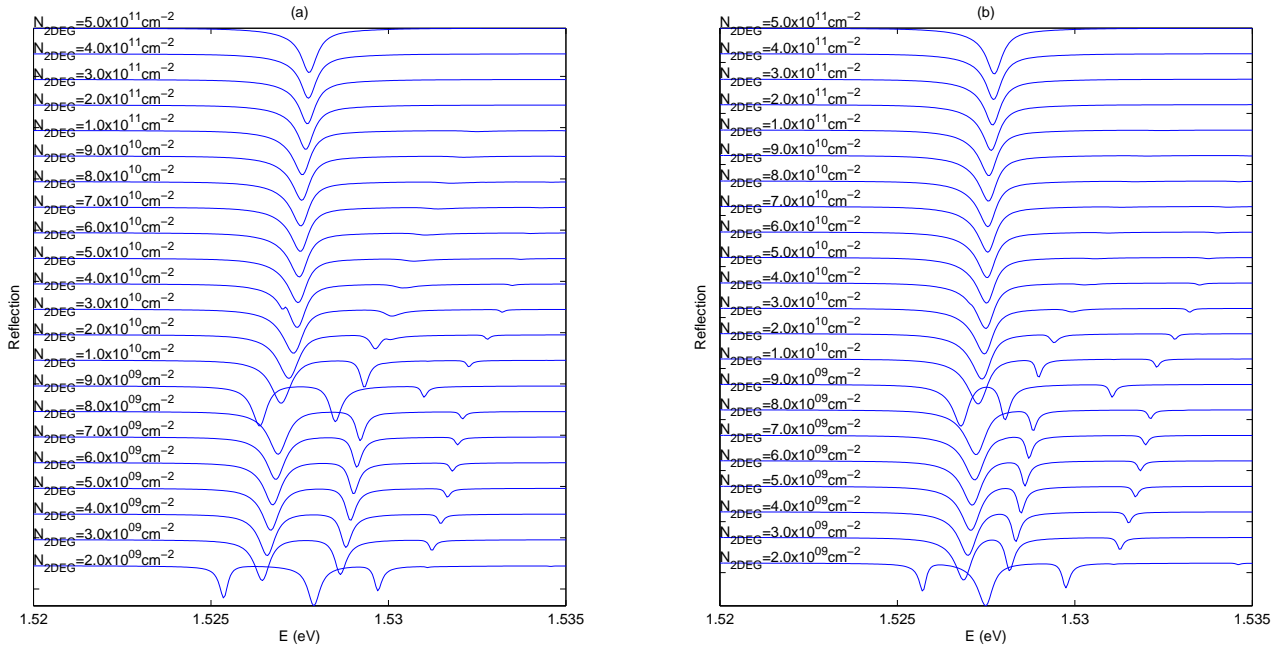


Figure 5.33: *Reflection spectra for various 2DEG concentrations calculated at width detuning of $\delta \approx 0.95$, for the (a) TE and (b) TM polarizations of the incident light.*

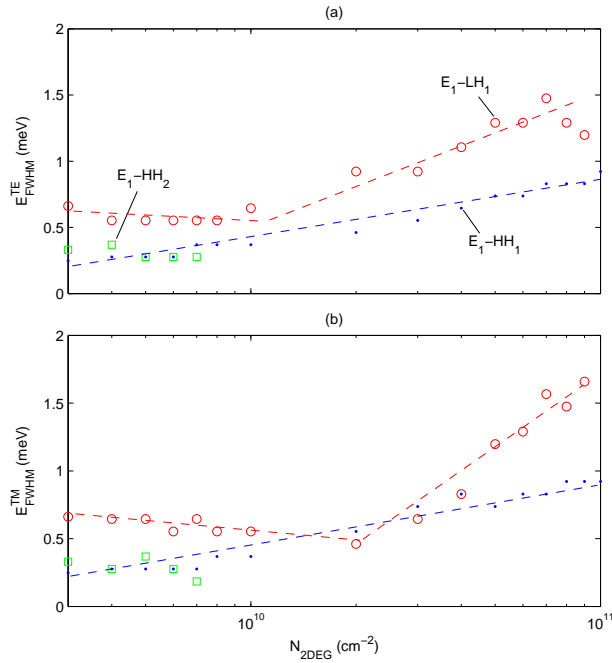


Figure 5.34: *The reflection spectra linewidths function of the 2DEG concentration, extracted manually (via FWHM calculation) for each of the present resonances at width detuning of $\delta \approx 0.95$, for (a) TE and (b) TM polarizations.*

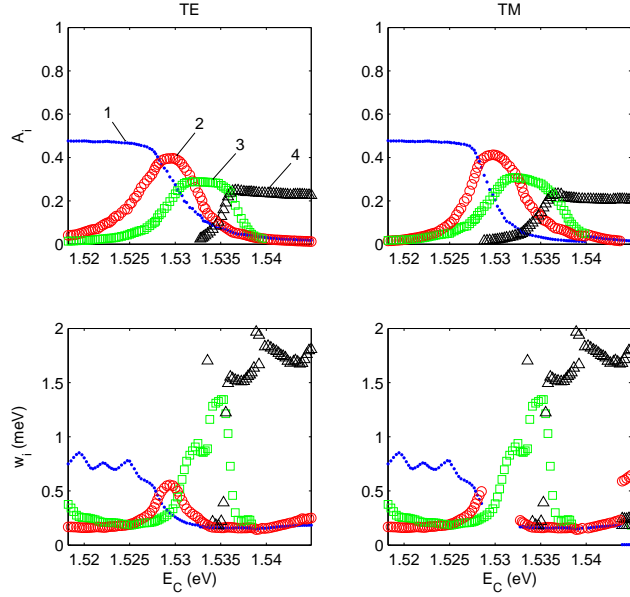


Figure 5.35: The fitted amplitude and width of the transmission peaks as a function of cavity mode energy, obtained for each resonance branch (numbered 1-4) for the TE (left panel) and TM (right panel) at $n_e = 3 \times 10^9 \text{ cm}^{-2}$.

to $n_e \approx 1 \times 10^{10} \text{ cm}^{-2}$ which then reverts and rises steadily up to the high 2DEG concentrations. Comparing the calculated coupling strengths between the cavity mode photon and the excitonic resonances, presented above in figures 5.30 and 5.31, to the linewidths discussed above, we can easily see that the strong interaction condition that $\hbar\Omega_{X_i} > \gamma_{X_i}$ is maintained for most of the discussed 2DEG concentrations diapason.

The previous discussion considered the evolution of the polaritonic linewidths with the 2DEG concentration in the considered diapason. Now we turn to the calculation of the linewidths dependence on the cavity mode energy for a particular gas concentration. As the manual FWHM calculation of the various spectral dips for each reflection spectrum for every value of the width detuning parameter δ is a rather daunting task, we opt to a more approximate approach. For each value of δ , we convert the reflection spectrum to transmission and subsequently fit the obtained curve with a Lorentzian target function of the form

$$T = 1 - |r|^2 = \sum_i A_i \frac{w_i}{2\pi} \frac{1}{(E - E_i)^2 + (w_i/2)^2}, \quad (5.5.2)$$

where the parameters A_i , w_i and E_i , including the range of i , are all determined through a least-squares fitting procedure. Figures 5.35, 5.36 and 5.37 present the results of such a fit, respectively for $n_e = 3 \times 10^9$, 3×10^{10} and $1 \times 10^{11} \text{ cm}^{-2}$ 2DEG concentrations. In each of these figures we present the amplitudes of the transmissions peaks and their width for both light polarizations.

The amplitudes A_i in each figures (and for each polarization) present a picture of the relative admixture of the various polaritonic branches in the resulting reflection spectrum picture. For the low 2DEG concentration, four of these branches are present, while with the rise of concentration the high energy resonances phase and only strongest of these remain. Moreover, a collective energetic shift can be seen with the rise of the 2DEG concentration in all of the present amplitude curves. The FWHM curves exhibit a somewhat more complicated behavior, but the overall trend of rising linewidth with the 2DEG concentration is still noticeable. This complex behavior can be analyzed qualitatively by considering the lineshapes of the individual excitons interacting with the cavity mode electron [62], a discussion which is outside the scope of this thesis.

Finally, we present in figures 5.38, 5.39 and 5.40 the polariton admixing coefficients extracted through the coupled oscillator model fitting of the reflection anti-crossing spectra, similarly to procedure employed in the previous section. Here, as for the undoped QW case, the strong presence of the cavity mode photon is clearly seen, maintaining its strong coupling with the individual excitonic resonances and thus ensuring their survival up the very high 2DEG concentration values.

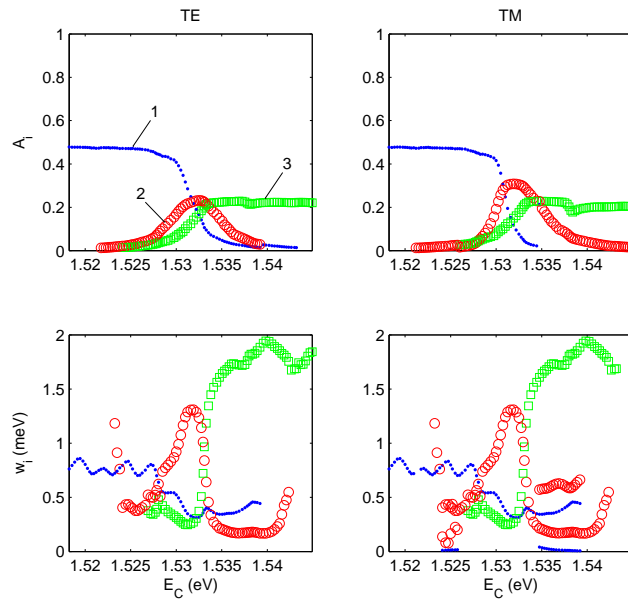


Figure 5.36: The fitted amplitude and width of the transmission peaks as a function of cavity mode energy, obtained for each resonance branch (numbered 1-3) for the TE (left panel) and TM (right panel) at $n_e = 3 \times 10^{10} \text{ cm}^{-2}$.

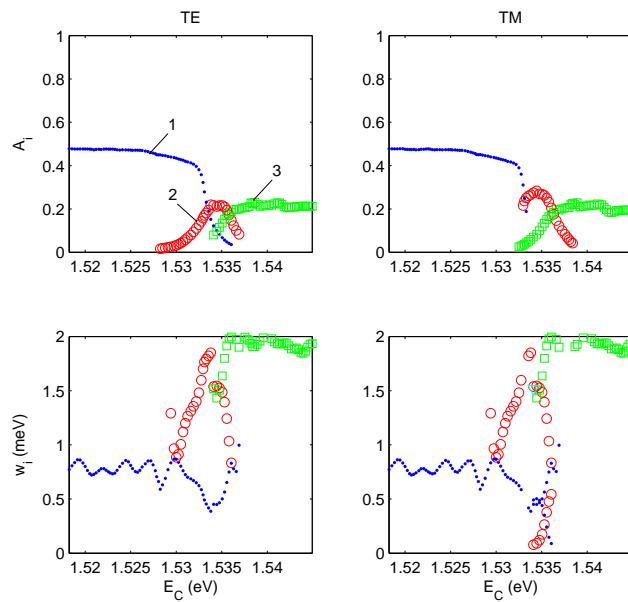


Figure 5.37: The fitted amplitude and width of the transmission peaks as a function of cavity mode energy, obtained for each resonance (numbered 1-3) for the TE (left panel) and TM (right panel) at $n_e = 1 \times 10^{11} \text{ cm}^{-2}$.

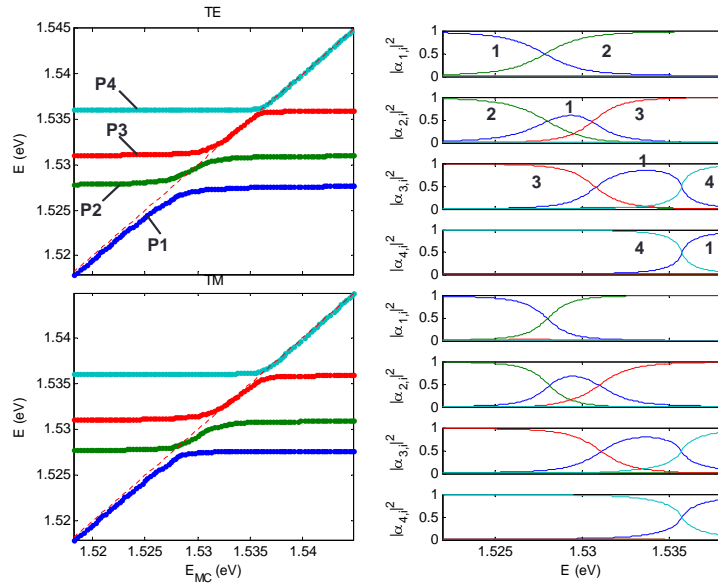


Figure 5.38: The polariton admixing coefficients extracted from the coupled oscillator model fit of the anti-crossing curves for $n_e = 3 \times 10^9 \text{ cm}^{-2}$.

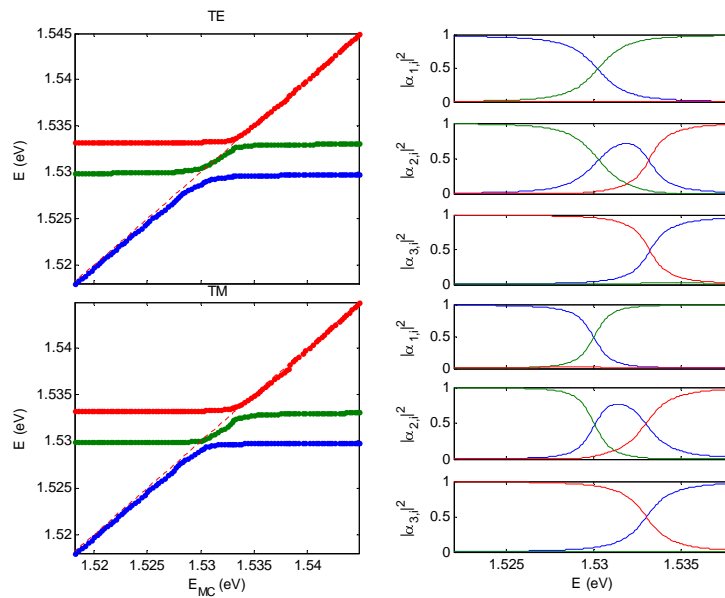


Figure 5.39: The polariton admixing coefficients extracted from the coupled oscillator model fit of the anti-crossing curves for $n_e = 3 \times 10^{10} \text{ cm}^{-2}$.

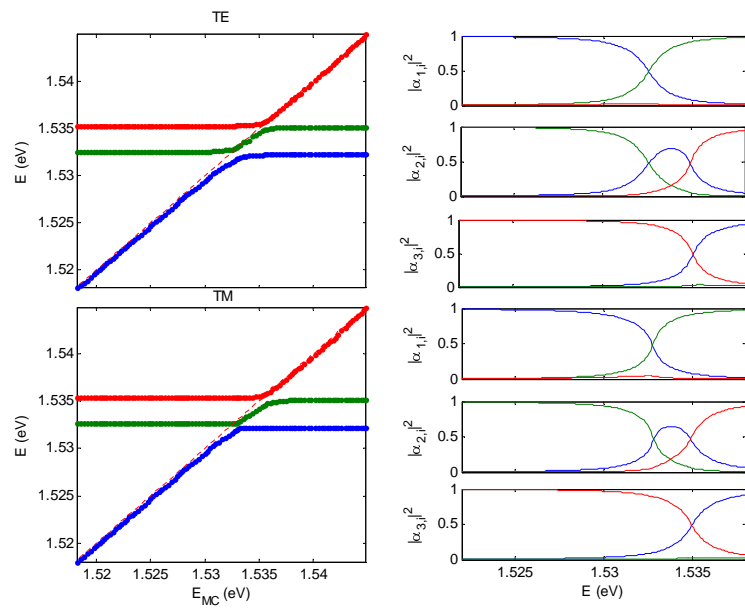


Figure 5.40: The polariton admixing coefficients extracted from the coupled oscillator model fit of the anti-crossing curves for $n_e = 1 \times 10^{11} \text{ cm}^{-2}$.

Summary and Outlook

In this work we presented a theoretical study of the various aspects of light-matter interactions taking place in variety of quantum structures, such as bare quantum wells and semiconductor microcavities, and the influence of the introduced 2DEG on their optical properties.

We start our discussion in chapter 2 by presenting the electronic properties of quantum well structures. After a general introduction of the approximate $\mathbf{k} \cdot \mathbf{p}$ approach, we concern ourselves with the two-band variation of this method, mainly due to its implementation simplicity. Using this approach we calculate the dispersion relations of the conduction and valence subbands in a bulk semiconductor and single bare quantum well. The influence of the crystallographic orientation on the results is examined and found to be minor in the relevant portion of the k -space. This observation allows us to simplify our calculations by assuming full angular symmetry of the QW in the k -space without a substantial loss to the generality. Next, we consider the introduction of doping inside the quantum well and explore its influence on the electronic properties. To this end, we add to our quantum mechanical approach a complementary electrostatic part in the form of Poisson equation solution for the specific charge distribution. Through this approach we attain doping dependent corrections to the band edges of the considered QW, which introduce minor corrections to the conduction and valence subband energies in the middle of the first Brillouin region.

Once we have obtained the electronic properties of bare QWs with introduced 2DEG of various concentrations, we turn to the investigation of the optical properties of these structures. Our approach to this task is semi-classical in its core, where only the matter, i.e. the semiconductor, is treated quantum mechanically. In chapter 3, we first assume that the carriers present in the semiconductor are free and noninteracting, and only simple dephasing mechanism is used. We complicate this simple picture in chapter 4 by the introduction of Coulombic interaction between the electrons and holes in the structure, together with a simple screening scheme to model the influence of the introduced high concentration 2DEG. Although these models are both approximate in nature, they enable us to compute various optical parameters of the bare QWs under the assumption of dipole interaction of the electronic system with the optical field. Using this approach we compute the electrical susceptibility and spontaneous emission spectra of the structure, through which the absorption and refractive indices can be easily computed. This computation is then performed for QWs with and without the presence of 2DEG carriers inside the well region, and for a wide diapason of these carriers' concentrations, all these for various ambient temperatures. By comparing the computation results of these two models, we reach the expected conclusion that the introduction of the Coulombic interaction changes dramatically the obtained results. The introduced Coulomb enhancement of reproduces strong bellow-bandgap resonance lines for the undoped QW absorption and spontaneous emission spectra, which are in good agreement with other theoretical models discussed in literature. The observed bandgap renormalization for the Coulomb correlated model results also match the classical theoretical dependence of the 2DEG carriers concentration. The results of the doped QW spectra computation lead to several noticeable effects. First, the introduction of additional 2DEG carriers leads to a significant reduction in the strength of the observed absorption resonance lines, causing their effective disappearance for concentrations above $\approx 6 \times 10^{10} \text{ cm}^{-2}$. Second, the added 2DEG carriers lead to the appearance of a characteristic inhomogeneous broadened line in the spontaneous emission at low ambient temperature of 2 K . Finally, through the dynamics of the spontaneous emission and the absorption spectra with the 2DEG carriers concentration, we observe a Burstein-Moss shift causing a split between the two types of spectra for high concentrations. As a consequence of the attained results for the bare QW, we chose the Coulomb correlated model to be used for the modeling of such structures in the subsequent calculations.

Being in a position to model the electronic and optical properties of a bare QW, we next consider microcavities and their optical properties in chapter 5. First we consider the reflectivity properties of such structures and the numerical method for their calculation, followed by a short discussion of the coupling of a quantum mechanical

absorber with the light field mode inside the cavity region. The results of the bare QW optical properties calculations are incorporated into the full MC reflectivity computation through an altered form of the linear dispersion model, effectively introducing a QW inside the cavity region of the MC. This procedure enables us to perform an investigation of the reflection spectra of the entire MC structure, and thereby investigate the coupling of the cavity mode with the various bare QW resonances. The reflection spectra of the MC with undoped QW inside the cavity region revealed a strong coupling of the cavity mode with the various QW resonances, seen through the characteristic splittings of the anti-crossing curves in the regions of interaction. This observation is backed by the parameters of a fit of the anti-crossing curves with the coupled oscillator model. Moreover, the polariton admixing coefficients, extracted through the fitting procedure, reaffirm this observation. As the next logical step, a doped bare QW is introduced inside the cavity region of the MC and the reflection spectra are calculated for various values of 2DEG concentration. The most striking feature of the obtained reflection anti-crossing curves is the appearance of strong coupling between the cavity mode photon and certain QW resonances at relatively high 2DEG concentrations, in contrast to the observed disappearance of all such resonances for the bare QW. By comparing the energetic locations of these resonances to the bare QW allowed energetic transitions, we identify them to be unbound electron-hole resonances at the Fermi edge energy. This finding coincides with earlier experimental results [43] for similar structures, and stands as the central finding of this work. When we compare the coupling strength parameters, extracted using the coupled oscillator fit of the reflection anti-crossing curves for various 2DEG concentrations, we find them to be generally larger from those obtained for the undoped QW case. This indicates to a higher coupling of the found electron-hole resonances with the cavity mode than the bare QW case. We conclude by stating that the main mechanism for the coherence between all the electron-hole pair excitations interacting with the confined cavity mode is the strong interaction itself, despite the existence of Coulomb attraction between the electron and hole.

Although this work presents a complete theoretical framework for the calculation of the optical properties of MC with embedded QWs, further research should be performed to gain better understanding of the origin of the strong interaction between the confined cavity mode and the electron-hole pair resonances at the Fermi edge. Here we present several possible pathways that may be taken to address this issues:

- As we have stated above, both the free carrier and Coulomb correlated models, used to calculate the bare QW electrical susceptibility, do not take into account higher order correlation effects and relaxation mechanisms. Such extensions are rarely easy to introduce into the current framework, probably at the expense of computational complexity.
- In addition to the improved modelling of the bare QW, a cavity damping mechanism can be introduced to the MC modeling in order to approximate the cavity mode behavior to the physical reality.
- An angular calculation of the reflection spectra of the MC with embedded QW can be performed, in order to obtain the dispersion relation of the various polaritonic branches and thereby attain a better insight into their electronic nature.
- In addition to the calculation of the reflection spectra of the entire MC, the spontaneous emission spectra should also be calculated and compared.
- Since excitons and unbound electrons and holes exhibit very different dependence on magnetic field (respectively diamagnetic and linear), the electronic model of the bare QW should be extended to include the influence of external magnetic field. Dispersion calculations in weak magnetic fields should provide a clue as to the nature of the various polaritonic branches.
- The temperature analysis performed in this work for the bare QW should be extended to the full MC calculations, especially when the linewidths of the various polaritonic branches are considered, as it may facilitate in differentiating between excitons and unbound electron-hole pair resonances.

Appendices

Appendix A

Symmetry Properties of Wavefunctions

In this appendix we present a short overview of the symmetry properties of bulk semiconductor wavefunction, expressed in the mathematical formulation of the group theory.

Let $H(\mathbf{r}) = T + U(\mathbf{r})$ be the Hamiltonian in (2.1.14) with the kinetic operator T and crystal potential $U(\mathbf{r})$, and let G be the point group¹ of the crystal such that the symmetry operator $g \in G$, the crystal potential is invariant, i.e.

$$\forall g \in G, \quad U(g^{-1}\mathbf{r}) = U(\mathbf{r}). \quad (\text{A.0.1})$$

The kinetic operator T is naturally invariant under the action of the elements in the point group G . Assuming that $\psi(\mathbf{r})$ is an eigenfunction of H with $H(\mathbf{r})\psi(\mathbf{r}) = E\psi(\mathbf{r})$ and applying the symmetry operator g , leads to

$$H(g^{-1}\mathbf{r})\psi(g^{-1}\mathbf{r}) = H(\mathbf{r})\psi(g^{-1}\mathbf{r}) = E\psi(g^{-1}\mathbf{r}). \quad (\text{A.0.2})$$

Obviously $\psi'(\mathbf{r}) = \psi(g^{-1}\mathbf{r})$ is also an eigenfunction of the Hamiltonian operator $H(\mathbf{r})$ with eigenvalue E . The wavefunction $\psi'(\mathbf{r})$ might be the same wavefunction as $\psi(\mathbf{r})$ or might be linearly independent. Applying all symmetry operations $g \in G$ therefore results in a set of wavefunctions with the same eigenvalue E , spanning a function space

$$I_\psi = \{\psi'(\mathbf{r}) | \psi'(\mathbf{r}) = \psi'(g^{-1}\mathbf{r}) \quad \forall g \in G\}. \quad (\text{A.0.3})$$

Now, the point group G is a closed group, meaning that for $g, f \in G : gf \in G$. Therefore, the function space I_ψ is invariant under the action of G ,

$$\psi(\mathbf{r}) \in I_\psi \Rightarrow \psi(g^{-1}\mathbf{r}) \in I_\psi. \quad (\text{A.0.4})$$

Suppose that $\{\psi_0, \psi_1, \dots, \psi_N\}$ is the basis of the subspace I_ψ , which is assumed to be of the dimension N . The basis is denoted as being the *irreducible representation* of the group G . The desirable property deduced from group theory is that for every symmetry group, there are only a few distinct irreducible representations. Every irreducible representation describes an unique way how wavefunctions are transformed under the action of the elements of a symmetry group G . Therefore, the eigenfunctions of the crystal Hamiltonian H can be classified according to the irreducible representation they form. It is clear that each eigenfunction does only belong to one irreducible representation and it is clear that eigenfunctions corresponding to different irreducible representations are always orthogonal. In the following, the theory will be focused on the zinc-blende crystal, for which the symmetry group of the Hamiltonian is T_d , the tetrahedral group. The elements are given by the 24 symmetry operations mapping a tetrahedron to itself. For an appropriate alignment and orientation, the symmetry operations are listed in Table A.1. T_d has in total five distinct irreducible representations, which are commonly labeled as $\Gamma_1, \Gamma_2, \Gamma_{12}, \Gamma_{15}$ and Γ_{25} . Γ_1 and Γ_2 are one dimensional representations, Γ_{12} is a two dimensional and Γ_{15} and Γ_{25} are three dimensional. The basis functions for all irreducible representations are given in Table A.2. The representation Γ_1 is the identity representation, also denoted as trivial representation, leaving the wavefunction invariant. An atomic wavefunction with s -like symmetry transforms accordingly, i.e. is left unchanged under the action of the elements of the group T_d . An example of the Γ_1 representation is given by the conduction band at the Γ point of zinc-blende, direct

¹A *crystallographic point group* is a set of symmetry operations, like rotations or reflections, that leave a point fixed while moving each atom of the crystal to the position of an atom of the same kind. That is, an infinite crystal would look exactly the same before and after any of the operations in its point group. In the classification of crystals, each point group corresponds to a crystal class.

Table A.1: Symmetry operations of the group T_d using the Schönflies notation (notations after [2]).

Type	Operation $(xyz) \rightarrow (\dots)$
E	(xyz)
$3C_2$	$(\bar{x}\bar{y}z), (xy\bar{z}), (\bar{x}\bar{y}\bar{z})$
$8C_3$	$(zxy), (yzx), (\bar{y}z\bar{x}), (\bar{z}\bar{x}y), (\bar{y}\bar{z}x), (z\bar{x}\bar{y}), (y\bar{z}\bar{x}), (\bar{z}\bar{x}\bar{y})$
$6C_4$	$(\bar{x}zy), (\bar{x}\bar{z}y), (z\bar{y}x), (\bar{z}\bar{y}x), (\bar{y}xz), (y\bar{x}\bar{z})$
6σ	$(\bar{y}x\bar{z}), (yx\bar{z}), (\bar{z}y\bar{x}), (zyx), (xzy), (x\bar{z}\bar{y})$

Table A.2: Basis functions of the tetrahedral symmetry group T_d .

Γ_i	Dimension	Basis functions
Γ_1	1	xyz
Γ_2	1	$x^4(y^2 - z^2) + y^4(z^2 - x^2) + z^2(x^2 - y^2)$
Γ_{12}	2	$(x^2 - y^2), z^2 - \frac{1}{2}(x^2 + y^2)$
Γ_{15}	3	x, y, z
Γ_{25}	3	$x(y^2 - z^2), y(z^2 - x^2), z(x^2 - y^2)$

bandgap III-V semiconductors. The conduction band at the Γ point is non-degenerate with a wavefunction obeying s -type symmetry. Another important irreducible representation is given by the top of the valence band at the Γ point. Neglecting the later considered spin-orbit splitting, the valence band is threefold degenerate, with p -type basis functions x, y and z , transforming under the action of T_d according to the elements of a vector. The p -type basis functions correspond to the representation Γ_{15} . The goal is now to use the introduced group theory to analyze the properties of the momentum matrix elements (2.1.17). The momentum operator \mathbf{p} is given by a vector of three operators

$$\mathbf{p} = \begin{pmatrix} p_x \\ p_y \\ p_z \end{pmatrix},$$

obviously transforming like the elements of a vector. Therefore, the momentum operator forms an irreducible representation of Γ_{15} . The action of the momentum operator on wavefunctions of the irreducible representation Γ_j leads to a new expression. The corresponding representation is given by the *direct product* $\Gamma_{15} \otimes \Gamma_j$ (see [2], p. 46), as one has p_u acting on the basis function ψ_v for $u = x, y, z$ and $v = 1, \dots, N$. The direct product is not *irreducible*, but can be decomposed into a *direct sum* of irreducible representations

$$\Gamma_{15} \otimes \Gamma_j = \sum_u \oplus \Gamma_i. \quad (\text{A.0.5})$$

Recall that functions not belonging to the same irreducible representation are orthogonal. Therefore, the matrix element $\langle \psi^{\Gamma_i} | \mathbf{p} | \psi^{\Gamma_j} \rangle$ between two wavefunctions belonging to the irreducible representation Γ_i and Γ_j is nonzero only if the direct sum (A.0.5) of the direct product $\Gamma_{15} \otimes \Gamma_j$ contains Γ_i . For the tetrahedral symmetry, the decomposition of the direct product into the direct sum is given in Table A.3, from which the vanishing momentum matrix elements (2.1.17) can be calculated. They are given by the matrix in A.4. Within the matrix, X denotes a non-vanishing and the 0 denotes a vanishing matrix element. In order to further reduce the number of unknowns, equivalent matrix elements can be determined using the basis functions defined in Table A.2 and symmetry operations of G . As an example, for the Γ_1 type conduction band, the only non-vanishing momentum matrix elements involve - according to Table A.4 - only bands belonging to Γ_{15} . Γ_1 is represented by the function xyz and Γ_{15} by x, y and z . The only non-vanishing matrix element is of the type $\langle xyz | p_x | x \rangle$. For the other, e.g. $\langle xyz | p_x | z \rangle$, a rotation of the crystal by 180° around the rotation axis [001] results in

$$\langle xyz | p_x | x \rangle = -\langle xyz | p_x | z \rangle,$$

which can only be met if the matrix element is zero.

Table A.3: Direct products of the Γ_{15} representation with all representations of T_d (after [2]).

Direct product	Direct sum
$\Gamma_{15} \otimes \Gamma_1$	Γ_{15}
$\Gamma_{15} \otimes \Gamma_2$	Γ_{25}
$\Gamma_{15} \otimes \Gamma_{12}$	$\Gamma_{15} \oplus \Gamma_{25}$
$\Gamma_{15} \otimes \Gamma_{15}$	$\Gamma_{15} \oplus \Gamma_{25} \oplus \Gamma_{12} \oplus \Gamma_1$
$\Gamma_{15} \otimes \Gamma_{25}$	$\Gamma_{15} \oplus \Gamma_{25} \oplus \Gamma_{12} \oplus \Gamma_2$

Table A.4: The non-vanishing momentum matrix elements between the states corresponding to different irreducible representations of the tetrahedral symmetry group. A zero denotes a vanishing and X a non-vanishing element.

P	$ \psi^{\Gamma_1}\rangle$	$ \psi^{\Gamma_2}\rangle$	$ \psi^{\Gamma_{12}}\rangle$	$ \psi^{\Gamma_{15}}\rangle$	$ \psi^{\Gamma_{25}}\rangle$
$\langle \psi^{\Gamma_1} $	0	0	0	X	0
$\langle \psi^{\Gamma_2} $	0	0	0	0	X
$\langle \psi^{\Gamma_{12}} $	0	0	0	X	X
$\langle \psi^{\Gamma_{15}} $	X	0	X	X	X
$\langle \psi^{\Gamma_{25}} $	0	X	X	X	X

Appendix B

Two-Band Model Numerical Implementation

The method used to solve the Hamiltonian equations in the two-band model is based on the shooting method formulated in [25] for the simple case of the conduction band.

As a starting point, we consider the general one-dimensional form of the Hamiltonian equation (2.2.55). In order to allow for a location dependent effective mass, we rewrite this equation as

$$\begin{pmatrix} \hat{H}_{hh} + V(z) & \hat{W} \\ \hat{W}^\dagger & \hat{H}_{lh} + V(z) \end{pmatrix} \begin{pmatrix} F_{hh} \\ F_{lh} \end{pmatrix} = E(\mathbf{k}) \begin{pmatrix} F_{hh} \\ F_{lh} \end{pmatrix}, \quad (\text{B.0.1})$$

with

$$\hat{H}_{lh} = -\frac{\partial}{\partial z} (\gamma_1(z) + 2\gamma_2(z)) \frac{\partial}{\partial z} + (\gamma_1(z) - \gamma_2(z)) k_t^2, \quad (\text{B.0.2})$$

$$\hat{H}_{hh} = -\frac{\partial}{\partial z} (\gamma_1(z) - 2\gamma_2(z)) \frac{\partial}{\partial z} + (\gamma_1(z) + \gamma_2(z)) k_t^2, \quad (\text{B.0.3})$$

$$\hat{W} = \begin{cases} \sqrt{3}k_t (\gamma_2(z)k_t - 2\gamma_3(z)\frac{\partial}{\partial z}) & \text{for } [100] \\ \sqrt{3}k_t (\gamma_3(z)k_t - 2\gamma_2(z)\frac{\partial}{\partial z}) & \text{for } [110] \end{cases} \quad (\text{B.0.4})$$

The potential $V(z)$ describes the valence band edge of the quantum well structure (in terms of hole energy), and F_{hh} and F_{lh} represent the hole wavefunction while under the effective mass and envelope function approximations.

We can rewrite the effective mass equations as

$$\begin{pmatrix} \hat{H}_{hh} + V(z) - E & \hat{W} \\ \hat{W}^\dagger & \hat{H}_{lh} + V(z) - E \end{pmatrix} \begin{pmatrix} F_{hh} \\ F_{lh} \end{pmatrix} = 0. \quad (\text{B.0.5})$$

The problem now is to find a numerical method for the solution of both the energy eigenvalues E and the eigenfunctions F for any $V(z)$. For this purpose, we can expand the first and second derivatives in terms of finite differences. The first derivative of a function $f(z)$ can be approximated to

$$\frac{df}{dz} \approx \frac{\Delta f}{\Delta z} = \frac{f(z + \delta z) - f(z - \delta z)}{2\delta z}. \quad (\text{B.0.6})$$

The second derivative follows as

$$\begin{aligned} \frac{d^2 f}{dz^2} &\approx \frac{\frac{df}{dz}\Big|_{z+\delta z} - \frac{df}{dz}\Big|_{z-\delta z}}{2\delta z} \\ &= \frac{f(z + 2\delta z) - 2f(z) + f(z - 2\delta z)}{(2\delta z)^2}. \end{aligned} \quad (\text{B.0.7})$$

As δz is an, as yet, undefined small step along the z -axis, and as it only appears in equation (B.0.7) with the factor 2, then we can simplify this expression by substituting δz for $2\delta z$

$$\frac{d^2 f}{dz^2} \approx \frac{f(z + \delta z) - 2f(z) + f(z - \delta z)}{(\delta z)^2}. \quad (\text{B.0.8})$$

Let us focus on the term $\hat{H}_{lh}^0 = -\frac{\partial}{\partial z}(\gamma_1 + 2\gamma_2)\frac{\partial}{\partial z}$ in the light hole Hamiltonian, and express it in terms of finite differences. We can rewrite this term as

$$\hat{H}_{lh}^0 = -\frac{\partial}{\partial z}(\gamma_1(z) + \gamma_2(z))\frac{\partial F_{lh}}{\partial z} + (\gamma_1(z) + \gamma_2(z))\frac{\partial^2 F_{lh}}{\partial z^2}. \quad (\text{B.0.9})$$

However, the shooting equations derived from this point by expanding the derivatives in terms of finite differences have led to significant computational inaccuracies in systems with a large discontinuous change in the effective mass (the Luttinger parameters), as occurs in the *GaAs/AlGaAs* system. The source of the inaccuracies is thought to arise from the δ -function nature of the effective mass derivative.

A more robust scheme can be derived by expanding \hat{H}_{lh}^0 starting from the left-hand derivative

$$\hat{H}_{lh}^0 \approx \frac{(\gamma_1 + \gamma_2)\frac{\partial F_{lh}}{\partial z}|_{z+\delta z} - (\gamma_1 + \gamma_2)\frac{\partial F_{lh}}{\partial z}|_{z-\delta z}}{2\delta z}. \quad (\text{B.0.10})$$

Recalling the centered finite difference expansion for the first derivative (B.0.6), we can write the numerator of the above expression as

$$2\delta z \hat{H}_{lh}^0 = (\gamma_1 + 2\gamma_2)|_{z+\delta z} \frac{F_{lh}(z + 2\delta z) - F_{lh}(z)}{2\delta z} + (\gamma_1 + 2\gamma_2)|_{z-\delta z} \frac{F_{lh}(z) - F_{lh}(z - 2\delta z)}{2\delta z}, \quad (\text{B.0.11})$$

or

$$(2\delta z)^2 \hat{H}_{lh}^0 = (\gamma_1 + 2\gamma_2)|_{z+\delta z} [F_{lh}(z + 2\delta z) - F_{lh}(z)] + (\gamma_1 + 2\gamma_2)|_{z-\delta z} [F_{lh}(z) - F_{lh}(z - 2\delta z)]. \quad (\text{B.0.12})$$

Making the transformation $2\delta z \rightarrow \delta z$ then yields

$$\begin{aligned} \hat{H}_{lh}^0 &= \frac{1}{(\delta z)^2} \left[(\gamma_1 - 2\gamma_2)^+ F_{lh}(z + \delta z) \right. \\ &\quad - \left((\gamma_1 - 2\gamma_2)^+ + (\gamma_1 - 2\gamma_2)^- \right) F_{lh}(z) \\ &\quad \left. + (\gamma_1 - 2\gamma_2)^- F_{lh}(z - \delta z) \right], \end{aligned} \quad (\text{B.0.13})$$

with

$$(\gamma_1 + 2\gamma_2)^+ = (\gamma_1 + 2\gamma_2)|_{z+\delta z/2}, \quad (\text{B.0.14})$$

$$(\gamma_1 + 2\gamma_2)^- = (\gamma_1 + 2\gamma_2)|_{z-\delta z/2}, \quad (\text{B.0.15})$$

$$(\gamma_1 - 2\gamma_2)^+ = (\gamma_1 - 2\gamma_2)|_{z+\delta z/2}, \quad (\text{B.0.16})$$

$$(\gamma_1 - 2\gamma_2)^- = (\gamma_1 - 2\gamma_2)|_{z-\delta z/2}. \quad (\text{B.0.17})$$

We now substitute the finite difference expressions for $\partial/\partial z$, \hat{H}_{lh}^0 and a similar expression for the heavy-hole

counterpart into the effective mass equations, and obtain

$$\begin{aligned} 0 &= -\frac{(\gamma_1 - 2\gamma_2)^+}{(\delta z)^2} F_{hh}(z + \delta z) + \frac{(\gamma_1 - 2\gamma_2)^+ + (\gamma_1 - 2\gamma_2)^-}{(\delta z)^2} F_{hh}(z) \\ &\quad - \frac{(\gamma_1 - 2\gamma_2)^-}{(\delta z)^2} F_{hh}(z - \delta z) + (\gamma_1 + \gamma_2) k_t^2 F_{hh}(z) \\ &\quad + (V(z) - E) F_{hh}(z) + \sqrt{3} \gamma_2 k_t^2 F_{lh}(z) - 2\sqrt{3} \gamma_3 k_t \frac{F_{lh}(z + \delta z) - F_{lh}(z - \delta z)}{2\delta z}, \end{aligned} \quad (\text{B.0.18})$$

$$\begin{aligned} 0 &= \sqrt{3} \gamma_2 k_t^2 F_{hh}(z) + 2\sqrt{3} \gamma_3 k_t k_t \frac{F_{hh}(z + \delta z) - F_{hh}(z - \delta z)}{2\delta z} \\ &\quad - \frac{(\gamma_1 + 2\gamma_2)^+}{(\delta z)^2} F_{lh}(z + \delta z) + \frac{(\gamma_1 + 2\gamma_2)^+ + (\gamma_1 + 2\gamma_2)^-}{(\delta z)^2} F_{lh}(z) \\ &\quad - \frac{(\gamma_1 + 2\gamma_2)^-}{(\delta z)^2} F_{lh}(z - \delta z) + (\gamma_1 - \gamma_2) k_t^2 F_{lh}(z) + (V(z) - E) F_{lh}(z). \end{aligned} \quad (\text{B.0.19})$$

The Luttinger parameters γ_i can be found at the intermediary points $z \pm \delta z/2$ by taking the mean of the two neighboring points z and $z \pm \delta z$.

It can be seen that we draw up a set of finite difference equations if we map the potential $V(z)$ and the Luttinger parameters γ_i to a grid along the z -axis. To solve these coupled equations and find the energies E and functions F we assume a equidistant grid z_i , with a grid step δz , we can substitute $z \rightarrow z_i$, $z - \delta z \rightarrow z_{i-1}$ and $z + \delta z \rightarrow z_{i+1}$. If we assume a given energy E , we are still left with 6 unknown parameters in the finite difference equations. However, we can rewrite these equations so that we are able to find $F_{lh}(z_{i+1})$ and $F_{hh}(z_{i+1})$ from their values at the two previous nodes, z_{i-1} and z_i

$$\begin{aligned} F_{hh}(z_{i+1}) \left[1 + 3 \frac{\gamma_3^2}{(\gamma_1 + 2\gamma_2)^+ (\gamma_1 - 2\gamma_2)^-} k_t^2 (\delta z)^2 \right] &= \\ F_{hh}(z_{i-1}) \left[-\frac{(\gamma_1 - 2\gamma_2)^-}{(\gamma_1 - 2\gamma_2)^+} + 3 \frac{\gamma_3^2}{(\gamma_1 + 2\gamma_2)^+ (\gamma_1 - 2\gamma_2)^+} k_t^2 (\delta z)^2 \right] & \\ + F_{lh}(z_{i-1}) \left[\sqrt{3} \frac{\gamma_3}{(\gamma_1 - 2\gamma_2)^+} k_t \delta z \left(1 + \frac{(\gamma_1 + 2\gamma_2)^-}{(\gamma_1 + 2\gamma_2)^+} \right) \right] & \\ F_{hh}(z_i) \left[\frac{(\gamma_1 - 2\gamma_2)^+ + (\gamma_1 - 2\gamma_2)^-}{(\gamma_1 - 2\gamma_2)^+} + \frac{\gamma_1 + \gamma_2}{(\gamma_1 - 2\gamma_2)^+} k_t^2 (\delta z)^2 \right] & \\ + \frac{V(z_i) - E}{(\gamma_1 - 2\gamma_2)^+} (\delta z)^2 - 3 \frac{\gamma_3 \gamma_2}{(\gamma_1 + 2\gamma_2)^+ (\gamma_1 - 2\gamma_2)^+} k_t^3 (\delta z)^3 \right] & \\ + F_{lh}(z_i) \left[\sqrt{3} \frac{\gamma_2}{(\gamma_1 - 2\gamma_2)^+} k_t^2 (\delta z)^2 \right. & \\ - \sqrt{3} \frac{\gamma_3}{(\gamma_1 - 2\gamma_2)^+} \frac{(\gamma_1 + 2\gamma_2)^+ + (\gamma_1 + 2\gamma_2)^-}{(\gamma_1 + 2\gamma_2)^+} k_t \delta z & \\ - \sqrt{3} \frac{\gamma_3 (\gamma_1 - \gamma_2)}{(\gamma_1 + 2\gamma_2)^+ (\gamma_1 - 2\gamma_2)^+} k_t^3 (\delta z)^3 & \\ \left. - \sqrt{3} \frac{\gamma_3}{(\gamma_1 + 2\gamma_2)^+ (\gamma_1 - 2\gamma_2)^+} (V(z_i) - E) k_t (\delta z)^3 \right], \quad (\text{B.0.20}) & \end{aligned}$$

$$\begin{aligned}
F_{lh}(z_{i+1}) \left[1 + 3 \frac{\gamma_3^2}{(\gamma_1 + 2\gamma_2)^+ (\gamma_1 - 2\gamma_2)^+} k_t^2(\delta z)^2 \right] = \\
F_{lh}(z_{i-1}) \left[-\frac{(\gamma_1 + 2\gamma_2)^-}{(\gamma_1 + 2\gamma_2)^+} + 3 \frac{\gamma_3^2}{(\gamma_1 + 2\gamma_2)^+ (\gamma_1 - 2\gamma_2)^+} k_t^2(\delta z)^2 \right] \\
+ F_{hh}(z_{i-1}) \left[\sqrt{3} \frac{\gamma_3}{(\gamma_1 + 2\gamma_2)^+} k_t \delta z \left(1 + \frac{(\gamma_1 - 2\gamma_2)^-}{(\gamma_1 - 2\gamma_2)^+} \right) \right] \\
F_{lh}(z_i) \left[\frac{(\gamma_1 + 2\gamma_2)^+ + (\gamma_1 + 2\gamma_2)^-}{(\gamma_1 + 2\gamma_2)^+} + \frac{\gamma_1 - \gamma_2}{(\gamma_1 + 2\gamma_2)^+} k_t^2(\delta z)^2 \right. \\
+ \frac{V(z_i) - E}{(\gamma_1 + 2\gamma_2)^+} (\delta z)^2 + 3 \frac{\gamma_3 \gamma_2}{(\gamma_1 + 2\gamma_2)^+ (\gamma_1 - 2\gamma_2)^+} k_t^3(\delta z)^3 \\
+ F_{hh}(z_i) \left[\sqrt{3} \frac{\gamma_2}{(\gamma_1 + 2\gamma_2)^+} k_t^2(\delta z)^2 \right. \\
+ \sqrt{3} \frac{\gamma_3}{(\gamma_1 + 2\gamma_2)^+} \frac{(\gamma_1 - 2\gamma_2)^+ + (\gamma_1 - 2\gamma_2)^-}{(\gamma_1 - 2\gamma_2)^+} k_t \delta z \\
+ \sqrt{3} \frac{\gamma_3 (\gamma_1 + \gamma_2)}{(\gamma_1 + 2\gamma_2)^+ (\gamma_1 - 2\gamma_2)^+} k_t^3(\delta z)^3 \\
\left. + \sqrt{3} \frac{\gamma_3}{(\gamma_1 + 2\gamma_2)^+ (\gamma_1 - 2\gamma_2)^+} (V(z_i) - E) k_t(\delta z)^3 \right]. \quad (\text{B.0.21})
\end{aligned}$$

These equations imply that, if the wavefunctions are known at the two points $z - \delta z$ and z , then the value at $z + \delta z$ can be determined for any energy E . This iterative equation forms the basis of a standard method of solving equations numerically, and is known as the *shooting method*.

The equations can be rewritten in a matrix notation, which allows easy programmable implementation. Using a coefficient notation for these two equations of the form

$$F_{hh}(z_{i+1}) = a_1 F_{hh}(z_{i-1}) + a_2 F_{lh}(z_{i-1}) + a_3 F_{lh}(z_i) + a_4 F_{hh}(z_i), \quad (\text{B.0.22})$$

$$F_{lh}(z_{i+1}) = b_1 F_{hh}(z_{i-1}) + b_2 F_{lh}(z_{i-1}) + b_3 F_{hh}(z_i) + b_4 F_{lh}(z_i), \quad (\text{B.0.23})$$

the effective mass equations can be written in a recursive transfer matrix expression

$$\begin{pmatrix} 0 & 0 & 1 & 0 \\ 0 & 0 & 0 & 1 \\ a_1 & a_2 & a_3 & a_4 \\ b_1 & b_2 & b_3 & b_4 \end{pmatrix} \begin{pmatrix} F_{hh}(z_{i-1}) \\ F_{lh}(z_{i-1}) \\ F_{hh}(z_i) \\ F_{lh}(z_i) \end{pmatrix} = \begin{pmatrix} F_{hh}(z_i) \\ F_{lh}(z_i) \\ F_{hh}(z_{i+1}) \\ F_{lh}(z_{i+1}) \end{pmatrix}. \quad (\text{B.0.24})$$

Provided that we have initial values for the wave functions at the first and second nodes, we can determine the wavefunction values at any node by an iterative procedure. By multiplying matrices, it is possible to obtain an expression for the wavefunction values at any node (as a function of the initial values)

$$\begin{pmatrix} F_{hh}(z_n) \\ F_{lh}(z_n) \\ F_{hh}(z_{n+1}) \\ F_{lh}(z_{n+1}) \end{pmatrix} = \mathbf{M}_{n+1} \mathbf{M}_n \mathbf{M}_{n-1} \cdots \mathbf{M}_3 \mathbf{M}_2 \begin{pmatrix} F_{hh}(z_0) \\ F_{lh}(z_0) \\ F_{hh}(z_1) \\ F_{lh}(z_1) \end{pmatrix}. \quad (\text{B.0.25})$$

The questions that remain are what is the suitable choice for these initial values, and how to determine whether an energy is an eigenenergy of the system.

Using four known values of the wavefunction components at z and $z + \delta z$, a fifth and sixth values can be predicted. Using the new point together with the known wavefunction components at z , we can subsequently find the wavefunctions at $z + 2\delta z$, and so on. Hence the complete wave function solution can be found for any particular energy. The solutions for steady states have wavefunctions that satisfy the standard boundary conditions

$$F \rightarrow 0 \text{ and } \frac{\partial}{\partial z} F \rightarrow 0, \text{ as } z \rightarrow \pm\infty. \quad (\text{B.0.26})$$

As argued in [25], in the one-band case of the conduction band only two initial values are required, and the suitable choice is 0 for the first node, and 1 for the second. The 1 can be any arbitrary number, as changing it will only scale the wavefunction (the finite difference equations are linear) and this does not affect the eigenenergy. The valence band case is a bit more complicated, as now there are two coupled wavefunction components, and one cannot be scaled independently from the other. Therefore, we choose the initial values to be 0 and 1 for one subband, and 0 and c for the other. Here c is a parameter, which is to be determined when the equations are solved.

The energy is varied systematically until both wavefunction components switch from diverging to $\pm\infty$ to $\mp\infty$, satisfying the boundary conditions. However, an additional problem arises from the parameter c defined above. On top of that, in many cases one of the wavefunction components exhibit a very sharp sign switching, often twice within a single energy search step. In order to work around these problems, we minimize the amplitude of the wavefunction at the end of the grid. The function to be minimized can be found by generating the transfer matrix which propagates the wavefunction from the first two nodes to the last two nodes

$$\begin{pmatrix} F_{hh}(z_{N-1}) \\ F_{lh}(z_{N-1}) \\ F_{hh}(z_N) \\ F_{lh}(z_N) \end{pmatrix} = \begin{pmatrix} m_{11} & m_{12} & m_{13} & m_{14} \\ m_{21} & m_{22} & m_{23} & m_{24} \\ m_{31} & m_{32} & m_{33} & m_{34} \\ m_{41} & m_{42} & m_{43} & m_{44} \end{pmatrix} \begin{pmatrix} 0 \\ 0 \\ 1 \\ c \end{pmatrix}. \quad (\text{B.0.27})$$

Minimizing the wavefunction amplitude at the final node leads to

$$(m_{33} + m_{34}c)^2 + (m_{43} + m_{44}c)^2 \rightarrow c_{min}, \quad (\text{B.0.28})$$

and then the minimum of $c_{min}(E)$ is searched to obtain the energy. A solution of the Hamiltonian equations is found when this minimum wavefunction amplitude is smaller than a certain threshold value. This guarantees a converging wavefunction, which can be found by substituting c_{min} into (B.0.25).

Note that the wavefunctions obtained in this procedure are not properly normalized and should be transformed into

$$\begin{pmatrix} F_{hh}(z) \\ F_{lh}(z) \end{pmatrix} \rightarrow \begin{pmatrix} F_{hh}(z) \\ F_{lh}(z) \end{pmatrix} \frac{1}{\sqrt{\int (F_{hh}^2(z) + F_{lh}^2(z)) dz}} \quad (\text{B.0.29})$$

Appendix C

Self-Consistent Solution of Schrödinger -Poisson Model

For a quantitative discussion of carriers that are strongly confined to a small area, it is necessary to consider not only the band-edge and external potential, but also the carrier-carrier electrostatic potential. We start by considering the Schrödinger equation in the slowly varying envelope approximation in one dimension

$$\frac{\hbar^2}{2} \frac{d}{dz} \left(\frac{1}{m^*(z)} \frac{d}{dz} \right) \varphi(z) + V(z)\varphi(z) = E\varphi(z) \quad (\text{C.0.1})$$

where $V(z)$ is the overall potential and $\varphi(z)$ is the slowly varying envelope. The Poisson equation (2.3.1) can be formulated as

$$\frac{d}{dz} \left(\epsilon(z) \frac{d}{dz} \right) V_\rho(z) = -e[N_D^+(z) - n(z) - N_A^-(z) + p(z)], \quad (\text{C.0.2})$$

where $\epsilon(z)$ is the position dependent dielectric constant, $V_\rho(z)$ is the electrostatic potential and e denotes the elementary charge. $N_D^+(z)$ represents the ionized donor distribution and $n(z)$ is the electron distribution. For now, we only consider the conduction-band, so we set $N_A^-(z) = p(z) = 0$.

The first coupling term between these two equations is the overall potential

$$V(z) = V_{CB}(z) - eV_\rho(z) \quad (\text{C.0.3})$$

where $V_{CB}(z)$ represents the conduction-band profile given by the material composition. The second coupling term is the electron concentration $n(z)$, which is calculated from the envelope function φ and the Fermi level E_F

$$n(z) = \frac{m^*(z)k_B T}{\pi \mathcal{L} \hbar^2} \sum_{\mathbf{k}} |\varphi_{\mathbf{k}}(z)|^2 \ln \left(1 + e^{\frac{E_F - E_{\mathbf{k}}}{k_B T}} \right), \quad (\text{C.0.4})$$

where k_B is the Boltzmann constant, T is the temperature, \mathcal{L} is the length of the heterostructure and E is the eigenenergy. The summation over \mathbf{k} represents the summation over all eigenstates (including spin). As a consequence, we have to solve for a given heterostructure with given donor concentration (C.0.1) and (C.0.2) self-consistently. We restrict ourselves to model only the mesoscopic part and not the whole device, so we have to define appropriate boundary conditions for the envelope function and the electrostatic potential. The boundary conditions for the envelope function are given by (B.0.26), whereas we set the electrostatic potential V_ρ to zero at the boundaries [4], which is equivalent to assume the device in equilibrium.

To solve (C.0.1) and (C.0.2) numerically, we apply the shooting method from Appendix B to the Schrödinger equation and to the Poisson equation a finite-difference scheme, which reads

$$\begin{aligned} 0 &= \frac{1}{2(\delta z)^2} ((\epsilon_i + \epsilon_{i-1})V_{\rho,i-1} - (\epsilon_{i-1} + 2\epsilon_i + \epsilon_{i+1})V_{\rho,i} + (\epsilon_i + \epsilon_{i+1})V_{\rho,i+1}) \\ &\quad + e(N_{D,i}^+ - n_i), \end{aligned} \quad (\text{C.0.5})$$

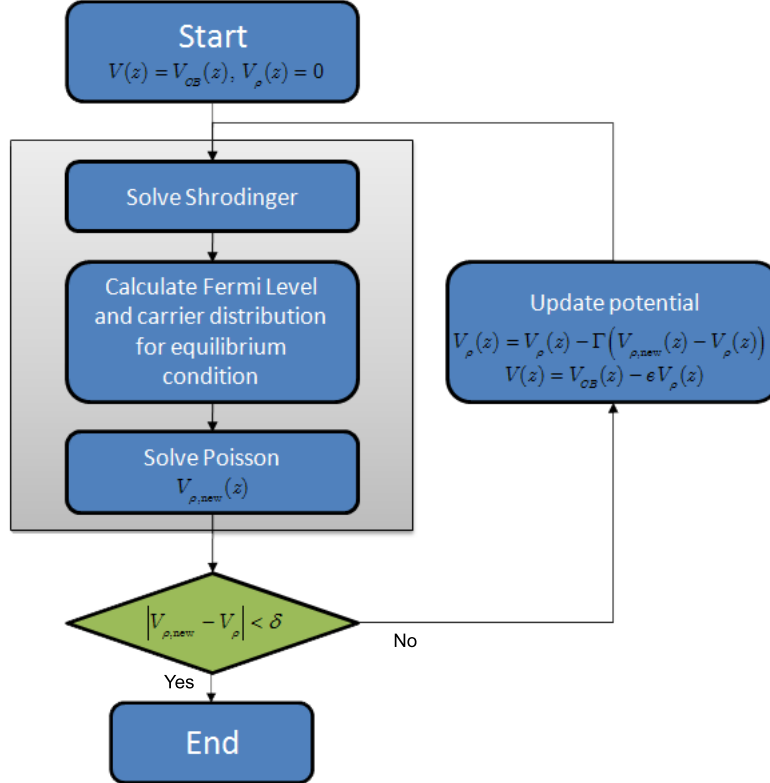


Figure C.1: Program flow for self-consistent solution of Schrödinger -Poisson under equilibrium condition with given donor concentration.

where δz is the spatial discretization. Equilibrium conditions require us to choose the Fermi level appropriate to allow that

$$\int_{-\infty}^{\infty} N_D^+(z) dz = \int_{-\infty}^{\infty} n(z) dz. \quad (\text{C.0.6})$$

To ensure this equilibrium condition, we solve (C.0.4) with the constraint (C.0.6) to obtain the Fermi level E_F .

Figure C.1 shows the program flow to obtain the self-consistent solution of the Schrödinger -Poisson system under equilibrium condition. First, Schrödinger's equation is solved assuming an initial potential $V(z) = V_{CB}(z)$, $V_\rho(z) = 0$. Next, the Fermi level E_F and the carrier distribution $n(z)$ are obtained by solving (C.0.4) with respect to (C.0.6). Then, the Poisson equation is solved resulting in a new electrostatic potential $V_{\rho,\text{new}}(z)$. If $|V_{\rho,\text{new}}(z) - V_\rho(z)|$ is smaller than a pre-defined value δ , we obtain the converged solution. Otherwise, the electrostatic potential is updated $V_\rho(z)(z) = V_\rho(z) + \Gamma(V_{\rho,\text{new}}(z) - V_\rho(z))$, where $0 < \Gamma < 1$ is a damping parameter used to improve convergence.

Appendix D

Lindhard Screening Model

To implement the screened Hartree-Fock approximation in chapter 4, we need a screening model. One approach is to use a self-consistent quantum theory of plasma screening involving arguments from classical electrodynamics and quantum mechanics [42]. Given an electron at the origin of our coordinate system, we wish to know what effect this electron has on its surroundings. To find out, we introduce a test charge, i.e., a charge sufficiently small as to cause negligible perturbation. In vacuum, the electrostatic potential due to the electron is $\phi(r) = e/r$. However, in a semiconductor there is a background dielectric constant ϵ_b which is due to everything in the semiconductor in the absence of the carriers themselves. Furthermore, there is the carrier distribution that is changed by the presence of the test electron at the origin (see Fig. D.1). The new carrier distribution, $\langle n_s(\mathbf{r}) \rangle$, in turn changes the electrostatic potential. We denote the carrier density distribution as an expectation value since we plan to calculate it quantum mechanically. To derive the induced carrier distribution, we first simplify the problem by assuming that the screening effects of an electron-hole plasma equal the sum of the effects resulting from the separate electron and hole plasmas. As such we neglect excitonic screening, which is not a bad approximation for the elevated carrier densities present in conventional semiconductor heterostructures. The density distribution operator can be defined as

$$\begin{aligned}\hat{n}(\mathbf{r}) &= \psi^\dagger(\mathbf{r})\psi(\mathbf{r}) \\ &= \frac{1}{V} \sum_{\mathbf{k}, \mathbf{k}'} e^{i(\mathbf{k}-\mathbf{k}') \cdot \mathbf{r}} \hat{a}_{\mathbf{k}'}^\dagger \hat{a}_{\mathbf{k}} \\ &= \sum_{\mathbf{q}} n_{\mathbf{q}} e^{i\mathbf{q} \cdot \mathbf{r}},\end{aligned}\tag{D.0.1}$$

where

$$n_{\mathbf{q}} = \frac{1}{V} \sum_{\mathbf{k}} \hat{a}_{\mathbf{k}-\mathbf{q}}^\dagger \hat{a}_{\mathbf{k}}\tag{D.0.2}$$

is the Fourier amplitude of the density distribution operator. Starting with the electron plasma, we can note from (D.0.1) that the corresponding quantum-mechanical operator for the screened electron charge distribution is $e\hat{n}_s(\mathbf{r})$ with

$$\hat{n}_s(\mathbf{r}) = \frac{1}{V} \sum_{\mathbf{k}, \mathbf{k}'} e^{i(\mathbf{k}-\mathbf{k}') \cdot \mathbf{r}} \hat{a}_{\mathbf{k}-\mathbf{q}}^\dagger \hat{a}_{\mathbf{k}}\tag{D.0.3}$$

$$= \sum_{\mathbf{q}} n_{s\mathbf{q}} e^{i\mathbf{q} \cdot \mathbf{r}}.\tag{D.0.4}$$

Here, the Fourier transform of the density operator is given by $n_{s\mathbf{q}} = \frac{1}{V} \sum_{\mathbf{k}} \hat{a}_{\mathbf{k}-\mathbf{q}}^\dagger \hat{a}_{\mathbf{k}}$, and V is the volume of the semiconductor medium. In a rigorous treatment we would use the electronic part of the many-body Hamiltonian to obtain an equation of motion for $n_{s\mathbf{q}}$. At the level of a self-consistent Hartree-Fock approach, we can treat screening effects on the basis of an effective single-particle Hamiltonian

$$\hat{H}_{eff} = \sum_{\mathbf{k}} E_e(\mathbf{k}) \hat{a}_{\mathbf{k}}^\dagger \hat{a}_{\mathbf{k}} - V \sum_{\mathbf{q}} V_{s\mathbf{q}} n_{s,-\mathbf{q}},\tag{D.0.5}$$

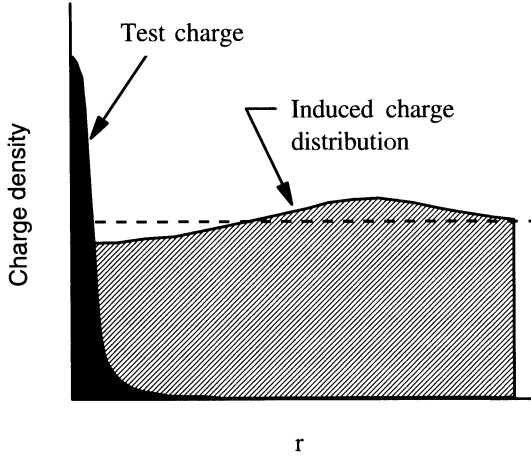


Figure D.1: *Change in the carrier distribution due to an electron at the origin (after [42]).*

where

$$V_{s\mathbf{q}} = \frac{1}{V} \int d^3r V_s(r) e^{-i\mathbf{q}\cdot\mathbf{r}}, \quad (\text{D.0.6})$$

with $V_s(r) = e\phi_s(r)$, and $\phi_s(r)$ is the screened electrostatic potential.

With the effective Hamiltonian (D.0.5), we get the equation of motion

$$\begin{aligned} i\hbar \frac{d}{dt} \hat{a}_{\mathbf{k}-\mathbf{q}}^\dagger \hat{a}_\mathbf{k} &= \left[\hat{a}_{\mathbf{k}-\mathbf{q}}^\dagger \hat{a}_\mathbf{k}, \hat{H}_{eff} \right] \\ &= (E_e(\mathbf{k}) - E_e(\mathbf{k} - \mathbf{q})) \hat{a}_{\mathbf{k}-\mathbf{q}}^\dagger \hat{a}_\mathbf{k} \\ &\quad + \sum_{\mathbf{p}} V_{s\mathbf{p}} \left(\hat{a}_{\mathbf{k}-\mathbf{q}}^\dagger \hat{a}_{\mathbf{k}+\mathbf{p}} - \hat{a}_{\mathbf{k}-\mathbf{q}-\mathbf{p}}^\dagger \hat{a}_\mathbf{k} \right). \end{aligned} \quad (\text{D.0.7})$$

Taking the expectation value and keeping only slowly varying terms, namely those with $\mathbf{p} = -\mathbf{q}$, we get

$$\begin{aligned} i\hbar \frac{d}{dt} \langle \hat{a}_{\mathbf{k}-\mathbf{q}}^\dagger \hat{a}_\mathbf{k} \rangle &= (E_e(\mathbf{k}) - E_e(\mathbf{k} - \mathbf{q})) \langle \hat{a}_{\mathbf{k}-\mathbf{q}}^\dagger \hat{a}_\mathbf{k} \rangle \\ &\quad + V_{s\mathbf{q}} (n_{\mathbf{k}-\mathbf{q}} - n_\mathbf{q}). \end{aligned} \quad (\text{D.0.8})$$

We suppose that $\langle \hat{a}_{\mathbf{k}-\mathbf{q}}^\dagger \hat{a}_\mathbf{k} \rangle$ has solution of the form $e^{(\delta-i\omega)t}$, where the infinitesimal δ indicates that the perturbation has been switched on adiabatically, i.e., that we had a homogeneous plasma at $t = -\infty$. We further suppose that the induced charge distribution follows this response. This transforms (D.0.8) to

$$\langle \hat{a}_{\mathbf{k}-\mathbf{q}}^\dagger \hat{a}_\mathbf{k} \rangle = V_{s\mathbf{q}} \frac{n_{\mathbf{k}-\mathbf{q}} - n_\mathbf{q}}{\hbar(\omega + i\delta) - E_e(\mathbf{k}) + E_e(\mathbf{k} - \mathbf{q})} \quad (\text{D.0.9})$$

and

$$\langle n_{s\mathbf{q}} \rangle = \frac{V_{s\mathbf{q}}}{V} \sum_{\mathbf{k}} \frac{n_{\mathbf{k}-\mathbf{q}} - n_\mathbf{q}}{\hbar(\omega + i\delta) - E_e(\mathbf{k}) + E_e(\mathbf{k} - \mathbf{q})}. \quad (\text{D.0.10})$$

The induced charge distribution is a source in Poisson's equation

$$\nabla^2 \phi_s(r) = -\frac{4\pi e}{\epsilon_b q^2} [n_e(\mathbf{r}) + \langle n_{s\mathbf{q}} \rangle]. \quad (\text{D.0.11})$$

The Fourier transform of this equation is

$$\phi_{s\mathbf{q}} = \frac{4\pi e}{\epsilon_b q^2} \left(\frac{1}{V} + \langle n_{s\mathbf{q}} \rangle \right), \quad (\text{D.0.12})$$

where for a point charge at the origin

$$n_{e\mathbf{q}} = \frac{1}{V} \int d^3r \delta^3(\mathbf{r}) e^{-i\mathbf{q}\cdot\mathbf{r}} = \frac{1}{V}. \quad (\text{D.0.13})$$

Using $V_{s\mathbf{q}} \equiv e\phi_{s\mathbf{q}}$, substitute (D.0.10) into (D.0.12) and solve for $V_{s\mathbf{q}}$ to find

$$V_{s\mathbf{q}} = V_{\mathbf{q}} \left(1 - V_q \sum_{\mathbf{k}} \frac{n_{\mathbf{k}-\mathbf{q}} - n_{\mathbf{q}}}{\hbar(\omega + i\delta) - E_e(\mathbf{k}) + E_e(\mathbf{k} - \mathbf{q})} \right)^{-1}, \quad (\text{D.0.14})$$

where V_q is the unscreened Coulomb potential. Repeating the derivation for the hole plasma, and adding the electron and hole contributions, we find the screened Coulomb potential energy between carriers

$$V_{s\mathbf{q}} = \frac{V_{\mathbf{q}}}{\epsilon_{\mathbf{q}}(\omega)}, \quad (\text{D.0.15})$$

where the longitudinal dielectric function is given by

$$\epsilon_{\mathbf{q}}(\omega) = 1 - V_{\mathbf{q}} \sum_{n\mathbf{k}} \frac{n_{n,\mathbf{k}-\mathbf{q}} - n_{n,\mathbf{q}}}{\hbar(\omega + i\delta) - E_n(\mathbf{k}) + E_n(\mathbf{k} - \mathbf{q})} \quad (\text{D.0.16})$$

This equation is the Lindhard formula. It describes a complex retarded dielectric function, i.e., the poles are in the lower complex frequency plane, and it includes spatial dispersion (\mathbf{q} dependence) and spectral dispersion (ω dependence).

Appendix E

Bandgap Energy Modeling of Semiconductors

The bandgap (or forbidden energy zone) is one of the most important semiconductor parameters. Various models define the temperature dependence of the bandgap energy in semiconductors (e.g. [63]). For an alloy $A_{1-x}B_x$, the temperature-dependent bandgaps of the constituents (A and B) are calculated first. The bandgap and the energy offset are then calculated depending on the material composition. This is important to assure consistency between the values for *alloy materials* at $x = 0$ and $x = 1$ and the values for the respective *basic materials*. For materials where the bandgap changes between direct and indirect the multiple valley conduction bands are considered.

E.1 Temperature dependence of the bandgap

The model of Varshni [63] is used for basic materials. The temperature dependence is calculated by

$$E_g(T) = E_g(0) - \frac{\alpha T^2}{\beta + T}, \quad (\text{E.1.1})$$

where $E_g(0)$ us the bandgap energy at 0K. The parameter values are summarized in Table E.1. Note, for these materials always the lowest conduction band valley minimum is taken into account. In addition, the resulting bandgaps at 300K, $E_g(300)$, are given in Table E.3. For *Si* two additional models can be chosen which are based on polynomial fits of second and third order.

Table E.1: Parameter values for modeling the bandgap energies (I)

Material	Minimum	$E_g(0) [eV]$	$\alpha [eV/K]$	$\beta [K]$	Ref.
<i>Si</i>	X	1.1695	4.73×10^{-4}	636	[64, 65]
<i>Ge</i>	L	0.7437	4.774×10^{-4}	235	[65]
<i>GaAs</i>	Γ	1.521	5.58×10^{-4}	220	[66, 67, 68]
<i>AlAs</i>	X	2.239	6.0×10^{-4}	408	[64, 69]
<i>InAs</i>	Γ	0.420	2.5×10^{-4}	75	[70, 68]
<i>InP</i>	Γ	1.421	3.63×10^{-4}	162	[67, 69, 65]
<i>GaP</i>	X	2.338	5.771×10^{-4}	372	[65, 64, 69]

Table E.3: Bandgap energies at room temperature compared to reported data (I).

Material	Minimum	$E_g(300) [eV]$	Reported value [eV]	Ref.
<i>Si</i>	X	1.124	1.12-1.1242	[64, 65]
<i>Ge</i>	L	0.663	0.66-0.67	[65, 64, 71]
<i>GaAs</i>	Γ	1.424	1.42-1.43	[72, 71]
<i>AlAs</i>	X	2.163	2.14-2.168	[64, 72]
<i>InAs</i>	Γ	0.360	0.354-0.37	[66, 73]
<i>InP</i>	Γ	1.350	1.34-1.351	[70, 64, 66]
<i>GaP</i>	X	2.261	2.26-2.272	[71, 70, 64]

E.2 Semiconductor Alloys

In the case of alloy materials the temperature-dependent bandgaps of the constituents, E_g^A and E_g^B , are calculated by (E.1.1). However, for materials where the bandgap changes between direct and indirect the multiple valley conduction bands are considered. For that purpose, additional model parameters are needed for the higher energy valleys in the respective III-V binary materials (Table (E.2.2)). In addition, the resulting bandgaps at 300K, are included in Table (E.2.3).

The bandgap and the energy offset of an alloy $A_{1-x}B_x$ are calculated by

$$E_{g,X}^{AB} = E_{g,X}^A \cdot (1-x) + E_{g,X}^B \cdot x + C_{g,X} \cdot (1-x) \cdot x, \quad (\text{E.2.1})$$

$$E_{g,\Gamma}^{AB} = E_{g,\Gamma}^A \cdot (1-x) + E_{g,\Gamma}^B \cdot x + C_{g,\Gamma} \cdot (1-x) \cdot x, \quad (\text{E.2.2})$$

$$E_g^{AB} = \min(E_{g,X}^{AB}, E_{g,\Gamma}^{AB}). \quad (\text{E.2.3})$$

The bowing parameters $C_{g,X}$ and $C_{g,\Gamma}$ are summarized in Table E.9.

Table E.5: Parameter values for modeling the bandgap energies (II).

Material	Minimum	$E_g(0) [eV]$	$\alpha [eV/K]$	$\beta [K]$	Ref.
<i>GaAs</i>	X	1.981	4.6×10^{-4}	204	[72]
<i>AlAs</i>	Γ	2.891	8.78×10^{-4}	332	[72]
<i>InAs</i>	X	2.278	5.78×10^{-4}	83	
<i>InP</i>	X	2.32	7.66×10^{-4}	327	[74]
<i>GaP</i>	Γ	2.88	8.0×10^{-4}	300	[74]

Table E.7: Bandgap energies at room temperature compared to reported data (II).

Material	Minimum	$E_g(300)$ [eV]	Reported value [eV]	Ref.
<i>GaAs</i>	X	1.899	1.9-1.91	[72, 75]
<i>AlAs</i>	Γ	2.766	2.671-2.766	[73]
<i>InAs</i>	X	2.142	1.37-2.14	[76, 75]
<i>InP</i>	X	2.21	2.21-2.30	[76, 75]
<i>GaP</i>	Γ	2.76	2.73-2.85	[74]

Table E.9: Parameter values for the bandgap of alloy materials.

Material	$C_{g,\Gamma}$ [eV]	$C_{g,X}$ [eV]	C_g [eV]	Ref.
<i>SiGe</i>	0	0	-0.4	[72]
<i>AlGaAs</i>	0	-0.143	0.7	[73]
<i>InGaAs</i>	0	0	-0.475	[69, 64]
<i>InAlAs</i>	-0.3	-0.713	1.2	[69, 64]
<i>InAsP</i>	0	0	-0.32	[69, 64]

Additional bowing parameters are given as a reference for the case when a one-valley bandgap fit is used

$$E_g^{AB} = E_g^A \cdot (1 - x) + E_g^B \cdot x + C_g \cdot (1 - x) \cdot x. \quad (\text{E.2.4})$$

As an example of the procedure elaborated above, we consider the properties of the $Al_xGa_{1-x}As$ alloy bandgap energy. In figure E.1 we plot the dependence of the bandgap energy on temperature with Al (x) content as a parameter. Figure E.2 presents the dependence of the bandgap energy on the Al composition for various temperatures. A direct-to-indirect (from Γ to X minimum) gap transition is observed at about $x = 0.4$.

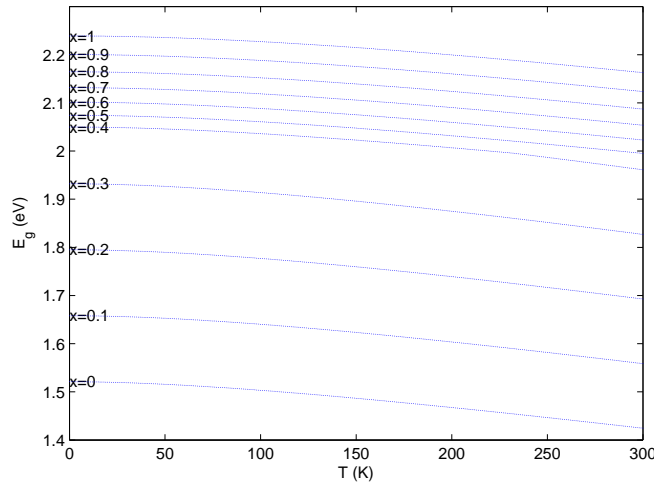


Figure E.1: Temperature dependence of the $Al_xGa_{1-x}As$ alloy bandgap energy for various values of x .

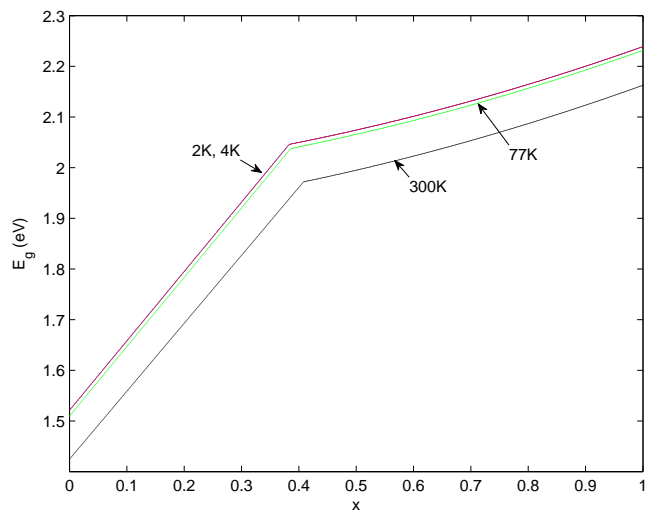


Figure E.2: $Al_xGa_{1-x}As$ alloy bandgap energy as a function of the Al composition for various temperatures.

Appendix F

Refractive Index of $Al_xGa_{1-x}As$ Alloy

$Al_xGa_{1-x}As$ is the main semiconductor alloy of interest to us throughout this report, and thus its properties are of paramount importance. This appendix deals with the determination of the complex refractive index of this alloy, for any Al atoms molar composition x and temperature. This parameter is mainly important in determining accurately the optical properties of microcavity structures, discussed in chapter 5.

The materials in the binary $Al_xGa_{1-x}As$ are essentially lattice matched over the entire composition range. This attribute has been of considerable technical importance, because it has made possible the growth of artificial structures with electronic energy levels tailored to a wide variety of fundamental and applied purposes. These structures and their interfaces can be characterized conveniently and non destructively by visible-near UV optical reflection techniques. However, these techniques require an accurate data base, but at present only incomplete dielectric function data are available.

There are two main approaches in literature towards the determination of the refractive index: theoretical modeling of the dielectric function of the material at hand and semi-empirical approximations of this property [72]. These methods are, obviously, carefully tailored to each material, and there is a considerable variation between them depending of various factor mainly the temperature. As the theoretical modeling is too complex or ill-adjusted to our needs we resort to the empirical approach.

In [77] the authors present a measurement of the room-temperature pseudo-dielectric function ϵ and related optical function data for $Al_xGa_{1-x}As$ alloys for energies E from 1.5 to 6.0 eV and for compositions x from 0 to 0.80 in steps of approximately 0.1. This numerical data has been organized into a database of files which can be downloaded from [78]. These files include the real and the imaginary parts of the dielectric function, $\Re(\epsilon)$ and $\Im(\epsilon)$, from which the refractive index can be calculated using

$$n = \Re(n) + i\Im(n) = \sqrt{\Re(\epsilon) + i\Im(\epsilon)}. \quad (\text{F.0.1})$$

With this experimental curve we can now go ahead and calculate the refractive index for any temperature and energy. The second goal is achieved by a strait-forward interpolation of the experimental curves to the requested energy. Of course, this procedure is valid only in the spectral support region of the experimental data.

The temperature dependent extrapolation is performed by shifting the experimental spectra in energy by an amount of $E_{shift}(T) = E_g(T) - E_g(300K)$, which accounts for the direct bandgap shift of the alloy as a function of temperature.

As a illustration, we present in figure F.1 the results of the calculation of the refractive indices for temperatures values relevant to this report ($T = 2, 77, 300 K$) and various values of x . In figures F.2, F.3 and F.4 we present a zoomed in view of the refractive indices at energy intervals and x values relevant to this report, calculated at $T = 2, 77, 300 K$, respectively.

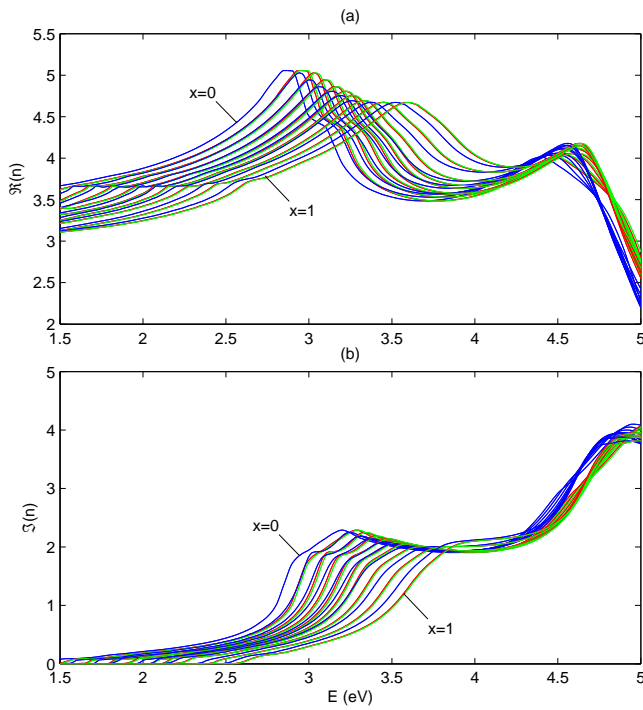


Figure F.1: The (a) real and (b) imaginary parts of the refractive index of $\text{Ga}_{1-x}\text{Al}_x\text{As}$ as a function of energy, for $T = 2\text{K}$ (green), $T = 77\text{K}$ (red) and $T = 300\text{K}$ (blue) and $x = 0 - 1$ (from left to right).

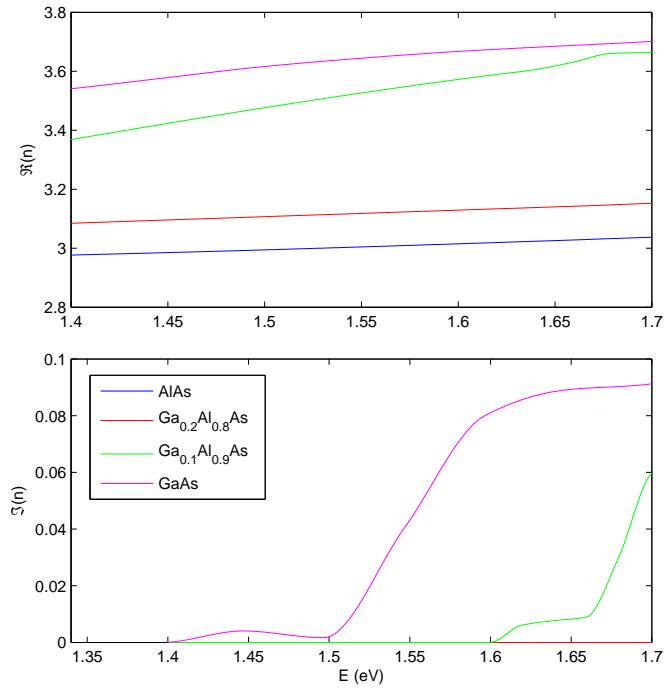
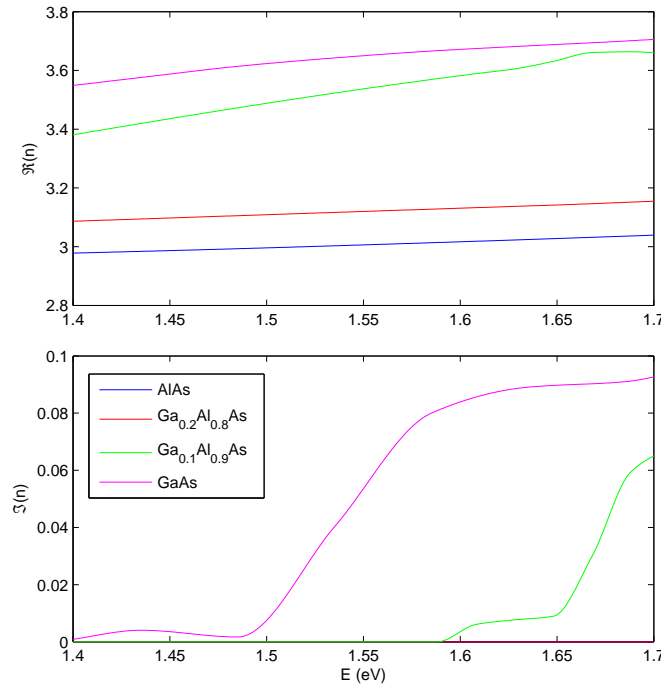
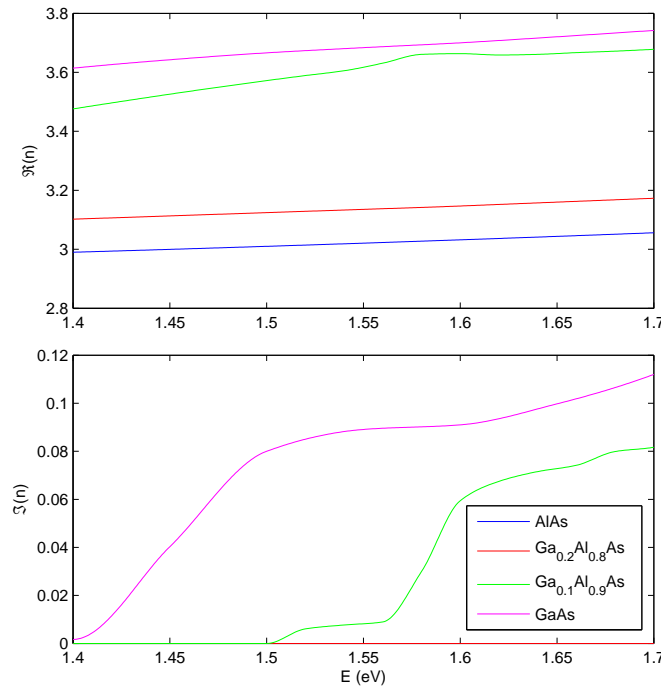


Figure F.2: Refractive indices for $T = 2\text{K}$.

Figure F.3: *Refractive indices for $T = 77K$.*Figure F.4: *Refractive indices for $T = 300K$.*

Bibliography

- [1] J. D. Jackson, *Classical Electrodynamics*. John Wiley and Sons, Inc., 3rd ed., 1998. 2.1.1, 2.1.1, 2.3.1, 3, 4
- [2] P. Y. Yu and M. Cardona, *Fundamentals of semiconductors: physics and materials properties*. Springer Verlag, 2nd ed., 2005. 2.1.1, 2.1.1, 2.1.3.1, 2.1.3.1, 2.2.3.1, A.1, A, A.3
- [3] J. Piprek, *Semiconductor optoelectronic devices: introduction to physics and simulation*. Academic Press, 2003. 2.1
- [4] S. L. Chuang, *Physics of Optoelectronic Devices*. Wiley-Interscience, 1995. 2.1.3.1, 2.2.2, 2.2.3.3, 1, 2.2.3.3, 2.2.4, 3, 3.4, 4, C
- [5] E. O. Kane, *Handbook on semiconductors*, vol. 1. W.Paul, 1982. 2.1.3.1, 2.2.3.1, 2.2.3.3
- [6] G. Bir and G. Pikus, *Symmetry and strain-induced effects in semiconductors*. New York: Wiley, 1974. 2.1.3.1
- [7] E. O. Kane, “Band structure of indium antimonide,” *Journal of Physics and Chemistry of Solids*, vol. 1, no. 4, p. 249, 1957. 2.1.3.2
- [8] J. M. Luttinger and W. Kohn, “Motion of Electrons and Holes in Perturbed Periodic Fields,” *Physical Review*, vol. 97, no. 4, p. 869, 1955. 2.1.3.2, 2.2.3.3
- [9] P. Lowdin, “A Note on the Quantum-Mechanical Perturbation Theory,” *The Journal of Chemical Physics*, vol. 19, no. 11, p. 1396, 1951. 2.1.3.2
- [10] D. J. BenDaniel and C. B. Duke, “Space-charge effects on electron tunneling,” *Physical Review*, vol. 152, no. 2, p. 683, 1966. 2.2.2
- [11] R. A. Morrow and K. R. Brownstein, “Model effective-mass Hamiltonians for abrupt heterojunctions and the associated wave-function-matching conditions,” *Physical Review B*, vol. 30, no. 2, p. 678, 1984. 2.2.2
- [12] M. Altarelli, “Electronic structure and semiconductor-semimetal transition in InAs-GaSb superlattices,” *Physical Review B*, vol. 28, no. 2, p. 842, 1983. 2.2.2
- [13] G. Bastard, “Superlattice band structure in the envelope-function approximation,” *Physical Review B*, vol. 24, no. 10, p. 5693, 1981. 2.2.2
- [14] G. Bastard, “Theoretical investigations of superlattice band structure in the envelope-function approximation,” *Physical Review B*, vol. 25, no. 12, p. 7584, 1982. 2.2.2
- [15] R. Eppenga, M. F. H. Schuurmans, and S. Colak, “New k.p theory for GaAs/Ga_{1-x}Al_xAs-type quantum wells,” *Physical Review B*, vol. 36, no. 3, p. 1554, 1987. 2.2.2
- [16] S. L. Chuang, “Exciton Green’s-Function Approach to Optical Absorbtion in a Quantum Well with an Applied Electric Field,” *Physical Review B*, vol. 43, p. 1500, 1991. 2.2.2
- [17] G. Dresselhaus, “Spin-Orbit Coupling Effects in Zinc Blende Structures,” *Physical Review*, vol. 100, no. 2, p. 580, 1955. 2.2.3.1
- [18] B. A. Foreman, “Exact effective-mass theory for heterostructures,” *Physical Review B*, vol. 52, no. 16, p. 12241, 1995. 2.2.3.2, 2.2.3.2

- [19] B. A. Foreman, "Effective-mass Hamiltonian and boundary conditions for the valence bands of semiconductor microstructures," *Physical Review B*, vol. 48, no. 7, p. 4964, 1993. 2.2.3.2
- [20] P. Enders, A. Borwolff, M. Woerner, and D. Suisky, "k.p theory of energy bands, wave functions, and optical selection rules in strained tetrahedral semiconductors," *Physical Review B*, vol. 51, no. 23, p. 16695, 1995. 2.2.3.3, 3.4
- [21] J. M. Luttinger, "Quantum Theory of Cyclotron Resonance in Semiconductors: General Theory," *Physical Review*, vol. 102, no. 4, p. 1030, 1956. 2.2.3.3, 2.2.3.3
- [22] L. C. Andreani, A. Pasquarello, and F. Bassani, "Hole subbands in strained GaAs-Ga_{1-x}Al_xAs quantum wells: Exact solution of the effective-mass equation," *Physical Review B*, vol. 36, no. 11, p. 5887, 1987. 2.2.4
- [23] D. A. Broido and L. J. Sham, "Effective masses of holes at GaAs-AlGaAs heterojunctions," *Physical Review B*, vol. 31, no. 2, p. 888, 1985. 2.2.4, 2.2.4
- [24] P. S. Zory, *Quantum well lasers*. Academic Press, 1993. 2.4, 2.5
- [25] P. Harrison, *Quantum wells, wires and dots: theoretical and computational physics of semiconductor nanostructures*. New York: Wiley-Interscience, 2005. 2.10, B, B
- [26] E. F. Schubert, *Delta-doping of semiconductors*. Cambridge University Press, 1996. 2.3.2, 2.18
- [27] G. D. Sanders and Y. C. Chang, "Theory of photoabsorption in modulation-doped semiconductor quantum wells," *Phys. Rev. B*, vol. 35, p. 1300, Jan 1987. 2.3.2
- [28] S. Schmitt-Rink, D. S. Chemla, and D. A. B. Miller, "Linear and nonlinear optical properties of semiconductor quantum wells," *Advances in Physics*, vol. 38, p. 89, 1989. 2.3.2
- [29] D. Huang, J. I. Chyi, and H. Morkoc, "Carrier effects on the excitonic absorption in GaAs quantum-well structures: Phase-space filling," *Phys. Rev. B*, vol. 42, p. 5147, Sep 1990. 2.3.2
- [30] H. Haug and S. W. Koch, *Quantum theory of the optical and electronic properties of semiconductors*. World Scientific Pub Co Inc, 4th ed., 2009. 3, 3, 3.2.3, 3.2.3, 3.2.3, 4, 4.1.1, 4.2.3.2, 4.2.5, 2, 4.13, 4.3.1, 5.4.1.2
- [31] M. Kira, F. Jahnke, W. Hoyer, and S. W. Koch, "Quantum theory of spontaneous emission and coherent effects in semiconductor microstructures," *Progress in Quantum Electronics*, vol. 23, no. 6, p. 189, 1999. 3
- [32] W. W. Chow and S. W. Koch, *Semiconductor-laser fundamentals: physics of the gain materials*. Springer, 1st ed., 1999. 3, 3.2.3, 3.2.4, 4, 4.2.1, 4.2.1, 4.2.2, 4.3, 4.2.3.2, 4.2.3.2
- [33] W. Schafer and M. Wegener, *Semiconductor optics and transport phenomena*. Springer Verlag, 1 ed., 2002. 3, 3.1.1.3, 4
- [34] P. C. Martin and J. Schwinger, "Theory of Many-Particle Systems. I," *Physical Review*, vol. 115, no. 6, p. 1342, 1959. 3.3
- [35] M. G. Burt, "Breakdown of the atomic dipole approximation for the quantum well interband dipole matrix element," *Semiconductor Science and Technology*, vol. 10, no. 4, p. 412, 1995. 3.4
- [36] M. G. Burt, "The evaluation of the matrix element for interband optical transitions in quantum wells using envelope functions," *Journal of Physics: Condensed Matter*, vol. 5, no. 24, p. 4091, 1993. 3.4
- [37] J. Hader, J. V. Moloney, S. W. Koch, and W. W. Chow, "Microscopic modeling of gain and luminescence in semiconductors," *IEEE Journal of Selected Topics in Quantum Electronics*, vol. 9, no. 3, p. 688, 2003. 4.1.2
- [38] H. Ehrenreich and M. H. Cohen, "Self-Consistent Field Approach to the Many-Electron Problem," *Physical Review*, vol. 115, no. 4, p. 786, 1959. 4.2.3.2
- [39] R. Binder, "Nonequilibrium semiconductor dynamics," *Progress in Quantum Electronics*, vol. 19, p. 30, 1995. 4.2.3.2, 4.2.3.2

- [40] G. D. Mahan, *Many-particle physics*. Plenum Pub Corp, 2000. 4.2.3.2
- [41] R. Cingolani and K. Ploog, “Frequency and density dependent radiative recombination processes in iii-v semiconductor quantum wells and superlattices,” *Advances in Physics*, vol. 40, p. 535, 1991. 4.2.5, 4.3.2, 4.3.2
- [42] W. W. Chow, S. W. Koch, and M. Sargent III, *Semiconductor-laser physics*. Springer-Verlag New York, Inc. New York, NY, USA, 1994. 4.2.5, D, D.1
- [43] A. Gabbay, Y. Preezant, E. Cohen, B. M. Ashkinadze, and L. N. Pfeiffer, “Fermi edge polaritons in a microcavity containing a high density two-dimensional electron gas,” *Phys. Rev. Lett.*, vol. 99, p. 157402, Oct 2007. 4.3.2, 5.5.3
- [44] M. Born and E. Wolf, *Principles of Optics: Electromagnetic Theory of Propagation, Interference and Diffraction of Light*. Cambridge University Press, 7th ed., 2002. 5.1
- [45] H. A. Macleod, *Thin-Film Optical Filters*. Institute of Physics Publishing, 3rd ed., 2001. 5.2
- [46] V. Savona and F. Tassone, “Exact quantum calculation of polariton Dispersion in semiconductor microcavities,” *Solid State Communications*, vol. 95, p. 673, 1995. 5.3.1, 5.3.1
- [47] M. S. Skolnick, T. A. Fisher, and D. M. Whittaker, “Strong coupling phenomena in quantum microcavity structures,” *Semiconductor Science and Technology*, vol. 13, p. 645, 1998. 5.3.2, 5.4
- [48] S. Haroche, *Quantum optics of confined systems*. Springer, 1996. 5.4
- [49] L. C. Andreani and A. Pasquarello, “Accurate theory of excitons in gaas-ga1-xalxas quantum wells,” *Phys. Rev. Lett. B*, vol. 42, p. 8928, 1990. 5.4
- [50] H. Yokoyama, K. Nishi, T. Anan, H. Yamada, S. D. Brorson, and E. P. Ippen, “Enhanced spontaneous emission from gaas quantum wells in monolithic microcavities,” *Applied Physics Letters*, vol. 57, p. 2814, 1990. 5.4
- [51] Y. Zhu, D. J. Gauthier, S. E. Morin, Q. Wu, H. J. Carmichael, and T. W. Mossberg, “Vacuum rabi splitting as a feature of linear-dispersion theory: Analysis and experimental observations,” *Phys. Rev. Lett.*, vol. 64, p. 2499, 1990. 5.4, 5.4
- [52] C. Weisbuch, M. Nishioka, A. Ishikawa, and Y. Arakawa, “Observation of the coupled exciton-photon mode splitting in a semiconductor quantum microcavity,” *Phys. Rev. Lett.*, vol. 69, p. 3314, 1992. 5.4, 5.4
- [53] J. J. Hopfield, “Theory of the contribution of excitons to the complex dielectric constant of crystals,” *Phys. Rev.*, vol. 112, p. 1555, 1958. 5.4, 5.4.2.1
- [54] V. Savona, *Confined Photon Systems: Fundamentals and Applications (Lecture Notes in Physics)*. Springer, 1999. 5.4, 5.4.2
- [55] S. Pau, G. Bjork, J. Jacobson, H. Cao, and Y. Yamamoto, “Microcavity exciton-polariton splitting in the linear regime,” *Phys. Rev. B*, vol. 51, p. 14437, 1995. 5.4, 5.4.2, 5.4.2.2
- [56] R. Girlanda and S. Savasta, “The particle-photon interaction in systems described by model hamiltonians in second quantization,” *Solid State Communications*, vol. 96, p. 517, 1995. 5.4
- [57] V. Savona, L. C. Andreani, P. Schwendimann, and A. Quattropani, “Quantum well excitons in semiconductor microcavities: Unified treatment of weak and strong coupling regimes,” *Solid State Communications*, vol. 93, p. 733, 1995. 5.4, 5.4.2, 5.4.2.2
- [58] R. Rapaport, *Electron-Polariton Interaction in Semiconductor Microcavity*. PhD thesis, Physics Dept., Technion - Israel Institute of Technology, May 2001. 5.4
- [59] E. T. Jaynes and F. W. Cummings, “Comparison of quantum and semiclassical radiation theories with application to the beam maser,” *Proceedings of the IEEE*, vol. 51, p. 89, 1962. 5.4.1.1
- [60] S. Haroche, *New Trends in Atomic Physics*. North-Holland Physics Pub, 1984. 5.4.1.1, 5.4.1.2

- [61] M. Raimond, *Quantum optics of confined systems*. Springer, 1996. 5.4.1.1
- [62] G. Ramon, *Polariton-Electron Scattering in Microcavities with Embedded Quantum Wells*. PhD thesis, Physics Dept., Technion - Israel Institute of Technology, July 2002. 5.5.3
- [63] Y. Varshni, “Temperature dependence of the energy gap in semiconductors,” *Physica*, vol. 34, p. 149, 1967. E, E.1
- [64] J. Singh, *Physics of Semiconductors and their Heterostructures*. McGraw Hill, 1993. E.2, E.2, E.2, E.4, E.4, E.4, E.4, E.10, E.10, E.10
- [65] S. Sze, *Physics of Semiconductor Devices*. Wiley, 1981. E.2, E.2, E.2, E.2, E.4, E.4
- [66] B. Nag, *Electron Transport in Compound Semiconductors*, vol. 11 of *Springer Series in Solid-State Sciences*. Springer, 1980. E.2, E.4, E.4
- [67] P. Wang, S. Holmes, T. Le, R. Stradling, I. Ferguson, and A. de Oliveira, “Electrical and magneto-optical studies of mbe inas on gaas,” *Semiconductor Science and Technology*, vol. 7, p. 767, 1992. E.2, E.2
- [68] P. Bhattacharya, ed., *Properties of Lattice-Matched and Strained Indium Gallium Arsenide*, vol. 8 of *EMIS Datareviews Series*, 1993. E.2, E.2
- [69] A. Katz, *Indium Phosphide and Related Materials*. Artech House, 1992. E.2, E.2, E.2, E.10, E.10, E.10
- [70] S. Tiwari, *Compound Semiconductor Device Physics*. Academic Press, 1992. E.2, E.4, E.4
- [71] K. Ng, *Complete Guide to Semiconductor Devices*. McGraw-Hill, 1995. E.4, E.4, E.4
- [72] S. Adachi, “GaAs, AlAs, and AlGaAs: Material Parameters for Use in Research and Device Applications,” *Journal of Applied Physics*, vol. 58, p. R1, 1985. E.4, E.4, E.6, E.6, E.8, E.10, F
- [73] E. Schubert, *Doping in III-V Semiconductors*. Cambridge University Press, 1993. E.4, E.8, E.10
- [74] S. Adachi, *Physical Properties of III-V Semiconductor Compounds*. Wiley, 1992. E.6, E.6, E.8
- [75] M. Krijn, “Heterojunction band offsets and effective masses in iii-v quaternary alloys,” *Semiconductor Science and Technology*, vol. 6, p. 27, 1991. E.8, E.8, E.8
- [76] M. Shur, *GaAs Devices and Circuits*. Plenum Press, 1987. E.8, E.8
- [77] D. E. Aspnes, S. M. Kelso, R. A. Logan, and R. Bhat, “Optical properties of algaas,” *Journal of Applied Physics*, vol. 60, p. 754, 1986. F
- [78] S. T. F. M. Company, “N&k database,” 2010. F